

FINAL REPORT

Handheld Frequency Domain Vector EMI Sensing for UXO Discrimination

SERDP Project MM-1537

JULY 2010

Benjamin Barrowes
Kevin O'Neill
**U.S. Army Corps of Engineers Research and
Development Center**

This document has been cleared for public release



REPORT DOCUMENTATION PAGE*Form Approved*
OMB No. 0704-0188

The public reporting burden for this collection of information is estimated to average 1 hour per response, including the time for reviewing instructions, searching existing data sources, gathering and maintaining the data needed, and completing and reviewing the collection of information. Send comments regarding this burden estimate or any other aspect of this collection of information, including suggestions for reducing this burden to Department of Defense, Washington Headquarters Services, Directorate for Information Operations and Reports (0704-0188), 1215 Jefferson Davis Highway, Suite 1204, Arlington, VA 22202-4302. Respondents should be aware that notwithstanding any other provision of law, no person shall be subject to any penalty for failing to comply with a collection of information if it does not display a currently valid OMB control number. **PLEASE DO NOT RETURN YOUR FORM TO THE ABOVE ADDRESS.**

1. REPORT DATE (DD-MM-YYYY) 01-06-2009			2. REPORT TYPE Final		3. DATES COVERED (From — To) 23 March 2006 — 01 June 2009	
4. TITLE AND SUBTITLE Handheld Frequency Domain Vector EMI Sensing for UXO Discrimination					5a. CONTRACT NUMBER W74RDV60807091	
					5b. GRANT NUMBER	
					5c. PROGRAM ELEMENT NUMBER	
6. AUTHOR(S) Barrowes, Benjamin, E., and O'Neill, Kevin					5d. PROJECT NUMBER MM-1537	
					5e. TASK NUMBER	
					5f. WORK UNIT NUMBER	
7. PERFORMING ORGANIZATION NAME(S) AND ADDRESS(ES) U.S. Army Corps of Engineers, Engineer Research and Development Center Cold Regions Research and Engineering Laboratory (CRREL) 72 Lyme Road Hanover, NH 03755					8. PERFORMING ORGANIZATION REPORT NUMBER	
9. SPONSORING / MONITORING AGENCY NAME(S) AND ADDRESS(ES) SERDP Program Office 901 North Stuart Street, Suite 303 Arlington, Virginia 22203-1821 (703) 696-2127					10. SPONSOR/MONITOR'S ACRONYM(S)	
					11. SPONSOR/MONITOR'S REPORT NUMBER(S)	
12. DISTRIBUTION / AVAILABILITY STATEMENT Approval for public release; distribution is unlimited.						
13. SUPPLEMENTARY NOTES The views, opinions and/or findings contained in this report are those of the authors and should not be construed as an official U.S. Government position, policy or decision, unless so designated by other documentation.						
14. ABSTRACT SERDP project MM-1537 entitled "Handheld Frequency Domain Vector EMI Sensing for UXO Discrimination" is complete. The GEM-3 ⁺ incorporated two new aspects of EMI instrumentation with encouraging results: frequency domain vector receivers, and a "beacon" positioning system. This report contains the final design, engineering challenges, modeling advancements, and data analysis results from this project. This vector receiver coupled with the beacon positioning system resulted in a versatile prototype instrument delivering high quality, diverse data well suited to rigorous models of UXO and soil. New algorithms aimed at utilizing the high quality data from the GEM-3 ⁺ was developed including the Generalized Standardized Excitations Approach (GSEA) and Normalized Surface Magnetic Source (NSMS). Results from this project suggest a further need for high quality, production instruments in the frequency domain suited to UXO remediation efforts.						
15. SUBJECT TERMS keywords; electromagnetic induction, handheld, frequency domain, rigorous models, inversion						
16. SECURITY CLASSIFICATION OF:			17. LIMITATION OF ABSTRACT	18. NUMBER OF PAGES	19a. NAME OF RESPONSIBLE PERSON	
a. REPORT	b. ABSTRACT	c. THIS PAGE			Benjamin E. Barrowes	
U	U	U	UU	169	19b. TELEPHONE NUMBER (include area code) (603)646-4822	

Contents

1	Objectives	1
2	Background	2
3	Materials and Methods: GEM-3\mathcal{D}^+ Hardware	7
3.1	GEM-3 \mathcal{D}^+ Design	7
3.1.a	GEM-3 \mathcal{D}^+ Specifications	7
3.1.b	Early Progress	7
3.2	GEM-3 \mathcal{D}^+ Continuing Development	8
3.2.a	Cord Sensitivity Issue	8
3.2.b	Head Deformation Issue	8
3.2.b.(1)	Final Head Design	16
3.2.b.(2)	Sensor Electronics	17
3.3	GEM-3 \mathcal{D}^+ as Beacon Positioning System	20
3.3.a	Straight Line Tests	23
3.4	GEM-3 \mathcal{D}^+ Complete	29
4	Materials and Methods: GEM-3\mathcal{D}^+ Software	32
4.1	A vector handheld frequency-domain sensor for UXO identification	33
4.1.a	Executive Summary	33
4.1.b	Introduction	33
4.1.c	The GEM-3 \mathcal{D}^+ Sensor	34
4.1.c.(1)	Integrating over the areas of the receivers	35
4.1.c.(2)	The other receivers	36
4.1.c.(3)	Beacon positioning	37
4.1.d	Forward models	38
4.1.d.(1)	The dipole approximation	38
4.1.d.(2)	The Generalized Standardized Excitation Approach	39
4.1.e	Results	41
4.1.f	Conclusion	41
4.2	Soil Response of the GEM-3 \mathcal{D}^+	44
4.3	Estimating magnetic susceptibility from EMI data	55
4.3.a	Executive Summary	55
4.3.b	Introduction	55
4.3.c	EMI Scattering for Magnetic Rough Soil	56
4.3.d	Estimation of Soil's Magnetic Susceptibility from GEM-3 Measurement Data	58
4.3.e	Results	61
4.3.f	Conclusion	61
4.4	Absolute Calibration of EMI Measurements	66
4.4.a	Introduction and Background	66
4.4.b	Test Instrumentation	67
4.4.c	Recovery of the Conversion Factor	68
4.4.c.(1)	Modeling of Metallic Spheres	69
4.4.c.(2)	Modeling of the Primary field	70
4.4.c.(3)	Modeling of the Receiver Loop	70
4.4.c.(4)	Measurements	71

4.4.c.(5) Matching Algorithm	71
4.4.d Results	72
4.4.e Application of the Conversion Factor	73
4.4.f Conclusion and Discussion	75
4.5 Generalized Standardized Excitations Approach	77
4.5.a Introduction	78
4.5.b Generalized Standardized Excitation Approach (GSEA)	80
4.5.c Frequency-Dependent Magnetic Susceptibility	83
4.5.d Numerical Results	83
4.5.d.(1) The universal RSS	83
4.5.d.(2) EMI response for soil with frequency-dependent susceptibility	86
4.5.e CONCLUSION	87
4.6 NSMS Modeling of GEM-3 \mathcal{D}^+ and HAP Method	88
4.7 EMI from Ellipsoidal Targets	92
4.7.a Introduction	92
4.7.b Secondary fields due to uniform incidence	95
4.7.c Secondary fields due to GEM-3 incidence	97
4.7.d Conclusion	103
5 Results and Discussion – GEM-3\mathcal{D}^+	104
5.1 Initial Data and Reasonableness Checks	104
5.2 Blind Test Suite #1 Training Data	112
5.3 Blind Test Suite #1 Results	114
5.4 Blind Test Suite #2	120
5.4.a Blind Test Suite #2 Results	123
6 Conclusions and Implications	126
APPENDICES	
A Appendices – Supporting Data	127
B List of Scientific/Technical Publications	127
C Other Supporting Materials	127
C.1 Data Acquisition Sequence from the GEM-3 \mathcal{D}^+	127
C.2 Beacon Positioning System Construction Details	132
C.3 GEM-3 \mathcal{D}^+ Data Processing - Static and Dynamic	137
C.3.a Introduction	137
C.3.b Reading the data	137
C.3.c Background subtraction	138
C.3.c.(1) Initial approach	138
C.3.c.(2) Two-height approach	139
C.3.d An example of the first approach	141
C.3.e Example of the second approach	147
References	147

Abstract

SERDP project MM-1537 entitled “Handheld Frequency Domain Vector EMI Sensing for UXO Discrimination” is complete. The original objectives of MM1537 consisted of both hardware and software goals. On the hardware side, the goal was to develop an innovative vector (multi-axis) handheld UWB electromagnetic induction sensor in the frequency domain, with precise 3-D positioning, for close interrogation of anomalies. This new instrument would allow a new higher level of UXO discrimination in the vicinity of a noteworthy magnetic response. Data processing software accompanying the new instrument would also be developed. The goal here was to develop clutter-tolerant signal processing for UXO discrimination using the data provided by the new sensor, based on new, high-fidelity, physically complete forward modeling (the Standardized Excitation Approach), rigorous instrument characterization, and on new processing techniques.

We have constructed the GEM-3 \mathcal{D}^+ along with a positioning system with subcentimeter accuracy at a range of about 2 meters. This new instrument has been successfully used to acquire data both under lab conditions and in test plots with emplaced targets. Results from all blind tests (see Sec. 5) indicate the GEM-3 \mathcal{D}^+ can acquire diverse and accurate vector data with a SNR similar to or better than prior GEM models. Single target inversion results for laboratory blind tests were 100% accurate. Blind tests from the test plots at CRREL, with either one or two targets in close proximity, were also very encouraging though less accurate.

A novel “beacon” positioning, which uses the primary field of the GEM-3 \mathcal{D}^+ itself to locate the sensor head, was developed and successfully deployed. Early ground and stiffness sensitivities were overcome with limited redesigning of the main sensor head. The GEM-3 \mathcal{D}^+ successfully acquires three axis data of the secondary field near the center of the instrument head while remaining portable for operators and reproducible by Geophex Ltd.. Details of the GEM-3 \mathcal{D}^+ hardware development can be found in Sec. 3.

Our group has developed algorithms and models which accompanied the development of the GEM-3 \mathcal{D}^+ hardware. These algorithms include EMI models of ground response including the effects of a non-flat surface/air interface, methods to calibrate EMI instruments based on the magnitude of the secondary field from canonical objects, models of the broadband EMI response of ellipsoids, extensions of the Standardized Excitations Approach (SEA), and improvements to the Normalized Surface Magnetic Source (NSMS) model. Details of these models and algorithms can be found in Sec. 4.

The GEM-3 \mathcal{D}^+ is now a fully functioning EMI instrument capable of vector sensing of magnetic anomalies while being well located within a limited range. For precise, queued interrogation of anomalies, the GEM-3 \mathcal{D}^+ provides diverse, accurate, frequency domain data of the secondary EMI field suitable for inversion and discrimination with high fidelity, rigorous models.

List of Acronyms (and page references to first use)

BOR	body of revolution – first used on page (55)
CRREL	Cold Regions Research and Engineering Lab – first used on page (1)
DSP	Digital Signal Processor – first used on page (2)
EM	ElectroMagnetic – first used on page (2)
EMI	Electromagnetic Induction – first used on page (iii)
ERDC	Engineering Research and Development Center – first used on page (1)
FD	Frequency Domain – first used on page (1)
GEM-3 ⁺	Geophex GEM-3 including a 3-dimensional receiver and integrated positioning system (subject of this final report) – first used on page (iii)
GPS	Global Positioning System – first used on page (2)
GSEA	Generalized Standardized Excitations Approach – first used on page (iii)
HAP	$\{\vec{H}, \vec{A}, \phi\}$ Vector magnetic field, Vector magnetic potential, scalar magnetic potential method – first used on page (6)
MAS	Method Auxiliary Sources – first used on page (55)
MM	Munitions Management – first used on page (iii)
MPV	Man-Portable Vector – first used on page (44)
MQS	magneto quasi-static – first used on page (56)
NSMS	Normalized Surface Magnetic Source – first used on page (iii)
PCB	printed circuit board – first used on page (v)
PCB	printed circuit board – first used on page (18)
ppm	Parts Per Million – first used on page (8)
RMS	Root Mean Squared – first used on page (28)
RSS	reduced source set – first used on page (79)
Rx	Receiver – first used on page (3)
SEA	Standardized Excitations Approach – first used on page (iii)
SERDP	Strategic Environmental Research and Development Program – first used on page (iii)
SNR	Signal-to-noise ratio – first used on page (iii)
SON	SERDP Statement of Need – first used on page (1)
SPA	small penetration approximation – first used on page (92)
TD	Time Domain – first used on page (3)
Tx	Transmitter – first used on page (3)
USACE	United States Army Corps of Engineers – first used on page (1)
UWB	Ultra-wideband – first used on page (1)
UXO	UnExploded Ordnance – first used on page (iii)
VRM	viscous remanent magnetization – first used on page (55)

Keywords: electromagnetic induction, handheld, frequency domain, rigorous models, inversion

Acknowledgements: This project was funded by the Strategic Environmental Research and Development Program (SERDP) under project MM-1537. We worked closely with Geophex personnel especially I. J. Won and Bill SanFilipo. Special thanks go to Jesse Stanley and Rosanne Stoops at CRREL who took much of the data presented here. Drs. Jeff Marqusee and Anne Andrews, and the review committee for SERDP, provided support and constructive reviews during the course of the project.

List of Figures

2.0.1	General representation of received time domain signal (R) vs log of time.	4
2.0.2	An EMI sensor field impinges on a UXO, which tends to respond most strongly along its axis, producing a response that strikes the receiver at an arbitrary angle relative to the vertical.	5
3.1.1	GEM-3 \mathcal{D}^+ basic geometrical design. Table showing coil parameters and frequency characteristics omitted: proprietary.	9
3.1.2	GEM-3 \mathcal{D}^+ preliminary drawing 1.	10
3.1.3	GEM-3 \mathcal{D}^+ preliminary drawing 2.	11
3.1.4	GEM-3 \mathcal{D}^+ preliminary drawing 3.	12
3.1.5	GEM-3 \mathcal{D}^+ preliminary drawing 4. Final design for receiver coils is shown in Fig. 3.2.6.	13
3.1.6	GEM-3 \mathcal{D}^+ preliminary drawing 5.	14
3.2.1	Pictures of the GEM-3 \mathcal{D}^+ in development at an intermediate stage before finalization of the sensor head.	15
3.2.2	Plexiglass gussets glued to GEM-3 \mathcal{D}^+ sensor head.	16
3.2.3	Foam-core gussets epoxied to GEM-3 \mathcal{D}^+ sensor head.	17
3.2.4	GEM-3 \mathcal{D}^+ sensing head and coil frames	18
3.2.5	Beginning stage of wiring. All three receiver coils are now potted, electrically shielded (silver coating), and epoxy-painted for protection. Notice a small preamp printed circuit board (PCB) for each receiver coil taped to the round z-axis receiver coil.	18
3.2.6	Final drawing of the CRREL GEM-3 \mathcal{D}^+ sensing head.	19
3.2.7	GEM-3 \mathcal{D}^+ electronic block diagram	20
3.2.8	Custom-designed DSP module for the GEM-3 \mathcal{D}^+	20
3.2.9	Transmitter block diagram with red lines showing power flow and orange lines data flow.	21
3.2.10	Detail of the transverse receiver coils on the GEM-3 \mathcal{D}^+	22
3.3.1	Concept of GEM-3 \mathcal{D}^+ positioning system. The (assumed) dipolar shape of the GEM-3 \mathcal{D}^+ primary field is recorded by two triaxial receivers held in a fixed relationship.	23
3.3.2	Beam holding the two triaxial receivers of the GEM-3 \mathcal{D}^+ positioning system. . .	24
3.3.3	Coordinate systems for the target, beam, and GEM-3 \mathcal{D}^+	24
3.3.4	Beacon positioning system and plank setup for initial demonstration at Geophex facility.	25
3.3.5	Beacon positioning system data along a board for the entire length.	25
3.3.6	Beacon positioning system data along a board. Near range.	26
3.3.7	Beacon positioning system data along a board. Intermediate range.	26
3.3.8	Beacon positioning system data along a board. Large range.	27
3.3.9	Beacon positioning system real time feedback of EMI data (not shown) and position.	27
3.3.10	GEM-3 \mathcal{D}^+ beacon positioning system principles.	28
3.3.11	Complete setup of the beacon positioning system tests at Geophex.	29

3.3.12	Results for beacon positioning system test #1. The nearest edge of the gridboard is 1m from the beam. The horizontal projection of locator measured relative position (blue diamonds) vs. template grid (red crosses). There are 50 samples at each position. The 3-dimensional rms error is 0.77 cm. Note, one grid point is missing due to data acquisition dropout.	30
3.3.13	Results for beacon positioning system test #2. The nearest edge of the gridboard is 1.5m from the beam. Relative measured position (blue) plotted on the ideal grid (red) for the template at 1.5 m closest edge from the locator beam. There are 50 samples superposed at each point. The 3-D rms error is 0.92 cm.	31
3.4.1	Final GEM-3 \mathcal{D}^+ instrument.	32
4.1.1	GEM-3 \mathcal{D}^+ sensor and measurement grid	33
4.1.2	(Left) The field H_z^{pr} due to the GEM-3 \mathcal{D}^+ slightly above the plane of the transmitter coils. The central cavity where the primary flux vanishes is clearly visible. (Right) The field H_z^{pr} due to the GEM-3 \mathcal{D}^+ on the plane of the transmitter coils, this time seen in profile.	35
4.1.3	Integrated (blue) and averaged (green) flux profiles on a grid above an upright dipole; from left to right we have the z -, x -, and y -components. The red is the difference between the two.	37
4.1.4	Integrated (blue) and averaged (green) flux profiles on a grid above an \hat{x} -directed dipole; from left to right we have the z -, x -, and y -components. The red is the difference between the two.	38
4.1.5	(Upper) Quadrature part of the flux through the three receiver coils for an H-83 UXO with nose tilted 45° down. (Lower) Extracted polarizability elements (dashed lines: inphase part; solid lines: quadrature part); it is clearly seen that the object exhibits cylindrical symmetry.	39
4.1.6	Integrated (blue) and averaged (green) flux profiles on a grid above a sphere; from left to right we have the z -, x -, and y -components. The red is the difference between the two.	42
4.1.7	(Upper) “Training” field used to extract the GSEA dipole moments of an aluminum sphere; (Lower) Picard plot showing the singular values of $\Gamma^T \Gamma$	43
4.2.1	Setup of GEM-3 \mathcal{D}^+ at Lebanon Crushed Stone over “sump sand”.	44
4.2.2	Burying a steel sphere in the “sump sand”.	45
4.2.3	Inphase and quadrature components of GEM-3 \mathcal{D}^+ taken over “sump sand” with height decreasing left to right.	46
4.2.4	EMI sensor above a halfspace, including a bump on the soil-air interface.	47
4.2.5	GEM-3 \mathcal{D}^+ setup comparing “sump sand” data to “sump sand”+sphere data.	47
4.2.6	GEM-3 \mathcal{D}^+ inphase response showing the substantial soil response contaminating the H_z receiver but not the H_y receiver.	48
4.2.7	Soil model match to GEM-3 \mathcal{D}^+ data using scale factor.	49
4.2.8	Soil model match to GEM-3 \mathcal{D}^+ data using scale factor.	49
4.2.9	Hypothesized relaxation type time response for real soil permeabilities.	51
4.2.10	Measured GEM-3 (“converted”) and MPV responses from a sphere, observed at the same distance, when each response has been scaled additionally by the primary field from each instrument.	52

4.2.11	Comparison of measured responses of the soil to the GEM-3 and from the MPV, from about the same observation point, when the illumination of the soil surface has been scaled to be the same for each instrument. The red GEM-3 response, converted to TD, is flat before the step shut off at time zero, at which point it theoretically goes to zero, instantaneously. The blue MPV data start some finite time after shutoff ($\sim 10^{-4}$ s) and decay thereafter.	53
4.2.12	Hypothetical relaxation curves in (log) time for different constituents of some soil.	54
4.3.1	3-D rough surface used for computational model.	57
4.3.2	Experimental setup of GEM-3 sensor at various heights above the ground.	58
4.3.3	Mean value of the predicted magnetic susceptibility versus frequency.	59
4.3.4	1-D Rough surface. In meters.	60
4.3.5	Scattered magnetic field for 1-D rough surface.	60
4.3.6	Standard deviation and mean value for the BOR rough surfaces versus RMS height and correlation length.	62
4.3.7	3-D random rough surface.	63
4.3.8	Scattered EMI field from 3d-rough surface.	63
4.3.9	Standard deviation and mean value for the 3d rough surfaces versus RMS height at fixed surface correlation length.	64
4.4.1	Flow chart of instrument's process, to be paralleled by the modeling sequence. If normalization is performed by the instrument then the lower, shaded set of boxes may be deleted in the model and an arbitrary (e.g., unit) current assumed.	68
4.4.2	Block diagram illustrating the search algorithm.	71
4.4.3	Figure showing the matching between model and measurement of a steel sphere at a single grid point.	72
4.4.4	Plot of the variation of the retrieved conversion factor, as a percent error from 4.933×10^3 , for the steel sphere as a function of position.	73
4.4.5	Plot of the variation of the retrieved conversion factor, as a percent error from 4.933×10^3 , for the brass sphere as a function of position.	74
4.4.6	Plot of the variation of the retrieved conversion factor, as a percent error from 4.933×10^3 , for the aluminum sphere as a function of position.	75
4.4.7	Plot of the variation of the retrieved conversion factor, as a percent error from 4.243×10^3 , for the aluminum sphere as a function of position. No integration was performed over the receiver loop.	76
4.4.8	Comparison between GEM-3 measured inphase (I) and quadrature (Q) ground response and prediction using half-space soil model with an applied scaling factor.	77
4.5.1	Problem geometry and reduced set of sources \bar{p}_i^{pmn} distributed along rings on the spheroid surface.	79
4.5.2	Frequency-domain EMI response for 81 mm UXO; (a) GEM-3 excitation; (b) nose up vertical, (c) nose up 45 inclination, (d) horizontal.	84
4.5.3	Time-domain EMI response for 81-mm UXO; (a) EM-3 excitation; (b) nose up vertical, (c) nose up 45 inclination, (d) horizontal.	85
4.5.4	EMI response for a magnetically susceptible soil versus the sensor height and frequency. (a) Inphase part; (b) quadrature part.	86
4.5.5	EMI response for 81 mm UXO; (a) Frequency domain, (b) Time domain.	87

4.6.1	Comparison of H_x from the GEM-3 \mathcal{D}^+ and NSMS model predicted response. Data at 90Hz over a steel sphere, inphase part.	90
4.6.2	Comparison of H_y from the GEM-3 \mathcal{D}^+ and NSMS model predicted response. Data at 90Hz over a steel sphere, inphase part.	91
4.6.3	Comparison of H_z from the GEM-3 \mathcal{D}^+ and NSMS model predicted response. Data at 90Hz over a steel sphere, inphase part. 3 levels with 81 points on each level.	91
4.7.1	Configuration of the problem: an ellipsoid of material parameters ($\mu_1 = 100\mu_0$, $\sigma_1 = 10^7$ [S/m]) is surrounded by free-space ($\mu_2 = \mu_0$, $\sigma_2 \approx 0$) and is excited by a GEM-3 instrument [1] modeled as two current loops (figure not to scale). The semi-axes of the ellipsoid are denoted by a , b , and c (with $a > b > c$) along the \hat{x} , \hat{y} and \hat{z} directions, respectively (see the Appendix for mathematical details on the ellipsoidal coordinate system).	94
4.7.2	Real and imaginary parts of the secondary field \bar{H}^s produced by spheroids of elongations shown in the legend, buried 10 cm below the sensor, and under axial (upper panels) and transverse (lower panels) excitations. The material parameters are $\mu_1 = 100\mu_0$ and $\sigma_1 = 10^7$ [S/m]. The sphere case (denoted by 'e=1 (n)') has been normalized by 1/3 for display convenience. The markers are obtained from the method presented in [2].	98
4.7.3	Similar to Fig. 4.7.2 for an object buried at 30 cm and rotated by 45 degrees. Upper panel: H_x . Lower panel: H_z . Note that for this specific case only, the ranges have been set to $v \in [0, 0.7]h$ for prolate spheroids and $\mu \in [0, 0.7](k - h) + h$ for oblate spheroids.	99
4.7.4	Real and imaginary parts of the secondary field produced by an ellipsoid of dimensions 1 cm in \hat{x} , 2 cm in \hat{y} , and 3 cm in \hat{z} . The material parameters are $\mu_1 = 100\mu_0$ and $\sigma_1 = 10^7$ [S/m], and the ellipsoid is buried 10 cm below the sensor. The reference markers have been obtained using the method of auxiliary sources [3].	100
4.7.5	Real and imaginary parts of the secondary field produced by a spheroid of elongation $e = 3$ (left panel) and $e = 1/3$ (right panel) buried 10 cm below the GEM-3 instrument. The material parameters are $\mu_1 = 100\mu_0$ and $\sigma_1 = 10^7$ [S/m]. The primary field is modeled using Eqs. (4.7.12). The reference markers (marked 'ref' in the legend) are obtained from the method presented in [2].	101
4.7.6	Simulated (solid lines) and experimentally measured (circles) real and imaginary parts of the magnetic field along the three axes of an ellipsoid: case A is along the longest dimension (15 cm), case B is along the second longest dimension (7.5 cm), case C is along the shortest dimension (3.75 cm). The location of the resonant frequency in the three cases follow this geometrical progression, as expected. The optimized parameters in the respective cases are: ($\mu_1 = 140\mu_0$, $\sigma_1 = 4.5 \times 10^6$ [S/m], $\gamma = 4.7 \times 10^3$) ($\mu_1 = 150\mu_0$, $\sigma_1 = 5 \times 10^6$ [S/m], $\gamma = 4.5 \times 10^3$) ($\mu_1 = 20\mu_0$, $\sigma_1 = 1.2 \times 10^6$ [S/m], $\gamma = 4.2 \times 10^3$). The dashed line in case C has been obtained with ($\mu_1 = 100\mu_0$, $\sigma_1 = 1 \times 10^7$ [S/m], $\gamma = 4.2 \times 10^3$). The numerical data have been obtained with tree modes in all cases ($N = 3$).	102
5.1.1	Initial reasonableness check of the GEM-3 \mathcal{D}^+ . Object is moved along a path below and offset to the GEM-3 \mathcal{D}^+	105
5.1.2	Initial reasonableness check of the GEM-3 \mathcal{D}^+ . Quadrature response at 450Hz.	106

5.1.3	GEM-3 \mathcal{D}^+ Z component of received field with sphere directly over the center of the instrument.	106
5.1.4	GEM-3 \mathcal{D}^+ Z component of received field with sphere to the sides of the instrument.	107
5.1.5	GEM-3 \mathcal{D}^+ X and Y component of received field at 3 positions. Inphase.	107
5.1.6	GEM-3 \mathcal{D}^+ X and Y component of received field at 3 positions. Quadrature.	108
5.1.7	H_z component of data from different transects of the received field over a 9x9 grid.	109
5.1.8	H_x component of data from different transects of the received field over a 9x9 grid.	110
5.1.9	H_z component of the received magnetic field over a steel sphere located the southeast of the sensor.	110
5.1.10	H_x, H_y components of the received magnetic field over a steel sphere located the southeast of the sensor.	111
5.1.11	Standard deviation of the raw 10Hz data of the 3 field components of the received magnetic field.	111
5.2.1	GEM-3 \mathcal{D}^+ on the lab grid for blind test suite #1.	112
5.2.2	Grid layout used for blind test suite #1.	113
5.2.3	60mm mortar in measurement setup for blind test suite #1.	113
5.2.4	Possible targets in library for test suite #1.	114
5.3.1	Total NSMS of blind test 1.	115
5.3.2	Total NSMS of blind test 2.	115
5.3.3	Total NSMS of blind test 3.	116
5.3.4	Total NSMS of blind test 4.	116
5.3.5	Total NSMS of blind test 5.	117
5.3.6	Total NSMS of blind test 6.	117
5.3.7	Total NSMS of blind test 7.	118
5.3.8	Total NSMS of blind test 8.	118
5.3.9	Geometry diagram and positions for blind tests derived from the HAP method compared to truth.	119
5.4.1	Contents of test plot #2 blind test suite #2.	120
5.4.2	Contents of test plot #3 blind test suite #2.	121
5.4.3	Contents of test plot #4 blind test suite #2.	122
C.3.1	Sensor position in the example data run. The convention in this and the following figures is: the sensor “warms up” as it takes data: <u>i.e.</u> , the trajectory is initially blue and transitions into red during the run. The background points are black dots.	141
C.3.2	Discrepancy in the x position between the first and third data files of a set.	142
C.3.3	Background-subtracted field at $f = 450$ Hz, inphase part	143
C.3.4	Background-subtracted field at $f = 450$ Hz, quadrature part	144
C.3.5	Background-subtracted 3D fields at $f = 450$ Hz.	145
C.3.6	Quiver plot showing the projection on the x - y plane of the quadrature part of the secondary field at $f = 450$ Hz. Joining the tails of the arrows can give a approximate estimate of the locations of the targets.	146
C.3.7	Sensor position in the second example data run.	147
C.3.8	Background-subtracted field at $f = 3930$ Hz, inphase part.	148
C.3.9	Background-subtracted field at $f = 3930$ Hz, quadrature part.	149
C.3.10	Background-subtracted 3D fields at $f = 3930$ Hz.	150

- C.3.11 Quiver plot showing the magnitudes of the x - and y -components of the quadrature part of the secondary field at $f = 3930$ Hz. Joining the tails of the arrows can give a approximate estimate of the locations of the targets. 151

List of Tables

1	Receiver coils characteristics	19
2	Correspondence between the elongations of spheroids and the size of the ellipsoids as shown in Fig. 4.7.1 and defined by Eq. (4.7.3).	96

1 Objectives

- Develop innovative vector (multi-axis) handheld UWB (ultra-wideband) electromagnetic induction sensor in the frequency domain, with precise 3-D positioning, for close interrogation of anomalies, i.e. for a new higher level of UXO discrimination in the vicinity of a noteworthy magnetic responses identified either by the new instrument or most likely by other surveying.
- Develop clutter-tolerant signal processing for UXO discrimination using the data provided by the new sensor, based on new, high-fidelity, physically complete forward modeling (the Standardized Excitation Approach), rigorous instrument characterization, and on new processing techniques (magnetic field pattern matching, general inversion for equivalent magnetic charge capacity, optimization by Differential Evolution, and classification with Support Vector Machines).

This project builds on SERDP SEED work (project #1353) in response to the needs expressed in UXSON-05-03, by developing innovative sensors and signal processing. The aim was and is to achieve a new level of UXO survey target characterization and false alarm rejection. The work will allow the Army and other DoD components to carry out mandated UXO cleanup more safely, effectively, and efficiently. The new fast processing and the portable nature of the products might also allow application in tactical situations and for active range maintenance, as well as for cleanup away from areas of conflict.

The positioning and measurement systems here are intended to link to dual mode navigation as may be developed under other SONs (Statement of Need). That is, these devices would provide the high density, fine mode, while positioning reference points are linked to locations identified in the coarse mode. More generally, the survey and processing systems contemplated are designed to be most effective under some degree of cuing. The default assumption is a high level of cuing, in which prior information indicates the approximate locale around an individual anomaly, on the order of meters. In both the small and larger scale areal coverage, surveying with a low level of cuing is also possible. That is, the cuing would simply consist of identification of some specific area some 10's to ≈ 100 m across, within which the new system would accomplish both coarse detection and fine interrogation. Reception of the horizontal magnetic field components would help indicate the direction of offset from a target location; and the user would then perform arbitrarily detailed sweeps around the indicated anomaly. Whether the system to be developed is employed in both coarse and fine mode of surveying or only in the latter, the primary focus of the work is on UXO discrimination during close interrogation of anomalies.

This work is designed in part to address realistic conditions: terrain with lumps, bumps, moguls, trenches, embankments... and possibly sparse vegetation. High density UWB EMI data will be obtained from a new man-portable, vector, FD (frequency domain) instrument with precise positioning (sub-cm local precision). The new system is designated below as the GEM-3Dplus (GEM-3 \mathcal{D}^+), meaning a fully integrated GEM-3D plus positioning. The instrument will be “handheld” in the sense that a reasonably hardy surveyor will be able to move the sensor head about freely in sweeps, tilts, and elevations, for perhaps a couple of hours, without relief. Ergonomic considerations are not given top priority here, as the result will be primarily a research instrument. The new data features provided by the instrument will be exploited by a new generation of original processing approaches based on the SEA and NSMS, as well as on other approaches described below. The potential benefits envisioned in some of the proposed processing approaches depend

on the new level of data content. Also, conversely, the precision and diversity of data contemplated only make sense if a new generation of processing can take advantage of it. Thus we will develop the instrumentation, survey techniques, and processing together.

Relative to the system produced during the antecedent SEED work, the new GEM-3 \mathcal{D}^+ will incorporate a number of desirable developments as listed below:

1. New small ($\approx 5 \times 8$ cm), stackable DSP's (Digital Signal Processor), each 1 cm in thickness, so total stacked height for 3 DSP's \approx approx 3 cm. The DSP's synchronization, power, and communication will all be on a bus line (no wiring) with only one communication line, and a single RS485 connection at 1MBit/sec to an RS485/USB2 converter as the link to a computer;
2. Each DSP will provide an additional RS232 port for GPS (Global Positioning System) or any other external device such as the laser positioning system;
3. The frequency range will be increased from 48KHz to 96kHz, with low frequency limit of 30 Hz;
4. Larger diameter sensor head (54 cm) for more uniform primary field and greater depth of view, without significant loss of portability;
5. The 3 DSP's will be configured to increase the system performance (convolution is done in parallel for all three channels);
6. The transmitter will be a separate module connected to the DSP via RS422 digital audio communication;
7. New higher power transmitter with four times the voltage of the older system.
8. Standardized interface and software for the positioning system connection, allowing EM (ElectroMagnetic) data synchronization with timing pulses from GPS, inertial, or laser positioning;
9. Integration of positioning system of choice with the EM system so that EM and position data files are merged;
10. The device will be easily reproducible.

The minimum CPU required for system control will be on board, while wireless links to other computers will serve for data storage and processing. This will allow quasi-real time application of the processing, including possibly parallelized processing, which can then guide the testing in a flexible way. In the least, it will streamline design by separating the control and the storage/processing functions.

2 Background

Detection and especially discrimination of buried unexploded ordnance (UXO) from omni-present metallic clutter is a persistent, expensive, and pressing problem. While it is not yet clear whether or which other technologies might be best used in conjunction with electromagnetic induction (EMI) for UXO discrimination, it is clear that EMI is currently a front runner in the development of

new, more effective approaches. Virtually all EMI sensors transmit a "primary" field and receive signals ("secondary" field) using wire coil antennas. Frequency domain (FD) EMI systems use such coils to transmit (Tx) a "primary" magnetic field with selection of frequencies over a chosen band - possibly only a single frequency - simultaneously receiving (Rx) and recording responses to those frequencies (the "secondary" field). Thus a central problem in frequency domain sensors is the isolation of the receiving coils from the primary field, the latter being very large relative to the secondary field, particularly when the receivers are near the transmitters, as contemplated here. Physical separation of the Tx and Rx coils is a possible approach. However this typically degrades spatial resolution and handy manipulation of the instrument. Therefore, remaining with co-located Tx and Rx coils, we implement a "bucking" coil, which transmits a field that opposes the primary field at the location of the receiving coil. By canceling out the primary field at the receiver as much as possible, one is left (ideally) with only the secondary field from the target. Other approaches are possible for finding the secondary field amidst the much stronger primary field, e.g. using differencing schemes between stacked or symmetrically distributed coils, but the fundamental problem is the same.

The "bucking" discussion above is particularly pertinent when one attempts 3-D vector definition of the secondary field. The geometrical arrangement of the main and the bucking coils is crucial to successful suppression of the primary field at the receiver. However, to our knowledge no FD EMI instruments have been produced to date that are capable of suppressing the primary field in one receiver orientation while also suppressing it in other directions as well. Most imaginable arrangements of two bucking coils that work well for one receiver orientation would in fact exacerbate the problem for other receiver orientations. This observation would appear to favor the development of time domain (TD) systems for obtaining vector EMI response. Most TD systems operate by transmitting a steady signal, saturating a metal object of interest, then shutting the transmitter off. A receiver then records the secondary field from the object as that field decays in response to the sudden shut off. The receiver only operates while the transmitter is off, thereby dodging the primary field. While this bypasses the bucking problem, a number of things motivate us to proceed in the FD: FD systems claim the advantage in having superior control of selection and power in the frequency content of data produced, and thus in the equivalent time domain signal, which can readily be obtained from the FD data. In practice, FD systems are less band limited than TD systems and can therefore offer a greater equivalent time range of response than the actual TD systems. Consider Fig. 2.0.1 below.

While there has been progress in "very early time" EMI devices, in general TD devices are unable to shut off the transmitter and damp the effects of the transition quickly enough to get very early time data. Information in such data is the equivalent of high frequency FD data. The latter is of strong interest because it provides information on asymptotic limits of scattering behavior: The induced currents penetrate the target negligibly and the secondary fields they produce do not depend on the type of metal encountered. This may offer hope of avoiding very substantial complications in UXO discrimination, given that many if not most UXO are composites of different metals. At the other end of the spectrum, TD signals naturally fade as the target's responses wind down. This means that very late time data is unlikely to be detectable above the noise. Thus the equivalent of low frequency asymptotic limits will be poorly defined or absent. While FD systems must also struggle with some challenges in the equivalent very low frequency range, on the whole it is much more feasible to get data from them in that part of the EMI band. Many UXO produce significant response patterns in the 10's of Hz. Low frequency asymptotic limits and fundamental signal features containing basic target shape information appear in many cases only well below 30

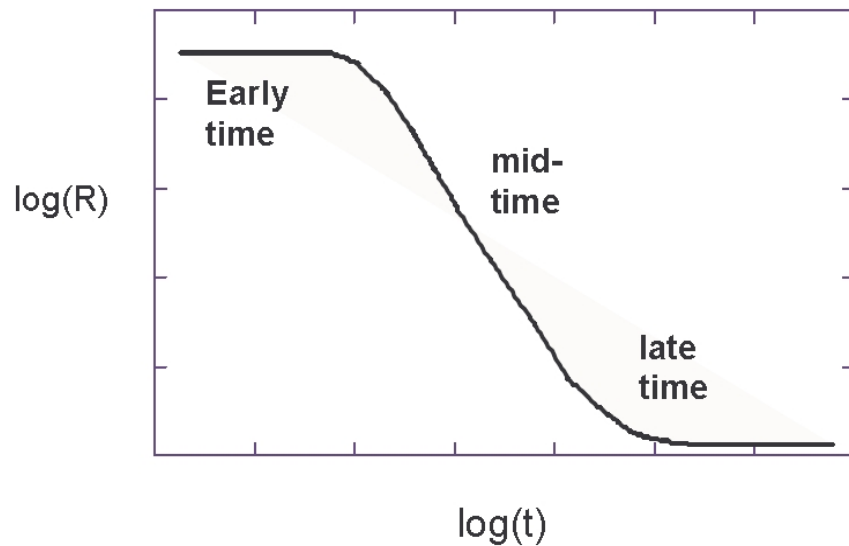


Figure 2.0.1: General representation of received time domain signal (R) vs log of time.

Hz [SERDP Project 1122, Final Report]. To get at the TD equivalent of these frequencies down to 1 Hz using TD instruments would require recording out to the order of tenths of a second. Highly unlikely. At least at the research level, FD EMI measurements have been made successfully over a continuous UWB ranging from a few Hz up to about 300 kHz, roughly the TD equivalent of spanning times from a micro-seconds to tenths of a second. Recent work by Geophex on TD systems in a GEM configuration may be an exception to the limitations cited above, and we look forward to encountering that new device.

Much of the motivation for this project derives from a desire to develop further a new generation of EMI forward modeling; to apply it in innovative processing; and to develop instrumentation that will provide the data most likely to support this new processing to best advantage. The new forward modeling will generally be based on the Standardized Excitations Approach (SEA), though all processing will not be restricted to SEA implementations. The theory and detailed development of SEA have been presented in various fora [1-12]. Here we only present a general sketch of the underlying ideas so that the direction taken in some of the proposed work may be understood. The essence of the method lies in its ability to provide physically complete forward modeling - including all target heterogeneity, near and far field, and internal interaction effects - while being fast enough for inversion and classification computations.

During antecedent SERDP SEED work, the configuration of the existing Geophex GEM-3 [4] was used as a starting point for the new vector device. The essential difference was that the new instrument would receive and record separately three orthogonal magnetic field components instead of one. This was accomplished by adding two receiver coils that are the same size as the original single coil but which are perpendicular to it and to each other. These additional coils escape being swamped by the primary field in part because they are near the null region engineered for the original in-plane receiver loop. For the most part, however, they are protected by their orientation. The plane of each of the new receiver coils is completely parallel to the transmitted field lines from the perpendicular transmitter coils (Fig. 2.0.2). Because the receiver coils respond only to rate of

change of magnetic flux that passes through them, in principle the additional coils do not register the primary field. The bench level instrument that was constructed and tested has an expanded bandwidth relative to established versions of the GEM-3, ranging from the same lower limit of 30 Hz up to at least 98 kHz, with a maximum of about 15 frequencies recordable in each channel, i.e. for each orthogonal signal component (using slightly fewer is recommended).

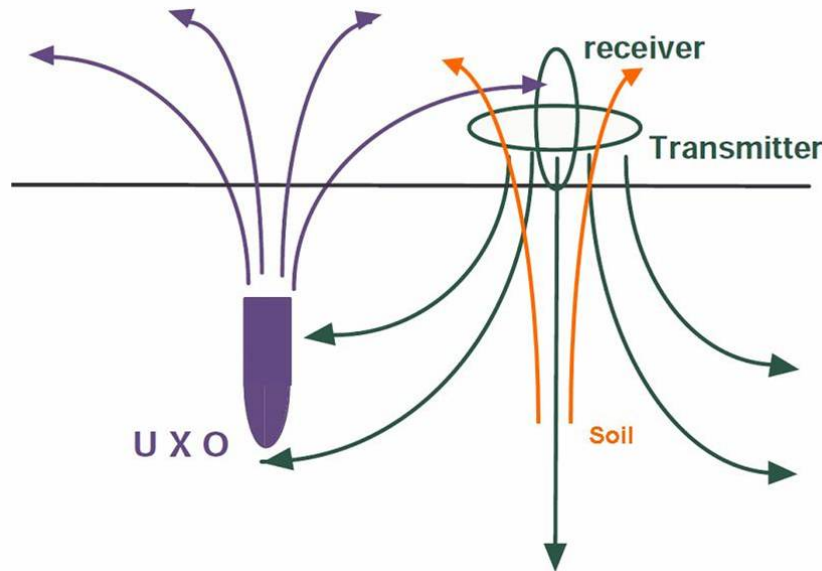


Figure 2.0.2: An EMI sensor field impinges on a UXO, which tends to respond most strongly along its axis, producing a response that strikes the receiver at an arbitrary angle relative to the vertical.

The bench version of the instrument that was produced appears to work well by both quantitative and qualitative criteria. Proper (and illuminating) symmetries and asymmetries appear in the different received field components as the sensor head is swept over UXO's and other objects. Measured data for machined spheroids of different materials and shapes compare very well to corresponding analytical solutions that account for the details of the GEM's primary field. The laser positioning system that was implemented is said (by the supplier) to be capable of sub-millimeter accuracy, and was configured to provide all tilt angles in a version of the instrument dubbed the GEM-3DL. In various benign tests the integration of the system performed well.

Regarding the EMI measurement system, the task that remains is proper design and implementation so that it is melded into an efficient and coherent unit, including direct integration with the positioning system via a conventionally recognizable timing pulses. Basically, for the sake of showing that the basic concept of FD vector EM measurement could work, the SEED work effectively patched together in parallel three traditional GEM-3's, one associated with each receiver loop. Given what was learned during the SEED exercise and also the recent advancement in components at affordable prices (e.g. digital signal processors – DSP's), we are now positioned to construct and integrate the instrument as it should be done. It has also become clear that the easiest and most reliable way to perform the EM-positioning integration is to key the EM measurement timing to a pulse from the positioning system, as opposed to vice versa.

The GEM-3D produced in the SEED effort used a laser positioning system: the ArcSecond laser positioning system. The laser positioning system provided accuracies on the order of a few

mm of the instrument head. The positioning data provided by this system allows free movement of the sensor head at any elevation and tilt angle thus leading to a rich and diverse data set. Data from multiple elevations has helped in distinguishing target signals from widespread clutter responses; and in the general inversion/optimization calculations we have done, it significantly reduced or eliminated ill-conditioning. Also, horizontally distributed observation points allow “multi-look” data, i.e. views that stimulate and also register response from all sides of an object to be studied. All this requires very flexible positioning, i.e. both antenna movement and tracking thereof. In fact, without such positioning the new (and older GEM-3) sensor will not be useful for the next generation of processing towards which we strive. However significant design and integration issues remain. Both inadequate calibration of the laser system and especially timing disparities between both the different laser receivers and between the laser and the EM system precluded continuous motion of the sensor in recent field tests at the Aberdeen Proving Ground UXO Standardized Test Site. This makes for impractically slow surveying, even for testing purposes.

Initially, we planned to use the ArcSecond system with the new GEM-3 \mathcal{D}^+ in order to achieve the same level of positioning accuracy. However, early on in the project we reconsidered this design decision in light of recent developments in the area of “beacon” positioning systems (see Sec. 3.3) and because of factors mentioned above regarding the GEM-3 \mathcal{D}^+ . Beacon positioning systems rely on the primary field of the instrument itself to provide an accurate position of the sensor head. Using external receivers to detect and sample the primary field of the GEM-3 \mathcal{D}^+ , the location of the primary field (assumed dipolar) source can be inferred. The design, implementation, and resulting accuracy of this system is detailed below. This positioning system, in theory, is simpler to operate and maintain than the ArcSecond system. For example, the calibration of the system is far simpler for the beacon system, and the setup time is also greatly reduced. On the other hand, the range of this system is less than the laser positioning system.

In simulations and lab measurements, we have seen distinct benefits from vector data in the task of defining unambiguously the response of UXO’s and of other objects to the basic modes of excitation. Vector or “3-D” data means that three orthogonal components of the scattered magnetic field are measured at the receiver location, thereby completely defining the field there that constitutes the object’s response. The idealized representation in Fig. 2.0.2 shows how a UXO response field will generally strike the receiver at some arbitrary angle relative to the vertical, i.e. relative to the direction in which the established sensors record the signal.

The rest of the report proceeds as follows. Sections 3 and 4 detail the materials and methods associated with the design and implementation of the hardware of the GEM-3 \mathcal{D}^+ as well as the software analysis algorithms developed in the course of this project. Section 4 includes discussions on some characteristics of the GEM-3 \mathcal{D}^+ (Sec. 4.1), the soil response of the instrument (Sec. 4.2), absolute calibration of the instrument (Sec. 4.4), the Generalized Standardized Excitations Approach (GSEA, Sec. 4.5), the NSMS and HAP methods (Sec. 4.6), and the response of the GEM-3 \mathcal{D}^+ to ellipsoidal targets (Sec. 4.7). These sections are followed by blind test results both from lab data and from test plot data at CRREL (Sec. 5). The Appendices contain supporting material such as operating procedures and a publication list follow the concluding section (Sec. 6).

3 Materials and Methods: Hardware Development of GEM-3 \mathcal{D}^+ Instrument

3.1 GEM-3 \mathcal{D}^+ Design

3.1.a GEM-3 \mathcal{D}^+ Specifications

The primary purpose of this project is to advance the existing GEM-3 EMI sensor to incorporate multiple axis viewing ("vector") capability that is expected to enhance the UXO detection and discrimination. Relative to the system produced during previous CRREL project, the new GEM-3 \mathcal{D}^+ will incorporate a number of advancements as listed below:

- Larger diameter sensor head (54 cm) for more uniform primary field and greater depth of view, without significant loss of portability
- The frequency range will be increased from 48 kHz to 96 kHz, with low frequency limit of 30 Hz
- Use of new small stackable DSPs, each about 1 cm in thickness. Synchronization, power, and communication will all be on a bus line. An RS485 connection at 1Mb/sec to an RS485/USB2 converter will serve as the link to a computer
- Each DSP with an additional RS232 port for GPS or any other external device such as the laser positioning system
- DSPs configured to increase the system performance (convolution is done in parallel for all four channels)
- A separate transmitter module connected to the DSP via RS422 digital audio communication
- New higher power transmitter with increased drive the voltage
- Standardized interface and software for the positioning system connection, allowing EM data synchronization with timing pulses from GPS, inertial, or laser positioning
- Integration of positioning system of choice with the EM system so that EM and position data files are merged
- Easily reproducible.

3.1.b Early Progress

This section describes our early design efforts for the GEM-3 \mathcal{D}^+ sensing head, transmitter and receiver coils, and structural assemblage of the coils and mechanical support structures. The GEM-3 \mathcal{D}^+ has two additional orthogonal vertical coils in addition to the existing GEM-3 geometry. Figure 3.1.5 shows the overall appearance of the GEM-3 \mathcal{D}^+ sensing head. The design provides the following features:

- Sensing head: 1/2" thick double-skin fiberglass foam core synthetic board with an overall diameter: 55 cm;
- Outer transmitter: 54 cm in diameter;

- Receiver coils: one circular horizontal coil in the magnetic cavity plus two rectangular vertical coils. The vertically offset rectangular shapes reduce the mandatory sensor ground clearance
- Maximum visibility of the target area by embedding many see-thru holes in the disk
- Minimum sensor head weight;
- The electronic console and battery to be mounted at the end of the handle bar, partly to act as a counter weight.

All three receiver coils, one circular and two rectangular, are designed to have an identical area-turn product. The two rectangular coils, as shown in Fig. 3.1.5, are symmetrically centered across the sensing disk. The main advantage for centering is that all three receiver coils are mathematically co-located (this was later changed, see below), which simplifies locating and interpreting targets. Otherwise, these coils may move arbitrarily upward.

Figure 3.1.1 shows the design sheet for this GEM-3 \mathcal{D}^+ . Basic design parameters include the diameters, turns, and wire sizes for Tx1 (outer transmitter), Tx2 (inner bucking transmitter), and Rx (the horizontal receiver coil). The two rectangular vertical coils (RxV1 & RxV2 -not shown in this design sheet) are made such that their area-turn product is identical to that of the horizontal coil. This sheet is based on the 12VDC supply, which is a mere scale factor for the transmitter moment. Higher supply voltages are used in the final design. The design shows a healthy transmitter moment of about 35 A·m² at 750 Hz, which compares favorably with the previous 40-cm diameter version having about 10 A·m² also at 750 Hz. The dipole loss due to Tx2 is only 5.37%. The sheet also shows the I- and Q-responses of the Rx in ppm to a known Q-coil between 30 Hz–96 kHz. The specs and location of the Q-coil are also indicated in the sheet.

Figures 3.1.2–3.1.6 show some preliminary drawings of the GEM-3 \mathcal{D}^+ . Later designs positioned the transverse receiver coils to be more flush with the bottom of the transmitter coil (see Fig. 3.2.6).

3.2 GEM-3 \mathcal{D}^+ Continuing Development

3.2.a Cord Sensitivity Issue

During the initial stages of testing the GEM-3 \mathcal{D}^+ at CRREL, we noticed an extreme sensitivity in the real part of the transverse components associated with any movement of the instrument. We eventually traced this sensitivity problem more specifically to issues of cord movement. Whenever the connecting cord from the sensor head to the electronics box was moved in the slightest amount, the transverse components of the received magnetic field were corrupted by a tens if not hundreds of ppm. Together with the Geophex engineers, the problem was traced back and solved so that this sensitivity issue was resolved.

3.2.b Head Deformation Issue

Prototype grade instruments often have several unforeseen issues arise during their development. After the sensitivity associated with cord movement was resolved, we noticed another type of sensitivity issue whenever we physically touched or moved the instrument. As it turned out, there was a further sensitivity associated with deformation of the relative position of the transverse receiver coils to each other. We decided to investigate whether it was the deformation of the entire head or

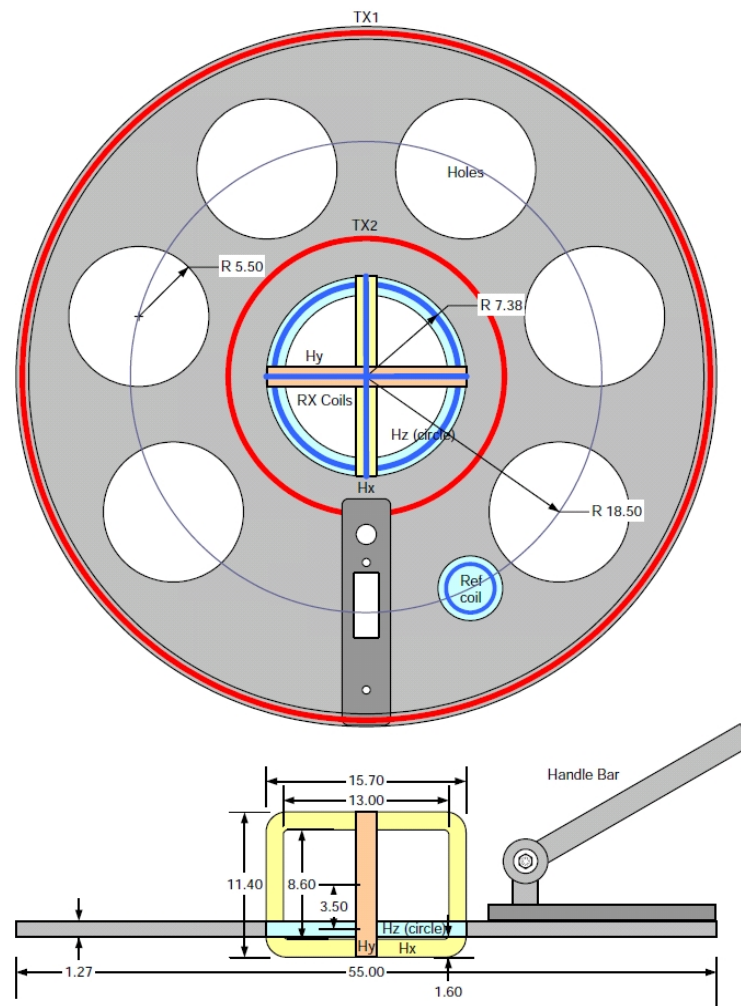
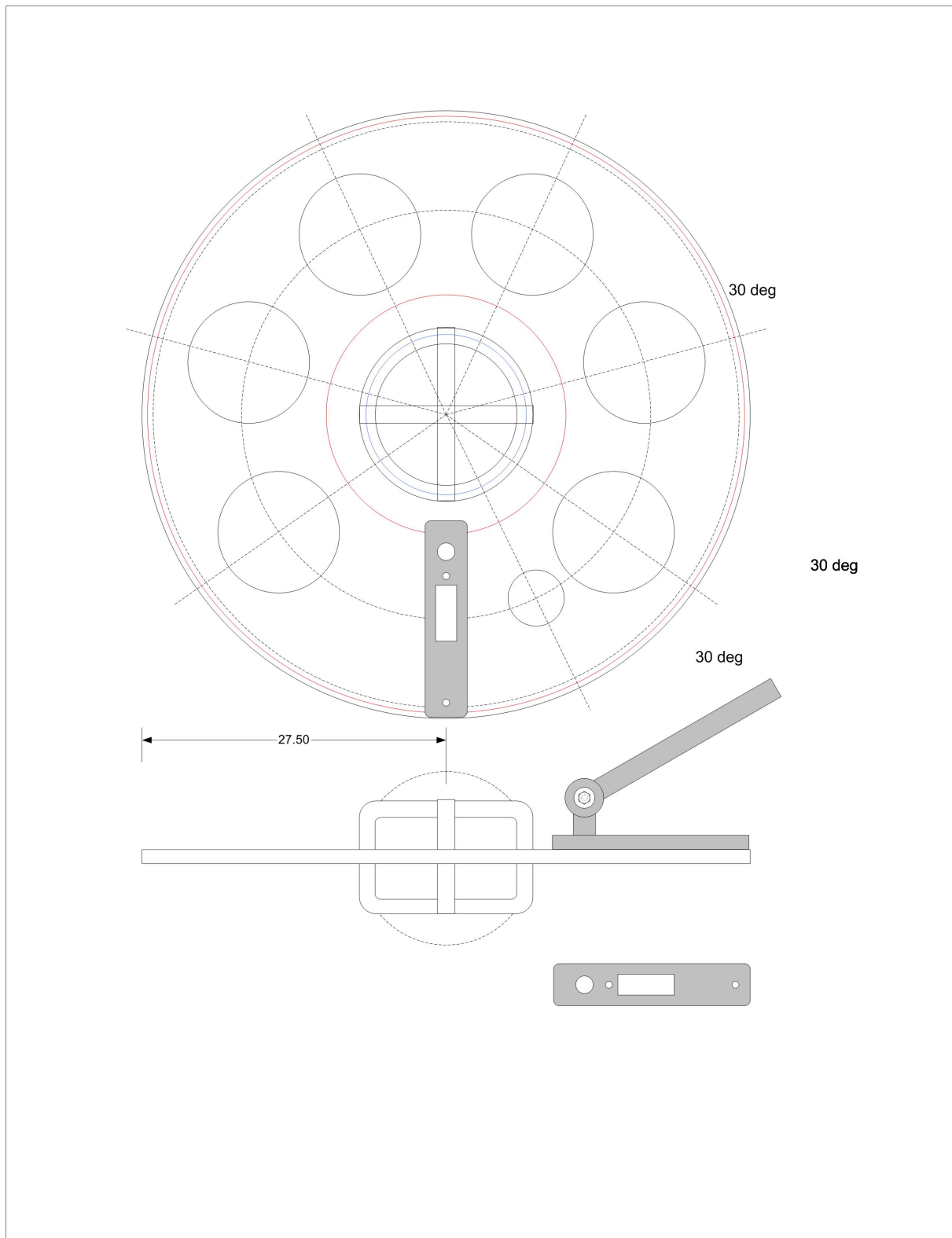
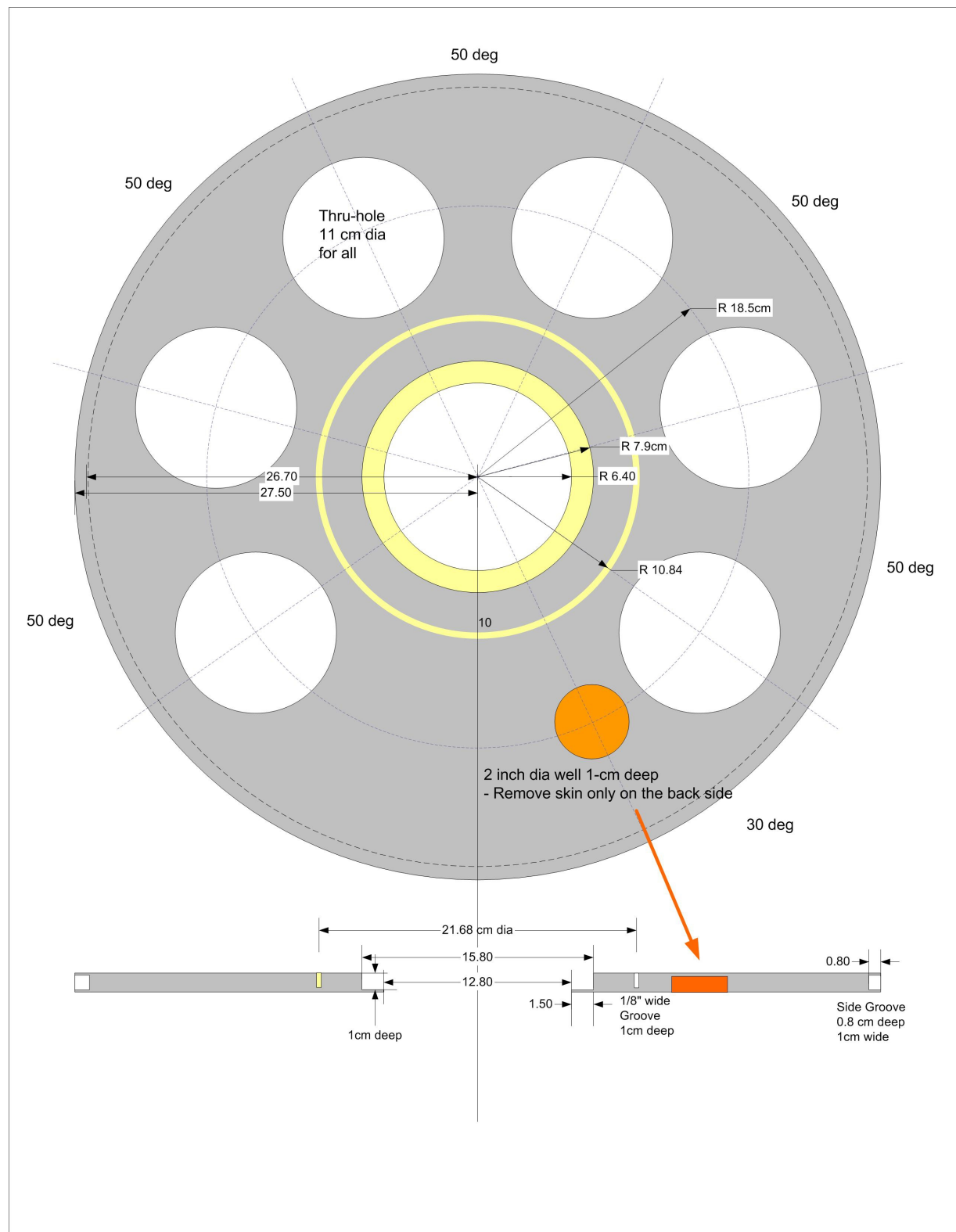
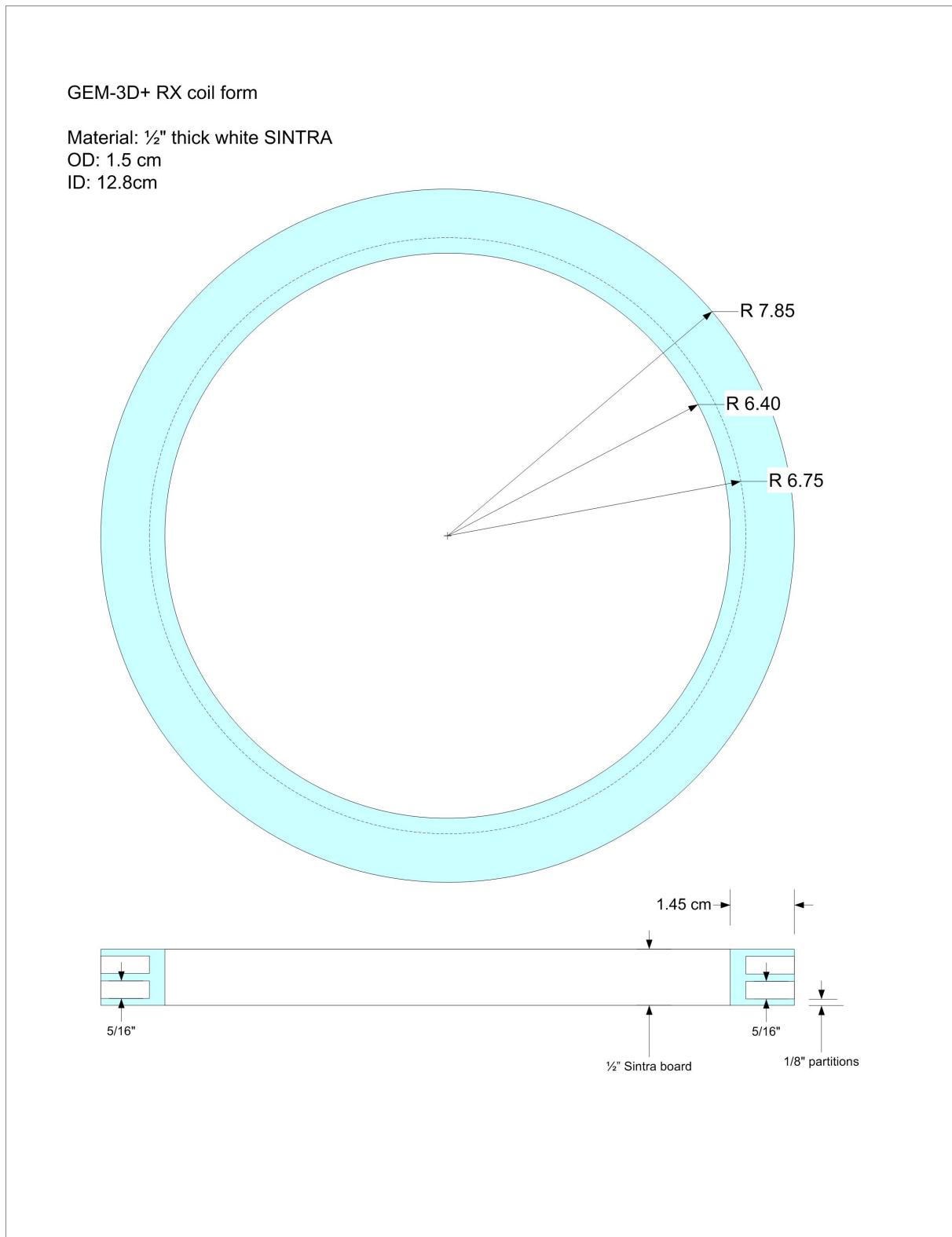


Figure 3.1.1: GEM-3 \mathcal{D}^+ basic geometrical design. Table showing coil parameters and frequency characteristics omitted: proprietary.

Figure 3.1.2: GEM-3 \mathcal{D}^+ preliminary drawing 1.

Figure 3.1.3: GEM-3 \mathcal{D}^+ preliminary drawing 2.

Figure 3.1.4: GEM-3 \mathcal{D}^+ preliminary drawing 3.

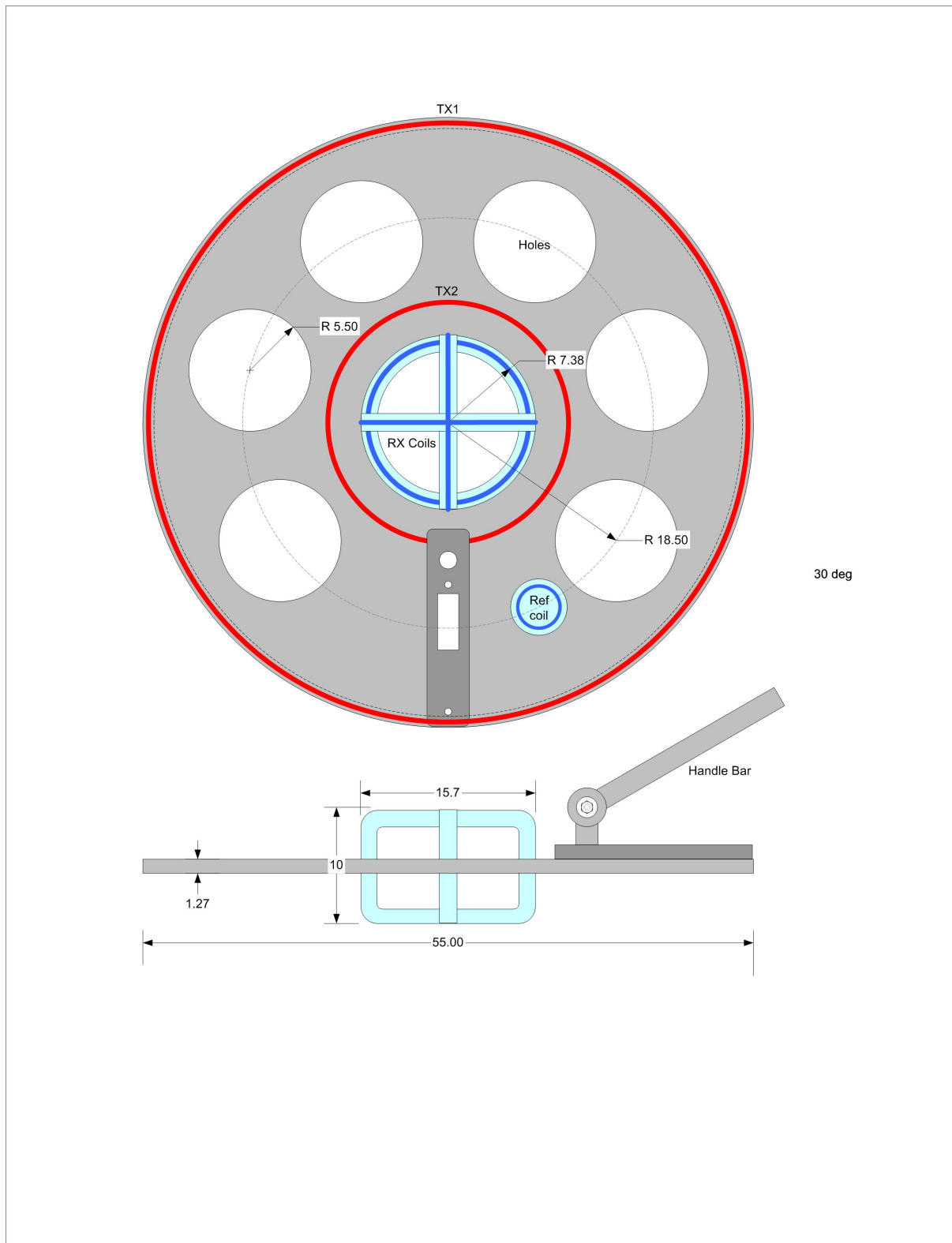


Figure 3.1.5: GEM-3 \mathcal{D}^+ preliminary drawing 4. Final design for receiver coils is shown in Fig. 3.2.6.

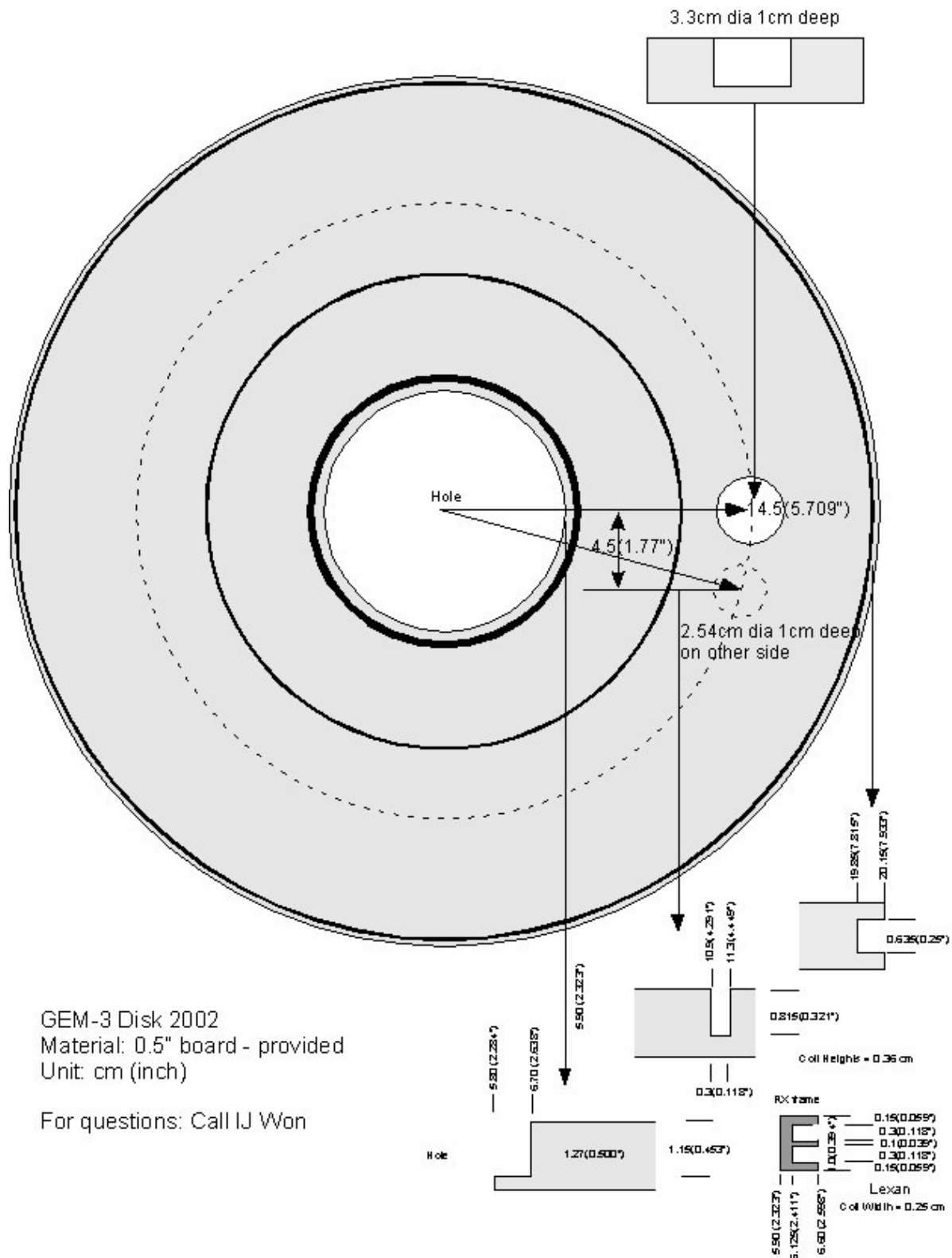


Figure 3.1.6: GEM-3 \mathcal{D}^+ preliminary drawing 5.

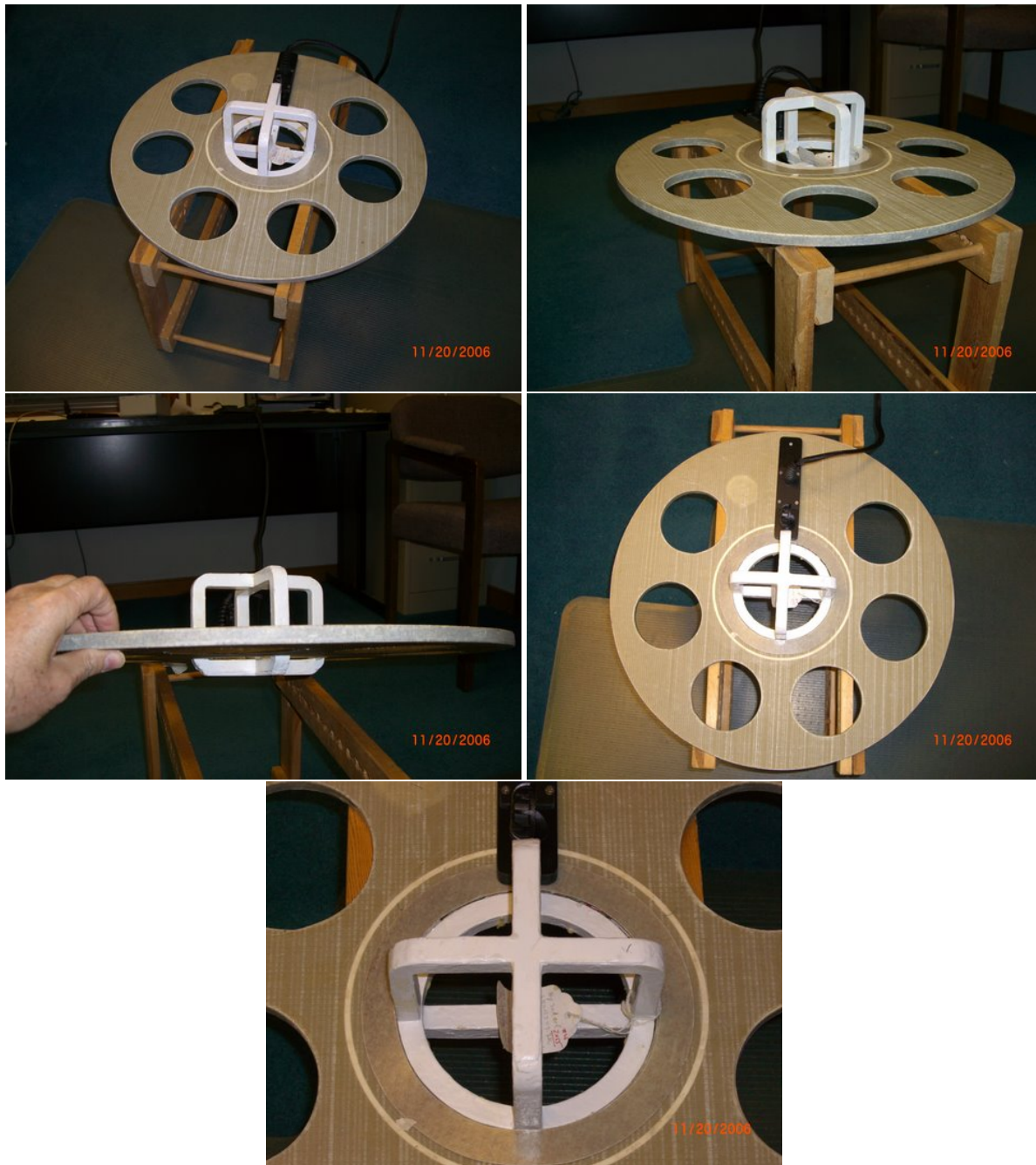


Figure 3.2.1: Pictures of the GEM-3 \mathcal{D}^+ in development at an intermediate stage before finalization of the sensor head.

just of the receiver coils that was causing this broadband shift. So, we squeezed the two transverse receiver coils toward each other, without touching the main head, and sure enough we got only in phase broadband shifts up or down depending on which direction we squeezed in.

Any slight misalignments from perfectly perpendicular to the primary field should be considered background and subtracted if it was constant. The problem is that these transverse receiver coils are not as rigidly fixed in their geometry with respect to the primary field as the Z receiver coil is. The transverse receiver coils are only embedded in a 1 cm square cross sectional scaffolding that is much less robust in terms of torsional and linear deformation. Similarly when I squeeze the receiver coils toward each other, even if I deflected them only by a few microns, it has this large effect of up to 100 or 200 ppm in the data. The fact that these deformations have a broadband, constant (with respect to frequency) inphase shift leads me to suspect it is the primary field response I am seeing.

To lessen this effect in the short-term we simply created some handholds on the supporting plexiglass structure we now have on the GEM-3 \mathcal{D}^+ so that we can pick it up from the center bottom of the instrument without putting any torque on the main head (see Fig. 3.2.2). We ended up stiffening the head with plexiglass as shown in Fig. 3.2.2. This helped the problem considerably, but it neither looked good nor was it very portable due to the increased weight. The engineers at

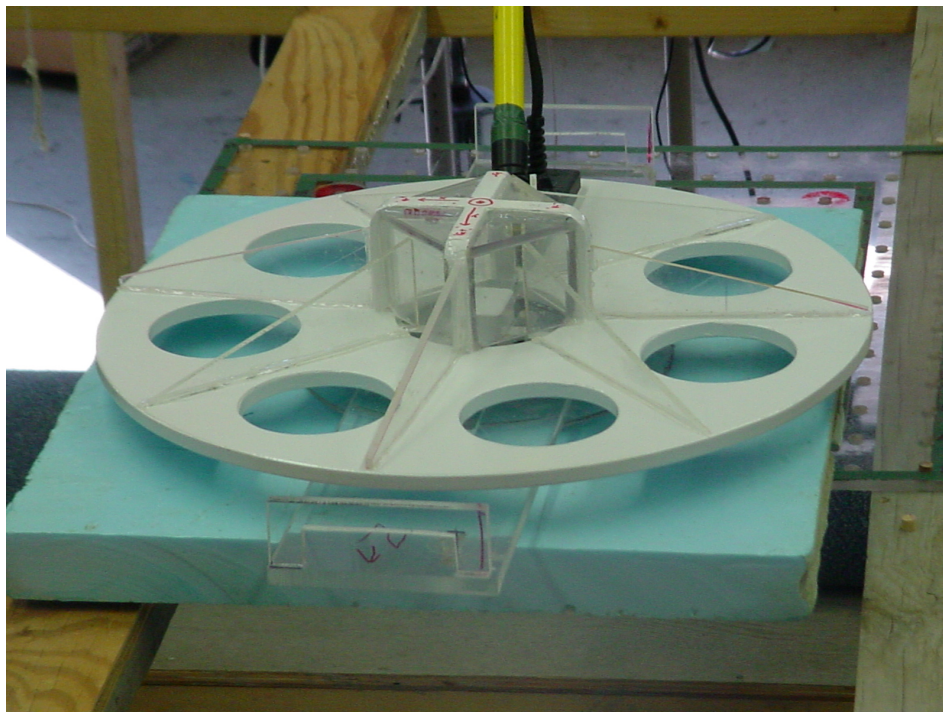


Figure 3.2.2: Plexiglass gussets glued to GEM-3 \mathcal{D}^+ sensor head.

Geophex redesigned the GEM-3 \mathcal{D}^+ sensor head using lightweight foam core epoxy coated stiffening members. A current picture of the GEM-3 \mathcal{D}^+ including these and members is in Fig. 3.2.3.

3.2.b.(1) Final Head Design Figure 3.2.6 shows the final design of the GEM-3 \mathcal{D}^+ sensing head. The only difference from the design above is that the two vertical coils (Hx and Hy) are raised by 3.5 cm, mainly to reduce the ground clearance distance. This was done at the request of the

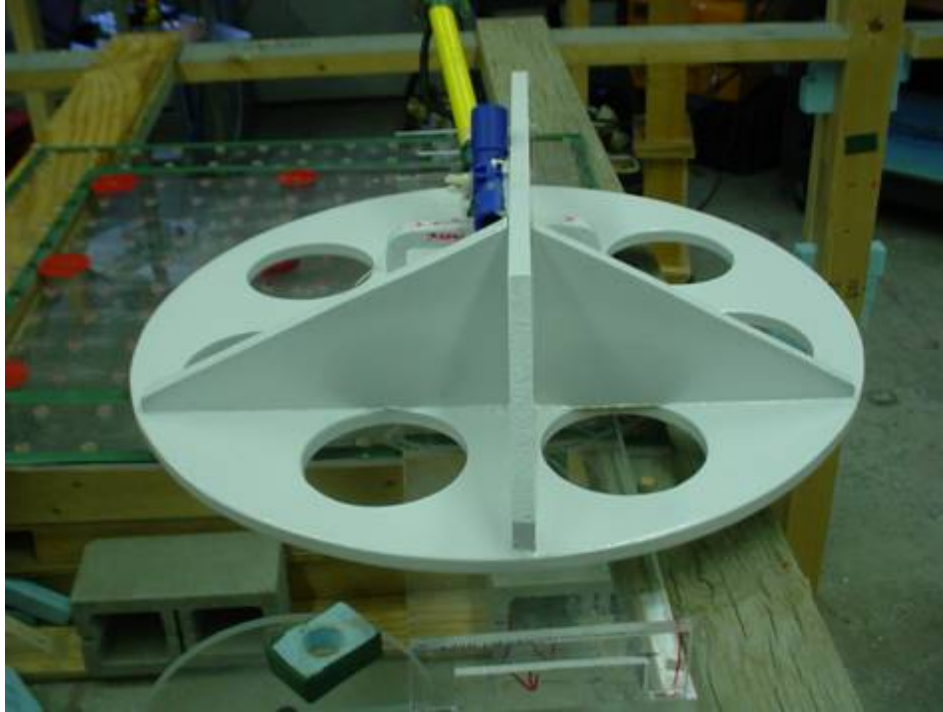


Figure 3.2.3: Foam-core gussets epoxied to GEM-3 \mathcal{D}^+ sensor head.

CRREL project manager, Dr. Ben Barrowes. Figures 3.2.4 and 3.2.5 show the sensor head during the construction and initial wiring stages.

3.2.b.(2) Sensor Electronics Figure 3.1.1 is the final design sheet for this GEM-3 \mathcal{D}^+ . The main change from the previous report includes the transmitter wire gauge that changed from 14 strands of AWG#30 to a Litz wire of 110 strands of AWG#30, substantially reducing its resistance (from 0.251 to 0.032) but adding about 0.45 kg (1 pound) of copper weight. The combined transmitter (TX1 + TX2) shows a measured inductance of 53 μ H (close to the predicted value) and a self-resonance frequency at 1.44 MHz (highlighted yellow in the upper right corner (of proprietary table)), well above the intended operating bandwidth.

The wire gauge of the three receiver coils has also been changed from AWG#30 to AWG#26 to reduce the resistance. The three coils, designed to have similar area-turn products, have the following measured electrical parameters (Table 1). Small variations are within acceptable tolerance and will be equalized through calibration procedures, once the sensor has been completed.

We assembled the sensor electronics beyond the sensor head in year 2 of the project. Basically, there is a single electronic console mounted at the end of the handlebar, partly acting as a counterweight for handheld operation. The console, including a rechargeable battery, communicates wirelessly thru Bluetooth with either a PDA or a laptop that will display data and graphics during a survey as well as archive the raw data. The Bluetooth also communicates with the GEM Beacon Navigator (fabricated in Year 2) to receive wirelessly the sensor location data.

Figure 3.2.7 shows the overall system functional block diagram for the GEM-3 \mathcal{D}^+ . The receiver diagram, Fig. 3.2.8, utilizes a custom-designed DSP board that, among others, performs discrete sine- and cosine-convolution operations at each transmitted frequency to obtain the ppm



Figure 3.2.4: GEM-3 \mathcal{D}^+ sensing head and coil frames

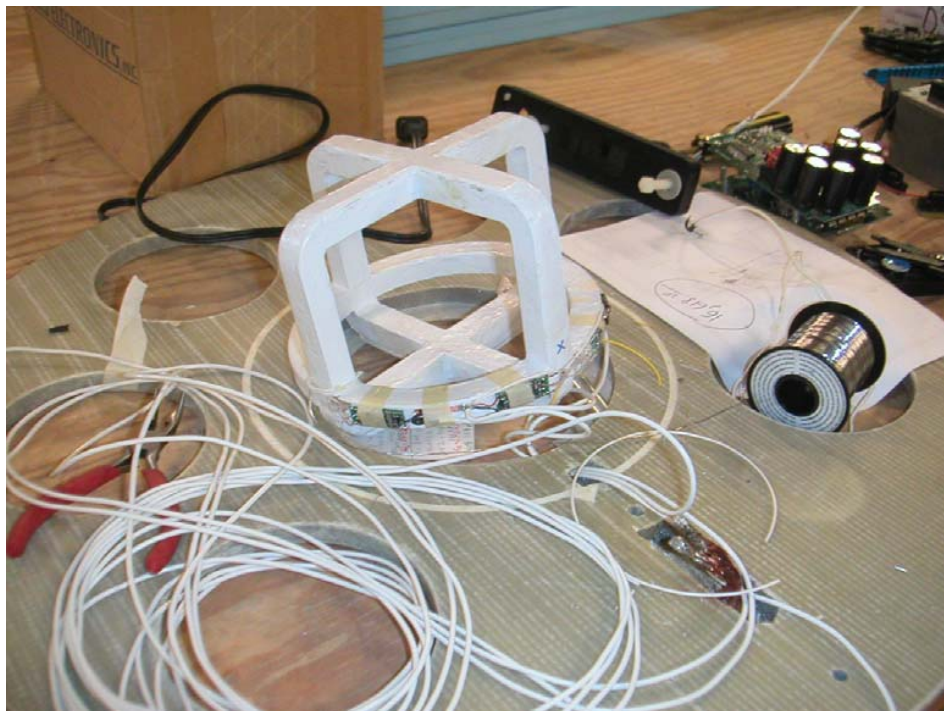
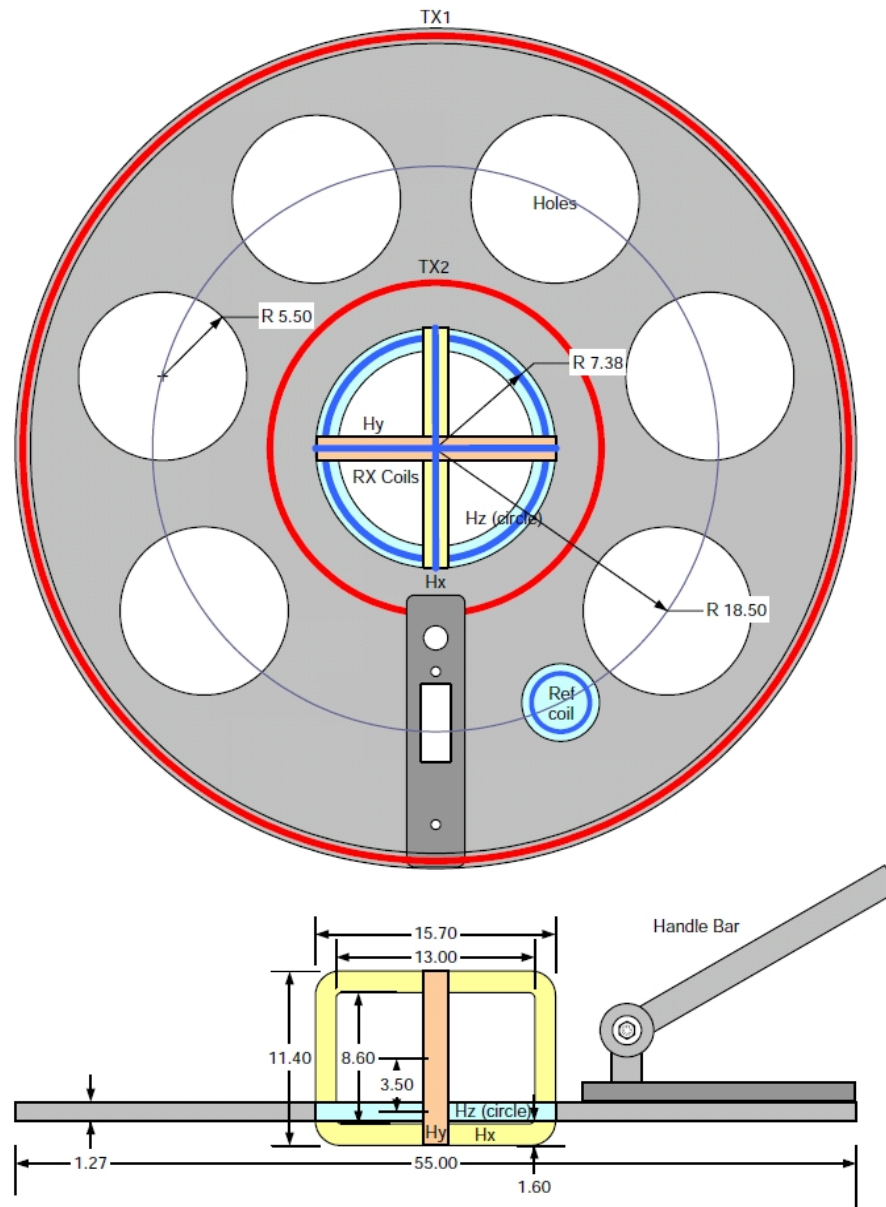


Figure 3.2.5: Beginning stage of wiring. All three receiver coils are now potted, electrically shielded (silver coating), and epoxy-painted for protection. Notice a small preamp printed circuit board (PCB) for each receiver coil taped to the round z-axis receiver coil.

Figure 3.2.6: Final drawing of the CRREL GEM-3 \mathcal{D}^+ sensing head.

coil	mean coil dimensions	offset from TX plane	# of turns	measured resistance	measured inductance	self-resonance frequency
Hz	7.25cm dia circle	0	100	6.2 Ω	2.78mH	254kHz
Hx	10.3cm x 14.6cm rect	+3.5cm	110	7.2 Ω	3.07mH	242kHz
Hy	10.4cm x 14.7cm rect	+3.5cm	106	7.0 Ω	2.92mH	242kHz

Table 1: Receiver coils characteristics

responses of the inphase and quadrature components. Figure 3.2.9 shows the transmitter functional diagram.

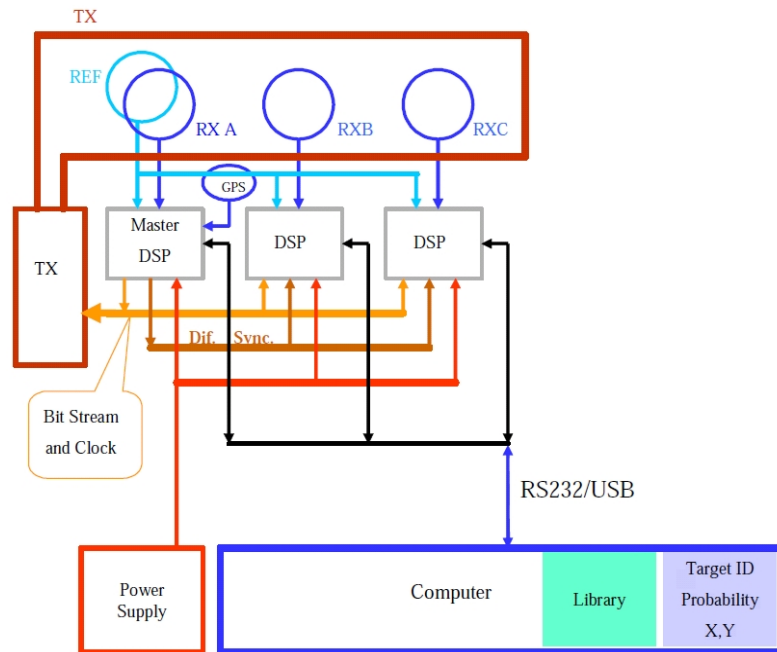


Figure 3.2.7: GEM-3 \mathcal{D}^+ electronic block diagram

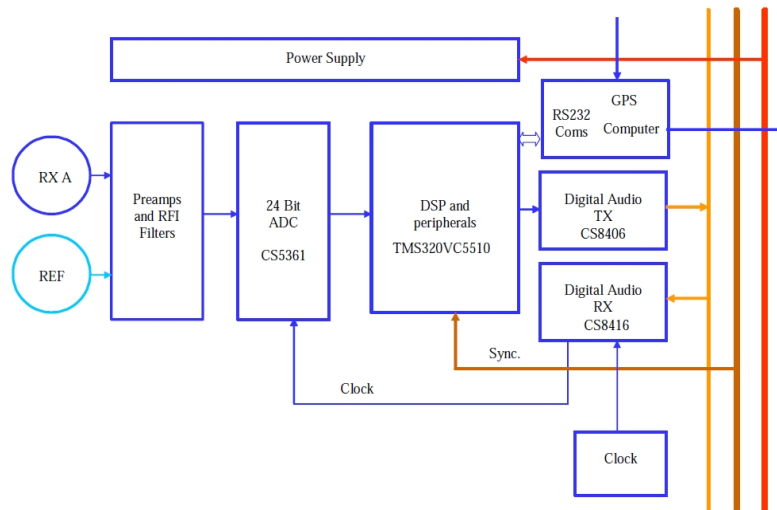


Figure 3.2.8: Custom-designed DSP module for the GEM-3 \mathcal{D}^+ .

3.3 GEM-3 \mathcal{D}^+ as Beacon Positioning System

The GEM-3 \mathcal{D}^+ acquires high quality data from its three receiver coils. However, for a hand-held instrument such as this, accurate positioning of the sensor head including all three Euler angles is very important. One reason why position is so important is that the depth to which the

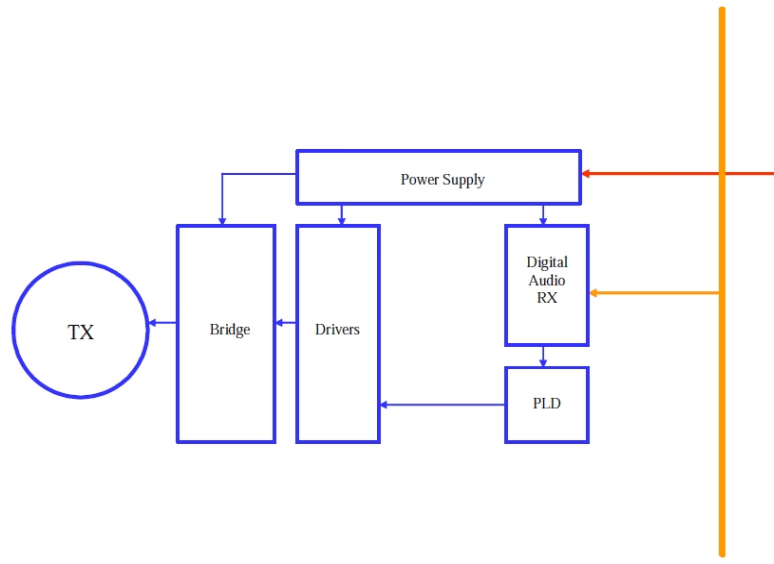


Figure 3.2.9: Transmitter block diagram with red lines showing power flow and orange lines data flow.

GEM-3 \mathcal{D}^+ can "see" is limited to approximately 70 cm for realistic size targets. At the shallow depths, a positioning error on the order of 2 cm can corrupt data and subsequent inversion schemes. Accuracy of all three orientation angles is important for translating local vector components to an invariant global system during rotations. As a consequence, we expended significant efforts at developing and integrating the beacon positioning system into the GEM-3 \mathcal{D}^+ .

Most currently used positioning systems rely on locating something attached to the sensor, for example the robotic total station, GPS receivers, and laser positioning systems. The beacon positioning system we have integrated into the GEM-3 \mathcal{D}^+ works on a different principle than these types of positioning systems. It makes the assumption that the primary field transmitted from the sensor head is dipolar in shape. Under this assumption, two triaxial receiver coils in a fixed configuration should theoretically allow the determination of the location and two of the three Euler angles associated with the sensor head. Because the dipole field is axially symmetric, the third Euler angle which describes the rotation of the sensor head around its axis of symmetry cannot be deduced simply from the dipolar primary field. In fact, for the usual GEM 3 sensor head, this last Euler angle is unnecessary. However, because the GEM-3 \mathcal{D}^+ has the additional transverse receiver coils whose responses depend on this rotation about the axis of symmetry, some method to find this last Euler angle was needed. We decided to install an electronic compass onto the main sensor head. This compass when combined with the data from the beacon positioning system, will provide the full set of Euler angles necessary to uniquely determine the location and orientation of the sensor head at all times.

The beacon positioning system that Geophex demonstrated to us in 2007 was for a different Geophex instrument. This other beacon positioning system had a constant electronic gain built into the system itself. This gain is an important factor in determining the sensitivity and accuracy of the final positioning system. Too small of a gain leads to a short range; too large of a gain will lead to saturation when the sensor is near the beacon's triaxial receivers. For the GEM-3 \mathcal{D}^+ , the decision was made to have a variable gain in order to have both a large range from the receiver coils and accuracy when the sensor head is in close proximity to the beacon receivers. This added

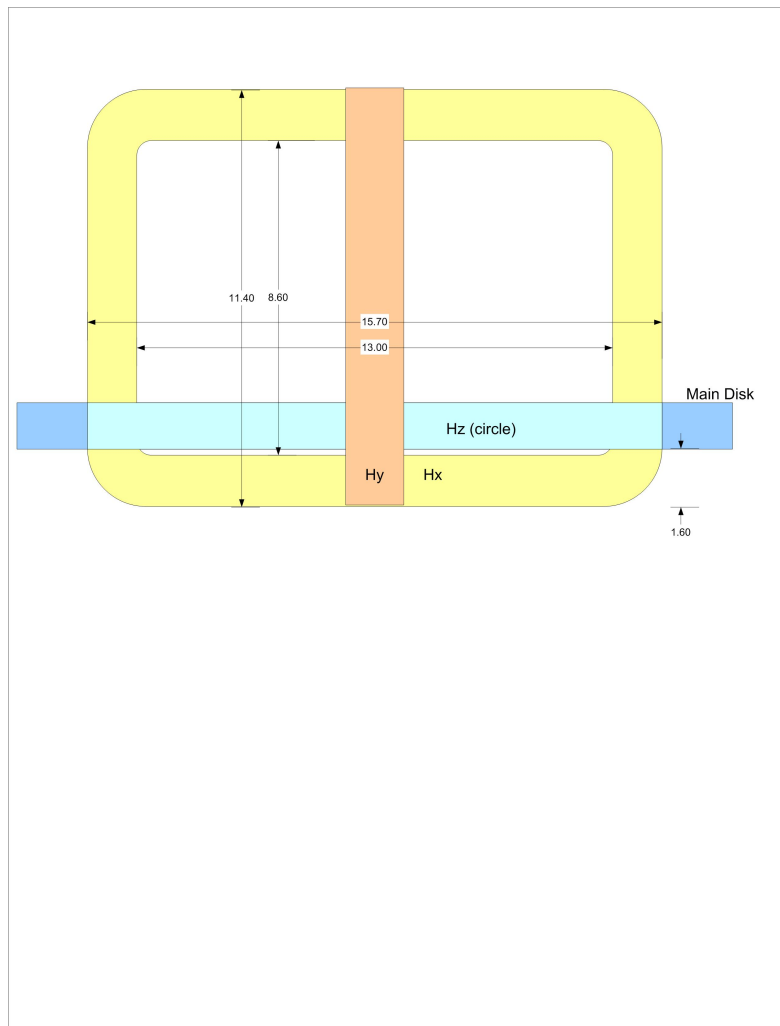


Figure 3.2.10: Detail of the transverse receiver coils on the GEM-3 \mathcal{D}^+ .

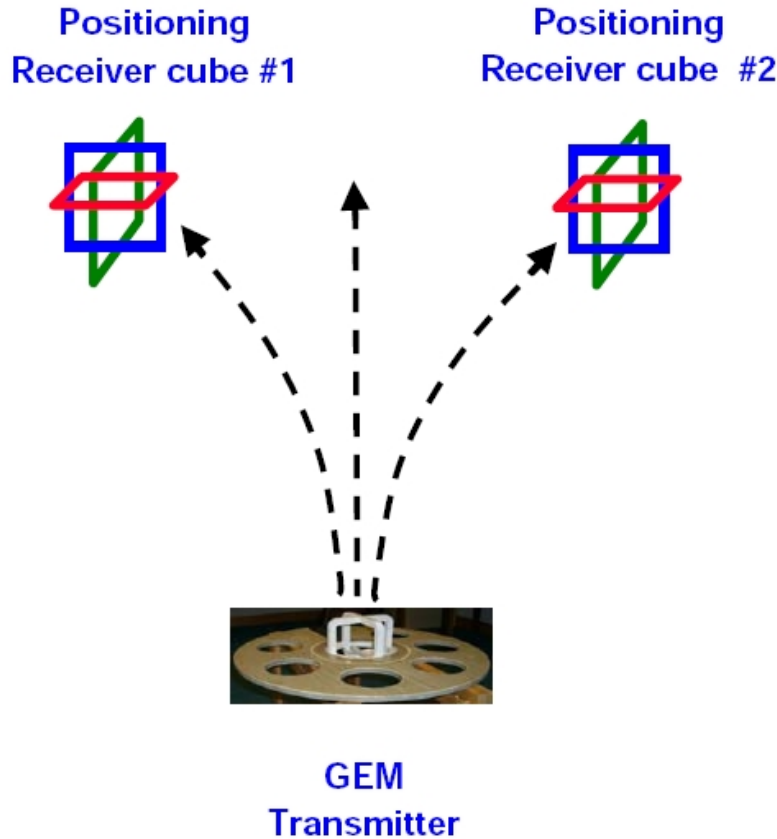


Figure 3.3.1: Concept of GEM-3 \mathcal{D}^+ positioning system. The (assumed) dipolar shape of the GEM-3 \mathcal{D}^+ primary field is recorded by two triaxial receivers held in a fixed relationship.

complexity to the positioning system delayed its final integration with the GEM-3 \mathcal{D}^+ .

Conceptually, the GEM-3 \mathcal{D}^+ beacon positioning system operates as depicted in Figs. 3.3.1 and 3.3.2. The data from the beacon system is fully incorporated into the GEM-3 \mathcal{D}^+ data stream. One important note about this positioning system is that the EMI primary field from the GEM-3 \mathcal{D}^+ penetrates trees and mounds as easily as it does the soil, so this system can operate in challenging environments with non-metallic obstacles.

A schematic of the coordinate systems involved in the GEM-3 \mathcal{D}^+ beacon system is shown in Fig. 3.3.3.

3.3.a Straight Line Tests

As an initial test of the beacon positioning system, we set up a 2x10 on the ground at the Geophex facility and moved the GEM-3 along straight lines next to the boards at different distances from the beam. Figure 3.3.4 shows the setup used in this test, while Figs. 3.3.5–3.3.8 shows the relative accuracy of the system at near, intermediate and far distances from the beam. The processing system infers the x , y , and z position of the sensor head as the instrument is moved around the plank. The merged data, EMI and positional, are then recorded simultaneously. If desired, the position of the sensor head in real time can be displayed (see Fig. 3.3.9). This display could be useful for real time detection of anomalies as both the EMI data and the sensor head position are

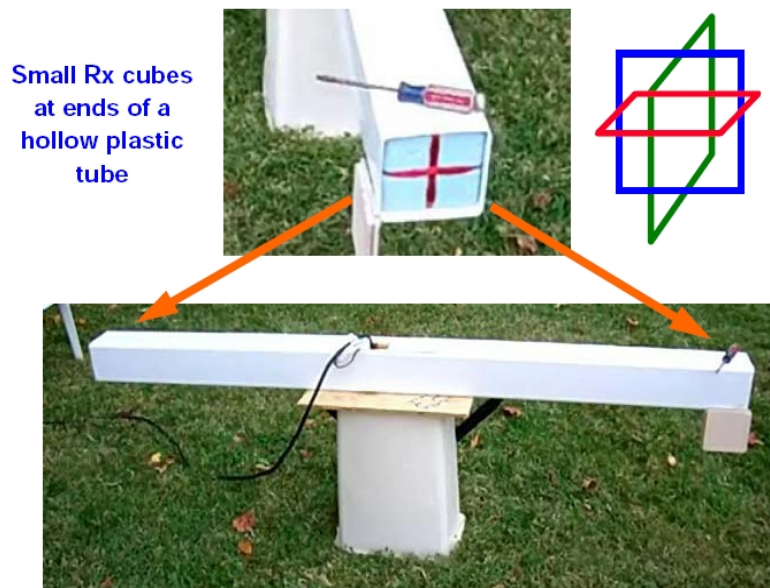


Figure 3.3.2: Beam holding the two triaxial receivers of the GEM-3 \mathcal{D}^+ positioning system.

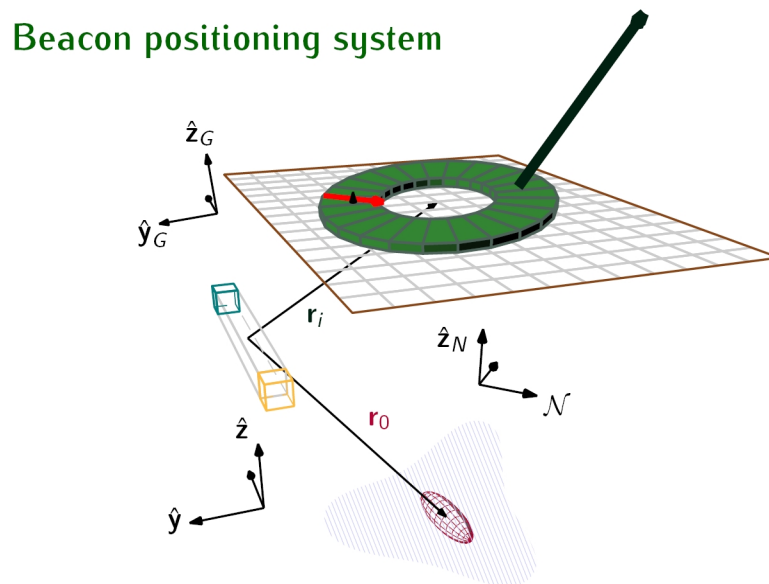


Figure 3.3.3: Coordinate systems for the target, beam, and GEM-3 \mathcal{D}^+ .



Figure 3.3.4: Beacon positioning system and plank setup for initial demonstration at Geophex facility.

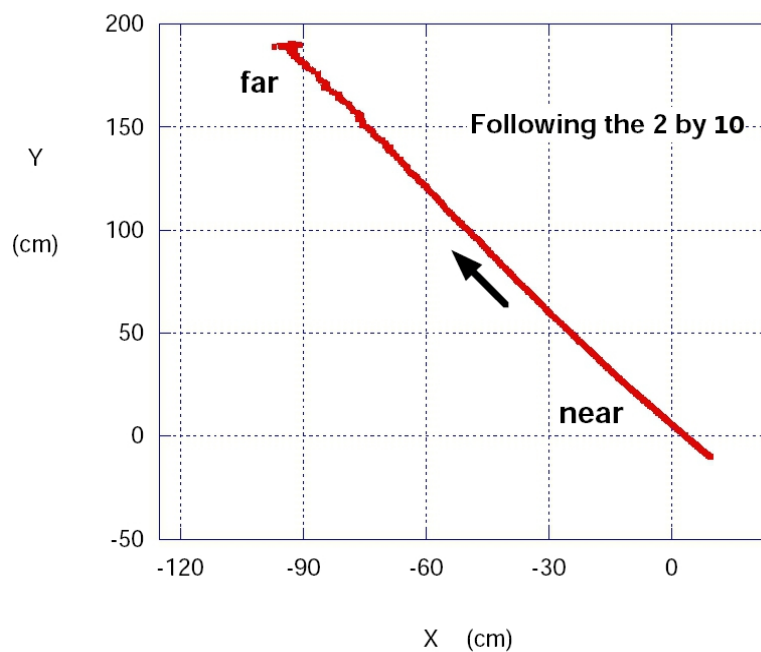


Figure 3.3.5: Beacon positioning system data along a board for the entire length.

overlaid.

The details of the beacon positioning system involve the nonlinear inversion of a dipolar source based on 6 measurement points. The instrument and the two triaxial receivers are shown conceptually in Fig. 3.3.10. An oscillating dipole magnetic field is generated by the EMI transmitter. The

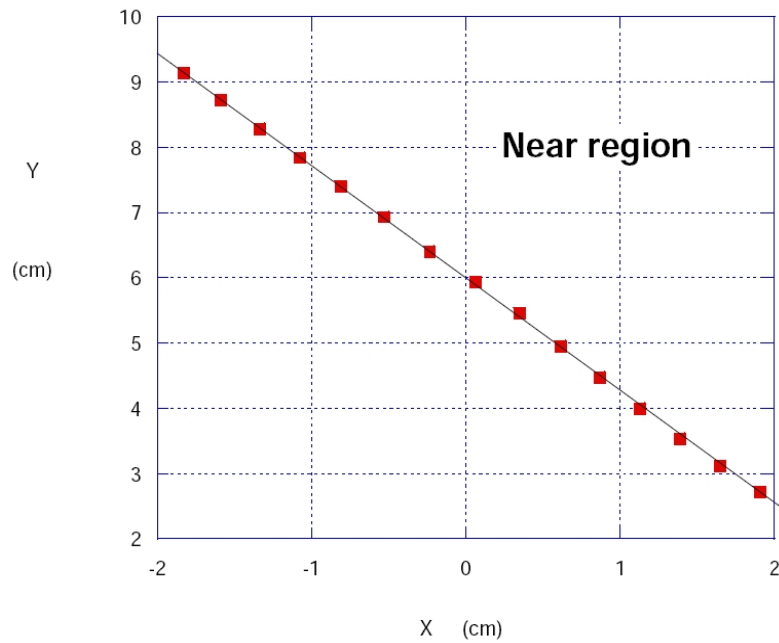


Figure 3.3.6: Beacon positioning system data along a board. Near range.

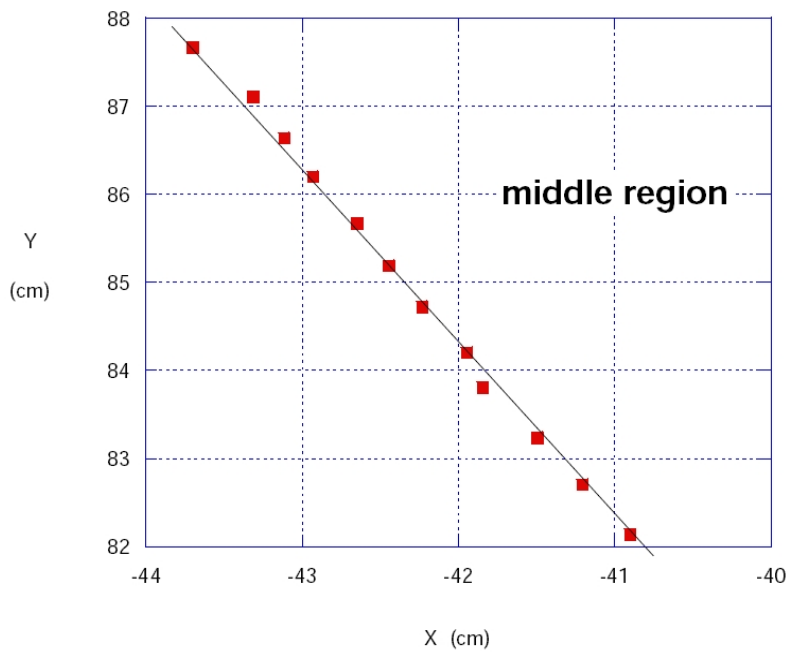


Figure 3.3.7: Beacon positioning system data along a board. Intermediate range.

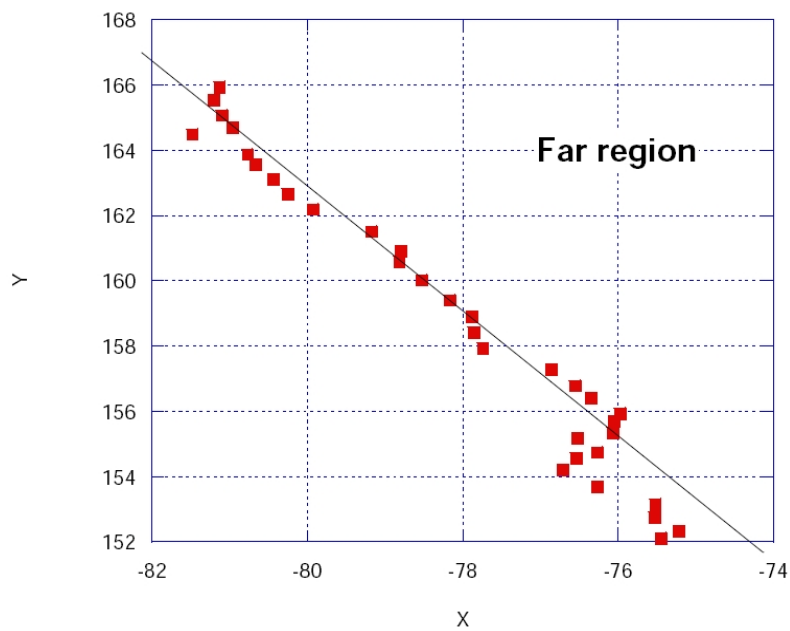


Figure 3.3.8: Beacon positioning system data along a board. Large range.

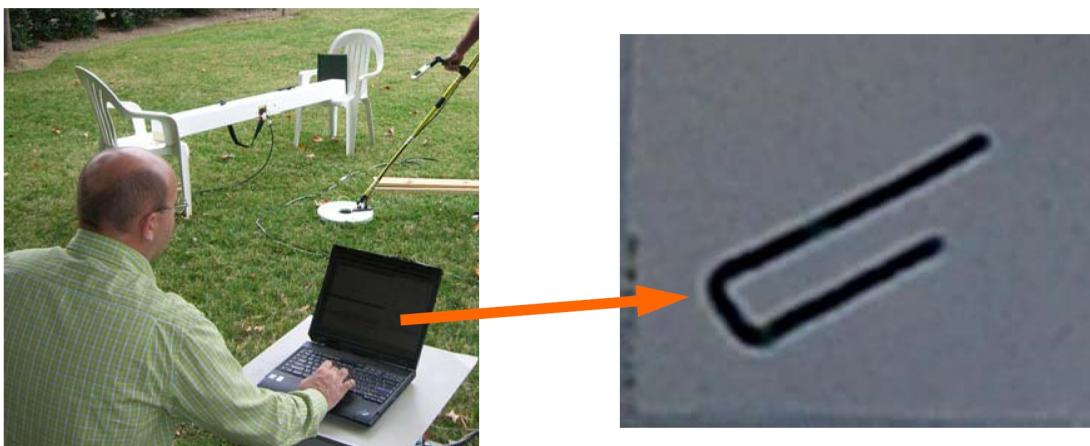
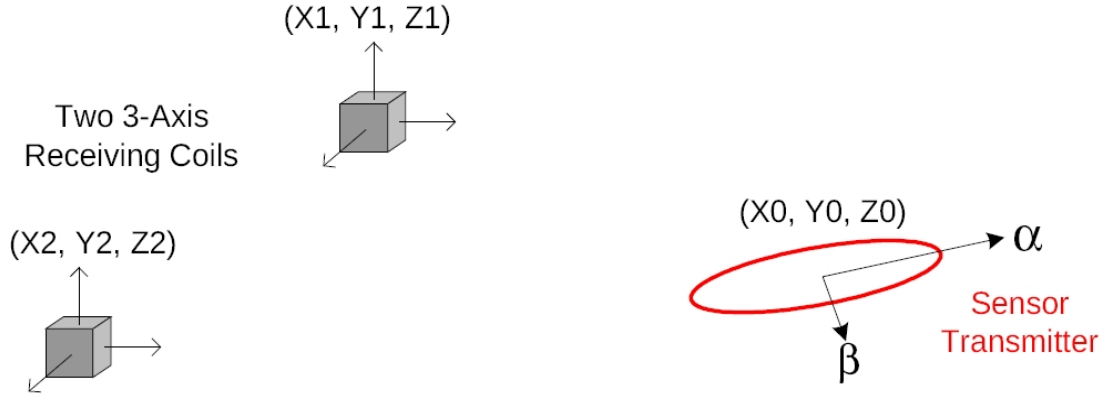


Figure 3.3.9: Beacon positioning system real time feedback of EMI data (not shown) and position.

Figure 3.3.10: GEM-3 \mathcal{D}^+ beacon positioning system principles.

dipole field equations are

$$\begin{aligned}
 B_x &= \frac{\mu_0}{4\pi} \left\{ m_x \left[\frac{2x^2 - (y^2 + z^2)}{R^5} \right] + m_y \left[\frac{3xy}{R^5} \right] + m_z \left[\frac{3xz}{R^5} \right] \right\} \\
 B_y &= \frac{\mu_0}{4\pi} \left\{ m_x \left[\frac{3xy}{R^5} \right] + m_y \left[\frac{2y^2 - (x^2 + z^2)}{R^5} \right] + m_z \left[\frac{3yz}{R^5} \right] \right\} \\
 B_z &= \frac{\mu_0}{4\pi} \left\{ m_x \left[\frac{3xz}{R^5} \right] + m_y \left[\frac{3yz}{R^5} \right] + m_z \left[\frac{2z^2 - (x^2 + y^2)}{R^5} \right] \right\}
 \end{aligned} \tag{3.3.1}$$

where $R = \sqrt{x^2 + y^2 + z^2}$ dipole-field point distance, μ_0 is the permeability of free space, the subscripts refer to field component/source dipole component, and the measurement (field) point is at the origin. For the locator system comprising two sets of coils at two field positions $(xa, 0, 0)$ and $(xb, 0, 0)$, two sets of equations as above are formed by replacing x with (xa, xb) . We reparametrize these equations in terms of a total dipole strength and the sine of the tilt angles in place of $m_{x,y,z}$. A non-linear iterative inversion algorithm is performed by a computer to solve for the x, y, z and tilts; at initialization we also solve for the dipole strength, then freeze it for stability.

The accuracy of the beacon positioning system was determined in tests at the Geophex facility in 2007. The complete setup can be seen in Fig. 3.3.11. The sensor head was then moved on a precise grid while the beacon positioning system was recording data. The calculated position was then compared to the actual position on the grid with results shown in Fig. 3.3.12. The horizontal projection of locator measured relative position (blue diamonds) vs. template grid (red crosses). There are 50 samples at each position. The 3-dimensional RMS error is 0.77 cm. Note, one grid point is missing due to data acquisition dropout. Figure 3.3.13 repeats the test except the nearest edge of the gridboard was 1.5m away from the sensor head. Relative measured position (blue) plotted on the ideal grid (red) for the template at 1.5 m closest edge from the locator beam. There are 50 samples superposed at each point. The 3-D rms error is 0.92 cm.

More information on the processing method used in analyzing dynamic data from the GEM-3 \mathcal{D}^+ beacon positioning system can be found in Sec. 4.1.c.(3). A more detailed explanation on the construction of the beacon hardware can be found in Appendix C.2.

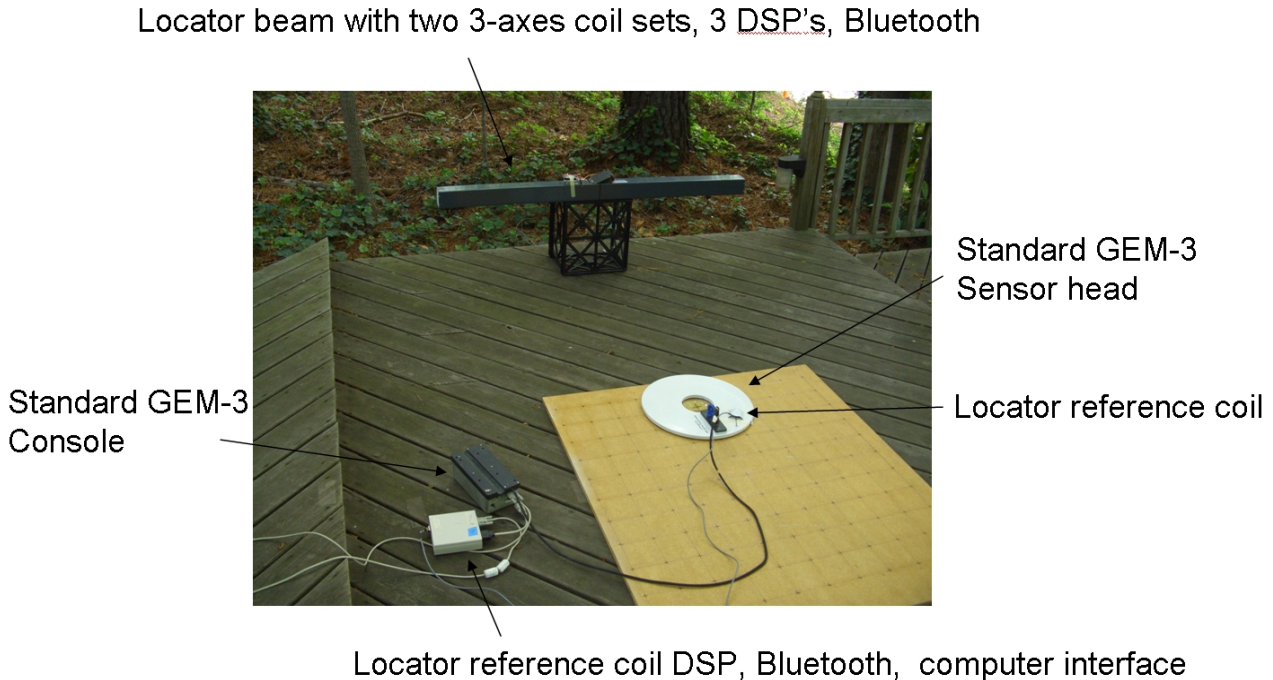


Figure 3.3.11: Complete setup of the beacon positioning system tests at Geophex.

3.4 GEM-3 \mathcal{D}^+ Complete

Figure 3.4.1 show the completed GEM-3 \mathcal{D}^+ before the stiffening was added (see below). Also see Fig. 4.1.1 for picture of the completed GEM-3 \mathcal{D}^+ instrument head.

The GEM-3 \mathcal{D}^+ instrument is now completed, including the receiver beam for the beacon positioning system. Software which runs both the beacon software and the GEM-3 \mathcal{D}^+ itself has been provided to CRREL by Geophex. Setup and operation is straightforward and is detailed in Appendix C.1. We have acquired both lab and test plot data and run blind tests of these data (see Sec. 5). As with most prototype instruments, the GEM-3 \mathcal{D}^+ is not a production ready instrument. There remain some issues with software stability and hardware communication (between the GEM-3 \mathcal{D}^+ and the beam). These issues cause software crashes and resets that restrict larger deployment. The head deformation issue described above is still relevant when the GEM-3 \mathcal{D}^+ is held in a dynamic data acquisition mode. Essentially, when the GEM-3 \mathcal{D}^+ is tilted beyond a nominal degree (beyond $\approx 10^\circ$), the primary field can leak into the transverse receivers and contaminate the data.

Frequency domain instruments such as the GEM-3 \mathcal{D}^+ are desirable for several reasons cited above (Sec. 2). Lessons learned from the GEM-3 \mathcal{D}^+ can assist future researchers in developing more sensitive and robust FD instruments and beacon positioning systems that can potentially resolve these issues.

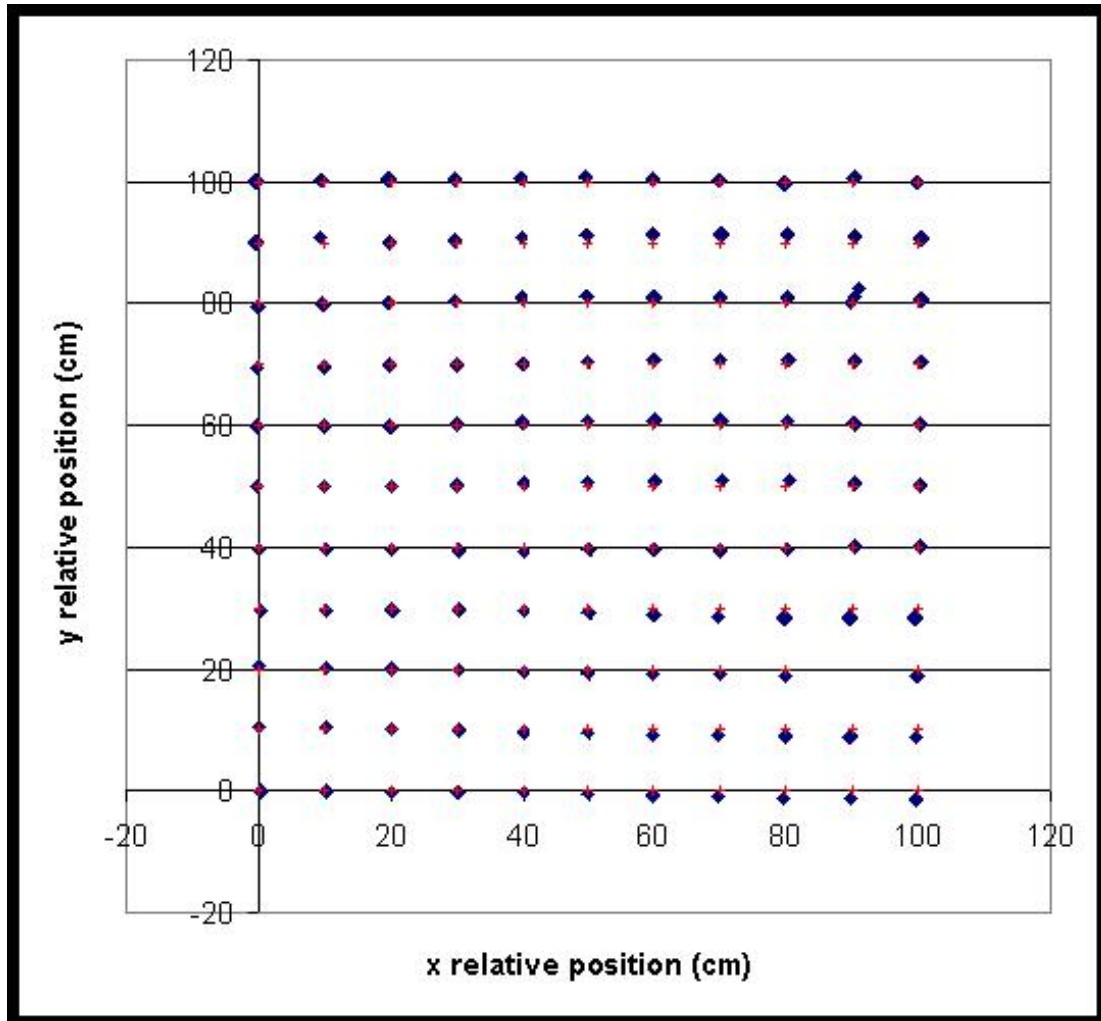


Figure 3.3.12: Results for beacon positioning system test #1. The nearest edge of the gridboard is 1m from the beam. The horizontal projection of locator measured relative position (blue diamonds) vs. template grid (red crosses). There are 50 samples at each position. The 3-dimensional rms error is 0.77 cm. Note, one grid point is missing due to data acquisition dropout.

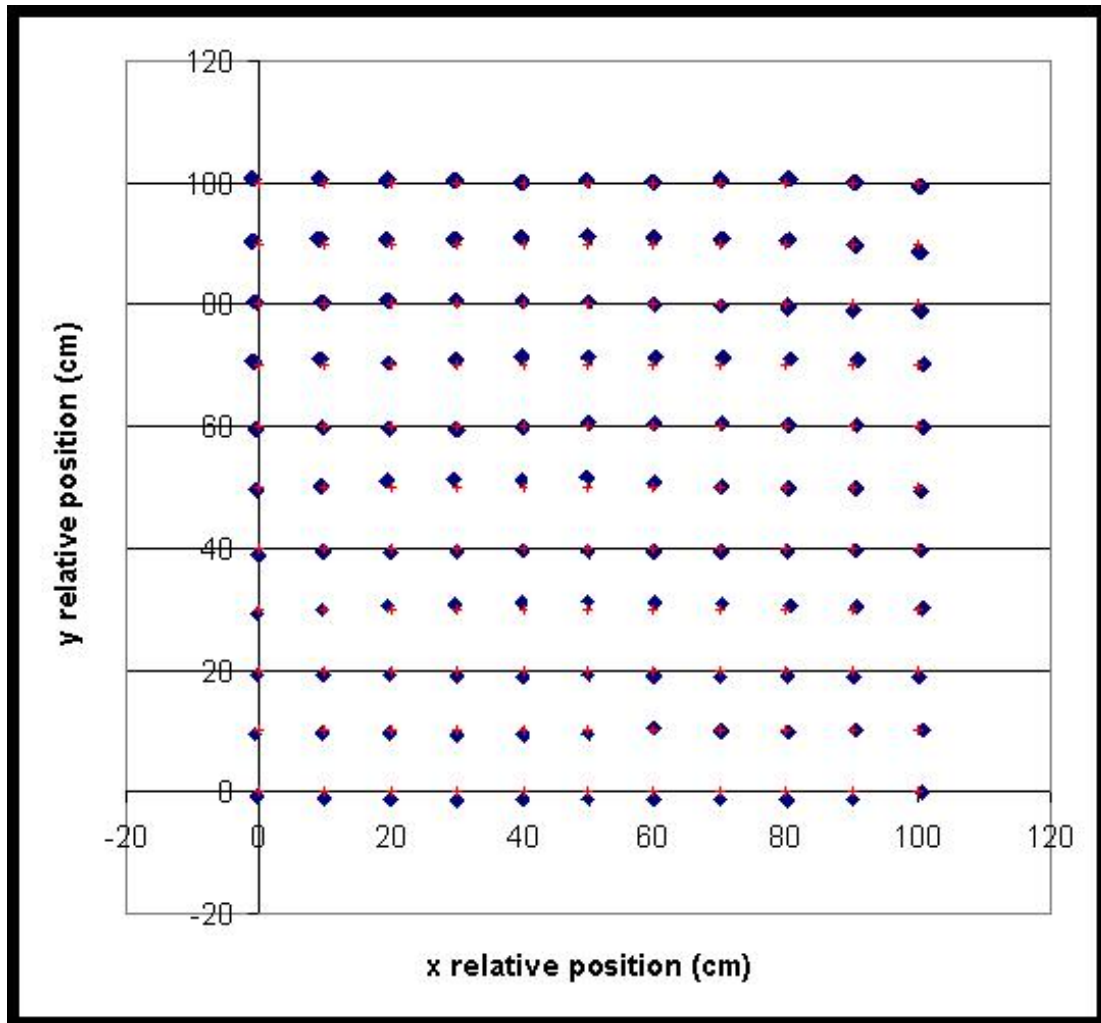


Figure 3.3.13: Results for beacon positioning system test #2. The nearest edge of the gridboard is 1.5m from the beam. Relative measured position (blue) plotted on the ideal grid (red) for the template at 1.5 m closest edge from the locator beam. There are 50 samples superposed at each point. The 3-D rms error is 0.92 cm.



Figure 3.4.1: Final GEM-3 \mathcal{D}^+ instrument.

4 Materials and Methods: Software Modeling and Analysis of GEM-3 \mathcal{D}^+ Data

During the course of MM1537, we developed models and algorithms which aid in helping to analyze not only the data from the GEM-3 \mathcal{D}^+ , but potentially from any other EMI instrument. This section will proceed as follows. Some general characteristics of the GEM-3 \mathcal{D}^+ and the beacon positioning system are presented as Sec. 4.1. Also in that section is a preliminary description of the GSEA (Generalized Standardized Excitations Approach), while a more detailed presentation is in Sec. 4.5. In Sec. 4.2, we first discuss the response of two different soils to the GEM-3 \mathcal{D}^+ acquired at a local gravel pit. We also discuss the form of the permeability of most soils at EMI frequencies and discuss implications for both FD and TD instruments. We also model soil properties such as surface roughness and discuss the estimation of soil susceptibility in Sec. 4.3. Section 4.4 documents our efforts to find an absolute scale factor of GEM ppm converting it to magnetic field H values. This can be useful for local soil characterization and background subtraction, in particular.

We have adapted our normalized surface magnetic source (NSMS) and GSEA models to the GEM-3 \mathcal{D}^+ geometry (see Sec. 4.6 and Sec. 4.5). These ultra-high fidelity, physically complete models facilitate discrimination processing by a) allowing detailed inspection of expected signals under any contemplated circumstances; b) enabling signal pattern matching to establish the presence of known or likely target types; and c) providing fully realistic synthetic input data on a large scale for training statistical learning machines. In addition, we also developed a model for EMI responses by elliptical metallic bodies, applicable at higher frequencies by design, but also matching fairly well with data at low frequencies if they are highly permeable (see Sec. 4.7). This is the

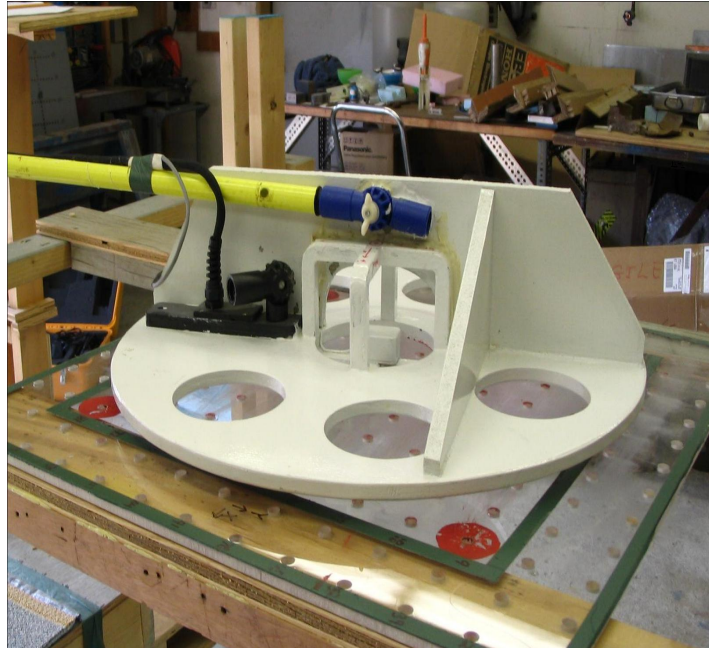


Figure 4.1.1: GEM-3 \mathcal{D}^+ sensor and measurement grid

only non-numerical solution available for objects with three dimensional geometry. We have also machined 6 ellipsoids of varying aspect ratios to compare our models with measured data [5]. These models will allow us to accommodate different size and shape targets whether they are in our library or not.

4.1 A vector handheld frequency-domain sensor for UXO identification

4.1.a Executive Summary

This section presents some methods and results related to UXO identification using the GEM-3 \mathcal{D}^+ . Our analyses exploit data provided by the sensor in both grid-based and dynamic measurements to characterize different objects, including metal spheres and actual UXO. For the data analysis we alternate between the dipole model and the more rigorous standardized excitation approach. We review some ill-conditioning issues encountered with the latter model and the different approaches that we use to overcome them. In applications, the availability of horizontal field components in the data allow us to identify UXO vs. non-UXO items while minimizing the nonnegligible effects of ground response.

4.1.b Introduction

The improvement in sensing methods represented by the GEM-3 \mathcal{D}^+ must be accompanied by fast, physically complete, and accurate forward models that can both reasonably pinpoint the location and orientation of an object and provide sufficient information on its electromagnetic properties so as to characterize it unambiguously. Here we adapt to the GEM-3 \mathcal{D}^+ some forward models that have shown success with other sensors. Perhaps the most widely used model treats each anomaly as a point dipole [6–10]; this procedure, while limited, is fast and provides good starting guesses

for more elaborate methods. An example of the latter is the data-derived Standardized Excitation Approach (SEA), which incorporates the finite size of the scatterer and the nonuniformity of the primary field in the relevant length scale. The approach decomposes the primary field striking the target into a set of standardized modes, whose relative importance in the expansion is given by the particulars of position and orientation. The object is replaced by rings of magnetic sources placed on a surrounding spheroid. The response of the rings to each mode of excitation can be described by a Green function, and the full response of the target is a superposition of these with the corresponding geometric coefficients as weights. Once the object's response to each mode is established, the response can be calculated for any variation of excitation and receiver location by just using an appropriately altered superposition of the modal responses. The method was previously adapted to the GEM-3 [11] and to various time-domain instruments [12, 13] using charges as the responding sources; a generalization replaces the charges by dipoles and uses Stokes's theorem to streamline the necessary integration over the receiver areas [14, 15].

The overall section is organized as follows. After describing the instrument in Section 4.1.c we present some studies related to UXO identification that use data produced by the GEM-3 \mathcal{D}^+ in both grid-based and dynamic measurements. We employ both the dipole model and the SEA, which we introduce in sections 4.1.d.(1) and 4.1.d.(2) respectively, to characterize different objects, including metal spheres and actual UXO. We look at the possibility of using the horizontal components of the secondary field to identify UXO vs. non-UXO items while minimizing the nonnegligible effects due to the ground. We conclude in Section 4.1.f.

4.1.c The GEM-3 \mathcal{D}^+ Sensor

The GEM-3 \mathcal{D}^+ sensor, designed and manufactured by Geophex, Ltd., is a wideband frequency-domain instrument that continuously transmits chosen frequencies and outputs FD spectra of response. The user can select up to 15 frequencies of operation for the sensor, ranging between 30 and 90030 Hz. The measured secondary field at each frequency is given in dimensionless units of parts per million (PPM), defined as [16, 17]

$$\text{PPM} = \frac{\text{Secondary magnetic flux through the receiver coil}}{\text{Primary magnetic flux through a reference coil}} \times 10^6, \quad (4.1.1)$$

which serve to divide out the frequency dependence and the value of the transmitted current and account for the fact that the actual measured quantities are voltages proportional but not identical to magnetic fluxes.

The sensor head contains two circular coplanar concentric transmitting coils connected in series. These transmitters have radii 27 cm and 10.84 cm and are wound 6 and 2 turns respectively, making the effective current on the outer coil three times larger [18]. This “transmitter bucked” arrangement is designed to produce no primary magnetic flux through a receiver coil, coplanar and concentric with the transmitters and of radius 7.25 cm, to which we henceforth refer as the H_z -coil (these numbers are determined by using an expression equivalent to (4.1.2) below but cast as an expansion in Legendre polynomials [16]). The H_z -coil can then measure the much smaller flux due to the secondary field.

The other two receiving coils on the GEM-3 \mathcal{D}^+ are

1. The “ H_x ” coil with dimensions 10.3 cm (in \hat{z}) by 14.6 cm (in \hat{y}), offset 3.5 cm from the plane of the transmitter coils;

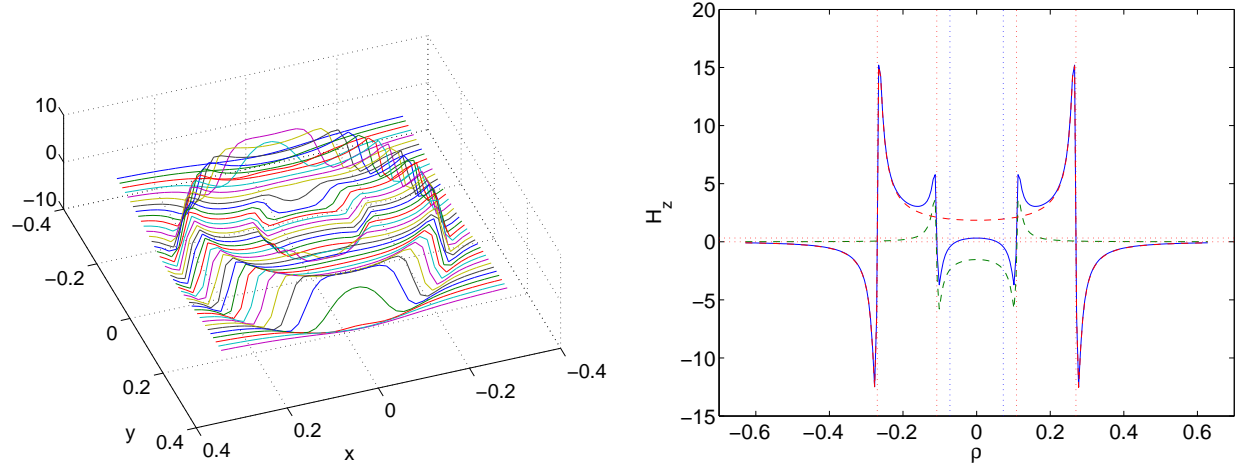


Figure 4.1.2: (Left) The field H_z^{pr} due to the GEM-3 \mathcal{D}^+ slightly above the plane of the transmitter coils. The central cavity where the primary flux vanishes is clearly visible. (Right) The field H_z^{pr} due to the GEM-3 \mathcal{D}^+ on the plane of the transmitter coils, this time seen in profile.

2. The “ H_y ” coil with dimensions 10.4 cm (in \hat{z}) by 14.7 cm (in \hat{x}), offset 3.5 cm from the plane of the transmitter coils.

The primary flux through these vertical receivers vanishes trivially.

The primary field due to a circular coil of radius χ in cylindrical coordinates is [19, 20]

$$\mathbf{H} = \frac{I}{\pi} \nabla \times \frac{\hat{\phi}}{k} \sqrt{\frac{\chi}{\rho}} \left[\left(1 - \frac{1}{2} k^2 \right) K(k) - E(k) \right], \quad \text{where the modulus } k^2 = \frac{4\rho\chi}{(\chi + \rho)^2 + z^2}. \quad (4.1.2)$$

where $K(k)$ and $E(k)$ are elliptic functions [21]

The field H_z^{pr} slightly above the plane of the transmitter coils is depicted in three dimensions and as a function of ρ in Figure 4.1.2. This figure also shows how the total field arises as the sum of the contributions of the two transmitter coils.

4.1.c.(1) Integrating over the areas of the receivers Consider an upright dipole located z_0 m below the origin. With $\mathbf{m} = m\hat{z}$, $\mathbf{r} = \rho\hat{\rho}$, and $\mathbf{r}' = -z_0\hat{z}$ we can use the general formula

$$\mathbf{H} = \frac{3(\mathbf{m} \cdot \mathbb{R})\mathbb{R}/R^2 - \mathbf{m}}{4\pi R^3} \quad \text{to obtain} \quad H_z = \frac{m}{4\pi} \frac{2z_0^2 - \rho^2}{(z_0^2 + \rho^2)^{5/2}}. \quad (4.1.3)$$

Integrating (4.1.3) over the area of the horizontal receiver we find

$$\Phi = 2\pi \int_0^a H_z \rho d\rho = \frac{m}{2} \frac{a^2}{(z_0^2 + a^2)^{3/2}}. \quad (4.1.4)$$

On the other hand, if we substitute the field at the center and multiply by the receiver area, we get the “average” flux

$$\Phi' = \frac{m}{4\pi} \frac{2}{z_0^3} \pi a^2 = \frac{m}{2} \frac{a^3}{z_0^3} \quad (4.1.5)$$

We see that the average flux is larger than the integrated counterpart when we are right above the target:

$$\frac{\Phi'}{\Phi} = \left[1 + \left[\frac{a}{z_0} \right]^2 \right]^{3/2} \quad (4.1.6)$$

For fixed a this effect grows as z_0 decreases; i.e., when the target gets closer to the sensor.

We can also let vary the horizontal position of the target. We take $\mathbf{r}' = x_0\hat{\mathbf{x}} - z_0\hat{\mathbf{z}}$, and we obtain for the field

$$H_z = \frac{m}{4\pi} \frac{2z_0^2 - \rho^2 - x_0^2 + 2\rho x_0 \cos \phi}{(z_0^2 + \rho^2 + x_0^2 - 2\rho x_0 \cos \phi)^{5/2}}. \quad (4.1.7)$$

There is probably a closed expression for the flux, but it is undoubtedly very complicated. An intermediate expression is

$$\Phi = -\frac{m}{8\pi} \int_0^a \frac{z_0^2 k^3 \rho d\rho}{(\rho|x_0|)^{3/2}(\rho - |x_0|)^2 + z_0^2} \left[K(k) + \frac{((\rho^2 - x_0^2)^2 - 2z_0^2(\rho^2 + x_0^2) - 3z_0^4)}{z_0^2((\rho - |x_0|)^2 + z_0^2)} E(k) \right], \quad (4.1.8)$$

where $K(k)$ and $E(k)$ are the complete elliptic integrals of the first and second kinds and the modulus

$$k^2 = \frac{4\rho|x_0|}{(\rho + |x_0|)^2 + z_0^2}. \quad (4.1.9)$$

Making $x_0 = 0$ in (4.1.8) we easily recover (4.1.4). If we merely substitute the field at the center and multiply by the receiver area, we obtain

$$\Phi' = \frac{m}{4\pi} \frac{2z_0^2 - x_0^2}{(z_0^2 + x_0^2)^{5/2}} \pi a^2 = \frac{ma^2}{4} \frac{2z_0^2 - x_0^2}{(z_0^2 + x_0^2)^{5/2}} \quad (4.1.10)$$

As part of the Generalized Standardized Excitation Approach to be considered later, it is possible to use a shortcut in this integration by employing Stokes's theorem:

$$\oint_C \mathbf{A} \cdot d\mathbf{l} = \int_S (\nabla \times \mathbf{A}) \cdot \hat{\mathbf{n}} ds \quad (4.1.11)$$

Defining a “vector potential” (which in rigor should be proportional to the permeability of the medium) by

$$\mathbf{A} = \frac{\mathbf{m} \times \mathbb{R}}{4\pi R^3} \quad (4.1.12)$$

we can easily verify that its curl is given by (4.1.3). For the situation considered in this section we have

$$\mathbf{A} = \frac{m\rho\hat{\phi}}{4\pi(\rho^2 + z_0^2)^{3/2}} \quad \text{in general and} \quad \mathbf{A} = \frac{ma\hat{\phi}}{4\pi(a^2 + z_0^2)^{3/2}} \quad (4.1.13)$$

along the circumference of the receiver, which trivially integrates to yield (4.1.4).

4.1.c.(2) The other receivers To verify that our integration routines are correct we compare the integrated flux to the average one for an upright dipole. In this case the depth is $z_0 = -35$ cm, and we have $x_0 = 4$ cm and $y_0 = 12$ cm. Interesting results: The H_x plots are very similar; the H_z plots show the same tendency we saw in the last section—the averaged flux tends to be larger than the integrated one; the H_y plots show the opposite tendency. See Figure 4.1.3. The dipole can also be tilted, as Figure 4.1.4 shows.

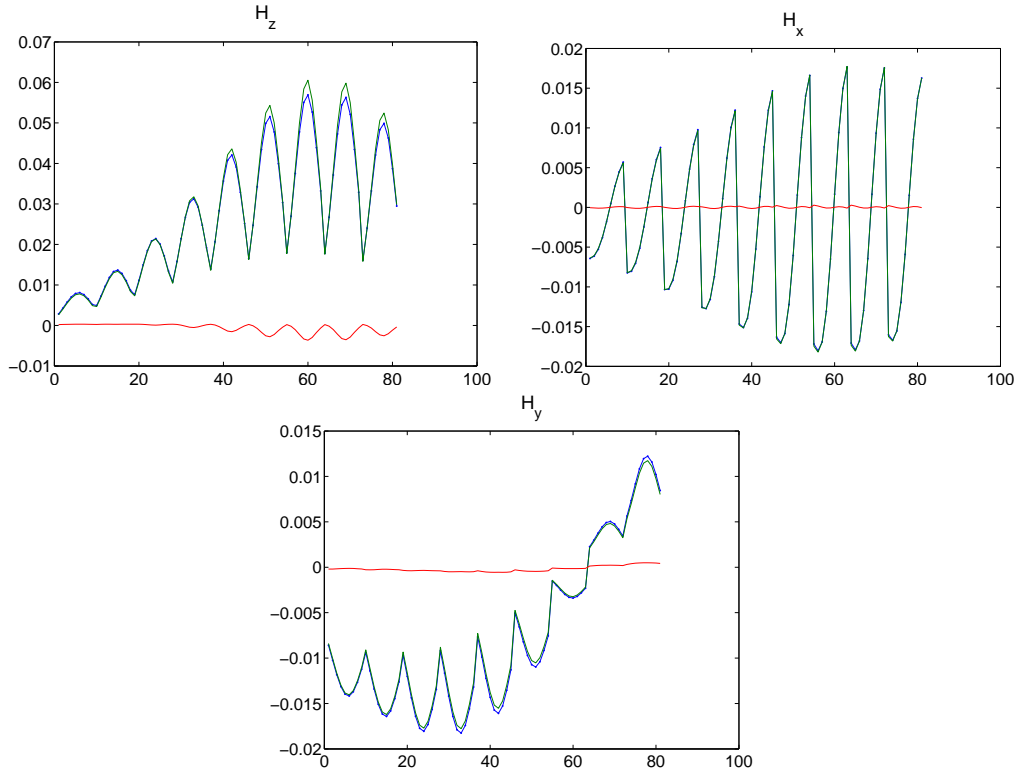


Figure 4.1.3: Integrated (blue) and averaged (green) flux profiles on a grid above an upright dipole; from left to right we have the z -, x -, and y -components. The red is the difference between the two.

4.1.c.(3) Beacon positioning One of the features that make the GEM-3 \mathcal{D}^+ potentially useful for dependable UXO identification is its positioning system, which provides sub-centimeter accuracy and can be used in treed or rugged terrain. The beacon is also lightweight and unobtrusive, requiring almost no hardware to be attached to the sensor itself.

For the data analysis it is necessary to have the tilt information referred to the same global coordinate system in which the sensor location is known. This cannot be inferred directly, however, since the field of a dipole is azimuthally symmetric: the GEM-3 \mathcal{D}^+ can be rotated about its z -axis and appear identical to the beacon system. To ameliorate this, the sensor head also has affixed to it a digital compass [22] that at every sensor location gives the three Euler angles, in the yaw-pitch-roll convention [23], in a coordinate system defined by magnetic North and the acceleration of gravity.

The connection between the compass and beacon coordinate systems can be determined in a least-squares sense from the fact that the direction of the dipole moment (\hat{z} in a reference frame fixed to the sensor head) is unique. We thus find

$$\mathbf{R}_{N \rightarrow b} = [\hat{z}_b^1 \ \hat{z}_b^2 \ \dots \ \hat{z}_b^M] [\hat{z}_N^1 \ \hat{z}_N^2 \ \dots \ \hat{z}_N^M]^\dagger \quad (4.1.14)$$

where the dagger denotes the pseudoinverse[24]. This rotation matrix can be polished further (i.e., made “more orthogonal”) by iterating[25]

$$\mathbf{R}_{n+1} = \frac{\mathbf{R}_n + (\mathbf{R}_n^T)^{-1}}{2}, \quad (4.1.15)$$

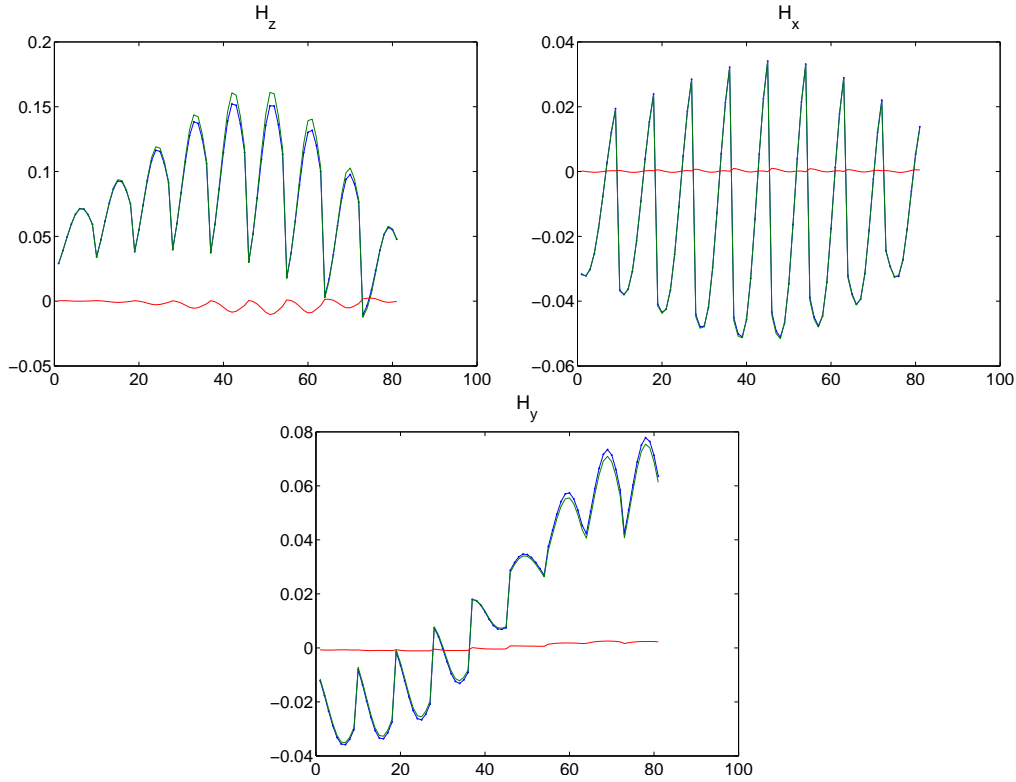


Figure 4.1.4: Integrated (blue) and averaged (green) flux profiles on a grid above an \hat{x} -directed dipole; from left to right we have the z -, x -, and y -components. The red is the difference between the two.

with \mathbf{R}_0 being the matrix found from (4.1.14). Very few iterations (rarely more than three) are needed.

4.1.d Forward models

4.1.d.(1) The dipole approximation A popular and useful model for UXO discrimination replaces the buried target by one or more triaxial point dipoles, either in the frequency domain [7, 26] or in the time domain [9]. The dipole model has been found to fit measured data adequately when bodies are small enough that the primary field can be assumed uniform along their extent, when they are far enough away from the sensor that higher moments vanish, and when their composition is homogeneous enough that there are no conflicting signals from different parts of the object [8, 27].

The signal picked up by the μ th receiver is when the sensor is centered at \mathbf{r}_j is

$$S_\mu(\mathbf{r}_j) = \int_{\mathbf{R}_\mu(\mathbf{r}_j)} \frac{3(\mathbf{m} \cdot \bar{\mathbf{R}})\bar{\mathbf{R}}/R^2 - \mathbf{m}}{4\pi R^3} \cdot \hat{\mathbf{n}}_\mu dS_{\mathbf{R}_\mu} \quad (4.1.16)$$

where $\bar{\mathbf{R}} = \mathbf{r} - \mathbf{r}'$, \mathbf{r} is any observation point, and \mathbf{r}' is the location of the dipole. The dipole moment $\mathbf{m} = \mathbf{B}\mathbf{H}^{\text{pr}}$. An example fit to actual UXO data using this model, as well as the extracted polarizability elements, can be found in Fig. 4.1.5.

We can use the results given by this approximation as a starting guess for the more demanding SEA approach, which we discuss next.

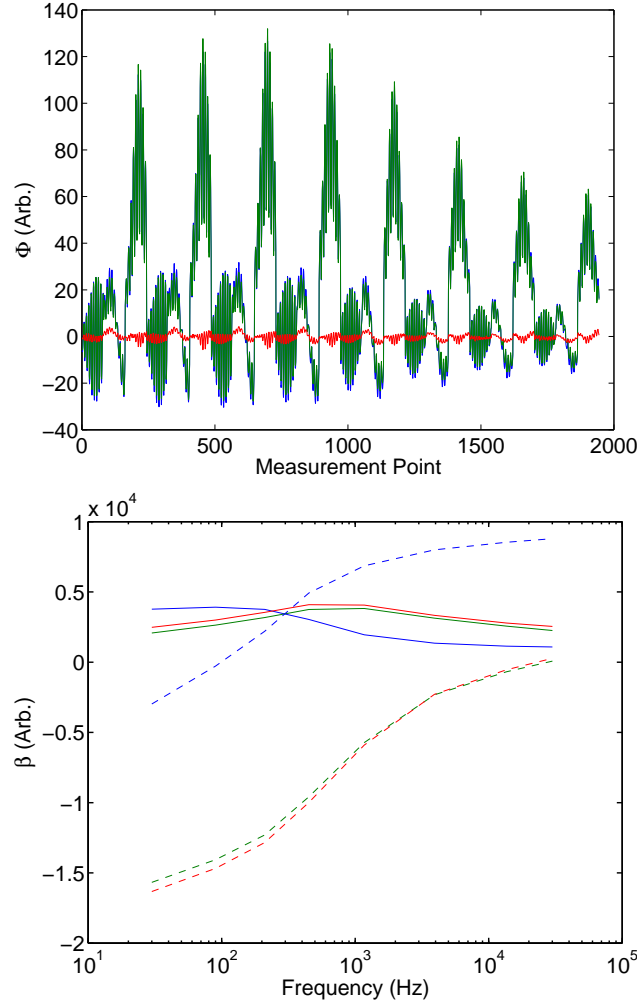


Figure 4.1.5: (Upper) Quadrature part of the flux through the three receiver coils for an H-83 UXO with nose tilted 45° down. (Lower) Extracted polarizability elements (dashed lines: inphase part; solid lines: quadrature part); it is clearly seen that the object exhibits cylindrical symmetry.

4.1.d.(2) The Generalized Standardized Excitation Approach The Generalized Standardized Excitation Approach (GSEA) [14, 15] is simultaneously a generalization and a simplification of the usual SEA[11]. For determining a superior set of equivalent sources to produce the fundamental modal responses, its starting point is the observation that in the EMI regime the fields outside a metallic target are irrotational and can hence be described by a scalar potential that obeys the Laplace equation, whose fundamental solution in a prolate spheroidal system ($-1 \leq \eta \leq 1$, $1 \leq \xi < \infty$, $0 \leq \phi < 2\pi$) centered at the scatterer is the superposition [28]

$$\psi(\mathbf{r}) = \frac{1}{2} H_0 d \sum_{m=0}^{\infty} \sum_{n=m}^{\infty} \sum_{p=0}^1 b_{pmn} P_n^m(\eta) P_n^m(\xi) T_{pm}(\phi), \quad \text{where} \quad T_{pm}(\phi) = \begin{cases} \cos m\phi, & p = 0 \\ \sin m\phi, & p = 1 \end{cases} \quad (4.1.17)$$

and the $P_n^m(\cdot)$ are associated Legendre functions. The interfocal distance for a prolate spheroid with semiminor and semimajor axes a and b is $d = 2\sqrt{b^2 - a^2}$; the surface of the spheroid is the

set of points $\xi = \xi_0 \equiv 2b/d$. We choose the scale factor $H_0 = 1$. It is easier and more efficient to perform the decomposition on the normal magnetic field over the spheroid, employing the fact that

$$H_\xi(\mathbf{r}) = -\hat{\xi} \cdot \nabla \psi(\mathbf{r}) = -\frac{1}{h_\xi} \frac{\partial \psi(\mathbf{r})}{\partial \xi}, \quad \text{where the metric coefficient } h_\xi = \frac{d}{2} \sqrt{\frac{\xi_0^2 - \eta^2}{\xi_0^2 - 1}}. \quad (4.1.18)$$

The orthogonality of the Legendre and trigonometric functions [29] yields

$$b_{pmn} = -\frac{\int_{-1}^1 d\eta P_n^m(\eta) \int_0^{2\pi} d\phi T_{pm}(\phi) h_\xi H_\xi}{\frac{1}{2} \alpha \pi H_0 d \frac{2}{2n+1} \frac{(n+m)!}{(n-m)!} \left. \frac{\partial P_n^m(\xi)}{\partial \xi} \right|_{\xi_0}}, \quad (4.1.19)$$

where $\alpha = 2$ for $p = m = 0$ and $\alpha = 1$ otherwise. To compute (4.1.19) we use for each transmitter coil the exact expression (4.1.2) for the field of a circular current and evaluate the integrals using Gauss-Legendre quadrature and the periodic trapezoid rule[30]. The signal in the μ th receiver when the sensor is at \mathbf{r}_j is given by

$$S_\mu(\mathbf{r}_j) = \sum_{m=0}^{\infty} \sum_{n=m}^{\infty} \sum_{l=1}^{N_r} \rho_{l,mn} \Gamma_{l,mn}^\mu(\mathbf{r}_j), \quad (4.1.20)$$

where

$$\Gamma_{l,mn}^\mu(\mathbf{r}_j) = \sum_{p=0}^1 b_{pmn}(\mathbf{r}_j) \int_{\mathbf{R}\mu(\mathbf{r}_j)} d\mathbf{s}_{\mathbf{R}\mu} \hat{\mathbf{n}}_\mu \cdot \int_0^{2\pi} T_{pm}(\phi') \frac{3(\hat{\xi}' \cdot \mathbb{R}_l) \mathbb{R}_l / R_l^2 - \hat{\xi}'}{4\pi R_l^3} \chi_l d\phi' \quad (4.1.21)$$

with $\mathbb{R}_l = \mathbf{r} - \mathbf{r}'_l \mathbb{I}$ and the position vector on the l th ring

$$\mathbf{r}'_l = \chi_l (\hat{x} \cos \phi' + \hat{y} \sin \phi') + \hat{z} \eta_l \xi_0, \quad \text{and} \quad \chi_l = \frac{d}{2} \sqrt{(1 - \eta_l^2)(\xi_0^2 - 1)}. \quad (4.1.22)$$

In other words, instead of the rings of charge considered before [11, 13] we use rings of radially directed dipoles. This is a simplification of the original SEA in that it is not necessary to force the total charge to vanish in order to comply with the Maxwell equations. Equivalently,

$$\Gamma_{l,mn}^\mu(\mathbf{r}_j) = \sum_{p=0}^1 b_{pmn}(\mathbf{r}_j) \oint_{\mathbf{R}\mu(\mathbf{r}_j)} d\mathbf{l}_{\mathbf{R}\mu} \cdot \int_0^{2\pi} T_{pm}(\phi') \frac{\hat{\xi}' \times \mathbb{R}_l}{4\pi R_l^3} \chi_l d\phi'. \quad (4.1.23)$$

Equation (4.1.20) can be turned into a linear system by finding an appropriate invertible mapping $(l, mn) \leftrightarrow k$

$$\mathbf{S}' = \begin{bmatrix} S'_x(\mathbf{r}_1) & \cdots & S'_x(\mathbf{r}_{N_p}) & S'_y(\mathbf{r}_1) & \cdots & S'_z(\mathbf{r}_{N_p}) \end{bmatrix}^T. \quad (4.1.24)$$

and

$$\mathbf{\Gamma} = \begin{bmatrix} \Gamma_{1,1}^x(\mathbf{r}_1) & \cdots & \Gamma_{N_r,1}^x(\mathbf{r}_1) & \cdots & \Gamma_{N_r,k_{\max}}^x(\mathbf{r}_1) \\ \Gamma_{1,1}^x(\mathbf{r}_2) & \cdots & \Gamma_{N_r,1}^x(\mathbf{r}_2) & \cdots & \Gamma_{N_r,k_{\max}}^x(\mathbf{r}_2) \\ \vdots & & \vdots & & \vdots \\ \Gamma_{1,1}^z(\mathbf{r}_{N_p}) & \cdots & \Gamma_{N_r,1}^z(\mathbf{r}_{N_p}) & \cdots & \Gamma_{N_r,k_{\max}}^z(\mathbf{r}_{N_p}) \end{bmatrix}. \quad (4.1.25)$$

Once we have this, we minimize the discrepancy to obtain

$$\min_{\rho} \frac{1}{2} (\Gamma \rho - \mathbf{S}')^T (\Gamma \rho - \mathbf{S}'). \quad (4.1.26)$$

This is a highly ill-conditioned system that requires regularization. We have employed two regularization methods: the truncated Singular Value Decomposition (TSVD) [31] and the Tikhonov procedure [24].

4.1.e Results

We start by stressing the necessity of integrating over the receivers when calculating responses for the case of monostatic measurements. We consider a sphere. It is well known[32] that a sphere of conductivity σ , relative permeability μ_r , and radius a placed in a uniform primary field behaves like a dipole of moment $\mathbf{m} = \mathbf{B}\mathbf{H}^{\text{pr}}$; for small spheres we can assume \mathbf{H}^{pr} from (4.1.2) to be approximately uniform over the target size, and the polarizability matrix $\mathbf{B} = \beta \bar{\mathbf{I}}$, where

$$\beta = 2\pi a^3 \frac{(2\mu_r + 1)(ka \coth ka - 1) - (ka)^2}{(\mu_r - 1)(ka \coth ka - 1) + (ka)^2}, \quad \text{and} \quad k = (1 + i)/\delta = \sqrt{i\mu_0\mu_r\omega\sigma}. \quad (4.1.27)$$

Equation (4.1.6), which is valid only right above a target, still applies in this case and lets us check the correctness of our results. The differences are dramatic when the target is very close to the sensor, as Figure 4.1.6 illustrates. In this case the depth is 10 cm, and the sphere is below the origin. Equation (4.1.6) is satisfied to 15 figures. It is evident that in the interest of realism we must integrate over the receiver areas when modeling responses.

We now turn to measured data taken over actual spheres at three different sensor heights (16, 21, and 26 cm above the surface of the sphere). We use two of the data files to extract the dipole moments of the rings and use these to predict the field in the unseen instance. We have used two methods to regularize (4.1.26): 1) We first perform Tikhonov regularization [11, 24] using the L-curve method [31] to determine the regularization parameter. 2) We also computed the Singular Value Decomposition (SVD) of $\Gamma^T \Gamma$, truncated it using the criterion suggested by the Picard plot [31], and used the truncated version to solve the normal equation (4.1.26).

4.1.f Conclusion

In this section we have presented a handheld frequency-domain sensor whose wide range of operating frequencies, three-dimensional vector receptivity, and innovative positioning system make it a strong candidate for providing robust and reliable discrimination of UXO.

After introducing the GEM-3 \mathcal{D}^+ and seeing the importance of obeying Faraday's law as exactly as possible when modeling the signal collected by each receiver, we proceeded to use the point dipole model and the Generalized Standardized Excitation Approach to model synthetic and measured data.

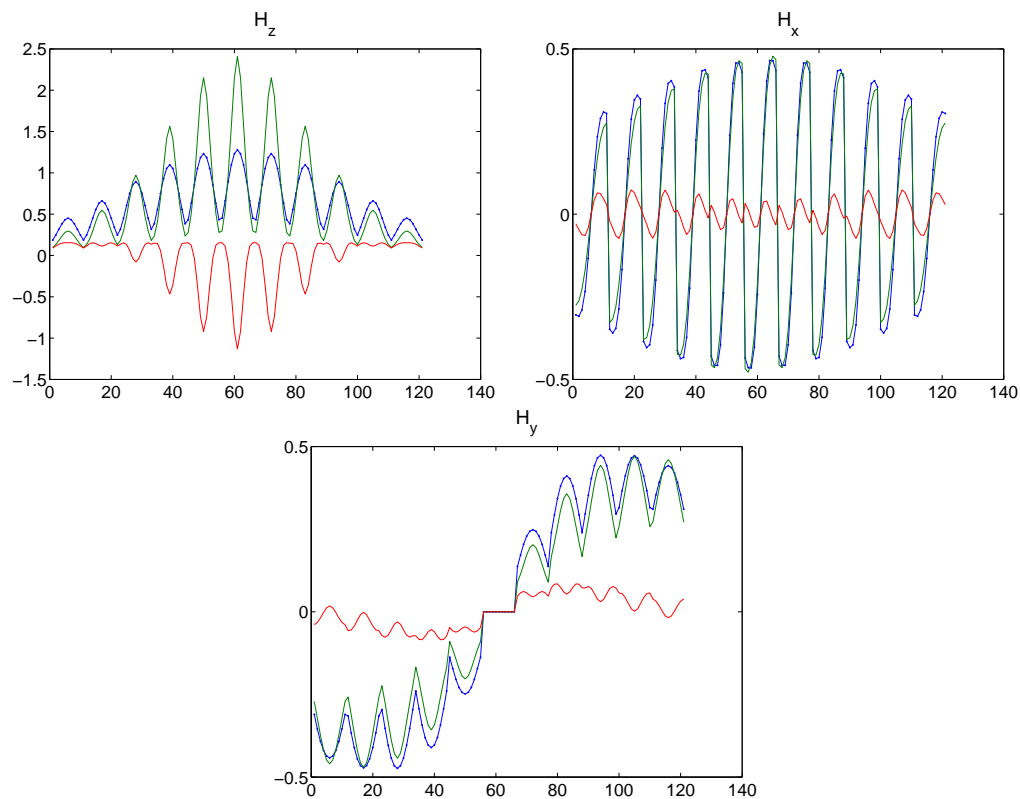


Figure 4.1.6: Integrated (blue) and averaged (green) flux profiles on a grid above a sphere; from left to right we have the z -, x -, and y -components. The red is the difference between the two.

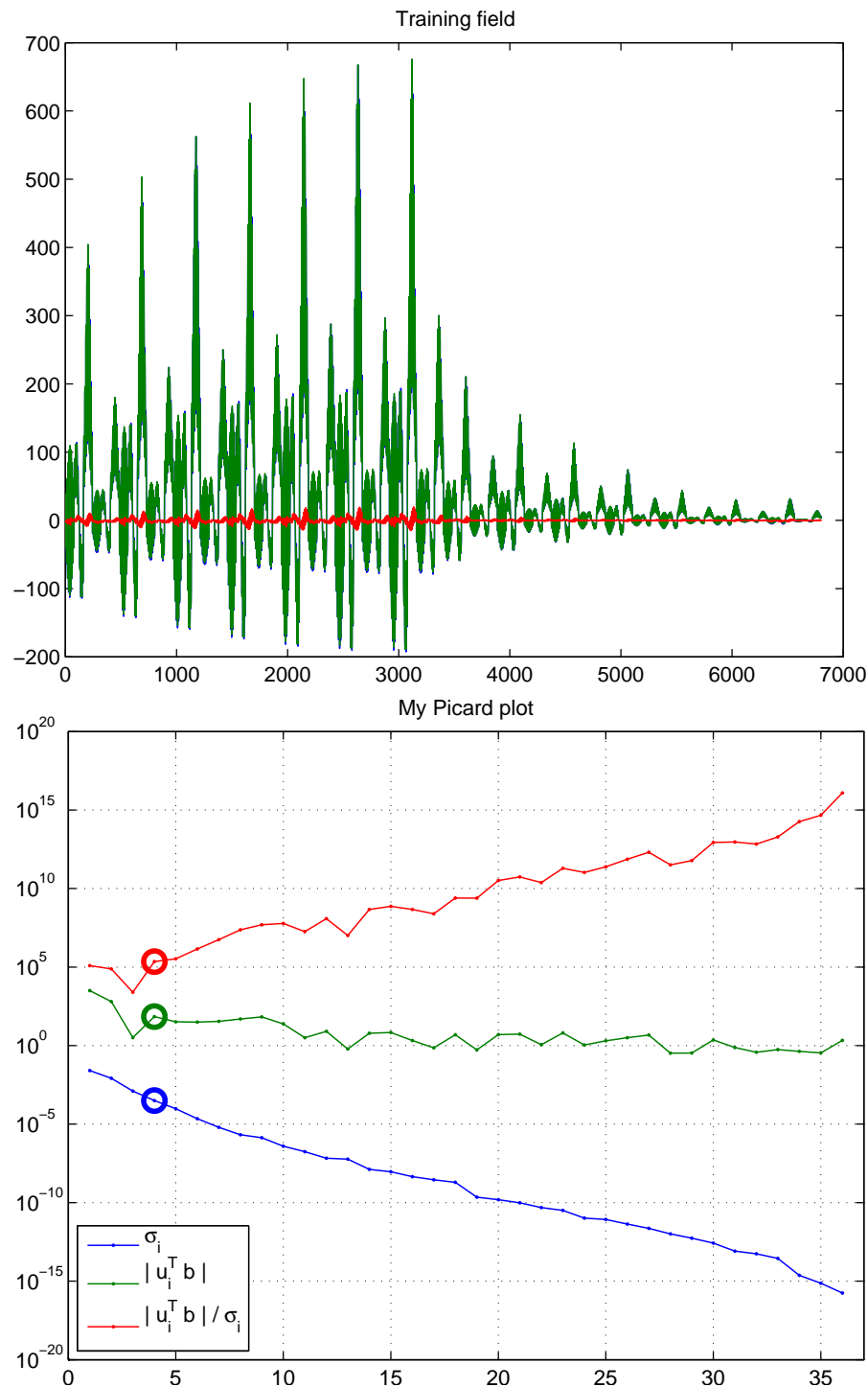


Figure 4.1.7: (Upper) “Training” field used to extract the GSEA dipole moments of an aluminum sphere; (Lower) Picard plot showing the singular values of $\Gamma^T \Gamma$.

4.2 Soil Response of the GEM-3 \mathcal{D}^+

Our April 2007 White paper for the GEM-3 \mathcal{D}^+ and the MPV instruments details the theory behind soil responses for both instruments. In this section, we will discuss some of the data we have taken from local soils with the GEM-3 \mathcal{D}^+ and the advantages afforded by the transverse receiver coils is their relative immunity to contamination from geological noise due to ground response.

We arranged to test some soils at a local gravel pit, Lebanon Crushed Stone. The main soil we tested was known as “sump sand” and it exhibited a large magnetic response in the frequency domain to the GEM-3 \mathcal{D}^+ . We acquired height profiles at 2 in. increments up to 36 in. over this soil. Our measurement set up can be seen in Fig. 4.2.1. We also took high profiles over the soil after burying a steel sphere northwest of the measurement position (see Fig. 4.2.2). Height profiles at different frequencies after background subtraction are shown in Fig. 4.2.3. As we have reported elsewhere, the inphase part of the GEM-3 \mathcal{D}^+ data displays a trend of increasing signal with decreasing height until a maximum at around 5 to 10 cm above the ground. The quadrature component of the heights profile, on the other hand, displays only a weak trend if at all.



Figure 4.2.1: Setup of GEM-3 \mathcal{D}^+ at Lebanon Crushed Stone over “sump sand”.

Because the primary field is oriented downward in the $-\hat{z}$ direction, the principal response from the soil is oriented in \hat{z} with only a secondary response in the transverse receivers (see Fig. 4.2.4). This effect can be seen by comparing the data from the height profiles with and without this sphere present (see Figs. 4.2.5 and 4.2.6). With whatever variations in magnitude, the isotropic response from the sphere target should be the same in all vector components. Notice in Fig. 4.2.6 top, that the apparent H_z response is shifted downward (c.f. bottom plot) as it also contains the soil response. These figures show the strong broadband soil response in the \hat{z} receiver coil and the almost negligible response in the transverse receiver coils (\hat{x} and \hat{y}).

Using the scale factors contained in Fig. 4.2.7 and derived from the comparison of analytical



Figure 4.2.2: Burying a steel sphere in the “sump sand”.

models with actual sphere data (see Sec. 4.4), we were also able to estimate the susceptibility, χ , of this soil. A plot of the match between model and data is provided in Fig. 4.2.8. The estimated susceptibility of this soil is $\chi = 0.0032$, a very realistic value based on the work of Janet Simms at the Standardized Test Sites [33–35].

Using this technique, we hope to be able to account for local geological noise at remediation sites by acquiring height profile data over local soil which is not contaminated by metallic targets; and also by inferring soil effects in the H_z component by analyzing the relatively uncontaminated horizontal components.

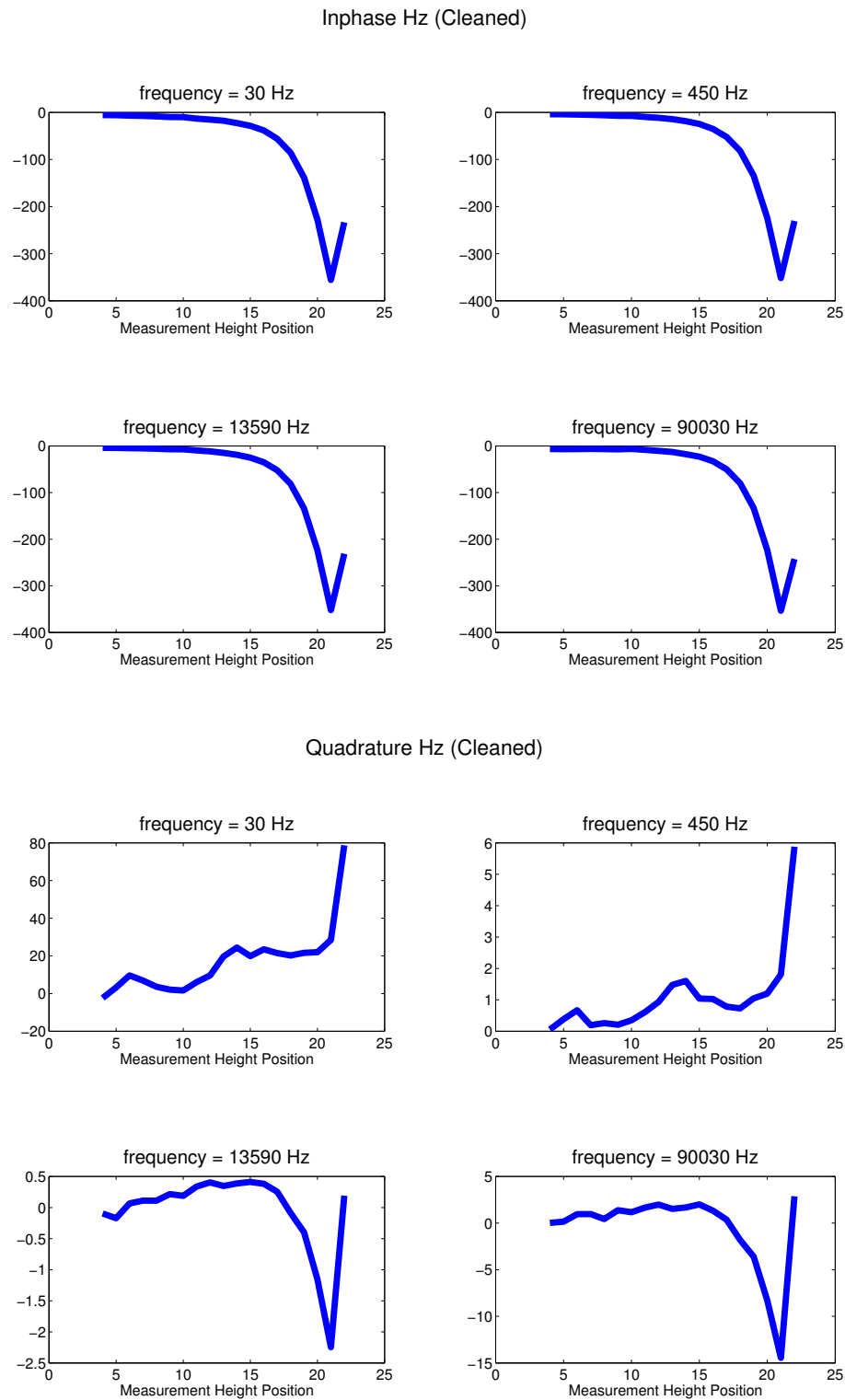


Figure 4.2.3: Inphase and quadrature components of GEM-3 \mathcal{D}^+ taken over “sump sand” with height decreasing left to right.

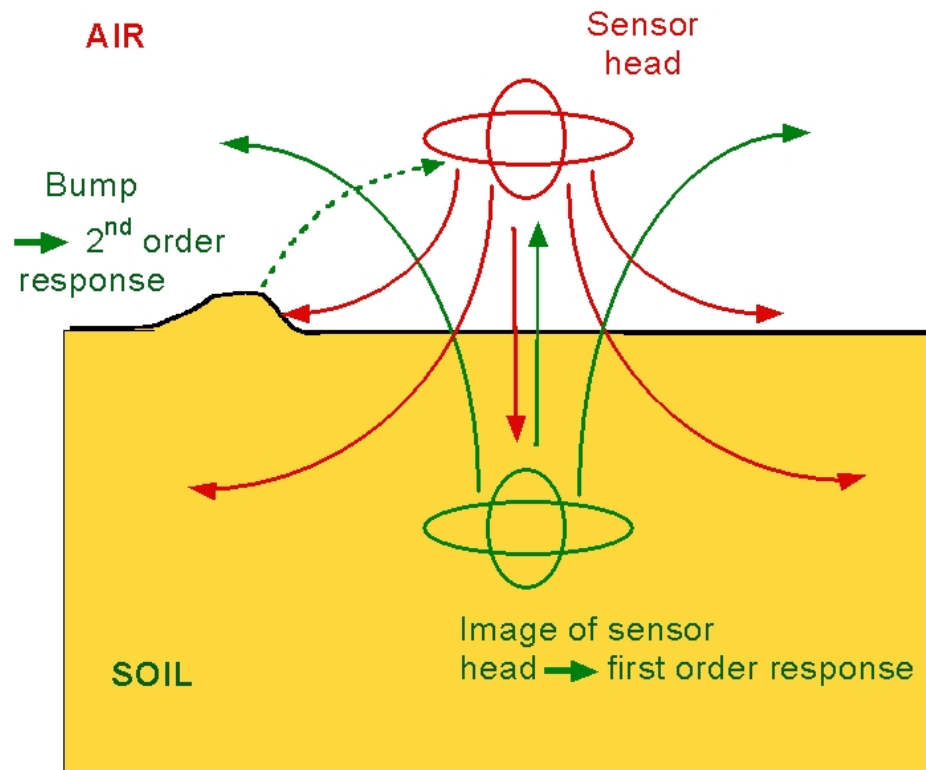


Figure 4.2.4: EMI sensor above a halfspace, including a bump on the soil-air interface.

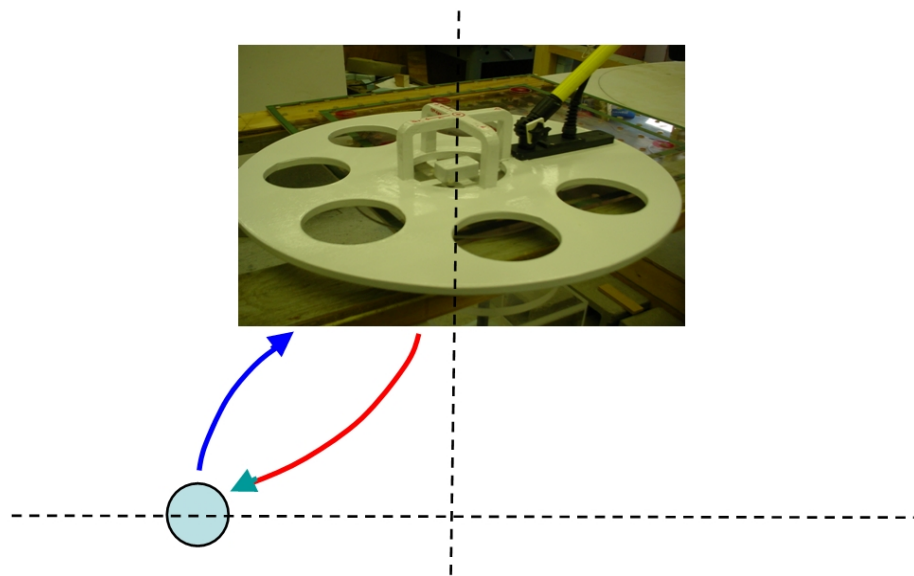


Figure 4.2.5: GEM-3 \mathcal{D}^+ setup comparing “sump sand” data to “sump sand”+sphere data.

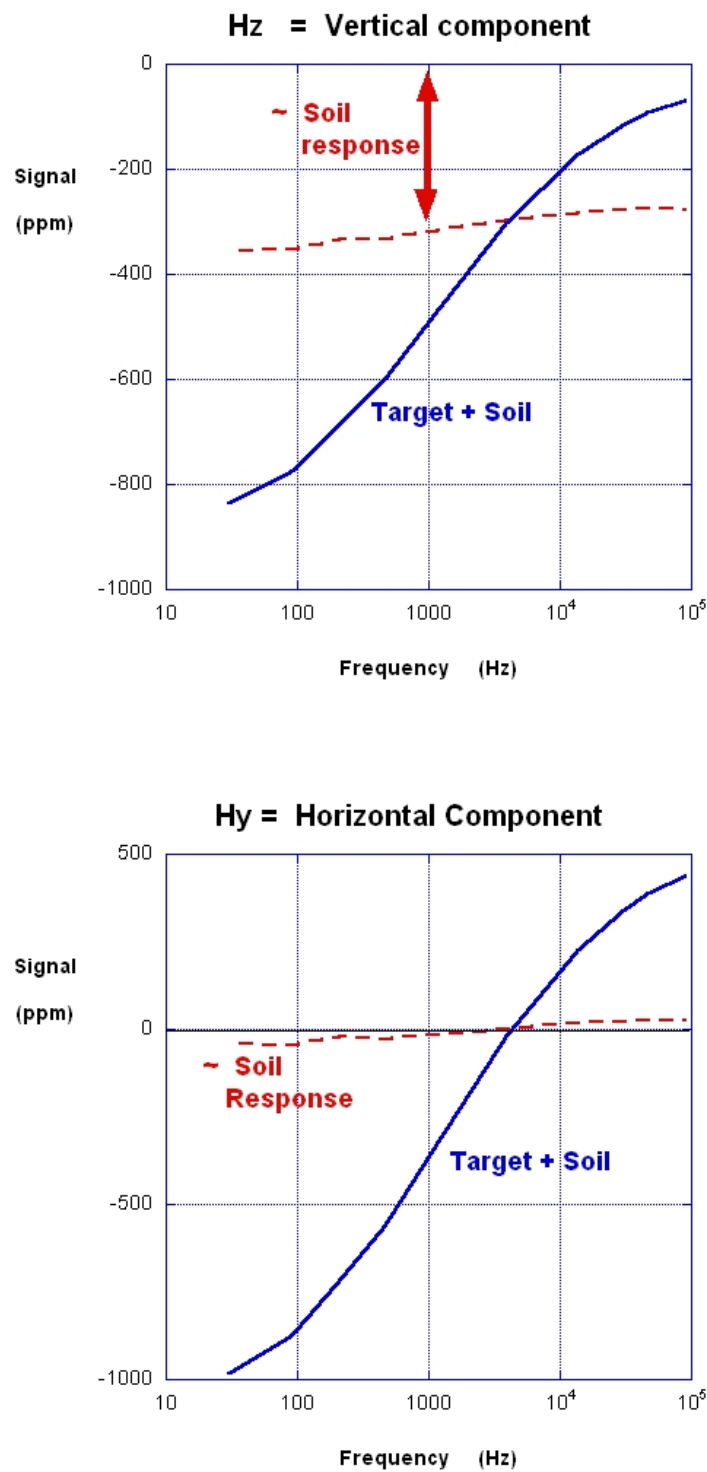
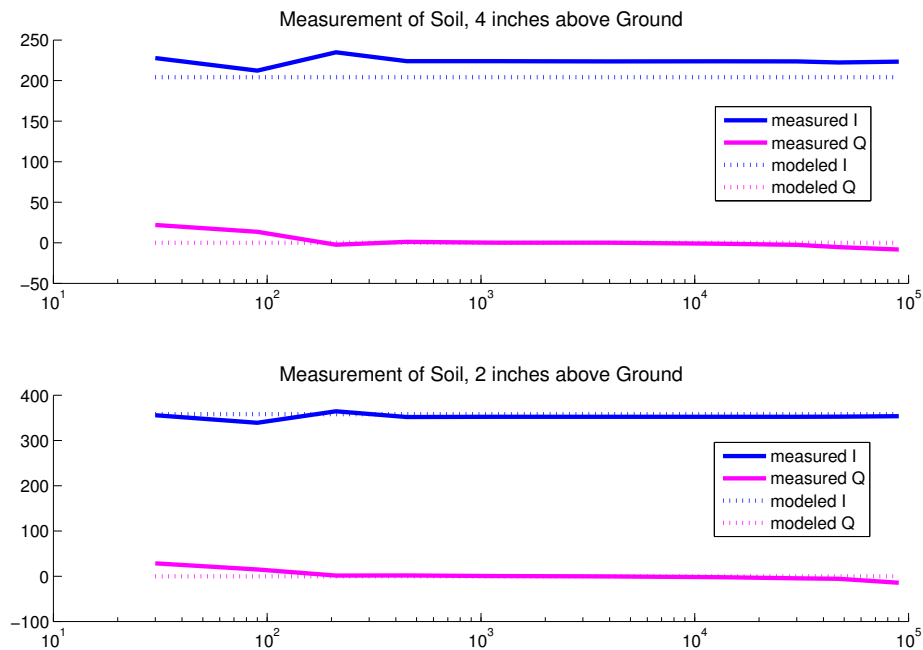


Figure 4.2.6: GEM-3 \mathcal{D}^+ inphase response showing the substantial soil response contaminating the H_z receiver but not the H_y receiver.

	Alum 16cm Avg.	Alum 21cm Avg.	Brass 16cm Avg.	Brass 21cm Avg.	Steel 17.5cm Avg.	Steel 22.5cm Avg.	Overall Avg. per Loop	Max. Dev. from Avg.
Hx	3252	3136	3174	3115	3203	3067	3159	2.943%
Hy	3338	3195	3283	3153	3312	3187	3245	2.866%
Hz	2129	2120	2183	2084	2160	2132	2135	2.248%

Figure 4.2.7: Soil model match to GEM-3⁺ data using scale factor.Figure 4.2.8: Soil model match to GEM-3⁺ data using scale factor.

See additional material relative to soil response – addendum to “White Paper” for MM1537 [36] that illustrates the use of the conversion factors for inference of geophysical conclusions, and for characterization of instruments relative to UXO discrimination.



The problem with the view encouraged by Fig. 4.2.8 is that it does not explain the fact that significant soil responses are seen by time domain instruments. To understand the issue, consider a FD expression for μ_r in terms of magnetic susceptibility χ as

$$\mu_r(\omega) = 1 + \chi(\omega) = 1 + \chi'(\omega) + i\chi''(\omega) \quad (4.2.1)$$

where i is the square root of negative one and the angular frequency ω is 2π times frequency in Hz. The implication of spectral patterns like that in Fig. 4.2.8 is that

$$\chi'(\omega) \approx \text{constant}, \chi''(\omega) \approx 0 \quad (4.2.2)$$

Such a constant, real valued χ should produce no response in time domain measurements. Given negligible electrical conductivity in a soil, its response would simply be proportional to χ' times the magnitude of the transmitted field at any given point in time, *with no delay*. All response would be instantaneous. When the transmitted field from a TD instrument is shut off during the recording of data, the soil response would also shut off, producing no data other than noise. However, many time domain measurements do indeed show some soil response in more or less orderly decay patterns. Evidently some kind of relaxation effect takes place, beyond the instantaneous response.

Overall, one might hypothesize a soil response in the form of the schematic in Fig. 4.2.9, given a downward step input in the primary field at $t = 0$.

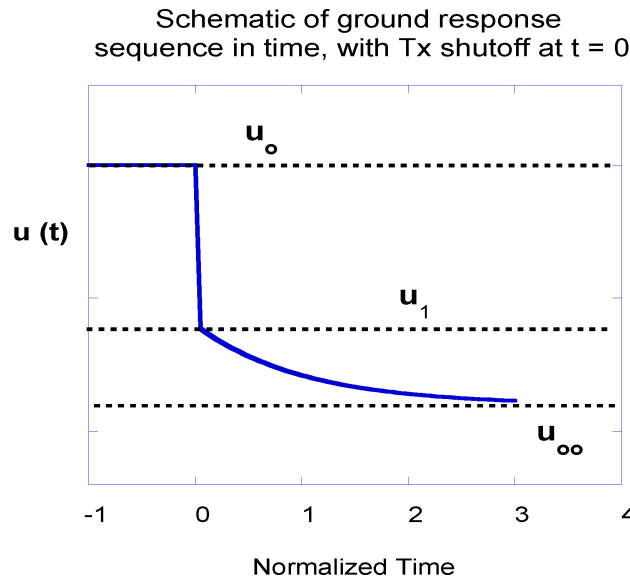


Figure 4.2.9: Hypothesized relaxation type time response for real soil permeabilities.

The instantaneous response of the system is from its initial value of u_o to u_1 . This response persists for all $t > 0$. It corresponds to the flat real-valued (i.e. inphase) impulse response in Fig. 4.2.9. On top of that is a relaxation to the ultimate response to u_{oo} .

The only way to explain measurable TD instrument response to the same soil as in Fig. 4.2.8 is to hypothesize that a relaxation type spectrum (see MM1537 white paper) lies within the spectrum shown in the Fig. 4.2.8, but that it is overshadowed by the larger instantaneous response, i.e. it is below the resolution of this data.

To investigate this, we also computed conversion factors for the TD MPV device (see Sec. 4.4). If the conversion/calibration factors for both the GEM and the MPV are correct, then when the primary fields are scaled so that a sphere is illuminated by the same intensity from each device, each instrument will report the same magnetic response at the same distance. Figure 4.2.10 below shows that this is the case, when the GEM-3 spectrum is converted to a TD response via Wait's analytical solution [37, 38].

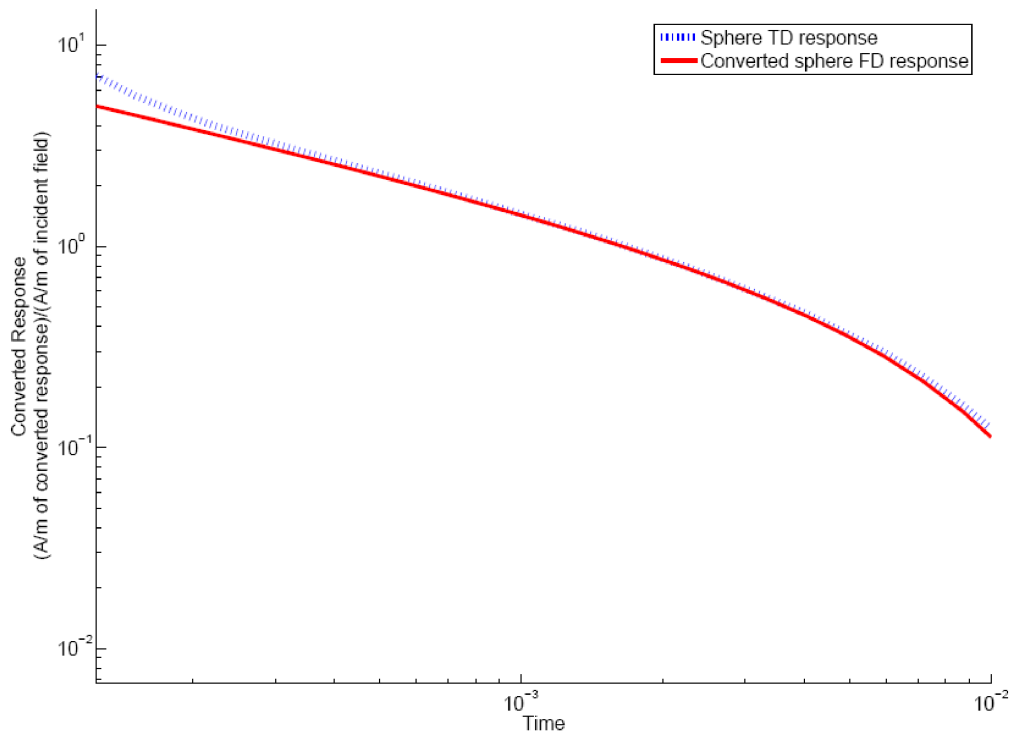


Figure 4.2.10: Measured GEM-3 (“converted”) and MPV responses from a sphere, observed at the same distance, when each response has been scaled additionally by the primary field from each instrument.

The implication of all this is apparent if one applies the same kind of scaling as in Fig. 4.2.10 to measured soil responses. For a CRREL backyard soil with FD spectra like that in Fig. 4.2.8 above, we also measured the MPV response. We then converted the GEM-3 soil response to a TD response, retaining the magnitude indicated by our conversion factor, with observation points about the same distance from the soil. When the GEM-3 and MPV soil responses are further scaled so that the illumination of the soil surface is the same magnitude for both instruments, one obtains Fig. 4.2.11 below.

That is, Fig. 4.2.11 shows approximately the same *kind* of thing as Fig. 4.2.10. The latter shows that, given our conversion factors, we can illustrate that a given metal object (sphere) produces the same response to the same to the same intensity of illumination, when observed from the same distance by different instruments. The reason that the similarly scaled soil responses in Fig. 4.2.11 are *different* is that the TD instrument only sees part of the soil response, namely the relaxation part. The instantaneous part has passed by the time the first time gate falls in the MPV. On the other hand, the GEM-3, and for that matter *any other frequency domain instrument*, is dominated

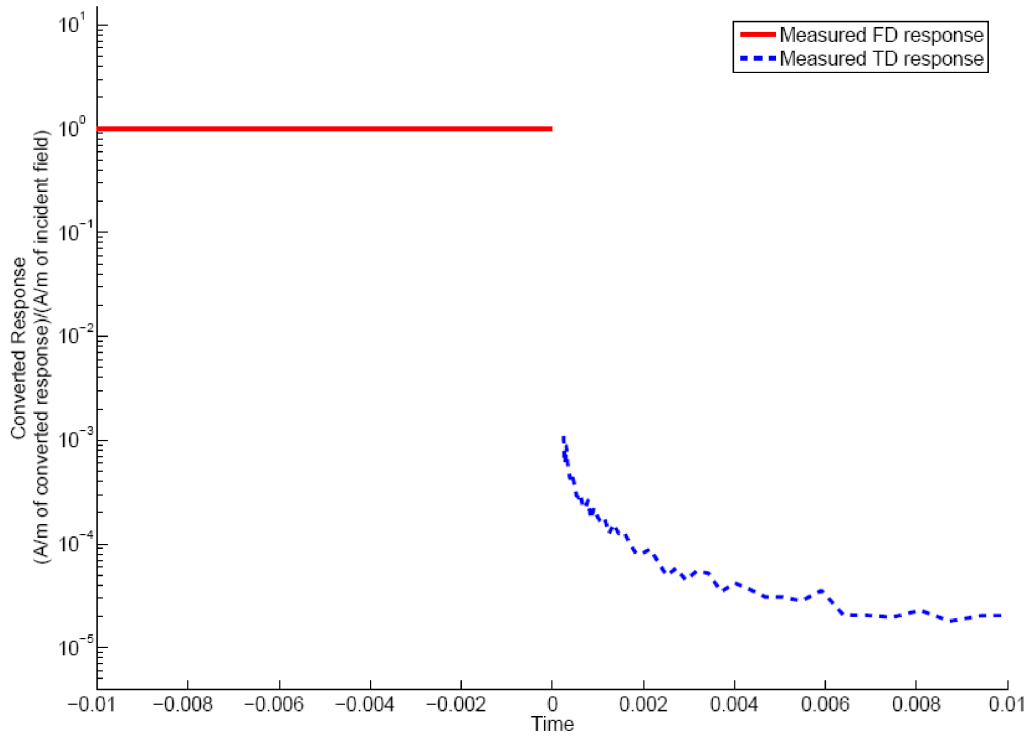


Figure 4.2.11: Comparison of measured responses of the soil to the GEM-3 and from the MPV, from about the same observation point, when the illumination of the soil surface has been scaled to be the same for each instrument. The red GEM-3 response, converted to TD, is flat before the step shut off at time zero, at which point it theoretically goes to zero, instantaneously. The blue MPV data start some finite time after shutoff ($\sim 10^{-4}$ s) and decay thereafter.

by the much larger (> 3 OM) instantaneous response, that appears at all frequencies.

With all this in mind, the most general representation of soil susceptibility may be something like:

$$\chi(\omega) = \chi_{o1} + \chi_{o2}R(\omega) \quad (4.2.3)$$

where χ_{o1} and χ_{o2} are constants and $R(\omega)$ is something like the commonly used expression:

$$R(\omega) = 1 - \frac{1}{\ln(\tau_2/\tau_1)} \ln\left(\frac{i\omega\tau_2 + 1}{i\omega\tau_1 + 1}\right) \quad (4.2.4)$$

where τ_1 and τ_2 are chosen relaxation time limits. The parameter χ_{o1} would account for the larger flat response in the figs above. χ_{o2} would be the separate magnitude of the relaxation response. In this view, all the FD data treated here reflect the fact that $\chi_{o2} \ll \chi_{o1}$.

A little more explanation in terms of relaxation times. The schematic below in Fig. 4.2.12 shows hypothetical relaxation responses by different constituents within some soil.

The commonly used expression in (4.2.4) corresponds essentially to the collection of blue curves. That model assumes that there is a continuous distribution of relaxation times, evenly distributed in log space, and that all the curves converge to the same magnitude of contribution.

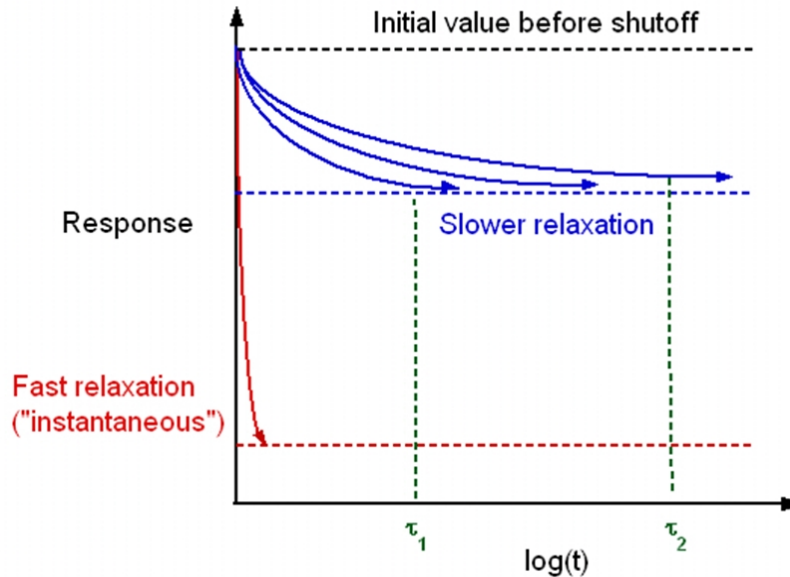


Figure 4.2.12: Hypothetical relaxation curves in (log) time for different constituents of some soil.

This has been said to model the TD responses effectively for many soils encountered in UXO studies [39–41]. What our research and conversion factor applications show is that an additional component with very short relaxation time is also typically present, converging to a much larger magnitude response (red curve/line). Treating the fast response as effectively instantaneous simply means adding the term χ_{01} in (4.2.3).

It has been suggested that one might cover all the effects mentioned here while retaining the older soil response model, i.e. (4.2.3)-(4.2.4) with $\chi_{01} = 0$, by stretching the relaxation time limits, in the very least to encompass virtually instantaneous responses. However this is likely to produce a muddled formulation, with limited generality. It would imply a continuous distribution of relaxation times between the “instantaneous” one and all the others, with equalization of magnitudes. Basically, these “cures” of the model’s shortcomings would constitute unphysical tweakings of the parameters or, in the least, an unsupported flight. While they might succeed in matching an individual FD spectral curve, the results would be unlikely to generalize successfully. That is, application of the resultant χ to other instruments or circumstances would likely fail.

CONCLUSIONS/ SIGNIFICANCE:

1. Application of the scaling/calibration/conversion factors so we can compare FD and TD responses in the same terms provides a fundamental insight into how different kinds of instruments respond to significantly different aspects of soil magnetic susceptibility. For the various backyard soils examined thus far, results suggest that the slow relaxation TD response is objectively much smaller than the FD response, which is dominated by effectively instantaneous response components.
2. The calibration factors that produced the evaluation of relative magnitude of FD/TD response, as in Fig. 4.2.10, can easily be applied further to calculate the factors in an expanded soil magnetic susceptibility model, as per (4.2.3). This information is then potentially transferable to other EMI instruments of whatever type. As the material above shows, existing

models are not transferable. Heretofore, FD data implied no TD response; TD data implied a much weaker, slower response than was seen in the FD. The expanded model covers all these bases.

3. Item #1 suggests that FD instruments will be at a disadvantage for discrimination in instances where significant ground responses cannot readily be subtracted as background. The GEM-3D+ counteracts this disadvantage by recording horizontal field components that are largely immune to ground response and that can help distinguish the contribution of target vs ground in typically stronger vertical components.

4.3 Estimating magnetic susceptibility from EMI data

4.3.a Executive Summary

Studies have showed that magnetically susceptible soils significantly affect EMI sensor performance, which in return reduce the sensors discrimination capabilities. In order to improve EMI sensors detection and discrimination performances first soil's magnetic susceptibility needs to be estimated, and then the soils EMI responses have to be taken into account during geophysical data inversion procedure. Until now the soil's magnetic susceptibility is determined using a tiny amount (up to 15 mg) of soil's probe. This approach in many cases does not represent effective magnetic susceptibility that affects on the EMI sensors performances. This paper presents an approach for estimating soil's magnetic susceptibility from low frequency electromagnetic induction data and it is designed namely for the GeoPhex frequency domain GEM-3 sensor. In addition, a numerical code called the method auxiliary sources (MAS) is employed for establishing relation between magnetically susceptible soil's surface statistics and EMI scattered field. Using the MAS code EMI scatterings are studied for magnetically susceptible soils with two types of surfaces: body of revolution (BOR) and 3D rough surface. To demonstrate applicability of the technique first the magnetic susceptibility is inverted from frequency domain data that were collected at Cold Regions Research and Engineering Laboratory's test-stand site. Then, several numerical results are presented to demonstrate the relation between surface roughness statistic and EMI scattered fields.

4.3.b Introduction

Active EMI sensors induce magnetization via their primary fields. The static magnetic sensors are sensitive to the presence of magnetic minerals because the earth's magnetic field creates an induced magnetization in them. This anomalous magnetic field produced by the soil magnetization will be superimposed on the magnetic anomalies produced by UXO's and other metallic objects and will therefore introduce adverse effects into the discrimination problem. There are three magnetic effects that impact the magnetic and electromagnetic characteristics of the subsurface: (4.3.1) induced magnetization, (4.3.2) viscous remanent magnetization (VRM); and (4.3.3) permanent/remanent magnetization

The magnetically susceptible and heterogeneous soils are a major problem for the near field EMI sensing technologies. Studies [42–51] showed that, magnetically susceptible soils can produce electromagnetic anomalies of the same magnitude as buried metallic targets. Even that in those studies, it is assumed that the spatial distribution of magnetic anomalies are constant, similar to a half space, and that this response can be subtracted from measured data, the practice shows that the magnetic soils significantly degrades performances and applicability of the EMI technologies

for UXO discrimination. Since, for discriminating between UXO and non-UXO targets accurately a dense measurement grid is required. Under these conditions, variations in sensor height and orientation, as well as small variations in the surface topography, can produce anomalies similar to those from UXO [44]. However, in most existing approaches to buried metallic object discrimination, the object of interest is assumed to be embedded in a medium with the same electromagnetic properties as free-space. Any influence of the background medium assumed to have been removed by pre-processing or filtering before the data are submitted to an inversion routine. Until now, techniques for calculating the background effects, which include the half layered-space earth and an equivalent dipole layer models that attempts to model the background geology, have almost exclusively neglected soils surface roughness and these techniques are limited to the use of one dimensional or layered Earth models. Such models are incapable of capturing the true process of geomagnetic induction that is associated with the surface roughness, as it is the case in real field environment. Therefore, one must characterize soil response so that it can be predicted, or so that it can at least be accounted for during data processing. The characterizing of soil's EMI response requires knowledge of its magnetic susceptibility. To date the soil's magnetic susceptibility is measured using a very small amount (up to 15 mg) of soil's probe, which in many cases does not represent effective magnetic susceptibility that affects on the state of the art EMI sensors performances.

This section investigates EMI scattering from magnetically susceptible random rough surfaces for establishing statistical relations between surface and signal characteristics. The study is done for the handheld GEM-3 sensor. First, to understand interaction between magnetically susceptible soil and the sensor here, an EMI magneto quasi-static (MQS) problem is solved using a numerical approach called the method of auxiliary sources (MAS) [52–55]. In MQS magnetic fields are irrotational, and can thus be represented efficiently using a magnetic scalar potential. In the MAS, boundary value problems are solved numerically by representing the electromagnetic fields in each domain of the structure under investigation by a finite linear combination of analytical solutions of the relevant field equations, corresponding to sources situated at some distance away from the boundaries of each domain. The "auxiliary sources" producing these analytical solutions are chosen to be elementary dipoles/charges located on fictitious auxiliary surface(s), usually conforming to but offset slightly from the actual surface(s) of the structure. Enforcement of standard electromagnetic boundary conditions at an array of points over the object's actual surface allows us to solve for the auxiliary sources, from which we can immediately express all EM fields in the problem.

The section is organized as follows: In section II, overviews very briefly EMI problem and the MAS Galerkin technique for MQS regime, Section III describes an approach for estimating soil's magnetic susceptibility from EMI data, section IV demonstrates several numerical results, and finally section V, presents conclusions and discussions.

4.3.c EMI Scattering for Magnetic Rough Soil

To illustrate the MAS for MQS problem, let us consider a permeable 3D magnetically susceptible rough surface. The surface is illuminated with an electromagnetic field produced by a GEM-3 sensor (Fig. 4.3.1). The computational region is divided into two regions: the region above the surface is referred to as Region 0 with free-space electromagnetic parameters, and Region 1 corresponding to the volume under the rough surface with $\epsilon_1=1$ but with a nonzero magnetic susceptibility. As is well established in the MQS regime, the displacement currents are negligible.

The primary field induces magnetic dipoles within the Region 1, which in turn produce secondary (scattered) fields. The magnetic field inside each region can be expressed as

$$\bar{H}_\alpha(\bar{r}) = -\nabla\Psi_\alpha(\bar{r}) \quad (4.3.1)$$

where

$$\Psi_\alpha(\bar{r}) = \frac{1}{4\pi\mu_\alpha} \int_{S_\alpha} \frac{\rho_\alpha ds'}{|\bar{r} - \bar{r}'_\alpha|} \quad (4.3.2)$$

$$\chi > 0$$

Here $\Psi_\alpha(\bar{r})$ is the fundamental solution of the Poisson equation, $\alpha=0,1$, μ_α is the permeability

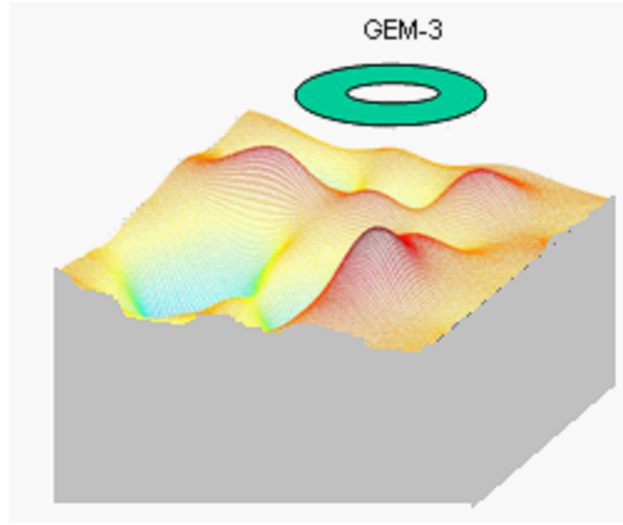


Figure 4.3.1: 3-D rough surface used for computational model.

of region α , and ρ_α is the n^{th} unknown magnetic charge source coefficient distributed on the α auxiliary surfaces. These sources reside on an auxiliary surface slightly outside and approximately conforming to the real surface. We compute the total field inside each $\alpha = 0,1$ region by assuming that these sources radiate into an infinite homogeneous medium with the properties of the corresponding region.

The electromagnetic fields at each interface between two regions are connected by boundary conditions. Specifically, the magnetic scalar potential and the normal component of the magnetic flux density must be continuous across the real surface:

$$[\hat{n} \times (\Psi_\alpha^{tot} - \Psi_{\alpha+1}^{tot})] = \bar{0} \quad (4.3.3)$$

$$\hat{n} \cdot (\bar{B}_\alpha^{tot} - \bar{B}_{\alpha+1}^{tot}) = 0 \quad (4.3.4)$$

where \hat{n} is the unit normal vector on the interface between the two regions. For achieving high accuracy and saving computational resources, the boundary value problem is solved using the MAS together with the standard Galerkin technique. To demonstrate the MAS-Galerkin approach, let us rewrite the boundary value problem in the following compact form

$$\hat{L}\rho = \psi \quad (4.3.5)$$

Here L is an integral-differential operator, ρ is auxiliary magnetic charge density and ψ is the right hand side of (4.3.2). Let a weighing function w and $\langle f, w \rangle$ denote the inner product of two scalar functions f and w , usually defined as

$$\langle f, w \rangle = \int f w ds' \quad (4.3.6)$$

here ds' is a surface element. Then, by using Galerkin's method, one can rewrite equation (4.3.6) as

$$\langle \hat{L}\rho, w \rangle = \langle \psi, w \rangle \quad (4.3.7)$$

upon discretization of equation (4.3.7) a linear system of equations for unknown ρ coefficients results. Once the amplitudes of the ρ coefficients are determined, the field at all points in both regions can be readily computed.



Figure 4.3.2: Experimental setup of GEM-3 sensor at various heights above the ground.

4.3.d Estimation of Soil's Magnetic Susceptibility from GEM-3 Measurement Data

The GEM-3 sensor consists of two transmitter loops. Based on the standard expression for the field from a wire loop in the magneto-quasistatic regime, the z component of the magnetic field radiated by the GEM-3 sensor along its z rotational axis can be expressed as:

$$H_z = \frac{I_o^1}{2} \frac{a_1^2}{(a_1^2 + z^2)^{3/2}} + \frac{I_o^2}{2} \frac{a_2^2}{(a_2^2 + z^2)^{3/2}} \quad (4.3.8)$$

According to image theory, for a GEM-3 sensor placed at an elevation z above a permeable half space, the magnetic field produced at z by the ground can be written as

$$H_z = \frac{\mu_{gr} - 1}{1 + \mu_{gr}} \frac{I_o a_1^2}{2} \left(\frac{1}{(a_1^2 + 4z^2)^{3/2}} - \frac{1}{(a_1^2 + 16z^2)^{3/2}} \right) \quad (4.3.9)$$

where $I_o^1 = I_o$, and $I_o^2 = -I_o/2$ has been assumed. So, if we know the I_o current and the a_1 radius then we can calculate the permeability of ground μ_{gr} . However, different EMI sensors record data in different units. For example, the GEM sensor produces field in “ppm” units relative to a separate reference receiver coil. Given the known geometry and assumed relation of the currents in the GEM, the actual scattering field from any target (metal or ground) with σ and μ , can be written in the following form

$$\bar{H} = I_{un} \bar{F}(\sigma, \mu, \text{geometry}) = \bar{H}_{data}/p \quad (4.3.10)$$

I_{un} is the unknown current and p is some unknown scaling factor (accounting for amplification, filtering, the size of the reference coil, etc.) that produces the GEM’s readings in terms of “ppm”. Once the scaling factor is known, then the soil’s magnetic susceptibility can be estimated as

$$\chi = \mu_{gr} - 1 = \frac{2\gamma}{1 - \gamma} \quad (4.3.11)$$

here

$$\gamma = \frac{H_{data}}{\bar{p}\beta}, \beta = \frac{I_o a_1^2}{2} \left(\frac{1}{(a_1^2 + 4z^2)^{3/2}} - \frac{1}{(a_1^2 + 16z^2)^{3/2}} \right) \quad (4.3.12)$$

Using methods explained in Sec. 4.4 the scaling factor p was determined in [56] for the GEM-3 sensor with $I_o = 10A$ current to be $p = 4.32 \cdot 10^5$. This value was determined from detailed measured data for a sphere.

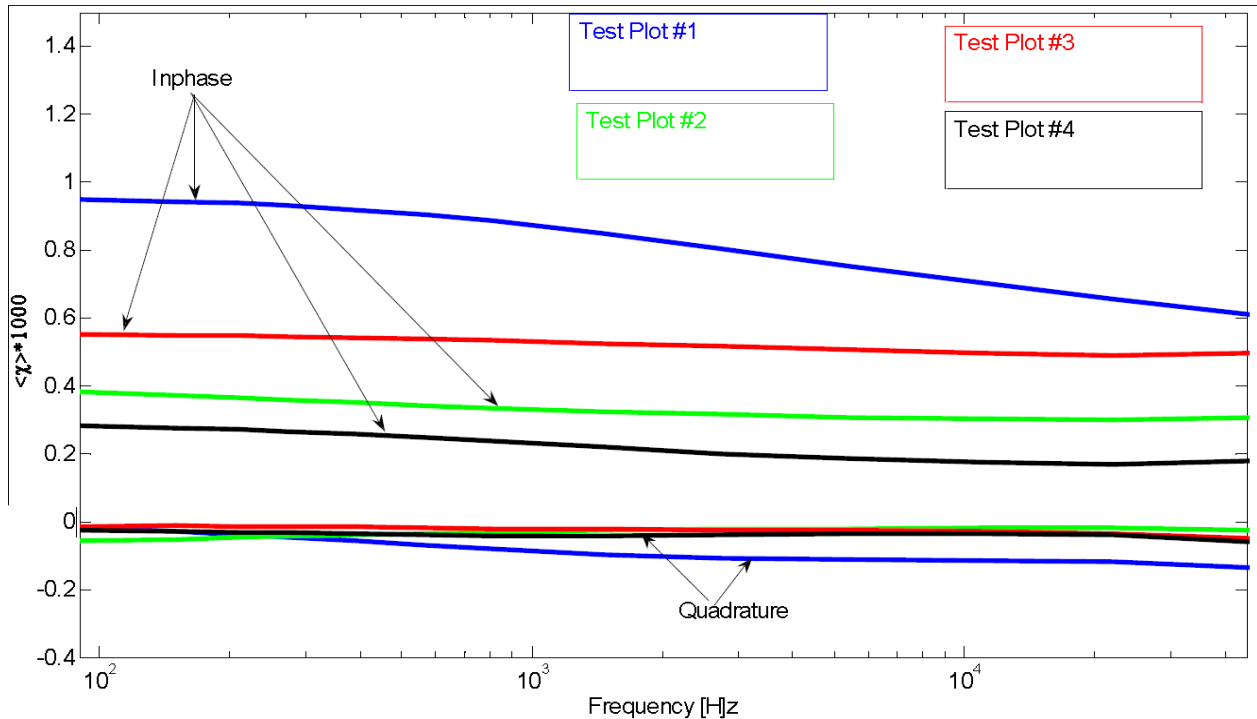


Figure 4.3.3: Mean value of the predicted magnetic susceptibility versus frequency.

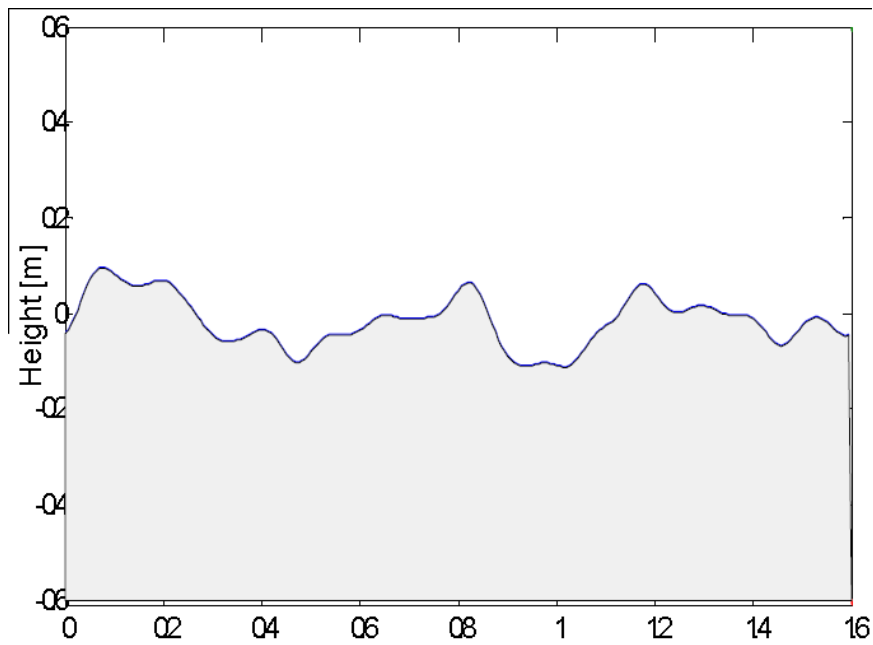


Figure 4.3.4: 1-D Rough surface. In meters.

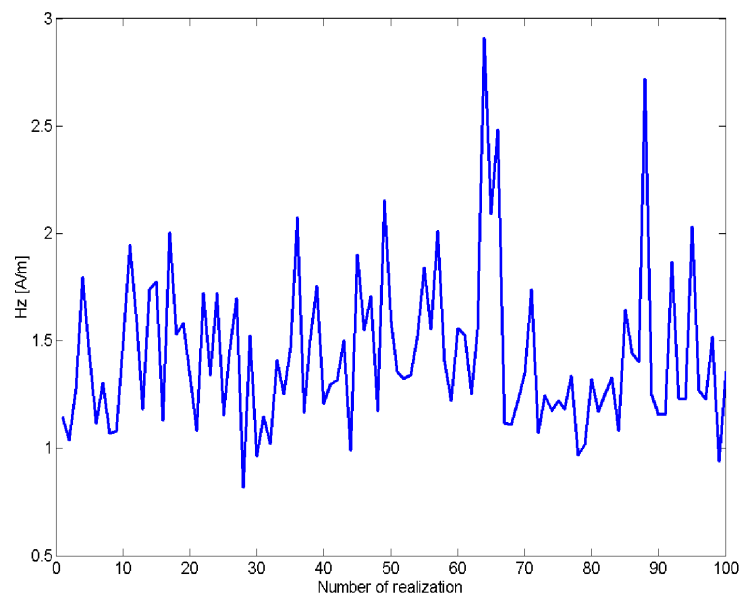


Figure 4.3.5: Scattered magnetic field for 1-D rough surface.

4.3.e Results

Experimental data were collected using GEM-3 sensor at CRREL facilities. To estimate soil's magnetic susceptibility the measurement were taken over a particular spot as a function of sensor elevation. For this the “blue rig” (see Fig. 4.3.2 left) was used. For the test 18 shots were taken as follows: three on the top of the rig, as in the picture above left; 9 descending from the top to within 10 cm of the base; then the rig was removed and 3 shots were taken at successive holes about 10 cm apart on a board placed on the ground where the rig had been (Fig. 4.3.2 right); then the blue rig was put back in position and 3 shots were again taken on the top. The mean value (respect to the evaluation) of predicted soil

susceptibility real and imaginary parts for CRREL soil versus frequency is shown on Fig. 4.3.3. The results show that the soil has a complex magnetic susceptibility. The amplitude of the real part is around 0.38×10^{-3} , and it is decreasing as frequency increases, as expected. The imaginary part also shows very small but frequency dependent trends, indicating that the present soil will affect on the time domain EMI sensors performances as well. We intend to deploy the time domain EM-63 sensor on the same soil in near future, and outcome investigations will be reported in subsequent publications.

Once the soil's magnetic susceptibility was determined then the MAS code was used for GEM-3 sensor for establishing statistical relation between surface roughness and EMI scattered field for magnetic soil. First BOR rough surfaces were generated using 1d code [57] for generating 1d BOR rough surface. A snap shot of the surface in a cylindrical coordinate system is depicted on Fig. 4.3.4. On this figure vertical and horizontal axis coincide with the z and ρ axis in the cylindrical coordinate system, respectively. 1D line on Fig. 4.3.4 was rotated around the vertical axis for generating the BOR surface. The GEM-3 sensor that is the excitation source was placed at 15 cm distance from the origin (0,0 point on Fig. 4.3.4).

For each fixed correlation length and RMS heights 100 realizations were simulated. One of such runs shown on Fig. 4.3.5. The standard deviation and mean are shown on Fig. 4.3.6. These results show that as correlation length and RMS height increases the EMI response from magnetic soil increases as expected. The results also show that for high correlation length (surface is becoming more flat) and for high RMS height (sensor is close to the surface), the standard deviation of the EMI response decreases slightly.

Finally, we studied EMI scattering for 3D rough surfaces. First, we construct 3d rough surfaces. One of rough surfaces is shown on Fig. 4.3.6. The GEM-3 sensor was placed 25 cm above the surface. Using the MAS-Galerkin technique the full EMI scattering problem was solved. For each fixed correlation length and RMC height EMI scattered field was computed for 100 realizations. Figure 4.3.8 shows the scattered magnetic field versus realization number. The standard deviation and mean values are depicted on Fig. 4.3.6 for 3d rough surface, with fixed correlation length. The results show that both standard deviation and mean values increase as RMS height of the 3d rough surfaces increases.

4.3.f Conclusion

In this section, the EMI secondary response from a magnetically susceptible soil with rough surfaces were investigated and analyzed. The combined MAS –Galerkin technique is employed for investigating EMI scattering from 3d-rough surfaces. The relation between surface statistics and EMI scattered field is investigated and presented. In future work the relation between sensors elevation, orientation and surface roughness statistic will be studied and reported in a subsequent

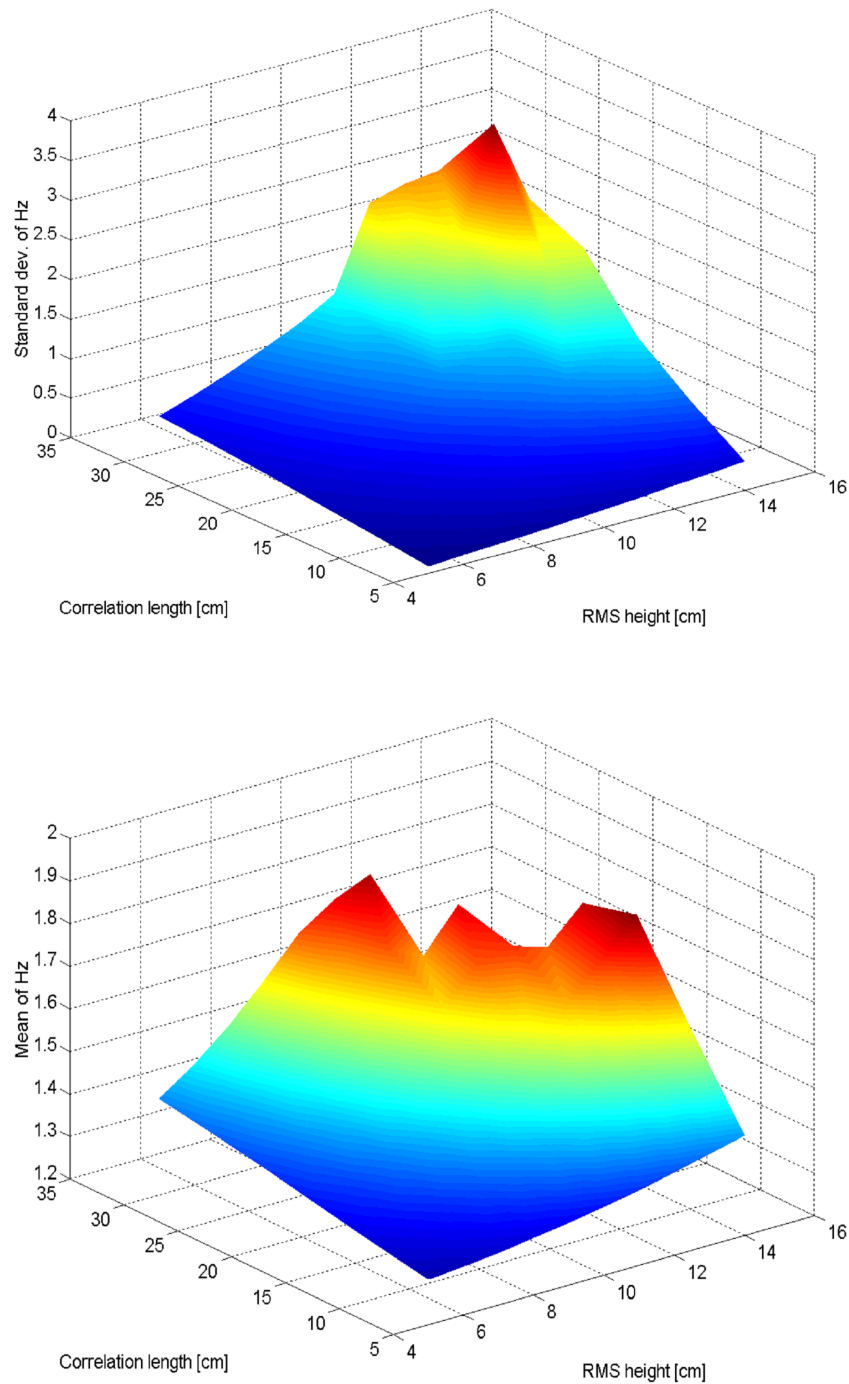


Figure 4.3.6: Standard deviation and mean value for the BOR rough surfaces versus RMS height and correlation length.

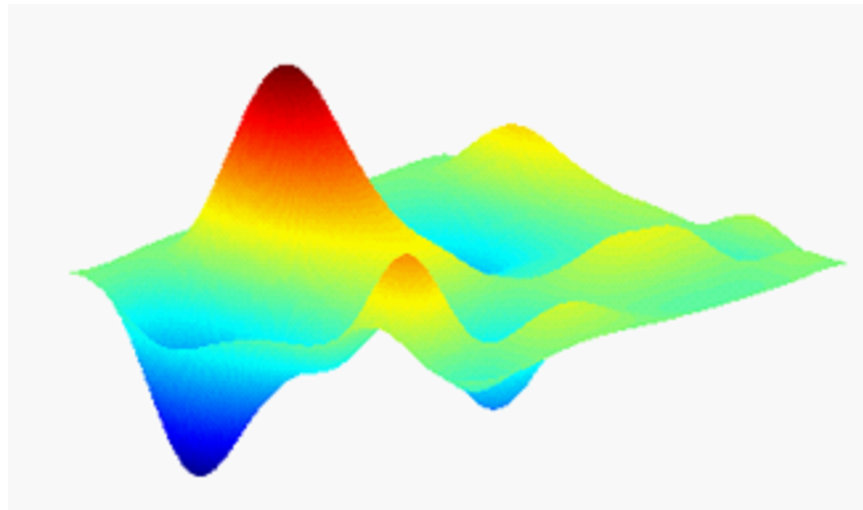


Figure 4.3.7: 3-D random rough surface.

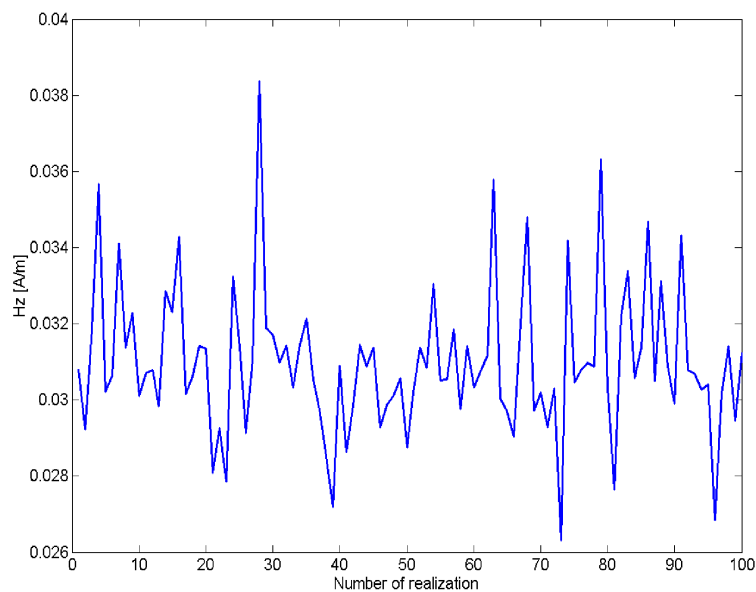


Figure 4.3.8: Scattered EMI field from 3d-rough surface.

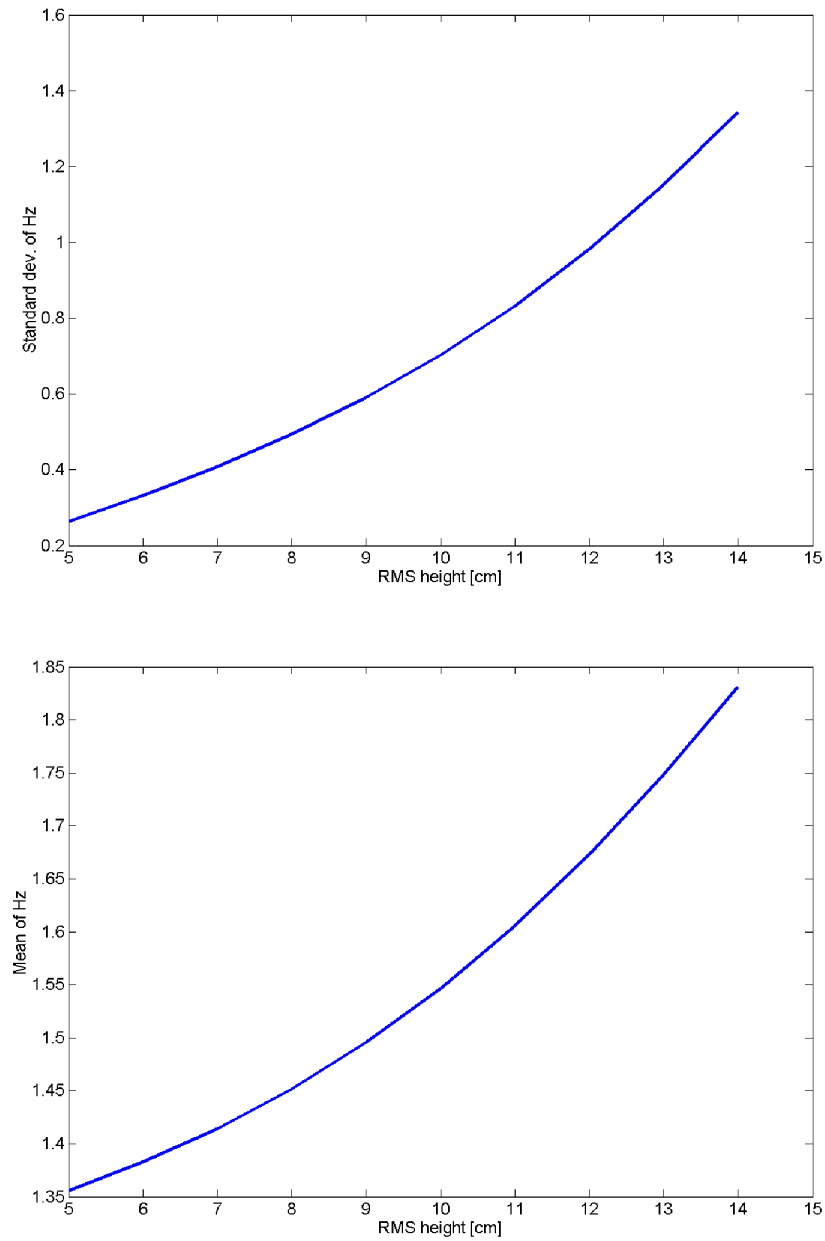


Figure 4.3.9: Standard deviation and mean value for the 3d rough surfaces versus RMS height at fixed surface correlation length.

publication.



4.4 Absolute Calibration of EMI Measurements and Application to Soil Magnetic Susceptibility Inference

This section presents a method for determining a conversion factor for electromagnetic induction (EMI) survey measurements so that fields received in an instrument's native units can be translated into standard ("absolute") EM units. The method is non-invasive, requiring only a rudimentary characterization of the instrument, such as loop geometry and the basic nature of the output such as the magnetic field, differencing of magnetic field, or time derivative of magnetic field. It does not require knowledge of the device's internal electrical engineering features, such as amplification, filtering, or transfer functions between components. The technique proceeds by comparing data from controlled measurements to model results and thus allows one to do similar comparisons henceforth. As an example application and reasonableness check, we use a particular frequency domain (FD) instrument to infer soil magnetic susceptibility value in-situ directly from survey data. The same methodology is applied to a new time domain (TD) instrument. This allows validation of the basic scaling methodology via benchmark cases and also illustrates its transferability. Conversion of data from both instrument types into standard units, for measurements from the same soil, illuminates the contrasting nature of the soil responses to TD and FD sensors. It also points to the fundamentally different magnitudes of different components of soil magnetic susceptibility in the soil studied, relating to instantaneous response and relaxation response.

We acquired data over canonical targets and over some different soil types when we first obtained the GEM-3 \mathcal{D}^+ . Using these data we were able to extract scaling factors for the three receiver coils on the GEM-3 \mathcal{D}^+ . We were also able to estimate the susceptibility of the soils we measured directly from the measured data.

Data Collected

- Data taken over Spheres and other canonical targets
- Data collected over 2 different soil types

4.4.a Introduction and Background

To understand the needed for an ability to convert a sensor's output into standardized units, it is helpful to view the UXO problem from an inversion perspective. Inversion studies use the secondary field to infer the target's properties. Possibly the most basic example is the estimation of soil properties, particularly broadband magnetic susceptibility. EMI responses caused by this property of soil can be a major problem in surveys seeking to discriminate UXO [45, 48, 50, 58, 59]. The ability to estimate susceptibility, in situ, directly from sensor data would provide valuable soil characteristic data in an extremely efficient manner. A commonly used method of inversion is to match the measured secondary response with an analytical model's response of homogenous or layered half-space media. The susceptibility of the soil will correspond to the values of the model's susceptibility parameters that produce the best match. In many prior studies of this nature, the secondary fields are reported in units of parts per million (ppm) of the primary field intensity [60–65].

Examining the past work reveals two key aspects which differentiate our work. First, all instruments in these prior studies use receiver and transmitter coils consisting of laterally separated horizontal current loops. To our knowledge, no similar study has been made with more compact, complex instruments where the transmitting and receiving coils may be coaxial. Secondly, more significantly, the prior studies assumed that the results reported by their instruments were truly

ppm relative to a specific primary field sample. However, modern EMI detectors include filters, amplifiers, etc, attached to particular components, the details of which a general user has no way of knowing. Therefore the user has no real way of knowing the relation between actual transmitted and received fields in A/m or Teslas and the actual units of measurements.

This situation argues for a simple, fast, non-invasive method of both assessing the performance and calibrating the measurements of instruments that do not report data in known, universal units to produce a match with the secondary fields predicted by a model. The latter is required to produce scientific inferences, such as estimates of ground magnetic susceptibility using the method described earlier. Thus, the calibration essentially amounts to translating reported ppm data to be consistent with the inversion researcher's model.

The need for this translation factor within UXO inversion studies can be seen in the research to discriminate UXO from clutter. Machine learning techniques can make use of the modeled responses of a wide range of metallic objects to train a systematic discriminator that separates UXO from clutter objects on the basis of their EMI responses [66, 67]. To classify objects with measured data, previous studies frequently normalize all measured and simulated data [67] to ensure consistency. This normalization entails a loss of valuable information about the magnitude of the response. For example, a very small piece of clutter may likely produce a weaker signal than a large UXO if both are equidistant from the sensor. Normalization would erase such basic distinction. However, if one were able to convert data into units consistent with the standardized units of the modeled data—in other words, to ensure that the modeled responses and measured responses are directly comparable—no information would be lost. Therefore, the recovery of this conversion relationship is a prerequisite for many types of advanced inversion studies.

4.4.b Test Instrumentation

As a handy example of an ultra-wideband frequency domain (FD) EMI instrument, here we use the GEM-3 sensor, manufactured by Geophex [4, 64] and used in inversion research [68, 69]. Our choice of the GEM-3 is largely due to availability and relative ease of use. As mentioned earlier, this section illustrates a general method of calibration that may be applied to many EMI instruments. This analysis of the GEM-3 instrument can be directly applied to any non-adaptive EMI instrument which reports measurements proportional the transmitted primary field or which utilizes a fixed but possibly unknown transmitted field strength. Following a detailed treatment of the method in application to the GEM-3, we then apply it to a new time domain (TD) instrument, the Man-portable Vector Time Domain Electromagnetic Sensor (MPV). This device has just recently been developed in an ongoing research project [70].

To determine, through non-invasive means, a conversion factor that can translate our particular GEM-3 instrument's record of the secondary field into standard units, we compare the actual received fields from a canonical object to the fields determined by a model. Thereby, this analysis permits one to acquire the ability to evaluate the sensor's data in standardized quantities in all other future applications. Furthermore, we examine the significance of the discrete size of the GEM-3 receiver loop in the isolation of the conversion factor. Ultimately, with proper calibration, data in the GEM-3's native units from magnetically responsive soil is used directly to estimate broadband magnetic susceptibility of the soil.

As an additional, comparative test we utilized a new time domain (TD) instrument designed and manufactured under the direction of one of the authors [70]. This time domain instrument consists of two coaxial coils of 37.5cm radius that generate a step down function. From 46 microseconds

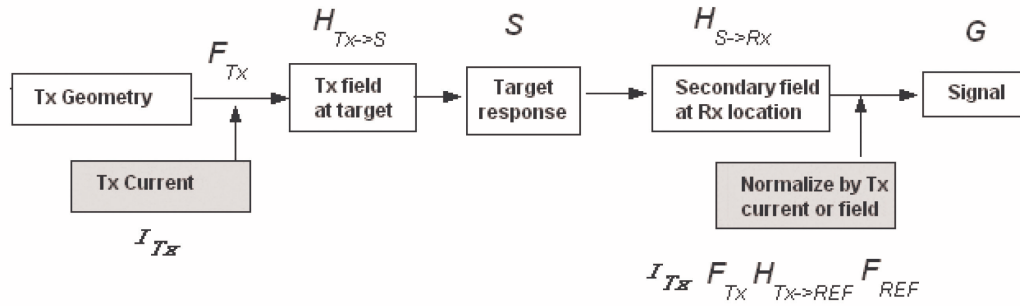


Figure 4.4.1: Flow chart of instrument's process, to be paralleled by the modeling sequence. If normalization is performed by the instrument then the lower, shaded set of boxes may be deleted in the model and an arbitrary (e.g., unit) current assumed.

to about 20 milliseconds after shut off, the step down response is then measured at a receiver loop located at the center of the transmitter coils.

4.4.c Recovery of the Conversion Factor

A given transmitter (Tx) current in any instrument will produce a particular magnetic field at a target's location (e.g. in A/m), which in turn will produce a particular secondary field value at the instrument's receiver (Rx). In the case of the GEM-3, the Rx signal is normalized, frequency by frequency, by a sample of the primary field in a secondary Rx coil. Thus, in effect, the instrument provides a signal at each frequency that is proportional to received field per unit Tx current, so we need not know the specific Tx current to model what occurs. We do require, however, knowledge of the geometry of the transmitter and receiver loops.

Through our analysis, we can confirm if the proportionality between the actual received field and the sensor measurement signal is truly fixed. While the signal may be selectively amplified or filtered, this manipulation is always done in the same way, without adaptive measures which would alter that relation. Therefore, the recovered conversion factor should have no dependence on measurement position or object type.

We can readily calculate the response of standard objects to fields produced by arbitrary assumed fixed Tx currents in the known Rx geometry, and thus determine the proportionality between measured and actual fields. The standard objects consist here of three spheres made of aluminum, brass, and steel. The underlying physical process by which the instrument produces signals is presented symbolically in the flow chart of Fig. 4.4.1 and equations that follow.

Production of the instrument's signal, in the case of the GEM-3, is

$$G(ppm) = \frac{I_{Tx} \cdot F_{Tx} \cdot H_{Tx \rightarrow S} \cdot S \cdot H_{S \rightarrow Rx} \cdot F_{Rx}}{I_{Tx} \cdot F_{Tx} \cdot H_{Tx \rightarrow REF} \cdot F_{REF}} \quad (4.4.1)$$

where I_{Tx} is the current in the transmitter loops. F_{Tx} is what the instrument does with this current in producing the Tx field. In the case of the GEM-3 this contains little besides the geometry of the coils, as we may simply assume that the current is continuously on during the measurement

portion of the cycle. $H_{Tx \rightarrow S}$ is a transfer function yielding the field produced by the transmitter at the target location. S is the inherent target response to a unit input, while $H_{S \rightarrow Rx}$ is the function that converts that response to the field at the Rx location. F_{Rx} is the process that is performed on that field by the receiver, including any associated amplification, filtering, etc. The quantities in the denominator are explicable in similar terms, except that REF refers to the reference coil, in a fixed position relative to the Tx coils, where the Tx field is sampled. We do not need to know any of its particulars.

The process producing the actual (modeled) field M at the Rx location can be represented as

$$M(A/m) = I_m \cdot F_{Tx} \cdot H_{Tx \rightarrow S} \cdot S \cdot H_{S \rightarrow Rx} \cdot F_{Rx}^m \quad (4.4.2)$$

where I_m is the current assumed in the transmitter. F_{Rx}^m may include integration of the secondary field over the area of the Rx coil but, unlike F_{Rx} for the actual instrument, need not contain any other functions performed by the sensor's electronics or processors. Note that both G and M contain the same product $F_{Tx} \cdot H_{Tx \rightarrow S} \cdot S \cdot H_{S \rightarrow Rx}$, which we consider known (calculable). The ratio of recorded data to actual (calculated) field values is thus

$$\frac{G}{M} = \left(\frac{F_{Rx}}{F_{Tx} \cdot H_{Tx \rightarrow REF} \cdot F_{REF}} \right) \frac{1}{I_m \cdot F_{Rx}^m} \quad (4.4.3)$$

The product $I_m \cdot F_{Rx}^m$ is known; we may also normalize by taking I_m to be unity and adjusting M accordingly. The quantity in parenthesis is a function of the internals of the instrument and is what we infer as a lumped factor from measurements of the ratio on the left. When this is done, the conversion factor has been obtained.

This method to recover the conversion factor can also be used for any comparable instrument by accounting for its particular loop geometry. Note that, to be fully comparable, an instrument must have the signal normalized by Tx field or Tx current or use a known, fixed Tx field or current. Also, the GEM-3 data is processed within the instrument so that it is proportional to the Rx field value, not to the time derivative thereof. Simple alterations of the method can be brought to bear to account for differences in any of these particulars. For example, in our TD MPV instrument, the current is shut off prior to measurement; the data is not inherently normalized by the Tx current or field; and the output is proportional to the time derivative of B and not to B. This simply means that we must heed these facts when comparing the calculated and measured responses from our standard objects, making sure that the processes parallel one another by adjusting, respectively, the content of F_{Tx} , the denominator in equation (4.4.3), and the contents of F_{Rx} and F_{Rx}^m .

4.4.c.(1) Modeling of Metallic Spheres For the frequency domain, we model metallic spheres as a special case of spheroids in the magnetoquasistatic regime. This analytical solution is well validated and produces EMI secondary field predictions for spheroidal objects with any conductivity and permeability values and in response to arbitrary excitation [71–73]. The solution provides secondary field predictions in terms of A/m. The values can be obtained at any observations point, e.g. at the nominal location of an Rx coil or over arrays of quadrature points within its area. The three specific spheres that were modeled were all 3 inches in diameter. In addition, we implemented the time domain step down response of a metallic sphere to a uniform field as given by Wait and Spies, 1969[38]. Given the relatively small size of the sphere and the distance between the sphere and MPV transmitter loops in all measurements, the incident field is approximately uniform. Therefore, Wait and Spies's solution is a valid model.

4.4.c.(2) Modeling of the Primary field The excitation field is generated by an analytical model that represents the GEM-3 instrument as a set of idealized wire loops. The transmitting sensor head consists of two concentric current loops in series with radii of 20 cm and 11.074 cm. The smaller loop is placed inside the larger loop and serves as a bucking coil, approximately nulling the primary field at the center of the sensor head, where the receiver coil resides. There are 8 windings in the outer and 4 windings in the inner transmitter coil. We assume in the calculations that the wires in the transmitter coils carry 10 Amps, which is the case at most frequencies. However, as mentioned earlier, this varies somewhat by frequency but because of the normalization by Tx field, the results are not affected.

We use the complete elliptical integral functions of the first and second kind to characterize the magnetic vector potential and vector field from a circular current loop in a cylindrical coordinate system. This calculation method is well established [19, 74, 75]. For a current loop of radius a and normal to the z axis in the $z = z_o$ plane and with I_o current flowing in the ϕ direction, the transverse and axial fields are,

$$B_r(r, \phi, z) = \frac{\mu_0 I_o}{2\pi} \frac{(z - z_o)}{r[(r+a)^2 + (z - z_o)^2]^{1/2}} \cdot \left[-K(k_c) + \frac{r^2 + a^2 + (z - z_o)^2}{(r-a)^2 + (z - z_o)^2} E(k_c) \right] \quad (4.4.4)$$

$$B_z(r, \phi, z) = \frac{\mu_0 I_o}{2\pi[(r+a)^2 + (z - z_o)^2]^{1/2}} \cdot \left[K(k_c) - \frac{r^2 - a^2 + (z - z_o)^2}{(r-a)^2 + (z - z_o)^2} E(k_c) \right] \quad (4.4.5)$$

where .

$$k_c = \sqrt{\frac{4ar}{(r+a)^2 + (z - z_o)^2}} \quad (4.4.6)$$

and μ_0 is the permeability of the surrounding medium. The standard cylindrical coordinates of radius, rotational angle around the z axis, and elevation are expressed by (r, ϕ, z) . K and E are the complete elliptical integral functions of the first and second kind, respectively. These equations will produce the magnetic field from a current loop at any observation position. The total primary field is created from the superposition of two current loops that correspond to the two actual transmitting loops in the sensor head. Our implementation of the model agrees with the alternative method of using numerical integration and application of Biot-Savart's Law but has the added benefit of being more computationally efficient.

For the time domain MPV instrument, the analytical TD solution for a sphere's response to a uniform step down function only requires calculation of the equivalent of a static uniform field generated by a current loop and observed at the location of the sphere. This can be done through the current loop equations provided above where the radius of the transmitter loop now 37.5cm and the number of windings is 100 to correspond to the MPV.

4.4.c.(3) Modeling of the Receiver Loop Given the finite size of the receiver loop, a circular loop with a radius of 6cm for the GEM-3, the secondary field will not necessarily be uniform across the area of this loop. This is especially true if the object is close to the instrument. Therefore all modeled secondary fields are numerically integrated over the loop area to parallel the actual secondary field measurement. This integration is calculated by partitioning the loop area into concentric rings. Then each ring is again segmented along its length such that the entire area is partitioned into curved trapezoids. In our experience, over 300 divisions are needed for consistent results.

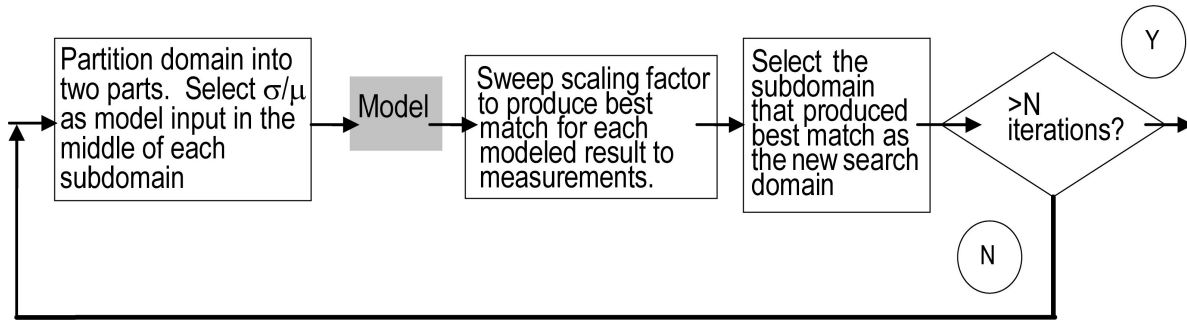


Figure 4.4.2: Block diagram illustrating the search algorithm.

4.4.c.(4) Measurements Measurements were taken above each metal sphere by placing the GEM-3 instrument at points in a vertical grid. This was accomplished by measuring along horizontal lines above one another at different elevations. The horizontal point spacing was in 2 cm increments from -30 cm to +30 cm from the position above the sphere. Vertical spacing of the lines was in 5cm increments from 13 cm to 28 cm above the surface of the sphere. The frequency range was from 30 Hz to 47 kHz. This wide range of measurement points both in space and frequency was taken to ensure that the recovered scaling factor is consistent: there must not be any variation due to object distance, frequency, or choice of target object. In other words, all the data must point to a scaling factor of the same value.

4.4.c.(5) Matching Algorithm We performed a Fibonacci search [76] within the range of possible values for the scaling factor and the sphere’s material properties to find the best match between the model’s prediction and the data. A Fibonacci search first partitions the search range into two halves. The median value within each half is given to the model as input to produce two different outputs. Whichever half produces the more accurate output will become the new search space and the process repeats. The overview of this algorithm is illustrated in Fig. 4.4.2. Accuracy is gauged by utilizing the normalized mean square error as an objective function. This type of simple search is relatively fast but usually prone to converging on a solution that is not the best overall match. In our investigation that difficulty was not encountered. The matching algorithm is independently repeated for the frequency response at each measurement point for each sphere. This independence allows us to examine the results for consistency over space and frequency.

The main difficulty in the search algorithm was that the metallic spheres’ exact permeability (μ) and conductivity (σ) values were not precisely known. These spheres were purchased off the shelf from a third party and not manufactured to any specifications other than that they were of the correct size and type of metal. Therefore, to match the model’s EMI prediction with measurements, both the scaling factor and μ and σ must be simultaneously recovered. As a simplification, the aluminum and brass spheres can be assumed to be non-permeable, and thus only their σ values and the scaling factor need to be recovered. Approximate values of sigma for these materials are available from standard textbooks, furnishing a reasonableness check. For the highly permeable steel sphere, only the ratio between σ and μ affects the secondary response [77]. Therefore, relative μ is assumed to be 100 and the normalized σ value is recovered along with the scaling factor. Adopting a higher relative μ value produces no change in the resulting conversion factor.

Fig. 4.4.3 shows the match between the modeled response and the measurement of the steel

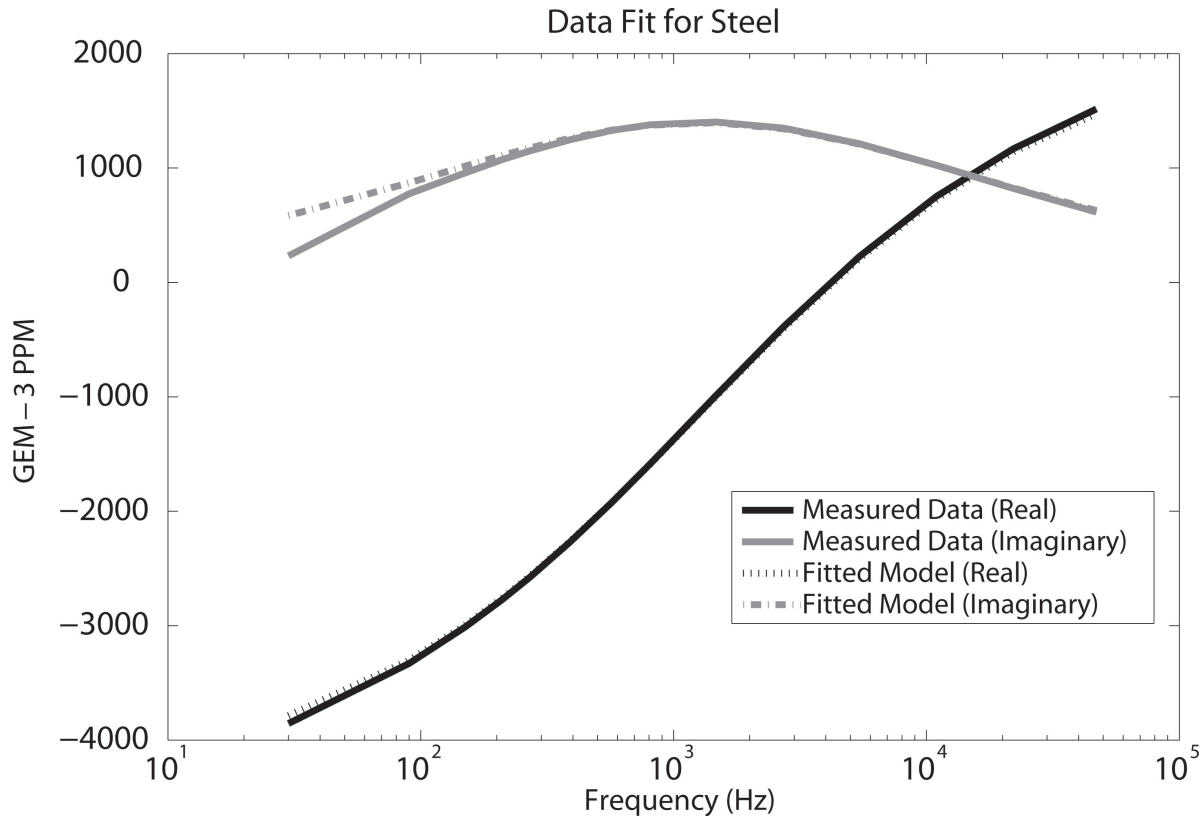


Figure 4.4.3: Figure showing the matching between model and measurement of a steel sphere at a single grid point.

sphere. The match does extremely well save for the lowest and highest frequency points. We have observed previously that the GEM-3 can have difficulties capturing consistent responses at very low and very high EMI frequencies. Therefore, the lowest and highest frequency data are ignored during the matching process. Furthermore, we proceeded to recover the scaling factor of the MPV instrument in the same fashion and with similarly good results. The matching results for only the GEM-3 will be presented to avoid redundancy.

4.4.d Results

After performing the Fibonacci search for the material parameters of the spheres and finding the best scaling factor for each GEM-3 measurement point, we then averaged the scaling factors for all objects recovered at the closest 9 measurement points. We arrived at an overall value of 4.93×10^3 . Division by this scalar will convert all GEM-3 measurements into the average magnetic field that would pass through the receiver coil within our model, given our specific transmitter loop.

All the data can be converted into a percent error from the averaged conversion factor of 4.93×10^3 . This variation of the scaling factor can likewise be plotted over space. Shown in Fig. 4.4.4 is the variation of the scaling over space for the steel sphere. As the figure demonstrates, the variation is minimal with most of the error under 5% error. We see similarly good results for the brass and aluminum spheres shown in Figs. 4.4.5 and 4.4.6, respectively. Since the model of the GEM-3

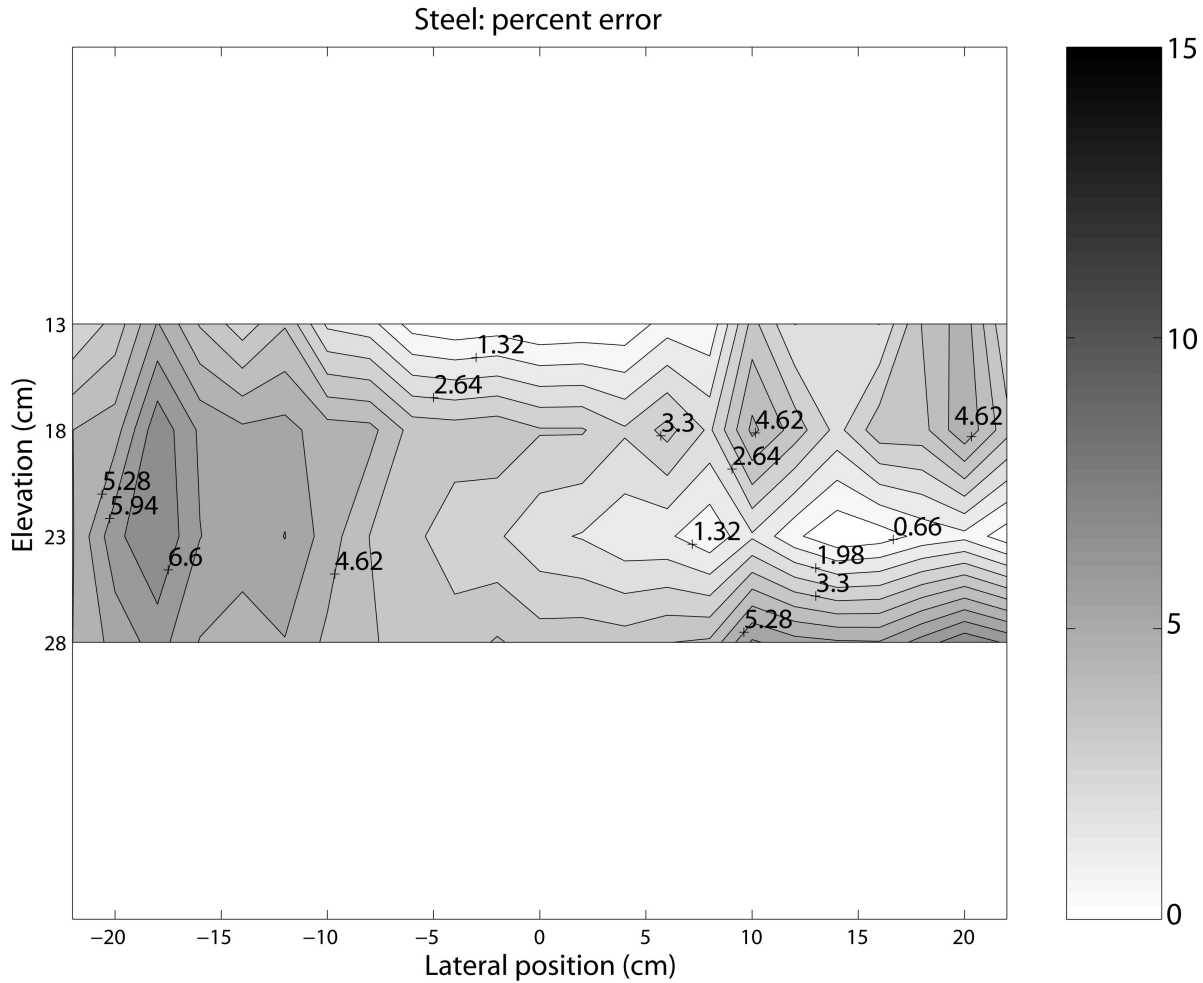


Figure 4.4.4: Plot of the variation of the retrieved conversion factor, as a percent error from 4.933×10^3 , for the steel sphere as a function of position.

used a fixed current in the transmitter coils, these results verify that the ppm reported by GEM-3 is consistently normalized by some sample of the primary transmitted field. In addition to providing a conversion factor, the method also potentially provides a quick way for inversion researchers to ascertain if their instruments are functioning correctly with respect to any normalization produced internally in the instrument.

If we can assume the secondary field is relatively constant over the receiver loop, then it would be unnecessary to numerically integrate the fields within the loop area. However, comparison of the consistency of results with and without such integration shows that significant errors are introduced by failure to integrate over the receivers.

4.4.e Application of the Conversion Factor

As an example application and reasonableness check, we apply the conversion factor to the problem of obtaining an estimate of in situ soil magnetic susceptibility. The solid curves in Fig. 4.4.8 show the Inphase and Quadrature response of a particular sample of soil queried with the GEM-3

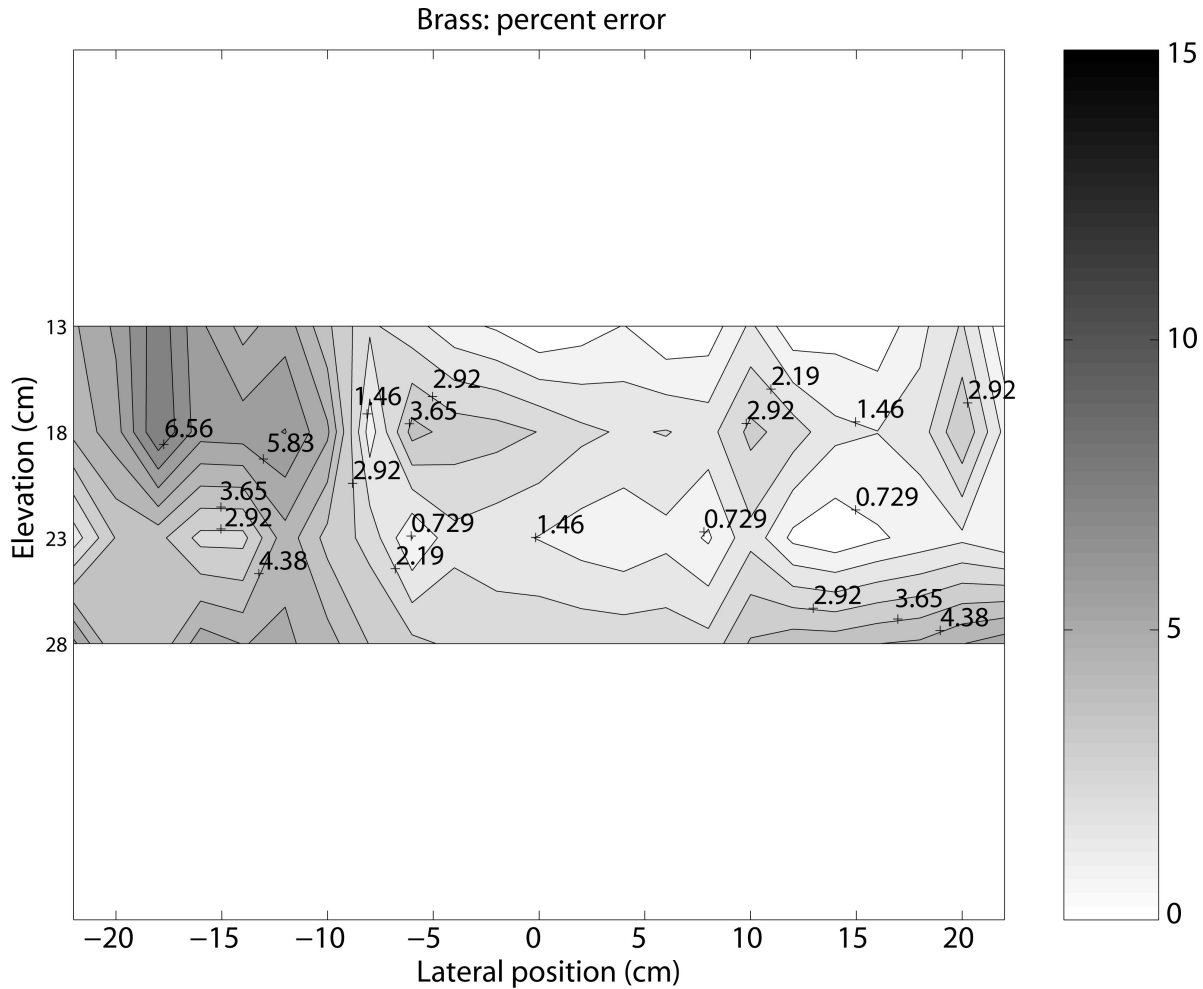


Figure 4.4.5: Plot of the variation of the retrieved conversion factor, as a percent error from 4.933×10^3 , for the brass sphere as a function of position.

at 12.5 cm above the surface. The Inphase curve shows virtually no change over frequency, and the Quadrature component is negligible. Therefore, we implemented a model of the homogeneous, permeable, non-conducting half-space response to the GEM-3 excitation by the image method, as per Wait, 1985[78]. The output of this model was converted from model units to GEM-3 ppm units through multiplication of the recovered conversion factor. Then a d.c. soil susceptibility value, $\kappa = 70 \times 10^{-5}$ SI, was found to provide the best match to data as shown in Fig. 4.4.8. This susceptibility value is solidly within the range of reasonable soil values as reported by others [33–35].

The example above provides primarily an order of magnitude check, which is often all we may require in terms of knowledge of soil susceptibility. It also provides an illustration of FD soil response, which we can now compare to TD response. By recovering the conversion factor for multiple instruments, one can also make meaningful comparison between data from those instruments, e.g. for soil response, illuminating the different aspects of the susceptibility that dominate the responses of the respective sensor types. To this end, the conversion factor of 6810 for the TD MPV instrument was obtained in exactly the same manner as for the GEM-3. Results of this

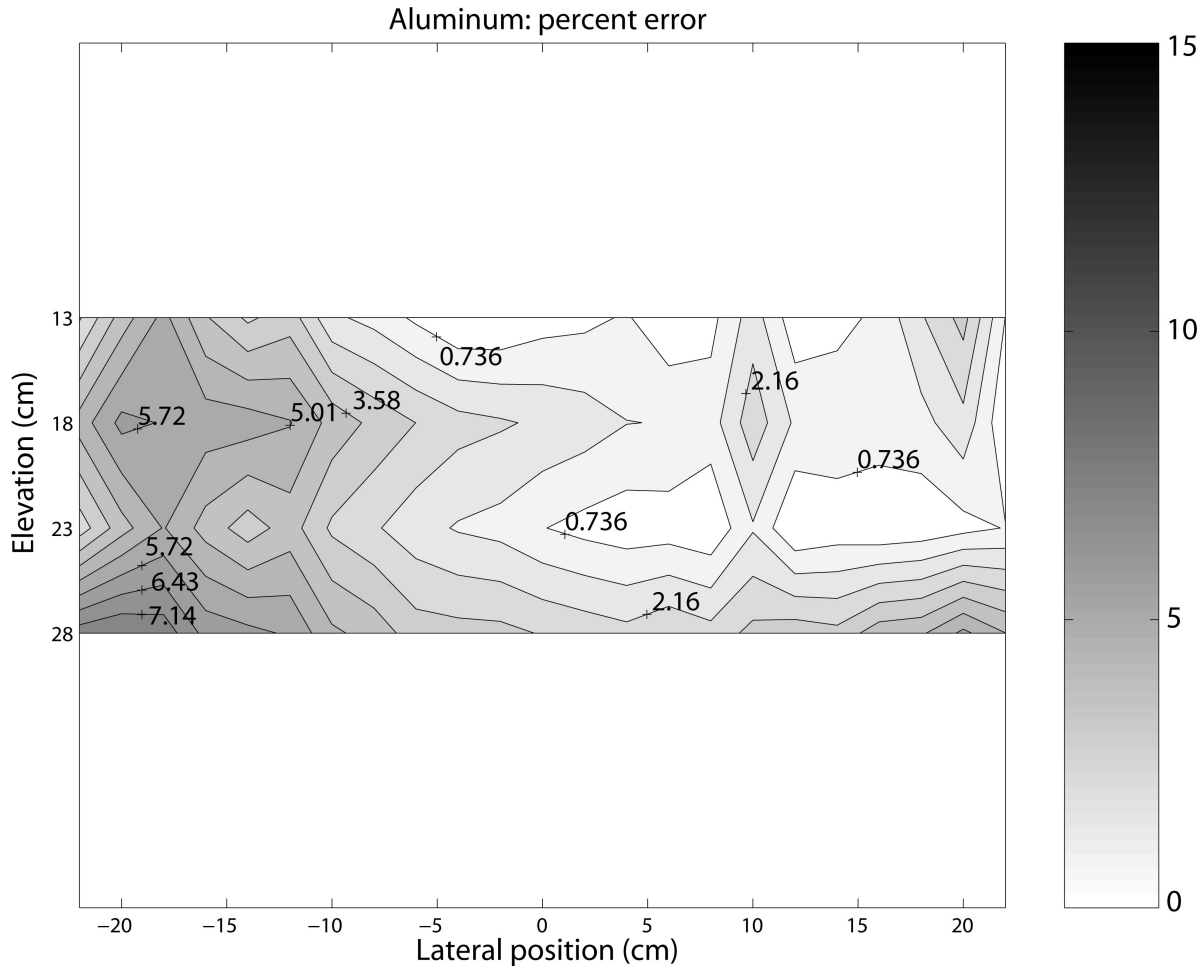


Figure 4.4.6: Plot of the variation of the retrieved conversion factor, as a percent error from 4.933×10^3 , for the aluminum sphere as a function of position.

comparison are shown in Sec. 4.2.

4.4.f Conclusion and Discussion

The formulation presented here shows how, by recourse to simple modeling, one may obtain factors to convert EMI instrument output to received field values in standard EM units. As all instruments, even of the same type, generally have at least slightly different calibration, the method is best applied to each individual sensor to be used. In any case, the formulation makes clear the adjustments needed to treat different instrument types. Tests reported here reveal that the finite size of receiver loops may have to be taken into account to obtain a precise scaling factor, even when those loops are small.

An appeal of the method is that it does not require any detailed knowledge of the internal electronics and processing of the instrument under consideration. As long as basic geometry of the transmitter coils is known together with a few other rudimentary instrument characteristics, one can obtain actual received field values from data by one-time non-invasive calculation.

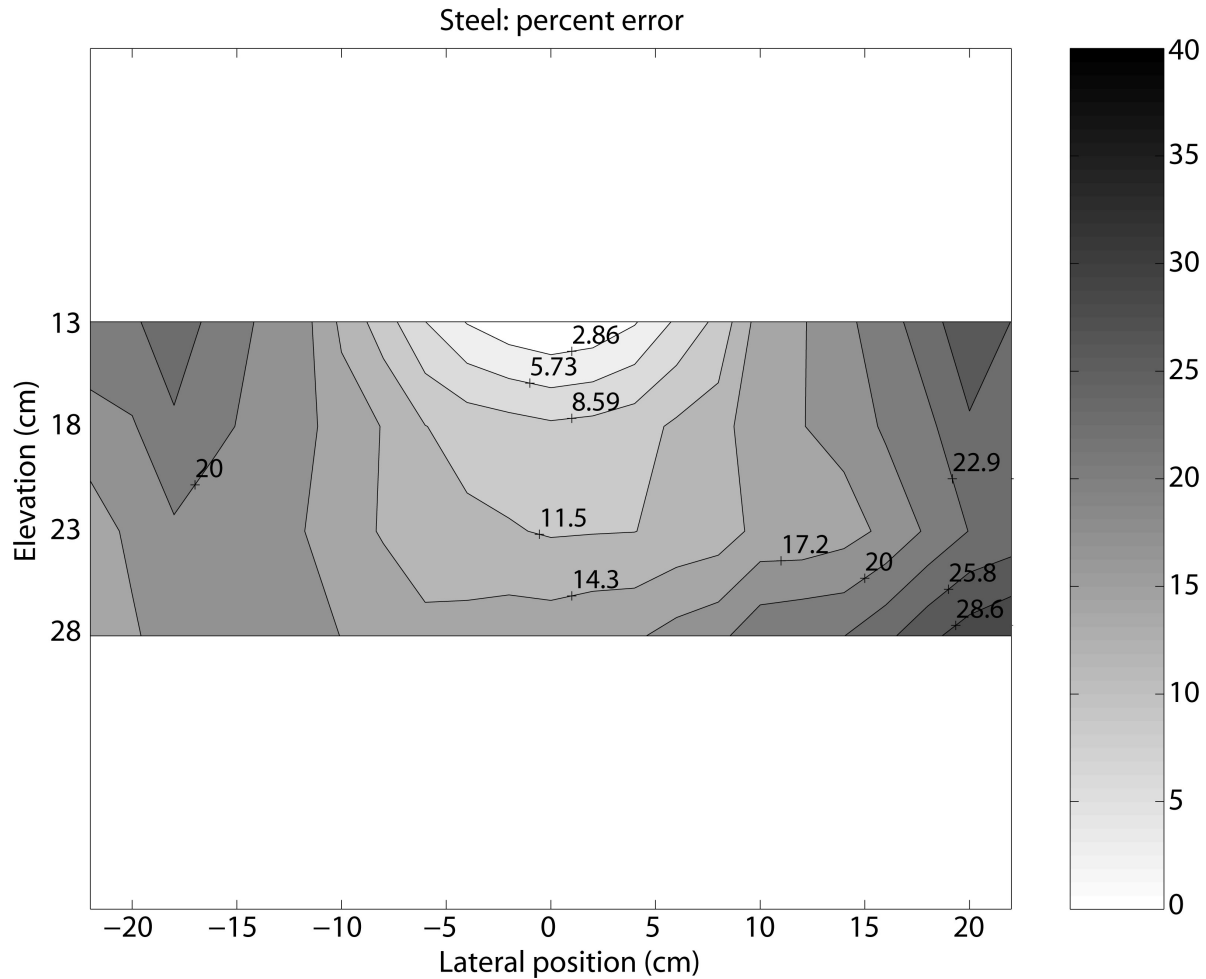


Figure 4.4.7: Plot of the variation of the retrieved conversion factor, as a percent error from 4.243×10^3 , for the aluminum sphere as a function of position. No integration was performed over the receiver loop.

As an example application and reasonableness test, we used our retrieved scaling factor to match the modeled response of permeable, susceptible soil to measurements of soil and have found reasonable soil susceptibility values. This not only supports the validity of our scaling factor but also points to the possibility of characterizing soil from sensor measurements alone, avoiding the need to conduct laboratory analysis on core samples outside of in situ conditions. By this means, one sensor's data can yield geophysical information directly that is applicable to other instruments.

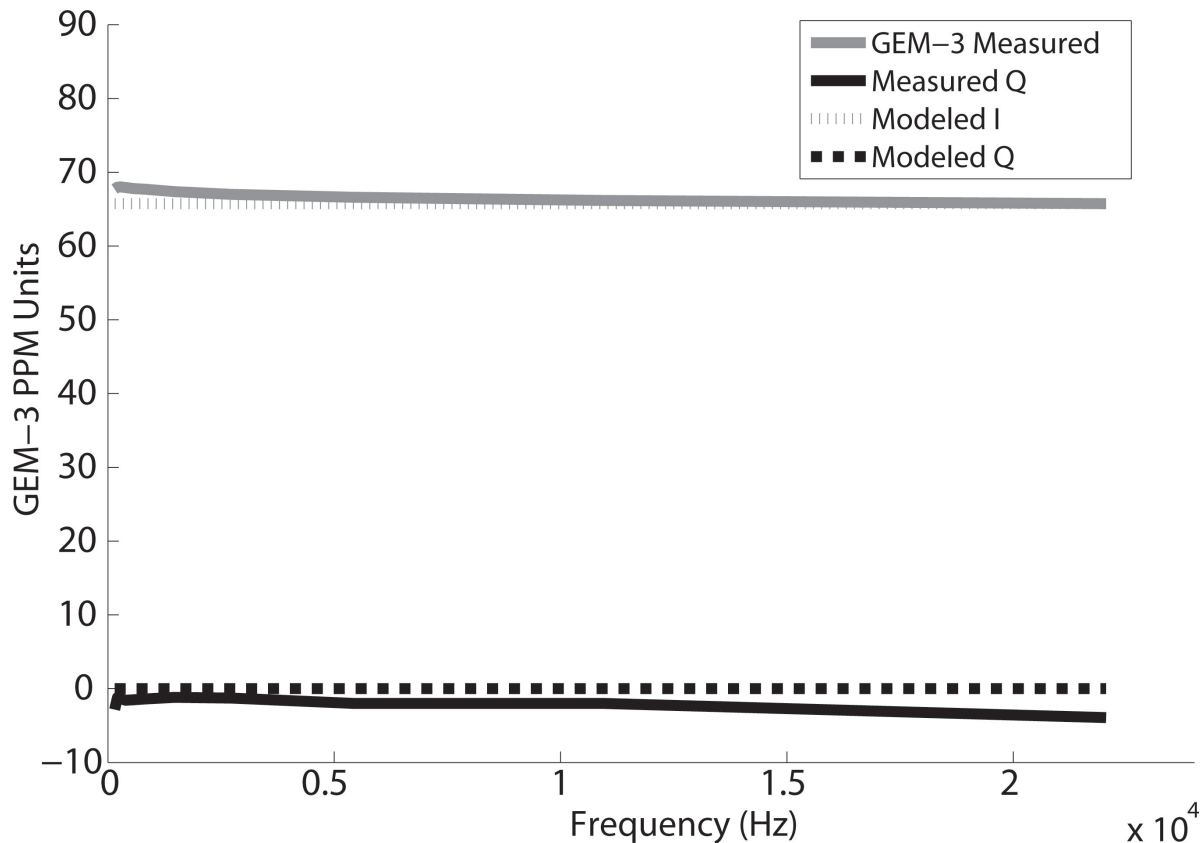


Figure 4.4.8: Comparison between GEM-3 measured inphase (I) and quadrature (Q) ground response and prediction using half-space soil model with an applied scaling factor.

4.5 Generalized Standardized Excitations Approach

The generalized standardized excitation approach (GSEA) is presented to enhance UXO discrimination under realistic field conditions. The GSEA is a fast, numerical, forward model for representing an object's EMI responses over the entire frequency band from near DC to 100s of kHz, including all physical relevant physical considerations, such as near and far field phenomena, arbitrary material and geometrical heterogeneity, and internal target interactions. It has been developed and tested in both the frequency and time domains for actual UXOs placed in free space. The GSEA, which uses magnetic dipoles instead of magnetic charges as responding sources, is capable of taking into account the background medium surrounding an object. Given a modeled UWB frequency domain (FD) response, the corresponding time domain (TD) response is easily obtained by the inverse Fourier transform. Thus the technique is applicable for any FD or TD sensor configuration and can treat complex data sets: novel waveforms, multi-axis, vector, or tensor magnetic or electromagnetic induction data, or any combination of magnetic and EMI data. Host media effects are taken into account via appropriate types of Green's function and equivalent dipole sources. Comparisons between simulations and experimental data illustrate that the GSEA is a unified approach for reproducing both TD and FD EMI signals for actual UXOs. The EMI response from a soil that has a frequency-dependent magnetic susceptibility is studied. The EMI responses in both FD and TD domains are analyzed for the model of an actual UXO that is buried

in a magnetically susceptible half space.

4.5.a Introduction

Cleanup of unexploded ordnance (UXO) is greatly complicated by the difficulties in distinguishing UXO from non-UXO metallic debris, found at most UXO sites. The problem becomes much more complicated when signals are contaminated by noise that originates from magnetically susceptible and electrically conductive soils [42–48, 50, 51, 79–81]. Until now, in most existing approaches to UXO classification, the object of interest is assumed to be placed in a free space [55, 68, 82–90]. Any influence of the host medium is considered to be removed by filtering before data are submitted to an inversion algorithm. Recent studies show that “geologically hostile” sites cause significant problems for magnetometers and electromagnetic induction (EMI) sensors, in terms of both decreased probability of detection and increased probability of false alarm. In regions of highly magnetic soil, magnetometry and electromagnetic sensors often detect large anomalies that are of geologic, rather than of metallic, origin. For instance, [79] documented the problems encountered at the former Naval Training Range on Kaho’olawe Island when using EMI sensors. During production surveys at the site, approximately 30% of identified anomalies were from false positives due to geology, attributed to the strong magnetic viscosity exhibited by the basaltic soils.

There is also a need for detection and discrimination of UXO in undersea environments [91]. In this case, unlike land surveys where the conductivity ($< 10^{-2}$ [S/m]) of non-permeable soils can be neglected, it is impossible to neglect EMI responses due to the conductivity of seawater and the ocean bottom in marine surveys. All of this leads to a high level of false alarms, which translates into an increased workload because each detected anomaly must be treated as if it were an actual UXO. Therefore, innovative discrimination techniques that apply to any field condition and that reliably, quickly, and accurately distinguish between hazardous UXO and non-hazardous metallic items are required. To address this issue here we present a generalized standardized excitation approach (GSEA) that is suitable for complex data sets: novel waveforms, multi-axis, vector, tensor magnetic or electromagnetic induction data, or any combination of magnetic and EMI data.

The SEA for objects placed in free space is described in detail in [55, 88, 90]. This work extends the SEA for more general cases by using magnetic dipoles as responding sources instead of magnetic charges as in [55, 88, 90]. By using magnetic dipoles with the corresponding dyadic Green’s function the GSEA becomes applicable for objects placed in a conducting as well as a permeable host medium.

The GSEA can be briefly outlined as follows. For any given object the amplitudes of the responding magnetic dipoles are determined and sorted in the universal library for any number of basic spheroidal modes. Then, any primary field is decomposed into a set of basis excitations, which are then multiplied by appropriate weights (e.g., spheroidal modal decomposition coefficients from which we can calculate the target’s complete response just by superposing responses of each basic excitation). The key element in the GSEA is to determine the amplitudes of the responding sources, which are characteristic only of the object, and are independent of sensor type, object location and orientation, and transmitted waveforms.

There are two ways to determine the amplitudes on the responding magnetic dipoles: (1) using measurement data and (2) solving the full 3-D EMI problem in detail. The most straightforward way to determine the amplitudes of the responding magnetic dipole sources is to solve a standard inverse problem based on the measured data. Obviously, this process requires very good experimental conditions and a sufficient number of independent measurements of an object of interest in

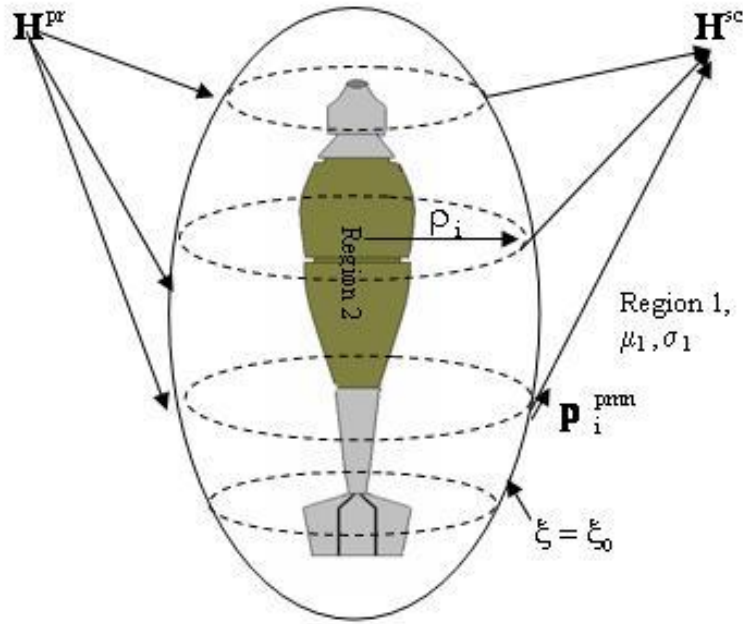


Figure 4.5.1: Problem geometry and reduced set of sources \bar{p}_i^{pmm} distributed along rings on the spheroid surface.

order to reduce the degree of ill-posedness. The ill-posedness makes the solution inaccurate. Recently, [88] applied such a data-derived approach to extracting the modal response coefficients for each candidate by carefully designing the measurements at different distances and orientations in free space. However, the accuracy and reliability of the model parameters determined in this way may not always be satisfactory due to unavoidable measurement noise and numerical difficulties arising from the inherent ill-conditioning of the problem, although a special treatment was applied in [88]. In addition, the model parameters were obtained from measurement data with the given sensor. Currently all available EMI sensors have certain limitations in both frequency band and time. Therefore, the amplitudes of the responding source that are derived from these measured data have limitations, they can't cover all possible EMI and magnetic data, and they could not be used to obtain EMI response in time domain for different wave forms and sensors.

Originally, in [55] and [90], to determine the amplitudes of responding sources, a numerical procedure based on the method auxiliary source (MAS) and hybrid MAS thin skin approximation (MAS/TSA) was proposed and it is generalized here. In this procedure, by utilizing a full 3-D EMI solver, the modal responding coefficients, or strengths of a reduced source set (RSS) [55, 90] are determined by employing a physically complete numerical simulation of the object's response to each fundamental excitation mode. The full MAS model-based approach has an advantage over the data-derived-based approach, because it is a well-posed EMI problem and it is not dependent on measurements. In this approach the RSS can be obtained very accurately for any excitation mode and in an ultra-wide band frequency range. Thus, the technique allows users to calculate the EM field in both the frequency and time domain and to control the number of input spheroidal modes. Here the TD EMI response for a given UXO is calculated directly from FD RSS sources just by using the convolution theorem [92–94].

The section is organized as follows: In Sec. 4.5.b, the generalized standardized excitation approach is presented, Sec. 4.5.c describes the frequency-dependent magnetic susceptibility model, and Sec. 4.5.d shows several experimental and numerical results, demonstrating the applicability of the GSEA in both frequency and time domain, and for frequency-dependent magnetic soil.

4.5.b Generalized Standardized Excitation Approach (GSEA)

Recently, the SEA has been developed and applied to UXO discrimination [55, 88, 90]. All those studies assume that an object is placed in free space. Here, the SEA is generalized to take into account conducting and magnetically susceptible host media effects. To illustrate the GSEA, let us assume that an object is placed in a background with magnetic permeability μ_1 and conductivity σ_1 , Fig. 4.5.1. The object is illuminated by an arbitrarily oriented, time-varying primary magnetic field. We surround the object with a fictitious spheroid, which is introduced only as a computational aide in the decomposition of the primary magnetic field into fundamental spheroidal modes. We choose spheroids because they can assume the general proportions of elongated objects of interest, such as UXO, which are also typically bodies of revolution (BOR). Oblate spheroids can also be used for flattened shapes. In general, the fictitious surface could be a smooth closed surface, as applicable for a related standardized source set approximation described in [55, 90]. On the fictitious spheroid given by $\xi = \xi_o$ (Fig. 4.5.1), the primary magnetic field can be expressed as:

$$\bar{H}^{pr} = \sum_{m=0}^{\infty} \sum_{n=m}^{\infty} \sum_{p=0}^1 b_{pmn} \bar{H}_{pmn}^{pr}. \quad (4.5.1)$$

The b_{pmn} are coefficients needed to express the primary field and \bar{H}_{pmn}^{pr} is the pmn mode of the primary magnetic field component when $b_{pmn}=1$. The normal component of the primary magnetic field on the fictitious spheroid, $H_{\xi}^{pr}(\eta, \xi_o, \phi)$, can be written as

$$H_{\xi}^{pr}(\eta, \xi_o, \phi) = -\frac{H_0 d}{2} \sum_{m=0}^M \sum_{n=m}^N \sum_{p=0}^1 b_{pmn} P_n^m(\eta) P_n^m(\xi_o) T_{pm}(\phi), \quad (4.5.2)$$

where (η, ξ, ϕ) are the standard spheroidal coordinates; d is the spheroid's interfocal distance, P_n^m are associated Legendre functions of the first kind, and $T_{pm}(\phi)$ represents the azimuthal functions given by

$$T_{pm}(\phi) = \begin{cases} \cos(m\phi), & p = 0 \\ \sin(m\phi), & p = 1. \end{cases} \quad (4.5.3)$$

By the orthogonality of the associated Legendre functions, the spheroidal expansion coefficients b_{pmn} can be derived as

$$b_{pmn} = -\frac{2n+1}{\gamma \pi H_0 d P_n^m(\xi_o)} \frac{(n-m)!}{(n+m)!} \int_{-1}^1 P_n^m(\eta) \int_0^{2\pi} H_{\xi}^{pr}(\eta, \xi_o, \phi) T_{pm}(\phi) d\phi d\eta, \quad (4.5.4)$$

where $\gamma=2$ for $m=p=0$ and $\gamma=1$ otherwise. The integration in (4.5.4) is evaluated by numerical integration. This completes the decomposition of the primary field $H_{\xi}^{pr}(\eta, \xi_o, \phi)$.

After the primary magnetic field is decomposed into the pmn spheroidal modes, then the complete solution for the target to each \bar{H}_{pmn}^{pr} field is obtained. Since the object is placed in a conducting and magnetically susceptible background, the magnetic field in the entire computational space

(Regions 1 and 2, Fig. 4.5.1) satisfies Helmholtz's wave equation and it can be represented with magnetic dipoles as

$$\bar{H}_\alpha(\bar{r}) = \int_S \bar{\bar{G}}_\alpha(\bar{r}; \bar{r}') \cdot \bar{P}_\alpha(\bar{r}') ds'. \quad (4.5.5)$$

Here $\bar{\bar{G}}_\alpha(\bar{r}; \bar{r}')$ is the Dyadic Green's Function, $\bar{P}_\alpha(\bar{r}')$ are amplitudes of magnetic dipoles, and $\alpha = 1, 2$ corresponds to region 1 or 2. Here

$$\bar{\bar{G}}_\alpha(\bar{r}; \bar{r}') = \left(\bar{\bar{I}} + \frac{\nabla \nabla}{k_\alpha^2} \right) G_\alpha(\bar{r}; \bar{r}'), G_\alpha(\bar{r}; \bar{r}') \equiv \frac{e^{-jk_\alpha R}}{4\pi\mu_\alpha\mu_o R} \quad (4.5.6)$$

$$k_\alpha = \sqrt{\omega\mu_\alpha\mu_o(\omega\epsilon_o + j\sigma_\alpha)}$$

where $\bar{\bar{I}}$ is the unit dyad, k_α is the wave-number in α region, σ_α and μ_α are the conductivity and relative permeability of α region respectively, and $R \equiv |\bar{r} - \bar{r}'|$ is the distance between source and observation points. We assume that the relative electric permittivities of both regions are 1; $G_\alpha(\bar{r}; \bar{r}')$ is the fundamental solution for the wave equation of the Hertzian magnetic vector potential, whereas the $\exp\{j\omega t\}$ time convention has been implied and suppressed.

On the surface of the object, total magnetic fields satisfy the following boundary conditions:

$$[\hat{n} \times (H_1^{sc} + H^{pr})] = [\hat{n} \times H_2] \quad (4.5.7)$$

$$\hat{n} \cdot \mu_1 (H_1^{sc} + H^{pr}) = \hat{n} \cdot \mu_2 H_2 \quad (4.5.8)$$

where \hat{n} is a unit normal vector on the real surface, \bar{H}^{pr} is the primary magnetic field, \bar{H}_2 is the total magnetic field in region 2, and μ_α is α region's relative magnetic permeability.

To determine amplitudes of the magnetic dipoles we have to solve the entire boundary value EMI problem for each mode of the primary field just once and then store the amplitudes of the responding sources. To do so, one extends each mode to the physical surface within the enclosing spheroid and applies the 3-D MAS-TSA method [55, 90]. Finally, the target's response for each primary magnetic field component $b_{pmn}\bar{H}_{pmn}^{pr}$ is expressed similar to (4.5.5) as:

$$\bar{H}_{pmn}^{sc}(\bar{r}) = b_{pmn} \sum_{k=1}^N \bar{\bar{G}}_1(\bar{r}, \bar{r}'_k) \bar{P}_{1,k}^{pmn} \quad (4.5.9)$$

where $\bar{P}_{1,k}^{pmn}$ is the amplitude of the k^{th} auxiliary magnetic dipole, located at the target's domain [24–25], corresponding to the \bar{H}_{pmn}^{pr} response, and N is the number of auxiliary magnetic sources. Using $\bar{P}_{1,k}^{pmn}$ for each fundamental mode, the total response at any point outside the scatterer can be represented as:

$$\bar{H}^{sc}(\bar{r}) = \sum_{m=0}^{\infty} \sum_{n=m}^{\infty} \sum_{p=0}^1 b_{pmn} \sum_{k=1}^N \bar{\bar{G}}_1(\bar{r}, \bar{r}'_k) \bar{P}_{1,k}^{pmn}. \quad (4.5.10)$$

Thus, after pre-computation of the $\bar{P}_{1,k}^{pmn}$ coefficients for any given object, the EMI scattering problem, for any particular 3-D configuration involving it, breaks down merely to determine the spheroidal modal expansion coefficients b_{pmn} .

In equation (4.5.10) a substantial number of responding sources $\bar{P}_{1,k}^{pmn}$ are required to represent the scattered magnetic field outside the object (including physical surface). Similar to (4.5.10) we

can re-express that field quite accurately in terms of a reduced number of sources from the fictitious spheroid. The amplitudes of this reduced number of sources $[\bar{p}^{pmn}]$ for each input pmn spheroidal mode can be determined by solving a linear system of equations for the normal component of the scattered magnetic field as it is shown in [55, 90], and finally the complete secondary magnetic field can be represented as

$$\bar{H}^{sc}(\bar{r}) = \sum_{m=0}^{\infty} \sum_{n=m}^{\infty} \sum_{p=0}^1 b_{pmn} \sum_{i=1}^{N_{red}} \bar{G}_1(\bar{r}, \bar{r}'_i) \bar{p}_i^{pmn}. \quad (4.5.11)$$

Note that, while we may ultimately be able to express the scattered field using a small number of sources, this is a fundamentally different strategy from what has been applied heretofore in the simple independent dipole models. In the latter, each source responds only to the primary field striking it locally. However, here the \bar{p}_i^{pmn} , $i = 1, 2, \dots, N_{red}$ responding sources act together, not in response to local stimuli but to express the response of the entire object to the distributed excitation of the pmn mode. In addition, using the MAS-MAS/TSA numerical code the \bar{p}_i^{pmn} can be generated and stored for any number of pmn spheroidal modes in the infinite series (4.5.11). Once this is done, then the truncation criterion can be determined from the input primary magnetic field easily.

Overall, the entire GSEA approach can be described briefly as follows:

1. For a given UXO amplitudes of responding magnetic dipoles \bar{p}_i^{pmn} , $i = 1, 2, \dots, N_{red}$ rings are determined and sorted in the universal library for any number of basic spheroidal mode excitations $pmn = 1, 2, \dots$
2. Once step 1 is done, then for a given sensor the primary field is decomposed into spheroidal modes, the spheroidal modal decomposition b_{pmn} coefficients are calculated, and the necessary number of spheroidal modes is determined.
3. Use reduced set of sources (RSS) \bar{p}_i^{pmn} to calculate EMI response for each pmn -th basic excitation. Scale each pmn -EMI response on the b_{pmn} coefficients and calculate the target's complete response by just superposing responses of each basic excitation.

The GSEA, which is based on the MAS-TSA and introduced here, can produce a target's ultra-wideband frequency response. Thus, the proposed GSEA can be used directly to obtain an object's TD EMI responses via convolution theorem without recalculating amplitudes of the responding sources. This makes the GSEA a unified model to treat both FD and TD data, and is attractive from a practical point of view, as many state-of-the-art EMI sensors (EM-63, EM-61, Zonge NanoTEM) are operating in TD.

Let us briefly describe the important formulas required to compute the TD EMI response for a general current waveform $I(t)$ flowing in a transmitter loop. By using the convolution theorem [29] the induced voltage in the receiver coil can be expressed as

$$\frac{dB}{dt} = - \int_0^t A'(t - \tau) I'(\tau) d\tau - A(0) I'(t) - A'(t) I(0), \quad (4.5.12)$$

where $A(t)$ represents an object's impulse response and the prime means the derivative with respect to time t . Equation (4.5.12) represents the TD response of an object to a general excitation current $I(t)$ source.

4.5.c Frequency-Dependent Magnetic Susceptibility

There are three types of magnetic susceptibility that generate soils' EM responses: (1) induced, (2) permanent/remanent, and (3) viscous remanent (VRM). The soil magnetic properties are determined by the presence of iron and iron-oxide particles. Permanent remanent magnetization is the magnetization that exists in the absence of any applied field. Induced magnetization is the magnetization that arises in the presence of an external magnetic field, and viscous remanent magnetization (VRM) is a phenomenon that occurs when magnetization of an object placed in an external magnetic field changes in a time relative to the applied field. This means that the object's susceptibility is a complex frequency-dependent [45]

$$\chi(\omega) = \chi'(\omega) + j\chi''(\omega) \quad (4.5.13)$$

where ω is the angular frequency, j is the unit complex number, and $\chi'(\omega)$ and $\chi''(\omega)$ are the real and imaginary parts for the frequency-dependent magnetic susceptibility. There are various references [31 and references therein] that discuss many aspects of soil magnetic properties. The most common frequency-dependent complex magnetic susceptibility, assuming that magnetic relaxation time constants are uniformly distributed between times τ_1 and τ_2 , is modeled as follows [49]:

$$\chi(\omega) = \chi_0 \left(1 - \frac{1}{\ln(\tau_2/\tau_1)} \cdot \ln \frac{j\omega\tau_2 + 1}{j\omega\tau_1 + 1} \right) \quad (4.5.14)$$

where χ_0 is the DC value of the susceptibility.

For magnetically susceptible ground in the presence of a metallic object, the field that is measured by the sensors contains two parts and can be written as

$$\overline{H}^{mes}(\omega) = \overline{H}^{gr}(\omega) + \overline{H}^{obj}(\omega) \quad (4.5.15)$$

where $\overline{H}^{gr}(\omega)$ and $\overline{H}^{obj}(\omega)$ are respectively magnetic fields produced by the magnetically susceptible soil and the object. The magnetic field \overline{H}^{obj} contains all interactions between the object and the susceptible host medium. For determining contribution of each magnetic field $\overline{H}^{gr}(\omega)$ and $\overline{H}^{obj}(\omega)$ in the measured field, a full EMI problem must be solved. In this section the soil is considered to be a uniform half-space, and interaction between the soil and the object is taken into account by using the image source method [49].

4.5.d Numerical Results

This section presents some numerical and experimental data that demonstrate the GSEA as a unified model for any FD or TD sensor configuration, and its applicability to complex data sets: novel waveforms, multi-axis, vector, or tensor magnetic, or electromagnetic induction data, or any combination of magnetic and EMI data; and ability to take into account the influence of conductive and magnetically susceptible geological soils on metal detectors.

4.5.d.(1) The universal RSS As it was discussed above, the reduced source set (RSS) \overline{p}_i^{pmn} in Eq. (4.5.11) depends only on the target's geometry and electromagnetic properties. To validate such a unique characteristic of the RSS, here comparisons between RSS modeled and experimental data are given for an actual UXO (81 mm) in both FD and TD. The data were collected by two EMI

systems that are widely used in the UXO discrimination community: (1) a wideband frequency-domain sensor (GEM3) developed by Geophex Ltd. [95] and (2) a time-domain instrument (EM63) developed by Geonics [96]. The data were collected on the U.S. Army Engineer Research and Development Center test stand site.

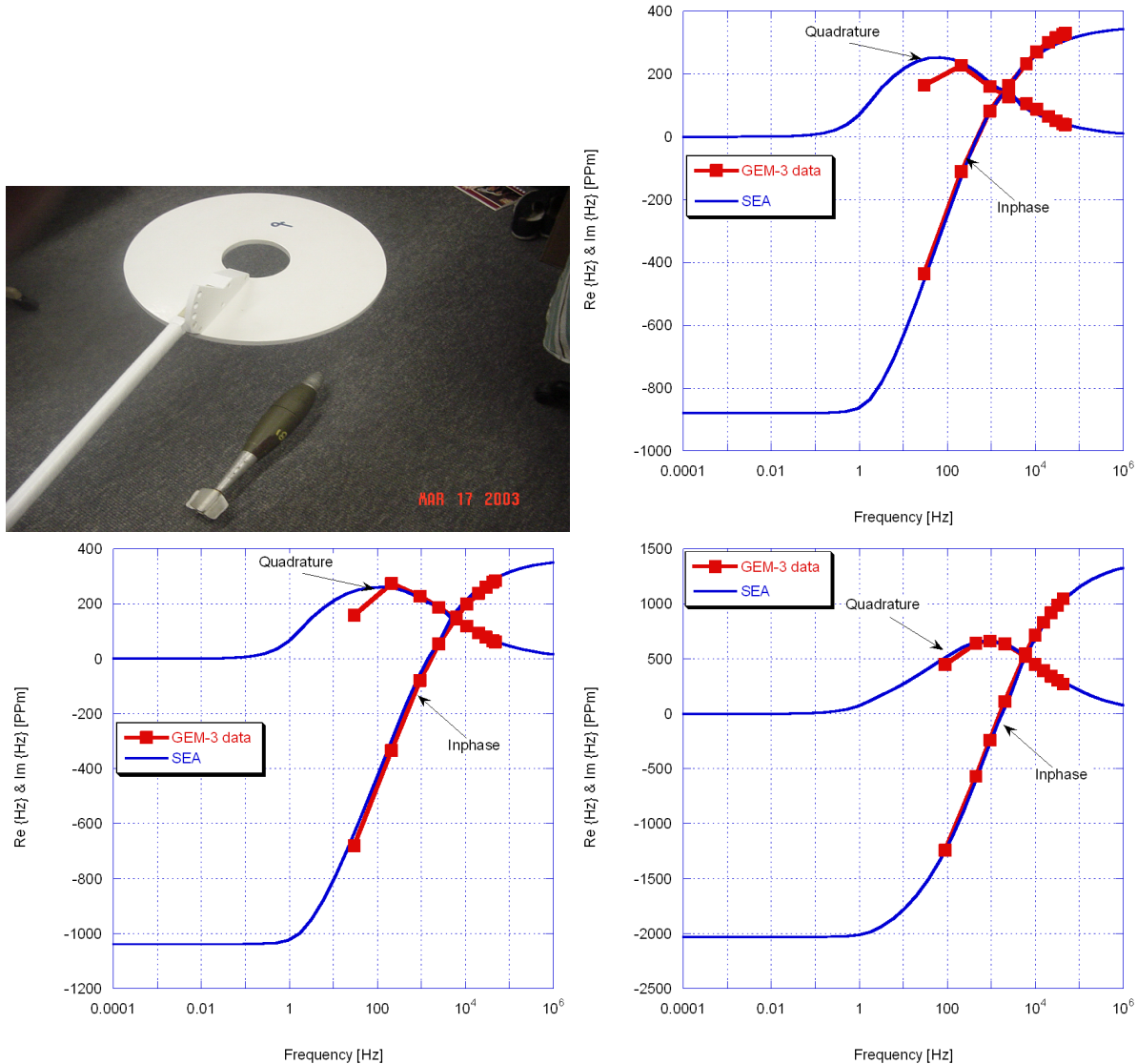


Figure 4.5.2: Frequency-domain EMI response for 81 mm UXO; (a) GEM-3 excitation; (b) nose up vertical, (c) nose up 45 inclination, (d) horizontal.

Figure 4.5.2 shows the comparisons between GSEA and actual data in the frequency domain. In this case data were collected for the UXO oriented in three different directions relative to the GEM-3 sensor's head: (1) vertical tail up, (2) 45° degree nose up, and (3) transverse. The GEM-3 frequency range is from 30 Hz to 50 kHz. The comparisons between measured and actual experimental data are in very good agreement for all orientations. Note that the RSS produces results in an ultra-wideband frequency range, from magneto-static (0 Hz) to EMI frequency limit. This allows users to accurately compute the scattered field at any required frequencies by simple interpolation and to obtain EMI responses readily in TD via inverse Fourier transforms. To illustrate

this capability, here the first impulse responses in TD are evaluated by applying the digital filter technique [92] to the inverse sine transform [93] as follows:

$$A(t) = \frac{2}{\pi} \int_0^{\infty} \text{Im}B(\omega) \sin \omega t d\omega \quad (4.5.16)$$

where $\text{Im}B(\omega)$ represents an imaginary part of the magnetic flux that is calculated via RSS. Then the induced voltage is calculated using the time convolution technique (4.5.12).

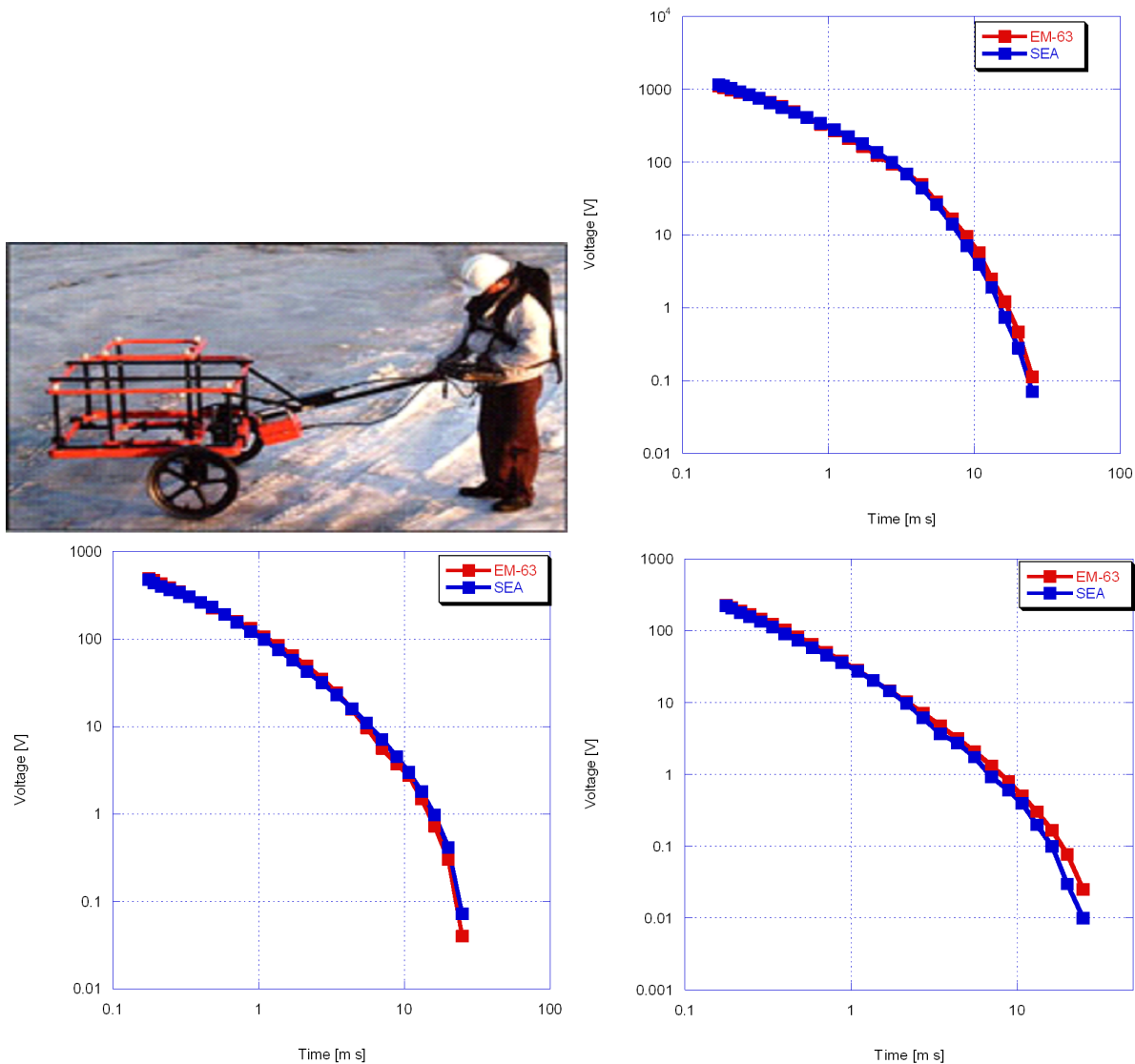


Figure 4.5.3: Time-domain EMI response for 81-mm UXO; (a) EM-3 excitation; (b) nose up vertical, (c) nose up 45 inclination, (d) horizontal.

In the EM63 instrument, the current waveform consists of an exponential current increase followed by a linear ramp off. The current has the three pulses per measurement. For comparisons between RSS and TD data, here the same 81-mm UXO is chosen. The object was excited in three orientations: (1) vertical tail up, (2) 45° degree nose up, and (3) transverse orientations. For all three excitations, the vertical distance between the sensor's transmitter loop and the center of the

cylinder is $h = 60.00$ cm. The TD induced voltage is calculated by an inverse Fourier transform of the frequency-domain magnetic field flux using equations (4.5.12) and (4.5.16). The comparisons are depicted in Fig. 4.5.3. They show very good convergence between the measured and modeled TD data. Therefore, the universal RSS should be able to produce EMI responses for a given target for any sensor in FD and TD domains.

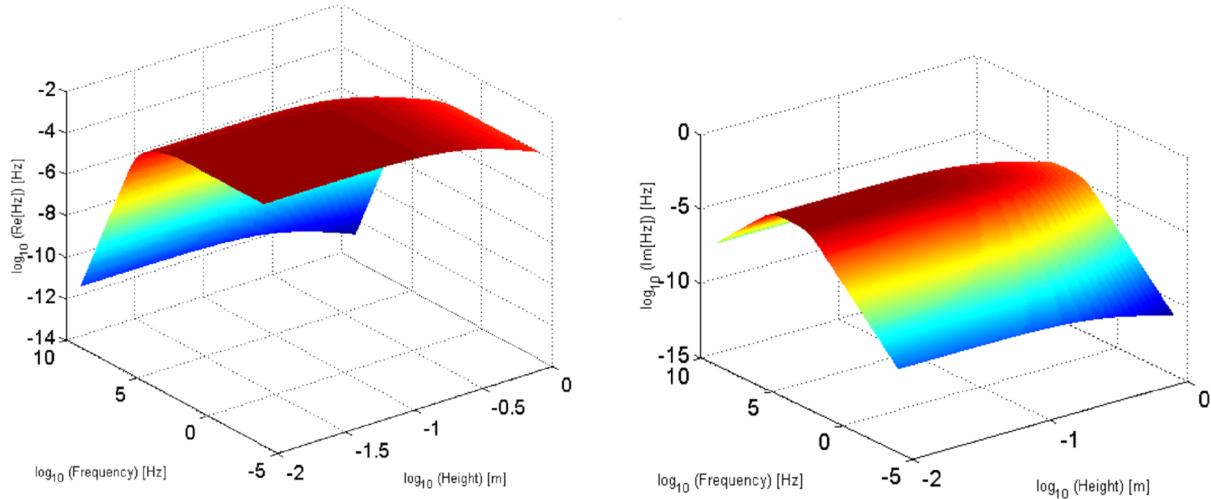


Figure 4.5.4: EMI response for a magnetically susceptible soil versus the sensor height and frequency. (a) Inphase part; (b) quadrature part.

4.5.d.(2) EMI response for soil with frequency-dependent susceptibility In this section, first FD EMI response is studied for a magnetically susceptible half-space. The half-space is illuminated by a FD sensor. In these simulations for the sensor model the following parameters are used: current $I_o = 1$ A, and a $100\text{-cm} \times 100\text{-cm}$ transmitter loop. The soil's frequency-dependent susceptibility is assumed to be the same as in equation (4.5.14) with a realistic $\chi_0 = 0.005$ D.C value of susceptibility [33], and $\tau_1 = 10^{-6}$ [sec] and $\tau_2 = 10^{-3}$ [sec] time constants. Figure 4.5.4 shows soil's responses in-phase (right) and quadrature (left) parts as a function of frequency and sensor height. The results illustrate that the soil's EMI responses strongly depend on both the frequency and sensor height. As the sensor approaches the soil, soil's response increases and it stays almost constant for antenna heights between 1 cm and 10 cm. Note that all parameters in Figure 4 are in Logarithmical scale. The soil response's quadrature part approaches to maximum between 10 kHz and 100 kHz, whereas at low frequencies the in-phase part is dominant. At highest frequencies (more than 100kHz) both parts of soil's response decrease. Thus the soil with frequency-dependent magnetic susceptibility produces significant EMI responses almost entire UWB frequency range.

Finally, to illustrate the soil effect on a buried object's EMI responses, several numerical experiments were done in both FD and TD. The 81-mm UXO was buried under a magnetically susceptible half-space. The half-space electromagnetic parameters are exactly the same ($\chi_0 = 0.005$, $\tau_1 = 10^{-6}$ [sec] and $\tau_2 = 10^{-3}$ [sec]) as in the previous paragraph. The entire structure is illuminated by (1) the GEM-3 sensor with current $I_o = 1$ A, 10- and 20-cm radii coils, and (2) the EM-63 with $I_o = 1$ A, $100\text{-cm} \times 100\text{-cm}$ transmitter loop. The sensors are placed 10 cm above the half-space. The UXO is oriented 45° nose up and its center is at 32-cm depth for the GEM-3 excitation and

50 cm for the EM-63 sensor. The results are depicted in Fig. 4.5.5. These results suggest that a magnetically susceptible half-space could significantly affect both frequency and time domain EMI responses.

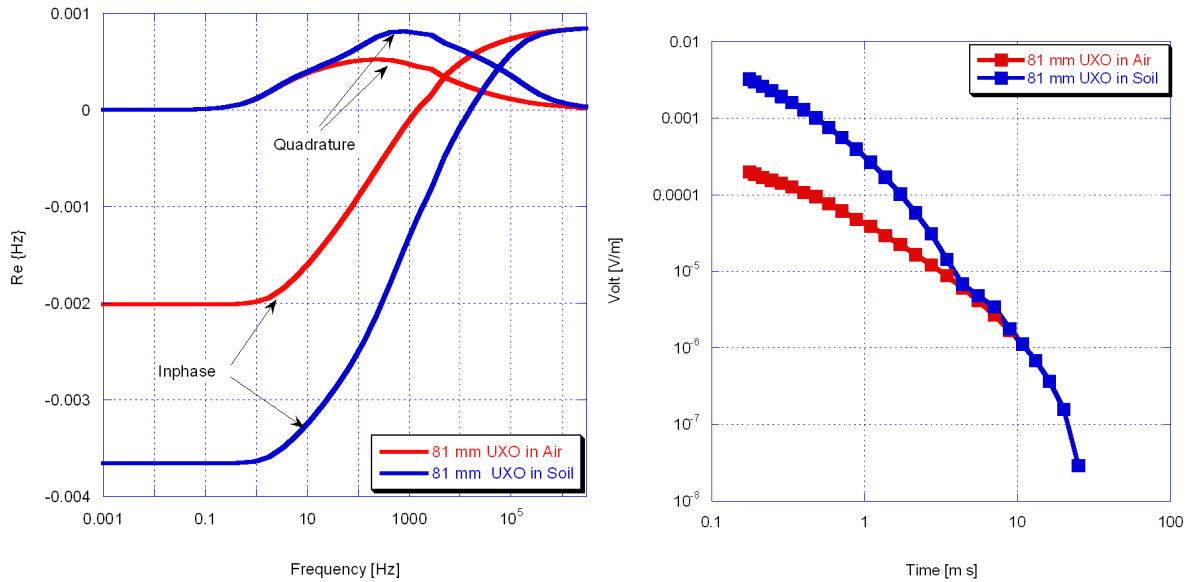


Figure 4.5.5: EMI response for 81 mm UXO; (a) Frequency domain, (b) Time domain.

These calculations are based on the functional form for ground susceptibility given by 4.5.14, which the Steve Billings, et al. at UBC/Sky state has “applied to every soil they’ve ever encountered” in the TD. Also, the value of 5×10^{-3} is on the order of magnitude of the single frequency susceptibility values obtained by Janet Simms in numerous measurements at the UXO standardized test sites [33–35]. However the question arises whether this is the appropriate value to insert for χ_0 . In particular, we have never seen FD soil effects of the magnitude and type shown in Fig. 4.5.5, left. This may mean that functional form 4.5.14 pertains successfully to TD, but that another larger effect appears in the frequency domain corresponding to the instantaneous soil response. The latter would not appear (or at least would only appear indirectly) in the TD measurements. The method used here to perform “absolute” calibrations of instrument data for conversion into actual magnetic field units allows us to infer actual broadband χ values from such data. Applying this to both the new GEM-3 \mathcal{D}^+ as well as emerging TD instruments should allow us to complete the characterization of soils of interest, modifying the functional form 4.5.14 as necessary to include all relevant FD and TD effects.

4.5.e CONCLUSION

The generalized standardized excitation approach, which is a fast, universal, and rigorous forward modeling system, has been developed and demonstrated. The GSEA is applicable to any FD or TD sensor configuration, and to any data set: novel waveforms, multi-axis, vector and tensor, or magnetic or electromagnetic induction data, or any combination of magnetic and EMI data.

The proposed system has been tested against actual data in both the frequency (GEM-3) and time (EM-63) domains. Excellent agreements between the GSEA and experimental data have been demonstrated here. The GSEA technique could be used for building a new type of EMI sensor as

well as for optimal survey designing.

By using an appropriate dyadic Green's function the GSEA takes into account a host medium. EMI response from a magnetically susceptible half-space is analyzed versus sensor height and frequency. Numerical tests show that a frequency-dependent, magnetically susceptible half-space significantly affects the 81-mm UXO's EMI responses in both FD and TD. This study suggests that a magnetically susceptible host medium must be taken into account in UXO discrimination problems.

4.6 NSMS Modeling of GEM-3 \mathcal{D}^+ and HAP Method

The normalized surface magnetic source (NSMS) model [97–100] is a rigorous physically complete model of any metallic target's interaction with an arbitrary primary field in the electromagnetic induction (EMI) regime. Based on a number of well-defined measurements for a given target, the system solves for its fundamental, characteristic response parameters. After target characterization, the response of that target to any combination primary field modes can be quickly and accurately calculated.

The NSMS model can be considered as a generalized surface dipole model [68, 82–87, 95, 96, 101, 102], which in a special limiting case coincides with the infinitesimal dipole approach. In the model, the response of an object to the exciting field of a sensor is taken to originate from a layer of equivalent magnetic dipoles distributed over a spheroidal surface surrounding the target. Such a distribution can be generated by spreading positive charge density Ω over the exterior of a thin smooth surface and an identical negative charge on its inner surface, resulting in a double layer of charge separated by an infinitesimal distance. This configuration introduces the proper discontinuities in the tangential components of the magnetic flux density vector \vec{B} but does not affect its normal component. (A single layer of charge, on the other hand, would in no way affect the transition of the tangential components of the flux density but could model a discontinuity in the normal component of \vec{B} .) Since there are no free magnetic charges in nature, the normal component of the magnetic flux density must always be continuous across the boundary between two media; the secondary magnetic field outside an object can thus be accounted for by a double magnetic charge layer of density Ω distributed on an auxiliary surrounding surface; this density is proportional to the component of the primary (exciting) magnetic field normal to the surface.

The amplitudes of the auxiliary sources are determined directly, and with great speed and accuracy, by minimizing the difference between measured and modeled data for a known object-sensor configuration. The charge density Ω is a property of the target, and its integral Q over the spheroidal surface constitutes a global magnetic “capacitance” of sorts that for a given object is invariant in the sense that different computational constructs – e.g., surrounding surface, measurement grid, object location or orientation – and different primary fields produce the same value. Once the source strengths are known, the NSMS model can be used in discrimination processing that either compares the measured fields to those stored in a library of known objects – i.e., a “pattern matching” technique – or uses the integrated NSMS as a discriminant – i.e., “genuine” inversion. In “pattern matching” discrimination processing, an optimization or search algorithm is used to determine which known UXO has the catalogued ultrawideband Ω distribution that best reproduces the signal received by the survey sensor. Used in this way, the NSMS system is a faster forward model than other physically complete forward models such as the standardized excitation approach (SEA) or the generalized SEA [88, 103–106].

We use the total NSMS, Q , of a target as a discriminant in Sec. 5. This Q may also be

parametrized by a Pasion Oldenburg type model and/or combined with other parameters, for example from the dipole model, in order to further characterize a target and classify it based on its EMI response [107]. When extracting Q from training data in order to create a given target's "fingerprint," the location of the target is generally known *a priori*. However, when the target's position and orientation are not known, then inverse algorithm has to combine inverting not only for which target is present, but where that target is. This turns out to be a combination of a linear and non-linear process and is often time consuming. To this end, we have developed the HAP method (\bar{H} (magnetic field), \bar{A} (magnetic vector potential), and ψ (magnetic scalar potential)) which under certain assumption can find the location and orientation of a dipolar source without an expensive inversion [107–110].

While it's easy to show that simple, infinitesimal dipoles are frequently deficient for modeling a target's general response under diverse circumstances, the HAP approach assumes that under any particular circumstances a dipole representation is likely to furnish a good first order representation of the response at hand. In order to find an estimate of the target's location and orientation in a rapid, robust manner, we temporarily assume that the sources of the anomalies being surveyed are caused by simple dipole sources. Using the magnetic dipole approximation in the EMI regime, the scattered magnetic field \bar{H} , magnetic vector potential \bar{A} , and magnetic scalar potential ψ can be written as:

$$H = \frac{1}{4\pi R^3} \left(\frac{3\bar{R}(\bar{R} \cdot \bar{P})}{R^2} - \bar{P} \right), \quad A = \mu_0 \frac{\bar{R} \times \bar{P}}{4\pi R^3}, \quad \psi = \frac{\bar{R} \cdot \bar{P}}{4\pi R^3} \quad (4.6.1)$$

where $\bar{R} = \bar{r} - \bar{r}'$ with \bar{r} and \bar{r}' being the position of the observation and of the source, respectively.

From (4.6.1), it can be shown also that $\psi = (\bar{H} \cdot \bar{R})/2$ and $\bar{A} = \mu_0(\bar{H} \times \bar{R})$. Now, taking $\bar{R} \times \bar{A}$, we can solve for \bar{R} as

$$\bar{R} = \frac{2\psi\bar{H} - (\bar{A} \times \bar{H})/\mu_0}{|\bar{H}|^2}. \quad (4.6.2)$$

Similarly, taking the cross product of \bar{A} in (4.6.1) from the left side, the magnetic dipole moment \bar{P} can be expressed as

$$\bar{P} = 4\pi R (\bar{R}\psi + (\bar{A} \times \bar{H})/\mu_0). \quad (4.6.3)$$

Thus, under magnetoquasistatic (MQS) assumptions of a dipole source, (4.6.2) and (4.6.3) represent an analytical method for finding the location, \bar{R} and orientation, \bar{P} of the dipole.

Currently, $\{\bar{H}, \bar{A}, \psi\}$ are found from EMI data through the Normalized Surface Magnetic Source Method (NSMS). An equivalent, flat, two dimensional NSMS surface located in between the measurement locations and the target can accurately reproduce the response from the target(s) being interrogated [100]. This NSMS surface consists of a layer of magnetic charges or dipoles from which $\{\bar{H}, \bar{A}, \psi\}$ and hence $\{\bar{R}, \bar{P}\}$ can be calculated. Note that no information regarding the target(s) is required to calculate this NSMS surface layer.

The NSMS model must be adapted to each unique instrument one time. This has been accomplished for the GEM-3 \mathcal{D}^+ and the results of matching GEM-3 \mathcal{D}^+ data to the predicted response from the NSMS model are shown in Figs. 4.6.1–4.6.3.

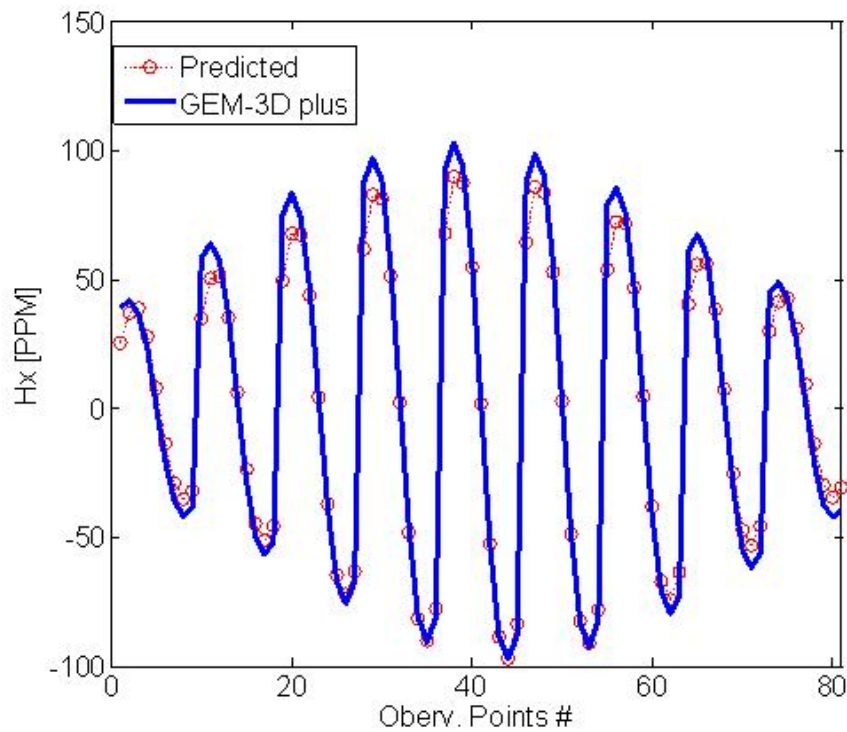


Figure 4.6.1: Comparison of H_x from the GEM-3 \mathcal{D}^+ and NSMS model predicted response. Data at 90Hz over a steel sphere, inphase part.

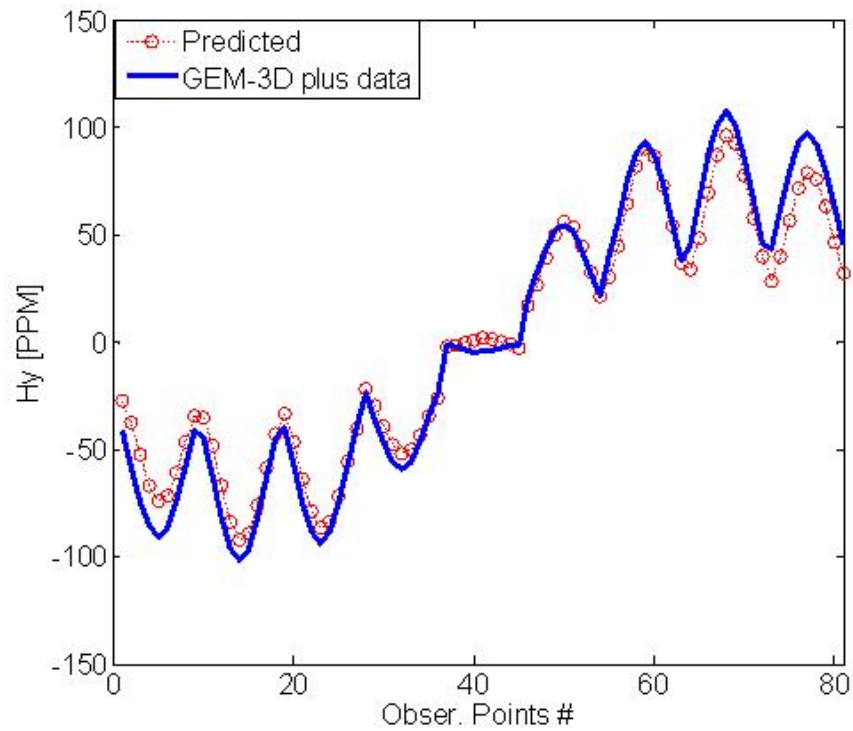


Figure 4.6.2: Comparison of H_y from the GEM-3 \mathcal{D}^+ and NSMS model predicted response. Data at 90Hz over a steel sphere, inphase part.

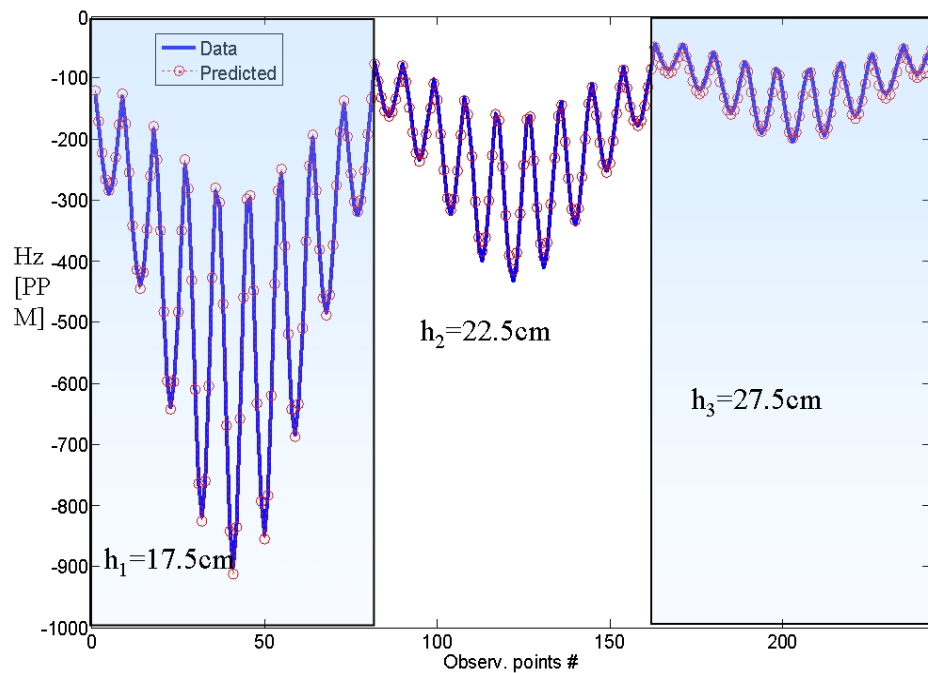


Figure 4.6.3: Comparison of H_z from the GEM-3 \mathcal{D}^+ and NSMS model predicted response. Data at 90Hz over a steel sphere, inphase part. 3 levels with 81 points on each level.

4.7 Electromagnetic induction from highly permeable and conductive ellipsoids under arbitrary excitation – Application to the detection of unexploded ordnances

Symmetrical objects such as spheres or spheroids may be useful as models of some subsets of possible targets; and for testing instruments they may be particularly useful when one can examine signals for expected symmetries. However, particularly when all vector components are being recorded and examined, a truly 3-D object solution offers the most general reference response. Heretofore there has been no broadband 3-D analytical solution available, except by relatively laborious numerical methods. The approximate solution produced here is rapidly evaluated under diverse conditions. It represents a milestone in benchmark cases that can be used hereafter in a wide variety of contexts. Specifically in our discrimination processing, with this new solution we can for the first time model the responses of unseen objects quickly without having to assume restrictive symmetries. We now have a 3-D solution to guide analysis, statistical learning machines, etc, for inferring overall geometrical properties such as volume and aspect ratios, from signals across the breadth of the EMI band.

The secondary field produced by three-dimensional highly permeable and conductive objects is computed in the electromagnetic induction regime, with the purpose of modeling unexploded ordnances and surrounding clutter. The analytical formulation is based on the ellipsoidal coordinate system, able to model real three dimensional geometries as opposed to bodies of revolutions like within a spheroidal approach. At the frequencies of interest (tens of Hertz to hundreds of kilo-Hertz), the conduction currents in the soil are negligible and the fields are computed in the magneto-quasistatic regime based on the Laplace equation. Inside the objects, where the wave equation governs the field distribution, the currents are assumed to have a small penetration depth, allowing for the analytical simplification of the field components, which become decoupled at the surface. This approximation, valid across the entire frequency spectrum because of the high permeability and conductivity, avoids the necessity of using ellipsoidal wave functions and results in a considerable saving of computational time. Numerical results compare favorably with numerical and experimental data. Finally, the optimization approach used to match our numerical predictions with experimental data demonstrates the possibility of remotely inferring the material properties of objects.

4.7.a Introduction

One theoretical approach models the UXO as a (possibly) magnetic and (possibly) conductive spheroid [2, 111–113]. The model is therefore mathematically more involved but offers important flexibility in terms of geometries (from elongated to flat objects within the same formalism), material parameters, and distance to sensor.

In this section, we extend the second approach to ellipsoidal geometries with the underlying motivation of providing an improved physical model of the clutter surrounding UXO, directly useful for example in statistical and optimization methods such as in [114–118]. Clutter is indeed most often composed of random three dimensional (3D) pieces of steel which are jamming the measured signals and are in part responsible for the high false positive alerts. Their proper modeling is therefore essential and the ellipsoidal coordinate system provides a general framework to do so, allowing for the modeling of real 3D geometries while retaining the speed advantage of analytical calculations, fundamental for example in inversion algorithms [119][120][121–123]. In addition, we use in this paper the small penetration approximation (SPA), justified by the major

steel component of clutter objects. SPA was originally developed as a high frequency approximation for spheroidal geometries [113] under the assumption that the currents induced on the surface of the object penetrate only slightly into its volume. Remarkably, however, SPA has been shown to yield accurate results over the entire EMI frequency range for highly permeable and highly conductive objects, such as those made of steel. This success has prompted various implementations of the SPA, both analytical [113] and numerical [124, 125]. In this paper, we generalize the SPA to ellipsoidal geometries and confirm the good agreement obtained over the entire frequency range by comparing our predictions with both well established numerical results and with measurement data.

The configuration under study is depicted in Fig. 4.7.1: a homogeneous ellipsoid of semi-axes ($a > b > c$) along the directions ($\hat{x}, \hat{y}, \hat{z}$) (see the Appendix for mathematical details), of permeability $\mu_1 = 100\mu_0$ and conductivity $\sigma_1 = 10^7$ [S/m] is embedded in a non-magnetic and non-conductive soil which, at the frequencies of interest, is essentially transparent and modeled as free-space. A sensor located above the object emits a primary field \bar{H}^o and measures the secondary field \bar{H}^s produced by the object. We subsequently use two models for the primary field: a simple uniform field, valid for small or deeply buried objects, and the field produced by the GEM-3 instrument [1], more realistic for large or close objects.

In the EMI regime, the magnetic field outside the ellipsoid is irrotational and can therefore be written in terms of a potential function which obeys the Laplace equation. Denoting the primary and secondary potentials as U^o and U^s , respectively, the total magnetic field in the region exterior to the ellipsoid is written as

$$\bar{H}_2 = \bar{H}^o + \bar{H}^s = -\nabla U^o - \nabla U^s. \quad (4.7.1)$$

In the interior region to the object, the magnetic field \bar{H}_1 obeys the wave equation

$$\nabla \times \nabla \times \bar{H}_1 - k_1^2 \bar{H}_1 = 0 \quad (4.7.2)$$

where $k_1^2 = i\omega\sigma_1\mu_1$. This limiting form of k_1 that applies in this parameter space means that (4.7.2) leads in fact to a diffusion equation representing magnetic diffusion, though it retains the form of a wave equation. The two quantities \bar{H}_1 and \bar{H}_2 are related by the usual boundary conditions.

For details on the ellipsoidal coordinate system, the separation of the wave equation in ellipsoidal coordinates, and the derivation of the secondary field \bar{H}^s in the ellipsoidal coordinate system as a function of the type of incidence (uniform and GEM-3) within the SPA approximation, see [126].

The ellipsoidal coordinate system is defined based on the definition of the master ellipsoid of semi-axes dimensions (a, b, c) along the ($\hat{x}, \hat{y}, \hat{z}$) directions respectively ($a > b > c$):

$$\frac{x^2}{a^2} + \frac{y^2}{b^2} + \frac{z^2}{c^2} = 1. \quad (4.7.3)$$

Upon defining the variable $k^2 = a^2 - c^2$ and $h^2 = a^2 - b^2$ [127], three families of orthogonal surfaces can be obtained [128], used to defined the ellipsoidal coordinate system (ρ, μ, ν):

$$\frac{x^2}{\rho^2} + \frac{y^2}{\rho^2 - h^2} + \frac{z^2}{\rho^2 - k^2} = 1, \quad (4.7.4a)$$

$$\frac{x^2}{\mu^2} + \frac{y^2}{\mu^2 - h^2} - \frac{z^2}{k^2 - \mu^2} = 1, \quad (4.7.4b)$$

$$\frac{x^2}{\nu^2} - \frac{y^2}{h^2 - \nu^2} - \frac{z^2}{k^2 - \nu^2} = 1, \quad (4.7.4c)$$

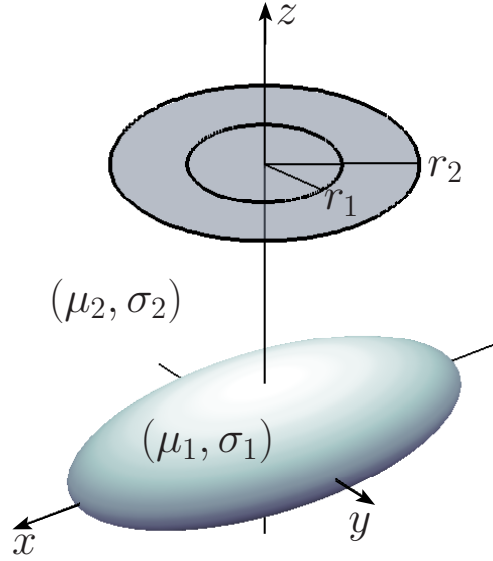


Figure 4.7.1: Configuration of the problem: an ellipsoid of material parameters ($\mu_1 = 100\mu_0$, $\sigma_1 = 10^7$ [S/m]) is surrounded by free-space ($\mu_2 = \mu_0$, $\sigma_2 \approx 0$) and is excited by a GEM-3 instrument [1] modeled as two current loops (figure not to scale). The semi-axes of the ellipsoid are denoted by a , b , and c (with $a > b > c$) along the \hat{x} , \hat{y} and \hat{z} directions, respectively (see the Appendix for mathematical details on the ellipsoidal coordinate system).

and where $\rho^2 \geq k^2 \geq \mu^2 \geq h^2 \geq v^2 \geq 0$.

The magnetic field is obtained from the gradient

$$\nabla U = \hat{\rho} \frac{1}{h_\rho} \frac{\partial U}{\partial \rho} + \hat{\mu} \frac{1}{h_\mu} \frac{\partial U}{\partial \mu} + \hat{v} \frac{1}{h_v} \frac{\partial U}{\partial v} \quad (4.7.5)$$

and is written as

$$\bar{H}^o = -\nabla U^o = -\hat{\rho} \frac{1}{h_\rho} \sum_{n,p} b_n^{(p)} E(\rho', \mu, v) - \hat{\mu} \frac{1}{h_\mu} \sum_{n,p} b_n^{(p)} E(\rho, \mu', v) - \hat{v} \frac{1}{h_v} \sum_{n,p} b_n^{(p)} E(\rho, \mu, v') \quad (4.7.6)$$

for the primary field.

Introducing the field expansions and separating the terms functions of $b_n^{(p)}$ and $B_n^{(p)}$ yields

$$\begin{aligned} & \sum_{n,p} B_n^{(p)} \left\{ ik_1 \frac{\mu_2}{\mu_1} [I'(a)E(a) + I(a)E'(a)] E(\mu, \nu) - \frac{h_\rho}{h_\mu h_\nu} \frac{\partial}{\partial \mu} \left(\frac{h_\nu}{h_\mu} f_\mu \right) I(a)E(a, \mu', \nu) \right. \\ & \quad \left. - \frac{h_\rho}{h_\mu^2} f_\mu I(a)E(a, \mu'', \nu) - \frac{h_\rho}{h_\mu h_\nu} \frac{\partial}{\partial \nu} \left(\frac{h_\mu}{h_\nu} f_\nu \right) I(a)E(a, \mu, \nu') - \frac{h_\rho}{h_\nu^2} f_\nu I(a)E(a, \mu, \nu'') \right\} \\ &= \sum_{n,p} b_n^{(p)} \left\{ -ik_1 \frac{\mu_2}{\mu_1} E(\rho', \mu, \nu) \Big|_{\rho=a} + \frac{h_\rho}{h_\mu h_\nu} \frac{\partial}{\partial \mu} \left(\frac{h_\nu}{h_\mu} f_\mu \right) E(a, \mu', \nu) + \frac{h_\rho}{h_\mu^2} f_\mu E(a, \mu'', \nu) \right. \\ & \quad \left. + \frac{h_\rho}{h_\mu h_\nu} \frac{\partial}{\partial \nu} \left(\frac{h_\mu}{h_\nu} f_\nu \right) E(a, \mu, \nu') + \frac{h_\rho}{h_\nu^2} f_\nu E(a, \mu, \nu'') \right\} \end{aligned} \quad (4.7.7)$$

and it is understood that this expression is evaluated at the surface of the ellipsoid $\rho = a$. It should be noted that most of the terms in Eq. (4.7.7) are straightforward to compute: the derivatives and second derivatives of the Lamé functions with respect to μ and ν do not present any extreme difficulty.

4.7.b Secondary fields due to uniform incidence

The first situation we shall consider is the one of a uniform incidence. The latter is not merely a theoretical idealization since objects that are far from the GEM-3 sensor, or those that are small (in the order of a few centimeters), do not see a very inhomogeneous primary excitation. The assumption of uniform incidence in these cases is therefore excellent.

For the sake of later comparison with known solutions, we first suppose the primary field to be in the (xz) plane, although the general case can be treated just as easily. A uniform field derives from a simple linear potential in x and z , which can also be expanded in the ellipsoidal coordinate system as

$$U^o = H_0 x \sin \theta + H_0 z \cos \theta = \sum_{n,p} b_n^{(p)} E_n^{(p)}(\rho, \mu, \nu) \quad (4.7.8)$$

where $\theta = 0$ for axial excitation and $\theta = \pi/2$ for transverse excitation, and where H_0 is the amplitude of the uniform field. Realizing that x and z can be directly expressed in terms of Lamé functions of the first kind with $n = 1$ we write

$$U^o = \frac{H_0 \sin \theta}{hk} E_1^{(1)}(\rho, \mu, \nu) + \frac{H_0 \cos \theta}{k\sqrt{k^2 - h^2}} E_1^{(3)}(\rho, \mu, \nu) \quad (4.7.9)$$

so that the $b_n^{(p)}$ coefficients of Eq. (4.7.7) are directly given by

$$b_1^{(1)} = \frac{H_0 \sin \theta}{hk}, \quad b_1^{(2)} = 0, \quad b_1^{(3)} = \frac{H_0 \cos \theta}{k\sqrt{k^2 - h^2}}, \quad b_{n \neq 1}^{(p)} = 0. \quad (4.7.10)$$

The expansion of the secondary field also deserves attention before proceeding with the numerical solution of the $B_n^{(p)}$. Indeed, there exist an analytical solution to the external potential due to a homogeneous ellipsoid [129]:

$$V(x, y, z) = \kappa_0 \int_\rho^\infty \left[1 - \frac{x^2}{s^2} - \frac{y^2}{s^2 - h^2} - \frac{z^2}{s^2 - k^2} \right] \frac{ds}{\sqrt{s^2 - h^2} \sqrt{s^2 - k^2}} \quad (4.7.11)$$

where κ_0 is a constant. We see that the first term of Eq. (4.7.11) is directly proportional to K_0 (i.e. $n = 0$), while the successive three terms are directly proportional to K_1 , L_1 , and M_1 (i.e. $n = 1$), respectively. The potential of Eq. (4.7.11) can therefore be expressed with exactly, and only, four ellipsoidal term, directly related to the demagnetization factors discussed in [130, 131]. In addition, since the $n = 0$ term is discarded in our solution (the ellipsoid being uncharged), the expansion of the secondary potential is reduced to $n = 1$ only ($p = 1, 2, 3$), and $B_{n \neq 1}^{(p)} = 0$. Moreover, in the specific case of a uniform primary field in the (xz) plane, $B_1^{(2)} = 0$ and we are left with only two unknowns to determine.

We first apply our method to the computation of the secondary field produced by a series of spheroidal geometries, under axial, transverse, and oblique incidences. The main purpose here is to being able to compare the results with those obtained in our previous work [2]. The correspondence between the elongation of the spheroids and the size of the ellipsoids is given in Table 2. The axial

Spheroidal elongation	Ellipsoidal dimensions $a > b > c$ (along \hat{x} , \hat{y} , \hat{z})	Measured field	
		Fig. 4.7.2(top)	Fig. 4.7.2 (bottom)
$e = 6$	$a = 1.5$ cm, $b = c = 0.25$ cm	H_x	H_z
$e = 3$	$a = 1.5$ cm, $b = c = 0.5$ cm	H_x	H_z
$e = 1$	$a = b = c = 1.5$ cm	H_x or H_z	
$e = 1/3$	$a = b = 1.5$ cm, $c = 0.5$ cm	H_z	H_x
$e = 1/6$	$a = b = 1.5$ cm, $c = 0.25$ cm	H_z	H_x

Table 2: Correspondence between the elongations of spheroids and the size of the ellipsoids as shown in Fig. 4.7.1 and defined by Eq. (4.7.3).

and transverse cases are shown in Fig. 4.7.2 for spheroids located 10 cm below the sensor and with elongations $e \in \{6, 3, 1, 1/3, 1/6\}$ ($e > 1$ corresponding to prolate objects while $e < 1$ to oblate ones). The overall responses of the objects as function of frequency follow the now well-understood trend: at low frequencies the secondary magnetic field is aligned with the exciting field while at high frequencies, the induced currents are confined to the surface of the ellipsoid and are out of phase by π due to Lenz' law. The imaginary part of the field therefore vanishes at both ends of the frequency spectrum and peaks at an intermediate frequency corresponding to the resonance of the object.

In the axial case, the magnetic field sees more object surface with prolate geometries, producing a stronger response than oblate geometries, while this tendency is reversed under transverse excitation for the same reason. The position of the peak in the imaginary part is directly related to the resonance of the object, also closely related to the size of the object along the direction of the primary field. In the transverse case, elongations of $e \in \{1/6, 1/3, 1\}$ present the same size along the primary field and therefore, a similar location of the resonant peak. Prolate objects, on the other hand, have a varying size along this direction and thus, different resonant peaks. Similar arguments can be applied to explain the results obtained under the axial excitation.

The first conclusion when examining Fig. 4.7.2 is that the agreement over the entire frequency range is reasonably good in most of the cases, thus proving that the SPA is an adequate approximation for highly magnetic and conductive objects, as already shown in [113]. The prolate cases are seen to usually agree better with the reference markers [2], and even more so under the transverse excitation. The worst agreement is obtained for oblate geometries under transverse excitation, with

increased disagreement as the objects flatten, in agreement with the conclusions reported in [125]. Although not shown for the sake of clarity, simulations have been extended up to extreme elongations of 10 and 1/10 and confirm these findings. A possible explanation is that under these circumstances, a very large portion of the object surface has a very high radius of curvature so that a dominant radial decay approximation of the currents may become less accurate.

Fig. 4.7.3 presents the results for a configuration similar to the one corresponding to Fig. 4.7.2 but where the object is rotated at 45 degrees. Similar conclusions to the previous case can be drawn: prolate spheroids are well modeled whereas oblate ones present the highest mismatch, the latter being more pronounced for more extreme geometries. The disagreement for $e \in \{1/3, 1/6\}$ is here seen to be more evident at low frequencies, while at high frequencies (where the SPA is more and more valid) the agreement is usually reasonably good.

Finally, Fig. 4.7.4 shows the secondary field produced by a real ellipsoid of dimensions 1 cm \times 2 cm \times 3 cm along the \hat{x} , \hat{y} , and \hat{z} directions, respectively, under an axial excitation. The depth and material parameters are otherwise identical to the previous cases. The reference solution is obtained from the method of auxiliary sources (MAS) presented in [132],[3], and has been truncated at 1 MHz because of the fine mesh and long computation time required at higher frequencies. At low frequencies, however, the MAS is very accurate and shows that our method suffers from some errors which we attribute to the choice of the location of the matching points. Nonetheless, the difference between the secondary field produced by an object of dimensions 1 cm \times 2 cm \times 3 cm (the present ellipsoid) and 1 cm \times 1 cm \times 3 cm (a spheroid of elongation $e = 3$) is quite significant and allows us to conclude that away from the lowest frequencies, the agreement between the two methods is reasonably good.

4.7.c Secondary fields due to GEM-3 incidence

Although the assumption of uniform primary field is sufficient in many cases, it is still beneficial to model the primary field generated in real field measurements, typically as obtained from the GEM-3 instrument. The GEM-3 is a broadband electromagnetic sensor manufactured by Geophex [1], whose transmitting sensor head consists of two current loops of radii of 20 cm and 11.074 cm. These two current loops are arranged as bucking coils with the smaller loop placed concentrically in the interior of the larger loop (schematically illustrated in Fig. 4.7.1). The two currents are optimized so that the primary magnetic field at the center of the instrument is minimal and the measurements closely correspond to the secondary field \bar{H}^s .

The analytical expression of the axial and transverse magnetic field components produced by a circular current loop in a cylindrical coordinate system, based on the complete elliptical integrals of the first and second kind, can be found in [74, 75, 133] and reads:

$$B_r(r, \phi, z) = \frac{\mu_0 I_o}{2\pi} \frac{(z - z_0)}{r[(r + r_0)^2 + (z - z_0)^2]^{1/2}} \cdot \left[-K(k_c) + \frac{r^2 + r_0^2 + (z - z_0)^2}{(r - r_0)^2 + (z - z_0)^2} E(k_c) \right] \quad (4.7.12a)$$

$$B_z(r, \phi, z) = \frac{\mu_0 I_o}{2\pi[(r + r_0)^2 + (z - z_0)^2]^{1/2}} \cdot \left[K(k_c) - \frac{r^2 - r_0^2 + (z - z_0)^2}{(r - r_0)^2 + (z - z_0)^2} E(k_c) \right], \quad (4.7.12b)$$

where r_0 is the radius of the current loop located in the $z = z_0$ plane, I_o is the current flowing in the $\hat{\phi}$ direction, and

$$k_c = \sqrt{\frac{4ar}{(r + a)^2 + (z - z_0)^2}}. \quad (4.7.13)$$

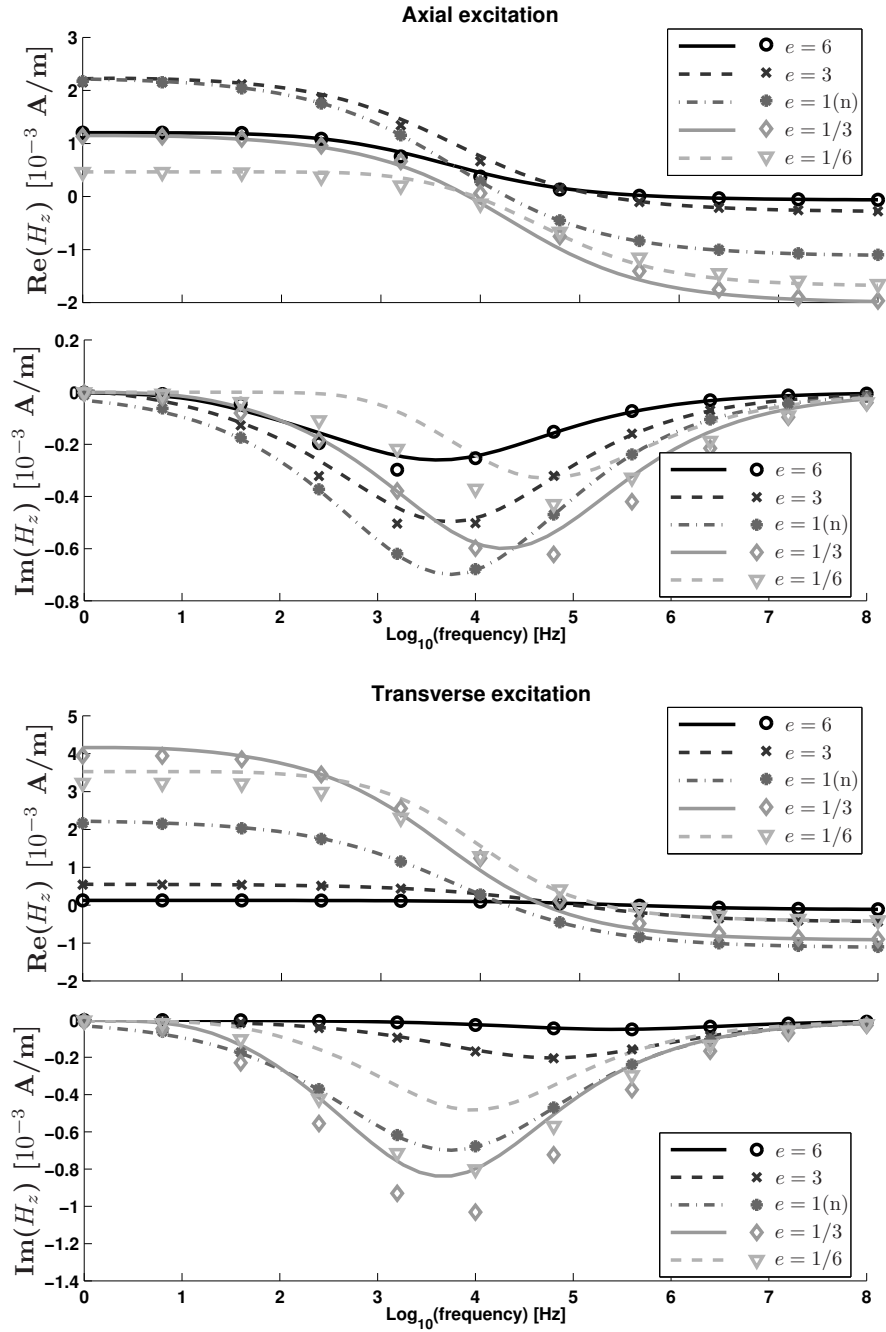


Figure 4.7.2: Real and imaginary parts of the secondary field \bar{H}^s produced by spheroids of elongations shown in the legend, buried 10 cm below the sensor, and under axial (upper panels) and transverse (lower panels) excitations. The material parameters are $\mu_1 = 100\mu_0$ and $\sigma_1 = 10^7$ [S/m]. The sphere case (denoted by 'e=1 (n)') has been normalized by 1/3 for display convenience. The markers are obtained from the method presented in [2].

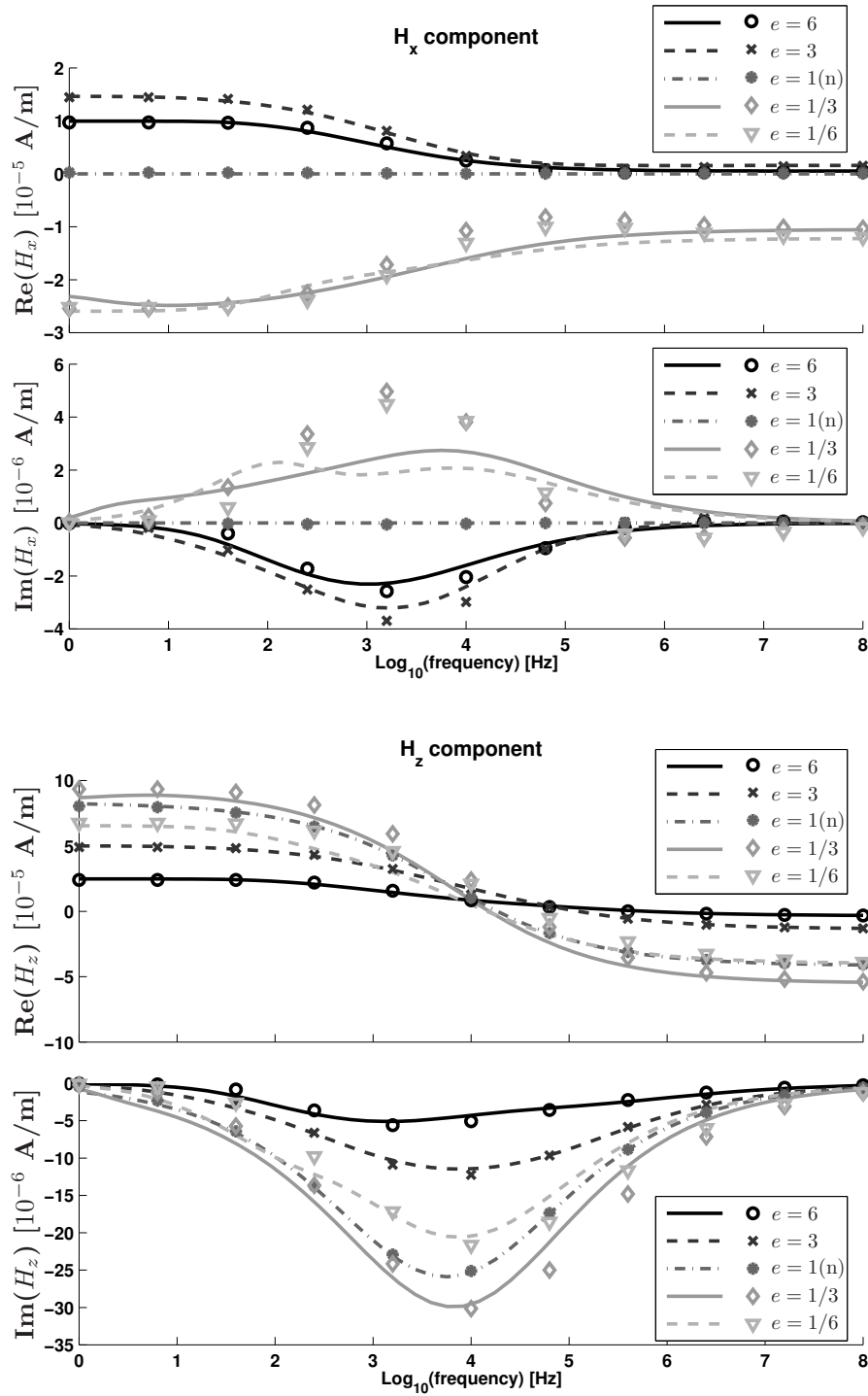


Figure 4.7.3: Similar to Fig. 4.7.2 for an object buried at 30 cm and rotated by 45 degrees. Upper panel: H_x . Lower panel: H_z . Note that for this specific case only, the ranges have been set to $v \in [0, 0.7]h$ for prolate spheroids and $\mu \in [0, 0.7](k - h) + h$ for oblate spheroids.

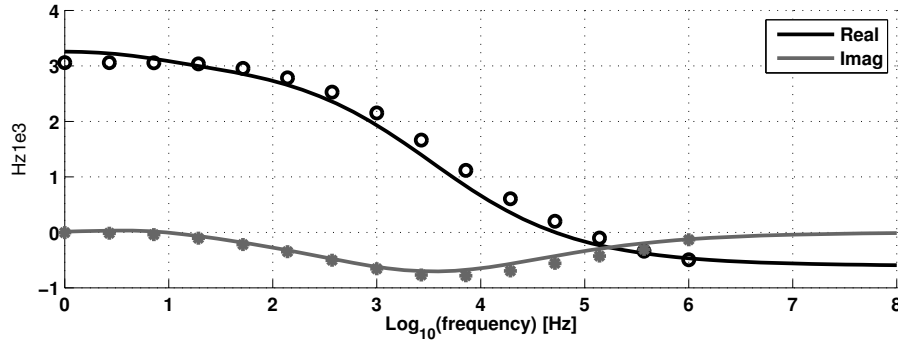


Figure 4.7.4: Real and imaginary parts of the secondary field produced by an ellipsoid of dimensions 1 cm in \hat{x} , 2 cm in \hat{y} , and 3 cm in \hat{z} . The material parameters are $\mu_1 = 100\mu_0$ and $\sigma_1 = 10^7$ [S/m], and the ellipsoid is buried 10 cm below the sensor. The reference markers have been obtained using the method of auxiliary sources [3].

K and E are the complete elliptical integral functions of the first and second kind, respectively. Note that this model agrees with the alternative methods of using a numerical integration or the application of the Biot-Savart's Law, and has the added benefit of being computationally less expensive.

The first step in modeling a GEM-3 incidence is to determine the expansion coefficients $b_n^{(p)}$ of the primary field in Eq. (4.7.6), simply done using a point matching technique. Hence an ellipsoid is first defined in space, yielding a series of (x, y, z) components. At those locations, the magnetic field is computed from Eq. (4.7.12), and the field components are transformed into (H_ρ, H_μ, H_ν) . Eq. (4.7.6) is then used across many points to compute the matrix of an over-determined system, from which the $b_n^{(p)}$ are solved for in the least square sense. In doing so, we find that the coefficients are more stable when the matching is done on H_ν for prolate-type objects and on H_μ for oblate-type objects. The matching using H_ρ , reasonably good in both cases, can also be used for the purpose of comparison.

Due to the non-uniform nature of the primary field, terms of higher degrees than $n = 1$ need to be included in the ellipsoidal expansion and therefore, all the $B_n^{(p)}$ coefficients need to be solved for simultaneously. The lack of direct orthogonality between the various terms of Eq. (4.7.7) results in a somehow unstable numerical solution: the influence of some modes (n, p) can leak into other modes and degrade the accuracy of the corresponding $B_n^{(p)}$. This is typically the case when some $B_n^{(p)}$ are very small, and need to be solved as zero numerically: although the results are numerically small as expected, the non-zero $B_n^{(p)}$ can be slightly modified, introducing errors in the secondary field values. In the previous examples, this phenomenon has been bypassed by using a physical argument to force some coefficients to zero and to solve for the non-zero ones only. In the non-uniform incidence case, however, such reasoning cannot in general be applied and all the $B_n^{(p)}$ need to be solved for simultaneously.

In order to minimize the numerical leakage problem, we resort to solving for the $B_n^{(p)}$ in two steps. First we solve for all the $B_n^{(p)}$ in a usual manner. Second, the $B_n^{(p)}$ are used to compute the field at the sensor location. The contribution of each mode is compared and those modes

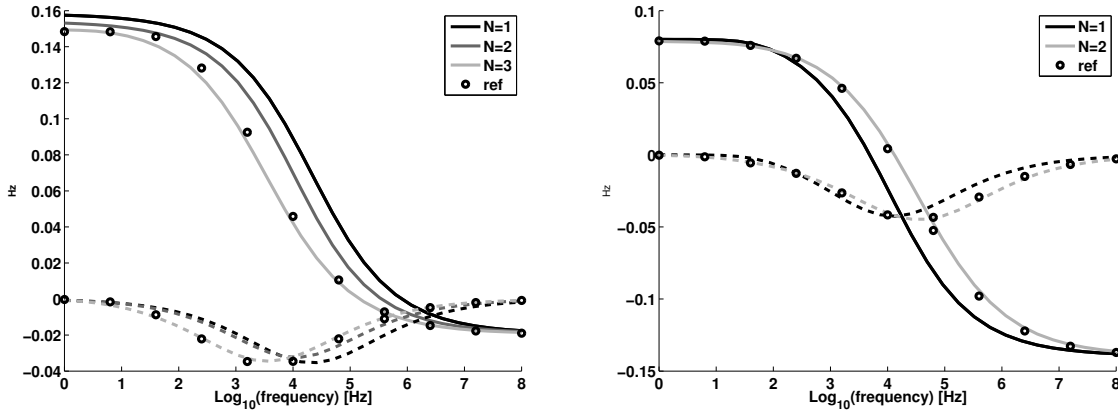


Figure 4.7.5: Real and imaginary parts of the secondary field produced by a spheroid of elongation $e = 3$ (left panel) and $e = 1/3$ (right panel) buried 10 cm below the GEM-3 instrument. The material parameters are $\mu_1 = 100\mu_0$ and $\sigma_1 = 10^7$ [S/m]. The primary field is modeled using Eqs. (4.7.12). The reference markers (marked ‘ref’ in the legend) are obtained from the method presented in [2].

contributing less than a threshold (1/1000 of the maximum contribution in our case) are discarded. The $B_n^{(p)}$ are then solved anew only for the contributing modes. Note that this selection works best if it is performed at the first frequency, and kept identical for subsequent frequencies.

The results for a GEM-3 axial excitation of a prolate ($e = 3$) and an oblate ($e = 1/3$) spheroid are shown in Fig. 4.7.5. The necessity of including more modes in the ellipsoidal expansion is apparent, although the number of modes is still significantly lower than under a spheroidal coordinate approach. The agreement obtained here with up to $n = 3$ for the prolate case and up to $n = 2$ for the oblate case is seen to be good. The transverse excitation exhibits a similar good agreement and is not shown for the sake of brevity.

Finally, measurement data are taken as a last validating element of our analytical approach. Measurements were performed using the GEM-3 instrument along the three axes of a steel ellipsoid of size $15\text{ cm} \times 7.5\text{ cm} \times 3.75\text{ cm}$ in the \hat{x} , \hat{y} , and \hat{z} directions, respectively (yielding an aspect ratio of 1:2:4). The magnetic permeability and electric conductivity of the steel are a priori unknown and can be optimized for when matching the experimental data to the theoretical ones.

The comparisons between measurements and analytical results are illustrated in Fig. 4.7.6 for the data collected along the three axes. The caption provides information on the scaling factors γ optimized when matching the data as well as on the values of the permeability and the conductivity for each case. It can be seen that overall, the numerical approach is very successful at predicting the EMI response of the ellipsoidal object across the entire frequency range. This good agreement represents an important validation of the method presented in this paper.

A more specific examination of the results reveals both good and less good aspects, however. First, the scaling factor, which converts the units of GEM-3 measurements into [A/m], is relatively constant in the three independent optimizations results and yields $\gamma \simeq 4.5 \times 10^3$. Along with the overall good agreement in the magnetic field, this is an important result which confirms the accuracy of our measurement technique. Second, the first and second cases in Fig. 4.7.6 produce very similar results for the permeability and the conductivity, which is another important positive result. The numerical values confirm the expectation that steel is a highly permeable and conduc-

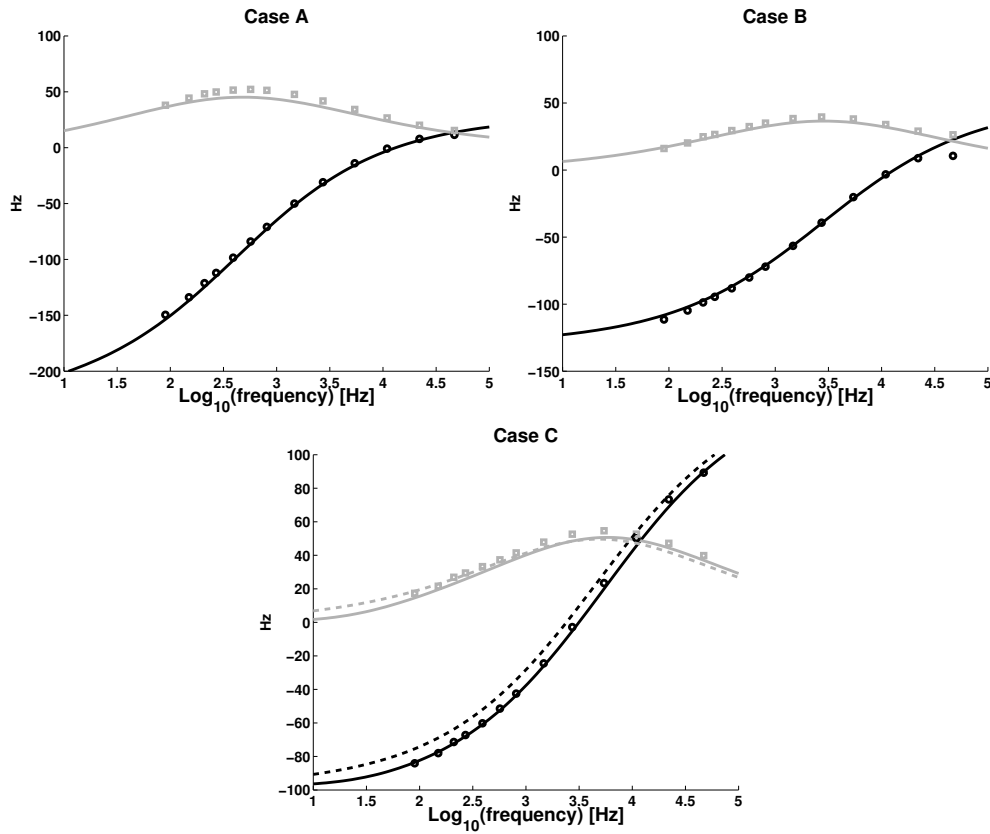


Figure 4.7.6: Simulated (solid lines) and experimentally measured (circles) real and imaginary parts of the magnetic field along the three axes of an ellipsoid: case A is along the longest dimension (15 cm), case B is along the second longest dimension (7.5 cm), case C is along the shortest dimension (3.75 cm). The location of the resonant frequency in the three cases follow this geometrical progression, as expected. The optimized parameters in the respective cases are: ($\mu_1 = 140\mu_0$, $\sigma_1 = 4.5 \times 10^6$ [S/m], $\gamma = 4.7 \times 10^3$) ($\mu_1 = 150\mu_0$, $\sigma_1 = 5 \times 10^6$ [S/m], $\gamma = 4.5 \times 10^3$) ($\mu_1 = 20\mu_0$, $\sigma_1 = 1.2 \times 10^6$ [S/m], $\gamma = 4.2 \times 10^3$). The dashed line in case C has been obtained with ($\mu_1 = 100\mu_0$, $\sigma_1 = 1 \times 10^7$ [S/m], $\gamma = 4.2 \times 10^3$). The numerical data have been obtained with tree modes in all cases ($N = 3$).

tive material, which is a necessary condition for our SPA approximation to be trustable across the entire frequency range. More importantly, these results show that we are able, to some extent, to infer the material properties of an object in a totally remote and non-invasive way. Third, it is seen that the last situation in Fig. 4.7.6 stands out from the other two, with different estimates of the permeability and of the conductivity. We believe that this case is tantamount to cases of very flattened oblate spheroids studied previously ($e = 1/6$), where the currents flowing around the object see a very large radius of curvature at all points around the circumference, producing less accurate results within an SPA approximation. Moreover, the cost-function associated with this third situation presents many local minima so that the optimized values $\mu_1 = 20\mu_0$ and $\sigma_1 = 1.2 \times 10^6$ [S/m] have to be understood as being one possible solution. In fact, the dashed lines correspond to the values of the magnetic field obtained with $\mu_1 = 100\mu_0$ and $\sigma_1 = 1 \times 10^7$ [S/m] (the initial guess in the optimization procedure), and yield a reasonably good match with the measured data as well. Consequently, we can consider this last case as less reliable than the other two, but yet constitutes an important situation to consider in future work.

4.7.d Conclusion

The motivation of modeling clutter surrounding unexploded ordnances (UXOs) as three-dimensional steel objects in the electromagnetic induction regime has prompted the study of the ellipsoidal coordinate system presented in this paper. The hybrid approach, combining a static formulation based on the Laplace equation in the region exterior to the object and a full-wave approach based on the wave equation in the region interior to the object, has been formulated based on the Lamé functions and the small penetration approximation (SPA). The latter, originally derived as a high frequency approximation, is shown to be valid across the entire frequency spectrum of the GEM-3 instrument for highly permeable and highly conductive objects, in agreement with previous conclusions. Importantly, the SPA bypasses the necessity of using ellipsoidal wave functions inside the object and results in a considerable reduction of computational time, yielding an algorithm that produces broadband secondary magnetic field responses in seconds under uniform excitation, and in tens of seconds under GEM-3 incidences.

Numerical results have been favorably compared with three independent results: those obtained with a well-established method for the study of spheroidal geometries (treated here as a special case of an ellipsoidal geometry), those obtained with the method of auxiliary sources for metallic objects (where the ellipsoidal geometry is a particular case of a general three-dimensional shape), and those obtained by GEM-3 measurements of a manufactured ellipsoid. The good agreement of all these results prompts us to conclude that the method presented in this paper is both fast and accurate, and can therefore be used in subsequent inversion algorithms for the classification of buried UXOs in clutter contaminated soils as well as for the estimation of material parameters in a non-invasive way.

5 Results and Discussion – GEM-3 \mathcal{D}^+

The GEM-3 \mathcal{D}^+ can be used in several different measurement modes, namely, dynamic mode, static mode, and hybrid mode. These correspond to what type of information the user wants to know. Dynamic mode may be used mostly for the detection of metallic objects, while static mode could give higher fidelity lower noise data for discrimination. The hybrid mode, which allows for measurements taken while the sensor head is in motion, and relies on post processing to extract individual data points, may turn out to be the most commonly used mode.

In static mode, the GEM-3 \mathcal{D}^+ would be placed on a certain location and held immobile while one data shot is taken. Because the sensor is not moving, the data may be integrated for a very accurate low noise data point. Several of these in a rough grid would aid inversion efforts toward discrimination. The main drawback to this mode is that the data acquisition sequence would require a longer time than data acquired in a dynamic or hybrid mode.

Acquiring data in the the dynamic mode would allow the user to hold and rotate the sensor head on the handle much more freely without having to pause between the data shots. At a 10 Hz measurement rate, substantial amounts of data could be acquired in a short period of time. One concern when acquiring data in dynamic mode is the effects of sensor head movement on data quality. Another concern would be data stability of each 10 Hz measurement without integrating to reduce noise. If the sensor head is not moved too quickly, movement issues can be kept to a minimum. Furthermore, when a post processing step is added (resulting in measuring in the hybrid mode) data acquired while the sensor head was moving too rapidly could be flagged and or discarded. To address stability concerns of the 10 Hz measurements, we plotted the standard deviation of a few seconds of data acquired while the instrument was not moving (see Fig. 5.1.11). The GEM-3 \mathcal{D}^+ has exceptional stability over short time periods even at the 10 Hz measurement rate and especially in the mid frequency band. Note that we normally only regard signals greater than 100 ppm as significant. During post processing, measurements taken sufficiently close together (for example, when the instrument was held immobile during dynamic acquisition mode) could be averaged together leading to higher quality, higher SNR data. All of these data collection modes rely explicitly on a very accurate positioning system such as the beacon system described above

5.1 Initial Data and Reasonableness Checks

We have taken some initial data shots of a spherical object. The main purpose of this initial data set was for a reasonableness check. That is, do the separate components of the received secondary field have the right sign, reasonable amplitude, range, etc. Figure 5.1.1 shows the path of a sphere as it is moved along a line below the sensor head and is offset in the positive y direction. Figure 5.1.2 shows the result if of extracting the quadrature data recorded at 450Hz and plot it as the sphere is moved along this path. Reasonableness checks on this data include

- H_y is always negative
- H_x starts negative then switches to positive
- H_z is always positive
- $|H_y| > |H_x|$ due to the proximity of the sphere to the $x - y$ plane
- results are symmetrical around the yz plane

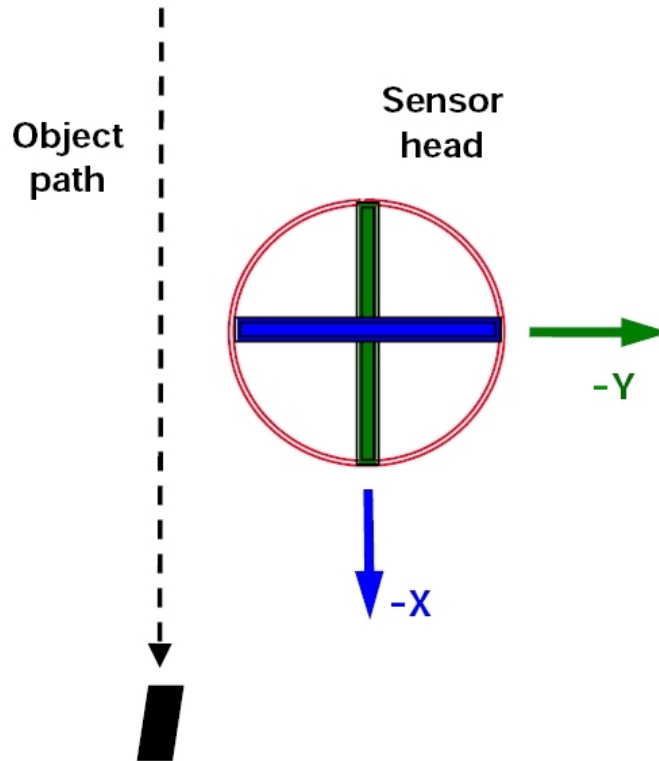


Figure 5.1.1: Initial reasonableness check of the GEM-3 \mathcal{D}^+ . Object is moved along a path below and offset to the GEM-3 \mathcal{D}^+ .

Figures 5.1.3 and 5.1.4 show shots from along a line crossing the center of the 3 GEM-3 \mathcal{D}^+ Rx coils, on a 45° angle relative to the Hx and Hy coils. Spectra are shown for three positions: the one (10 cm) before crossing the origin ("pre"), over the center, and after ("post") crossing the origin. Symmetry & appropriate pattern (magnitude) similar to those noted above are evident.

Figures 5.1.5 and 5.1.6 show the components from Rx coils 1 & 2 (horizontal: Hx and Hy). Values are pretty small, not far above the noise/background variation floor (the sphere was quite small). The responses pass both quantitative and quantitative reasonableness checks based on the amplitudes and signs of the 3 components.

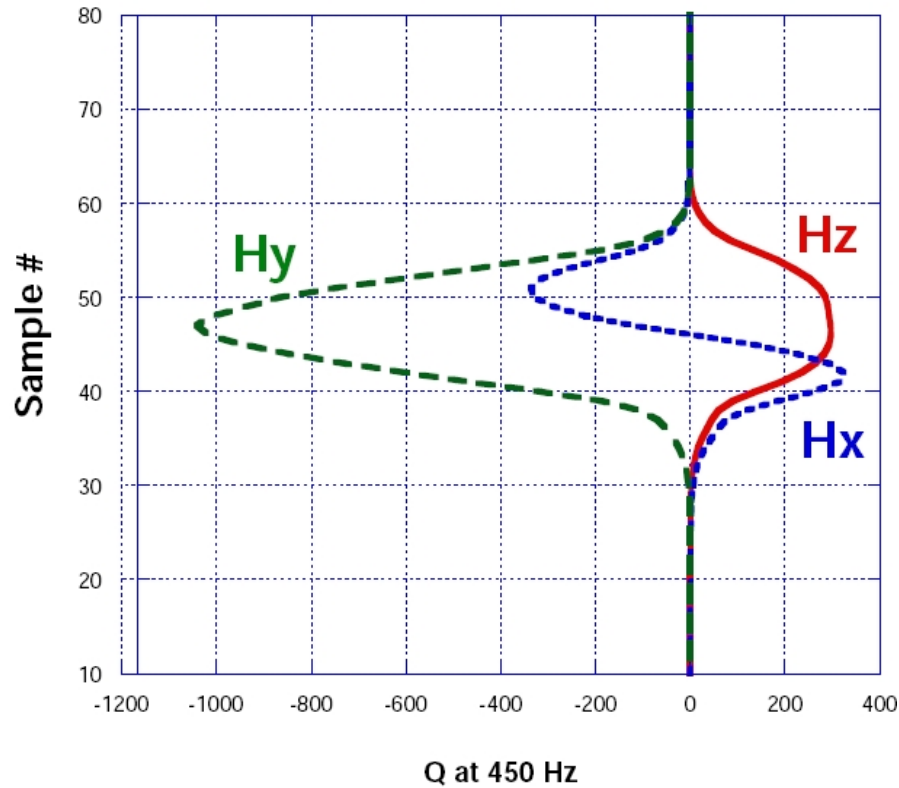


Figure 5.1.2: Initial reasonableness check of the GEM-3 \mathcal{D}^+ . Quadrature response at 450Hz.

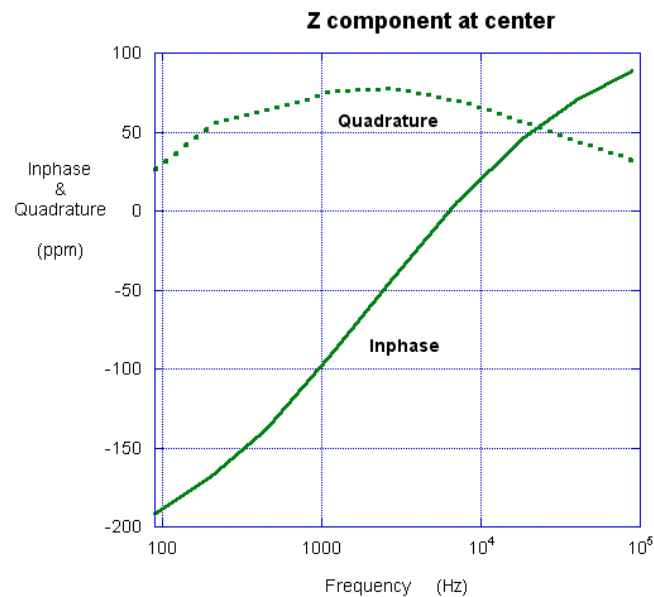
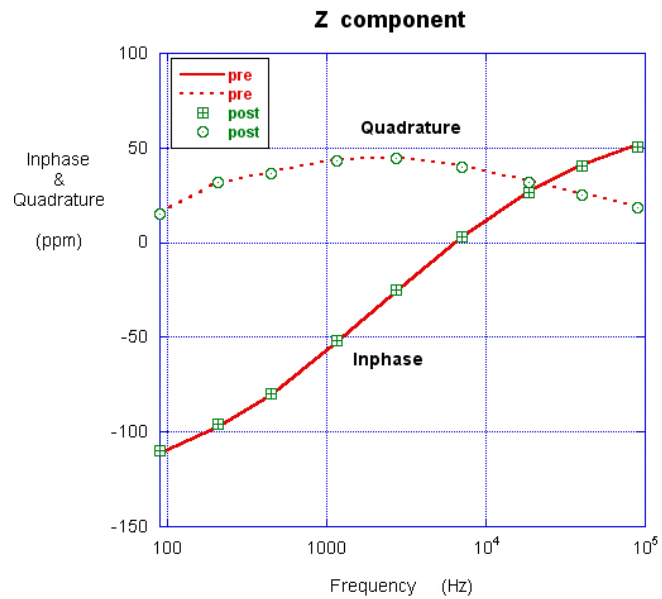
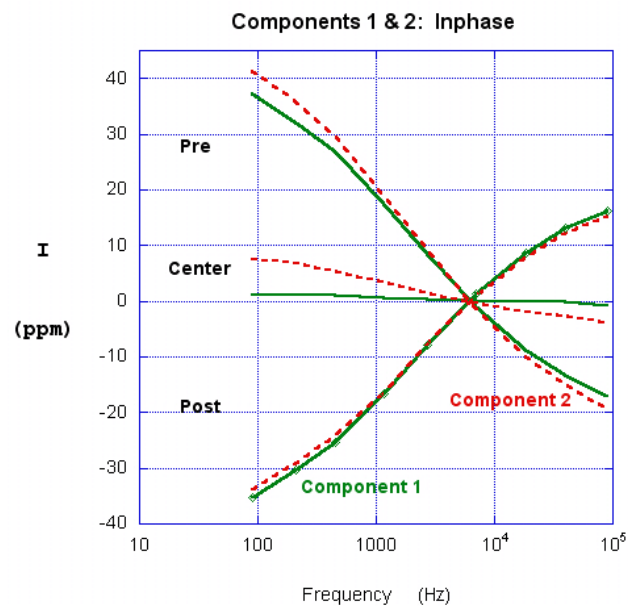


Figure 5.1.3: GEM-3 \mathcal{D}^+ Z component of received field with sphere directly over the center of the instrument.

Figure 5.1.4: GEM-3 \mathcal{D}^+ Z component of received field with sphere to the sides of the instrument.Figure 5.1.5: GEM-3 \mathcal{D}^+ X and Y component of received field at 3 positions. Inphase.

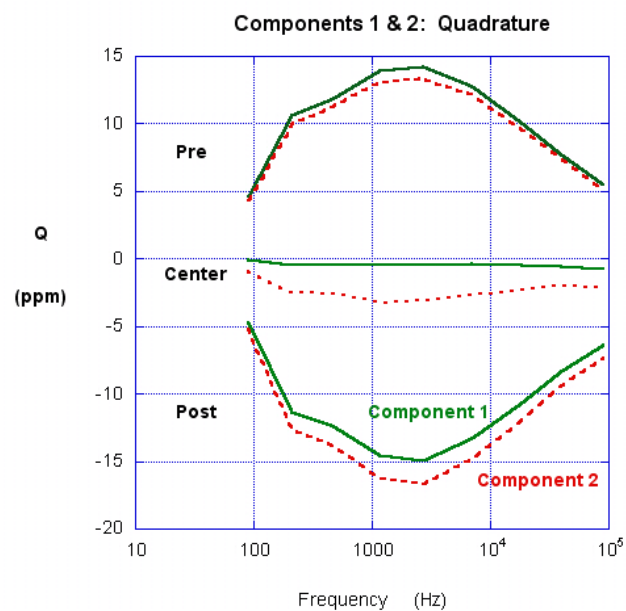


Figure 5.1.6: GEM-3 \mathcal{D}^+ X and Y component of received field at 3 positions. Quadrature.

We also acquired data over 3in spheres of brass, aluminum, and steel in a 9x9 grid. Figures 5.1.7 and 5.1.8 show data from different transects of the received field for the H_z and H_x components respectively for the steel sphere. These data traces should be on top of each other if the sphere was exactly aligned. Since the data are slightly off but in a consistent direction, we conclude that we are in fact seeing the results of a slight misalignment from center.

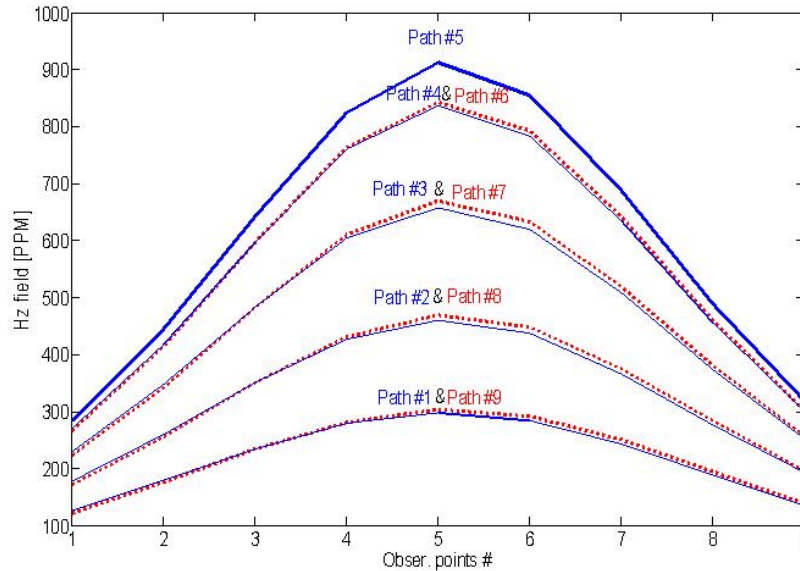


Figure 5.1.7: H_z component of data from different transects of the received field over a 9x9 grid.

Figures 5.1.9 and 5.1.10 show the H_z and the H_x , H_y components of the received magnetic field respectively over a steel sphere located southeast of the sensor. As expected the transverse components of the received magnetic field are negatives of each other. Also, all three components of the received magnetic field are available across the entire band from 30 Hz 100 kHz.

Figure 5.1.11 shows the standard deviation of the measured \overline{H} from the GEM-3 \mathcal{D}^+ combining 10 seconds of 10Hz data. The values are seen to be quite stable over the short time periods of collecting one data show. The GEM-3 \mathcal{D}^+ does exhibit some slight drift during the warm up phase (≈ 15 minutes) especially, similar to other GEM's.

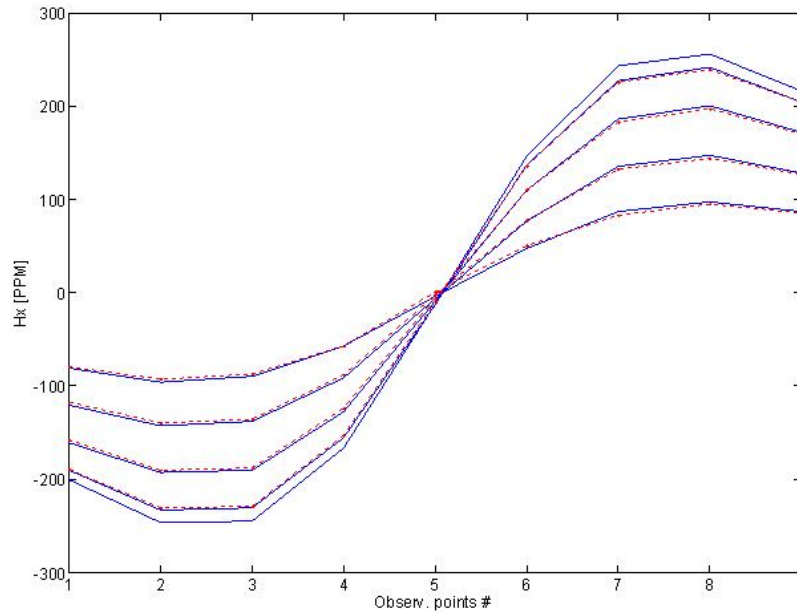


Figure 5.1.8: H_x component of data from different transects of the received field over a 9x9 grid.

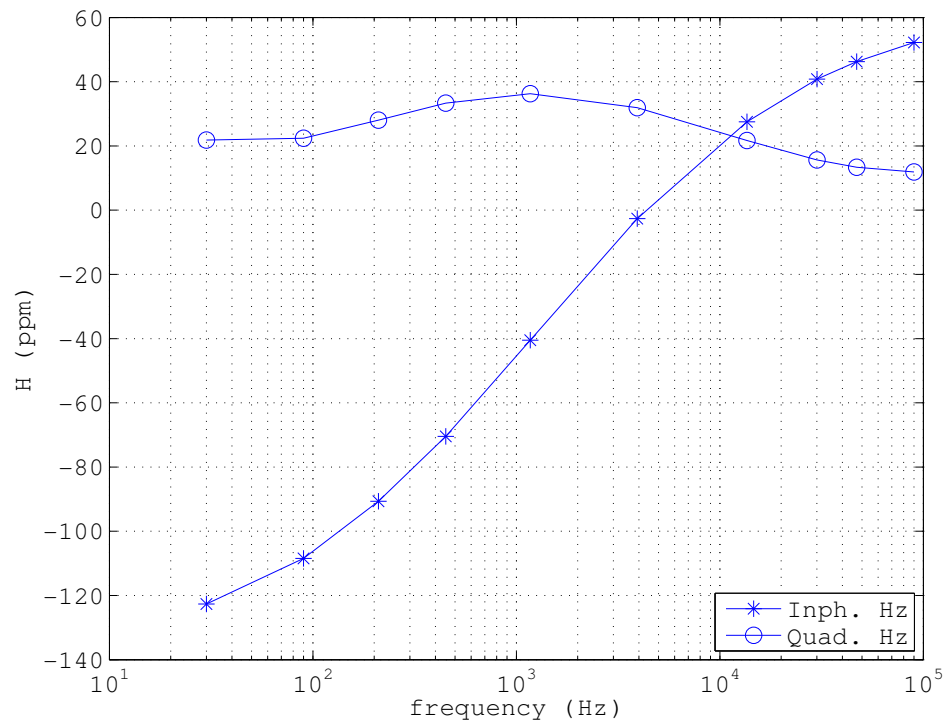


Figure 5.1.9: H_z component of the received magnetic field over a steel sphere located the southeast of the sensor.

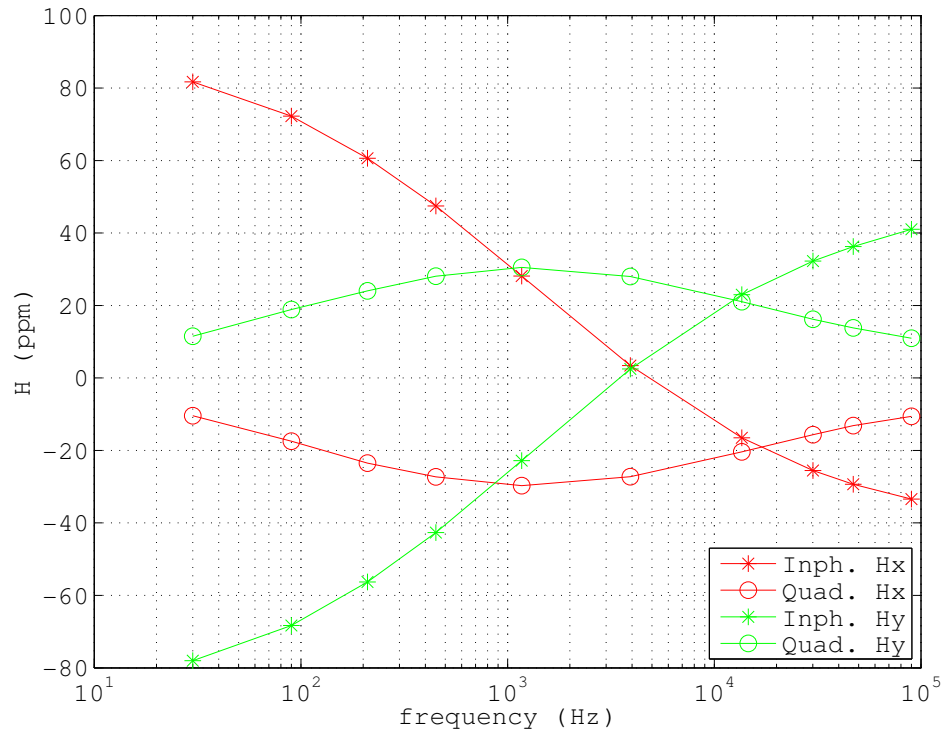


Figure 5.1.10: H_x , H_y components of the received magnetic field over a steel sphere located the southeast of the sensor.

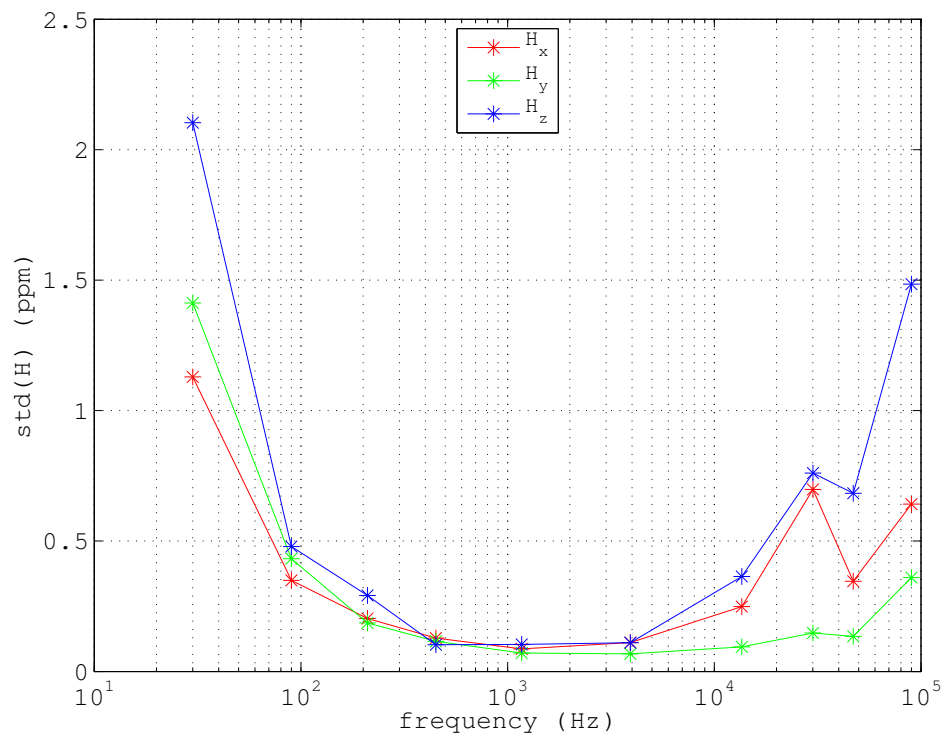


Figure 5.1.11: Standard deviation of the raw 10Hz data of the 3 field components of the received magnetic field.

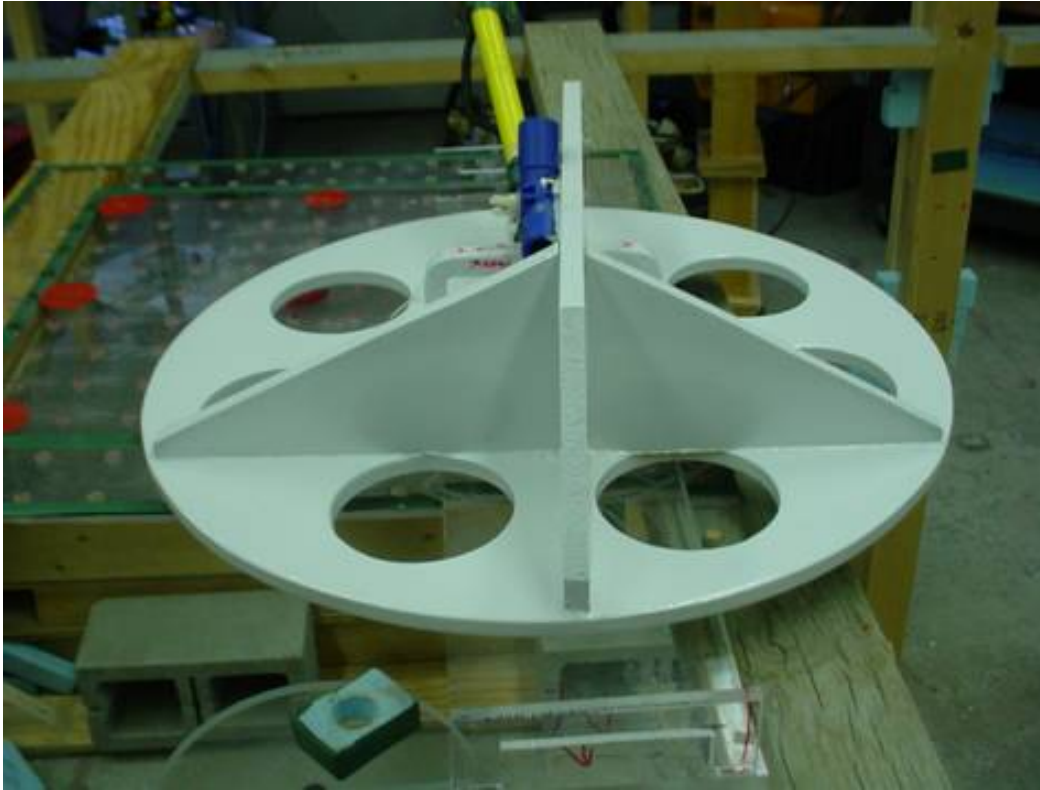


Figure 5.2.1: GEM-3 \mathcal{D}^+ on the lab grid for blind test suite #1.

5.2 Blind Test Suite #1 Training Data

Blind tests were performed for the GEM-3 \mathcal{D}^+ in that laboratory data was acquired at CRREL and handed to our colleague Fridon Shubitidze at Dartmouth College. There are two stages to blind testing with the NSMS or SEA models. The first stage involves acquiring characterization data of a target in order to set up a library of responses from possible targets in the test. The second stage is inverting for position, orientation, and which target is in each test. These were single target tests.

The characterization phase for this round of blind tests was complete in April, 2008. Data was taken on a 3x3 (20cm spacing, blue dots in Fig. 5.2.2 for background data) or a 9x9 (5cm spacing) grid at multiple elevations and orientations of each library target. Figure 5.2.1 shows the GEM-3 \mathcal{D}^+ on the lab measurement grid, and Fig. 5.2.2 shows the grid numbering system used for this data. Figure 5.2.3 shows a 60mm mortar in the 3 test configurations used to acquire characterization data. Generally, the three 9x9 measurement grids were taken at:

- horizontal, nose north (or +y), abbrev HNN.
- nose north 45degrees down from horizontal, abbrev NND
- nose north 45degrees up from horizontal, abbrev NNU

Depth measurements are to the nearest point with the center of the target centered at (0,0), and background grids of 3x3 were acquired in between, before, and after each 9x9 measurement grid. The suite of targets we acquired characterization data for this test are pictured in Fig. 5.2.4.

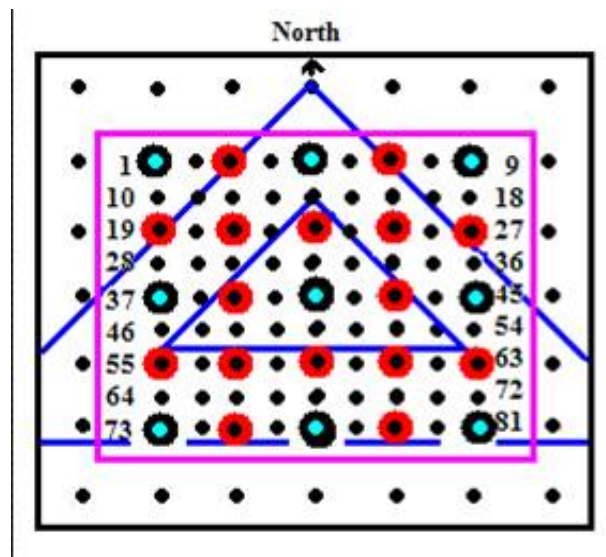


Figure 5.2.2: Grid layout used for blind test suite #1.



Figure 5.2.3: 60mm mortar in measurement setup for blind test suite #1.



Figure 5.2.4: Possible targets in library for test suite #1.

5.3 Blind Test Suite #1 Results

A library was constructed based upon the lab characterization data described above. The the HAP method and the NSMS model (see Sec. 4.6) were applied to subsequent blind test data (also on a 9x9 grid). The total normalized magnetic charge, Q for each blind test target was compared to the library Q and ranked according to best match. Figures 5.3.1–5.3.8 show Q for the blind test data compared to that of the best match from the library. In summary, Fig. 5.3.9 shows the geometry and tabulates the results from this blind test. All 8 targets were identified successfully with positions and orientations very close to the actual. This blind test is encouraging in that it suggests the NSMS model, combined with the HAP method for fast target pinpointing, is very effective at correctly discriminating between targets with vector data such as that provided by the GEM-3 \mathcal{D}^+ .

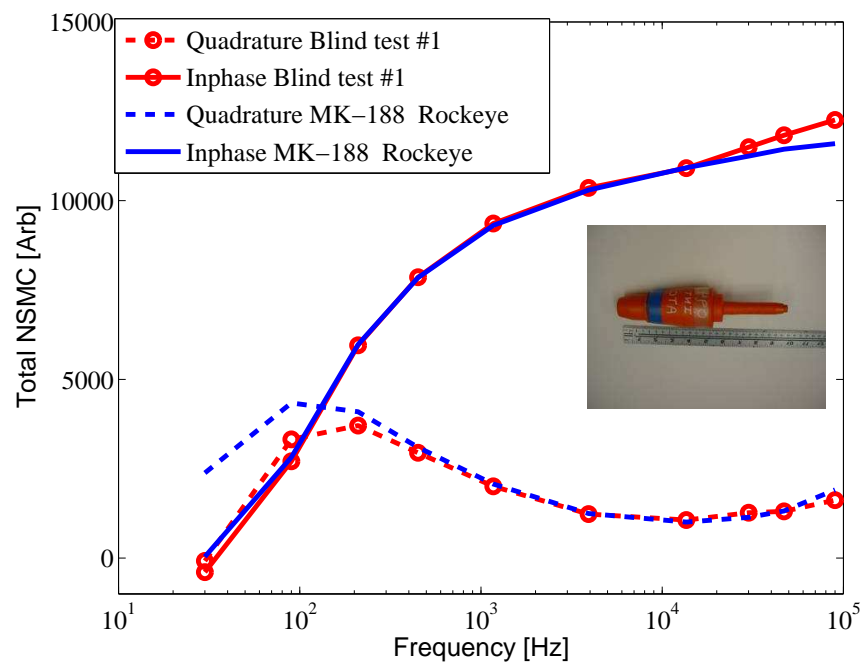


Figure 5.3.1: Total NSMS of blind test 1.

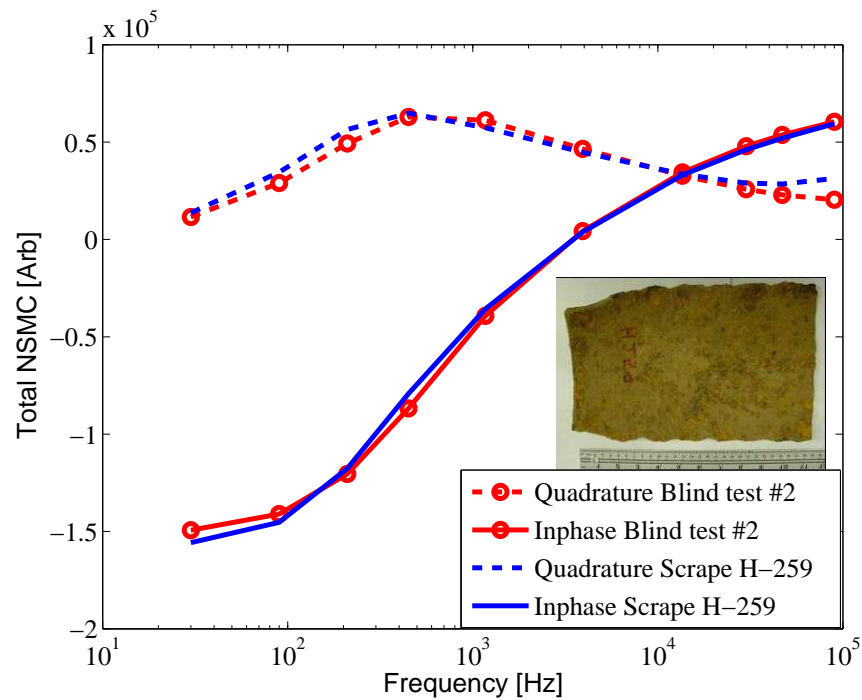


Figure 5.3.2: Total NSMS of blind test 2.

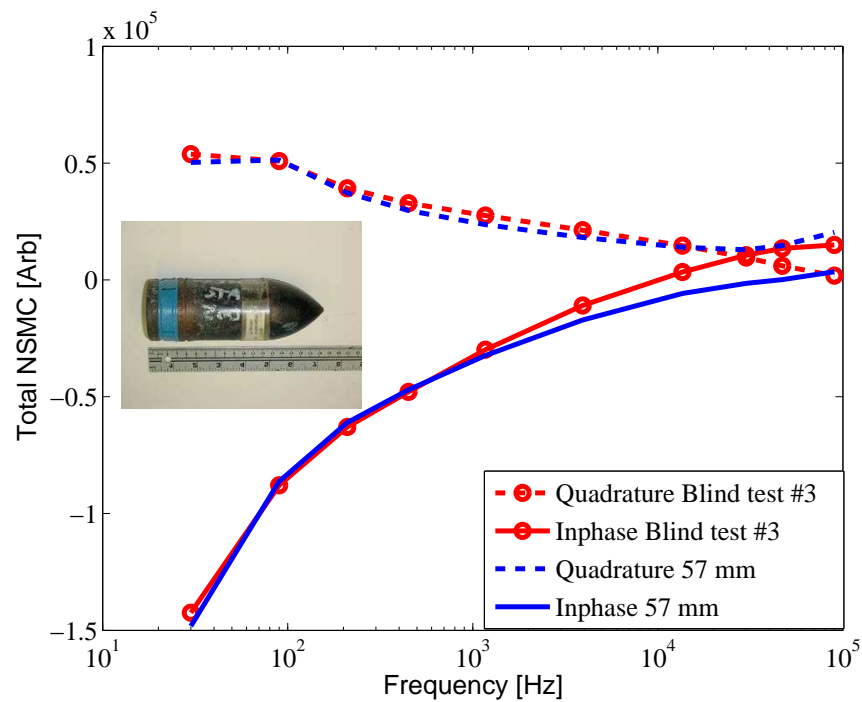


Figure 5.3.3: Total NSMS of blind test 3.

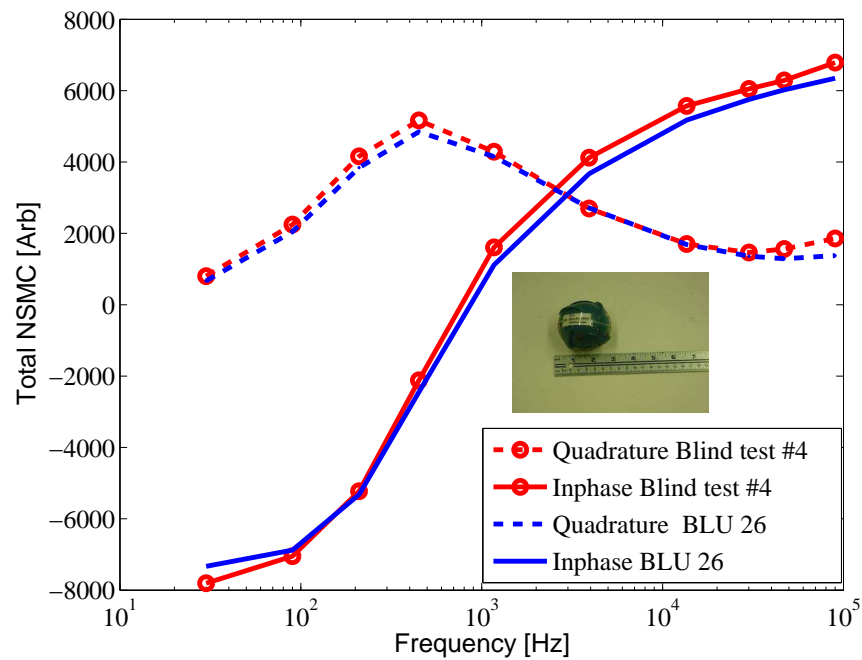


Figure 5.3.4: Total NSMS of blind test 4.

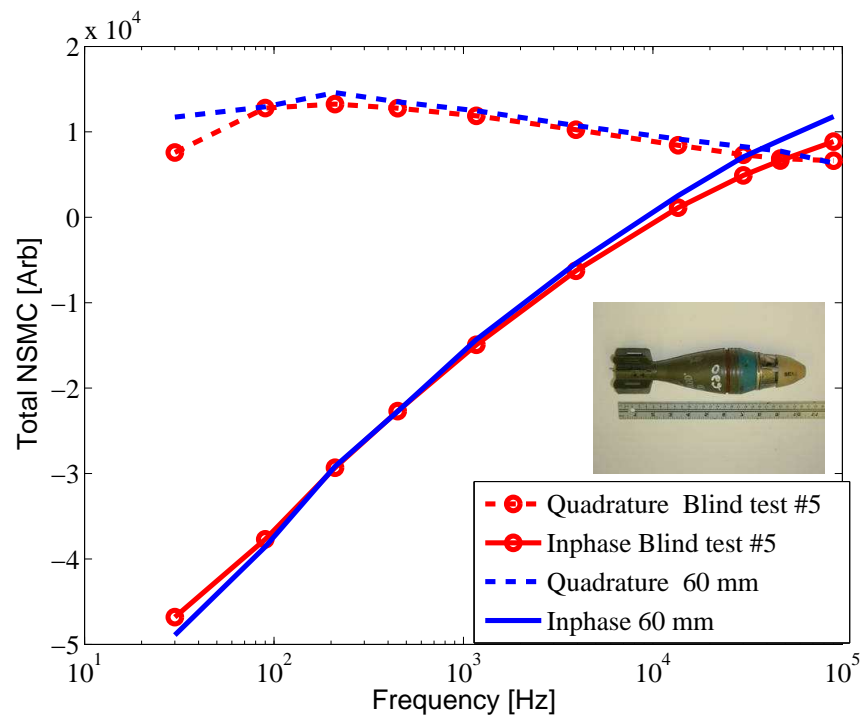


Figure 5.3.5: Total NSMS of blind test 5.

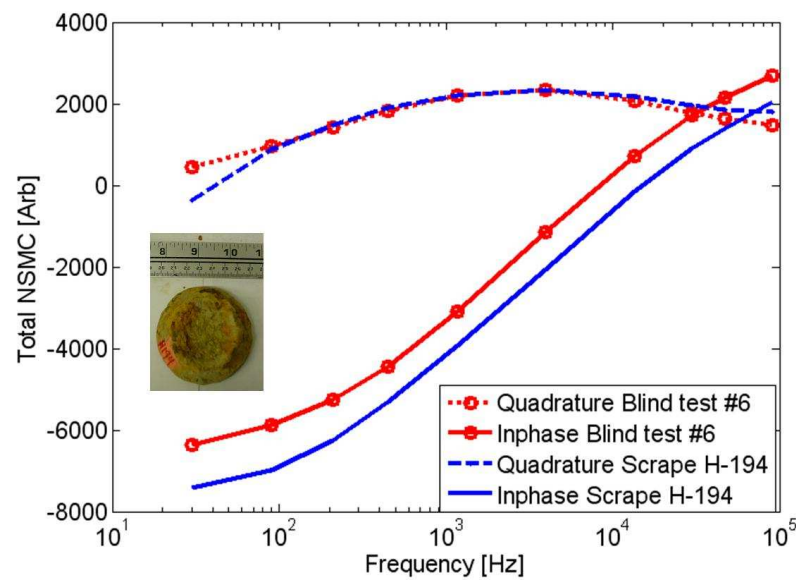


Figure 5.3.6: Total NSMS of blind test 6.

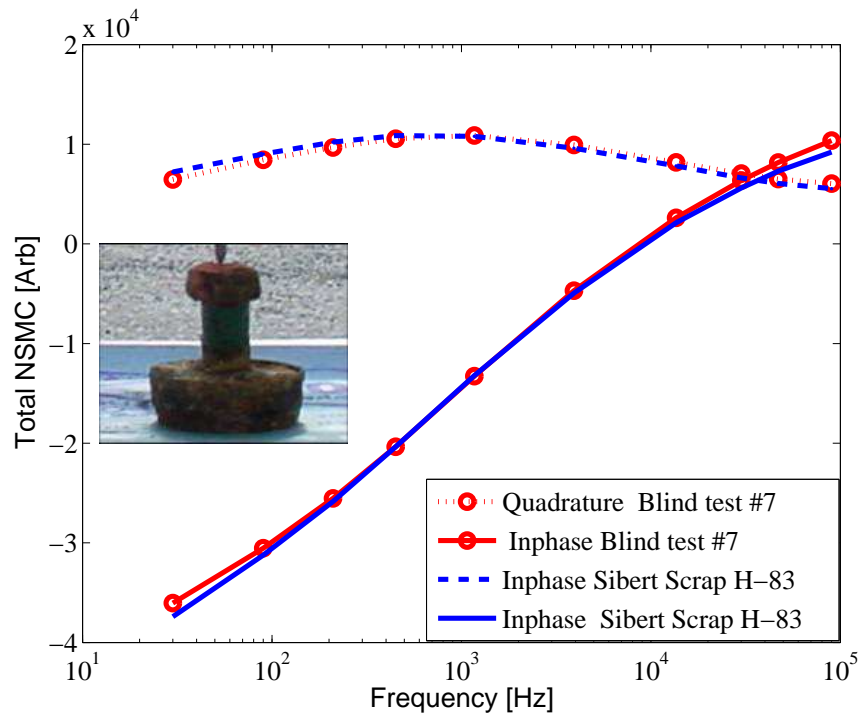


Figure 5.3.7: Total NSMS of blind test 7.

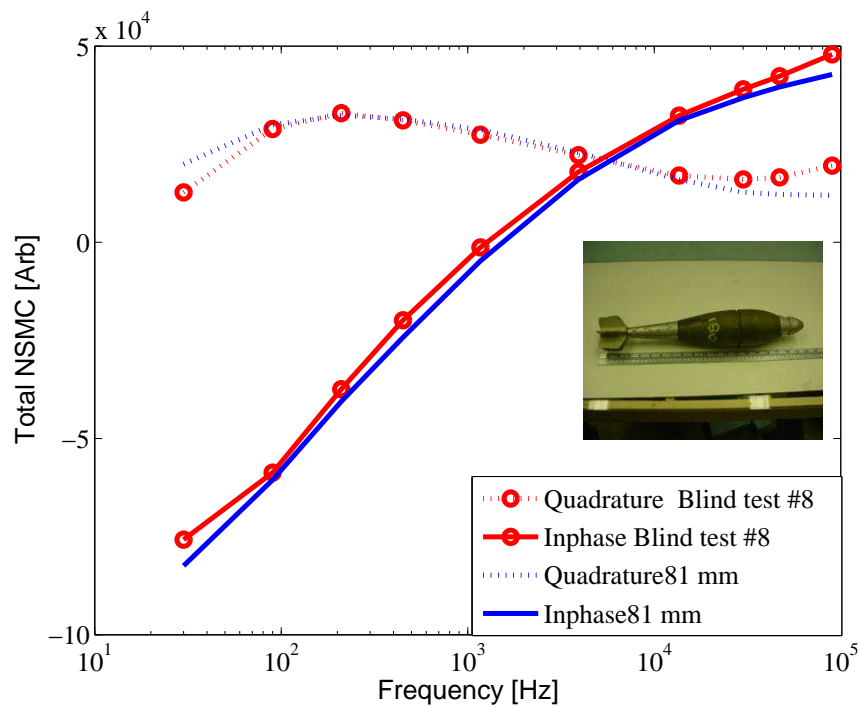


Figure 5.3.8: Total NSMS of blind test 8.

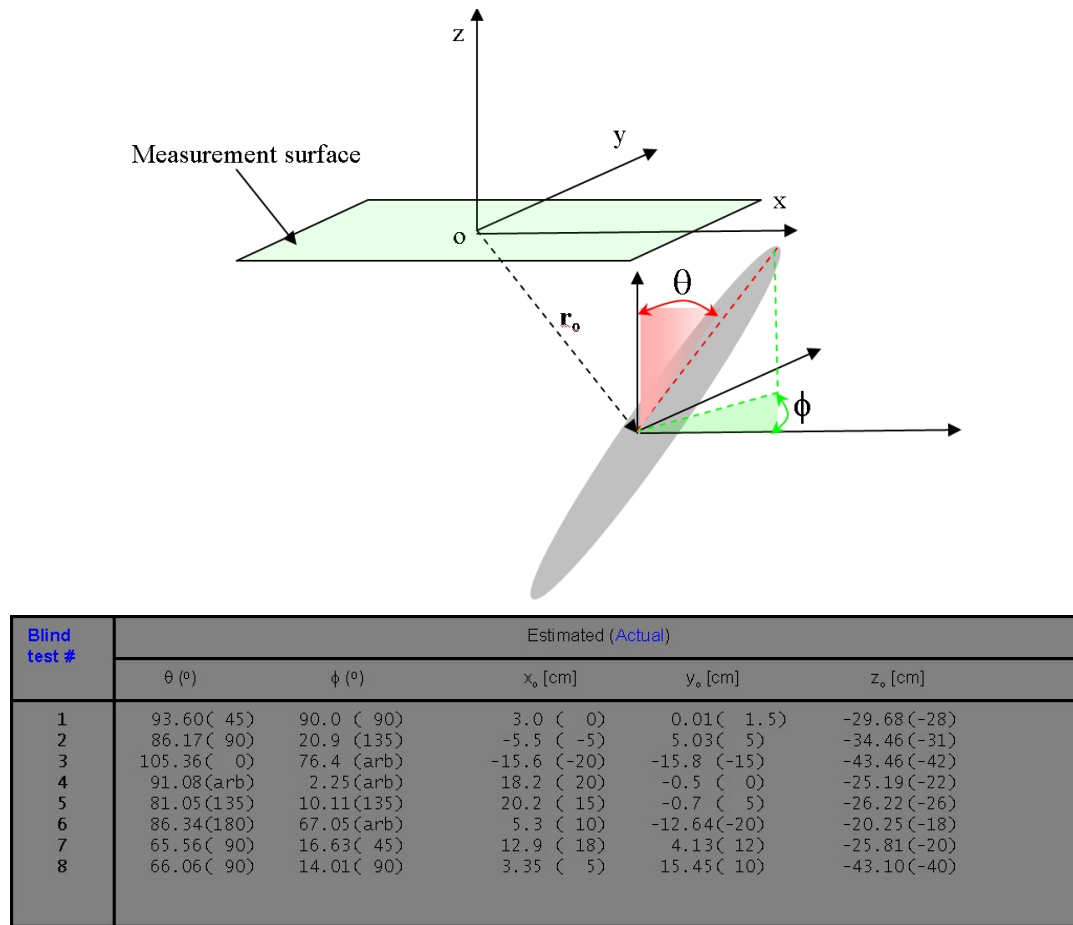


Figure 5.3.9: Geometry diagram and positions for blind tests derived from the HAP method compared to truth.

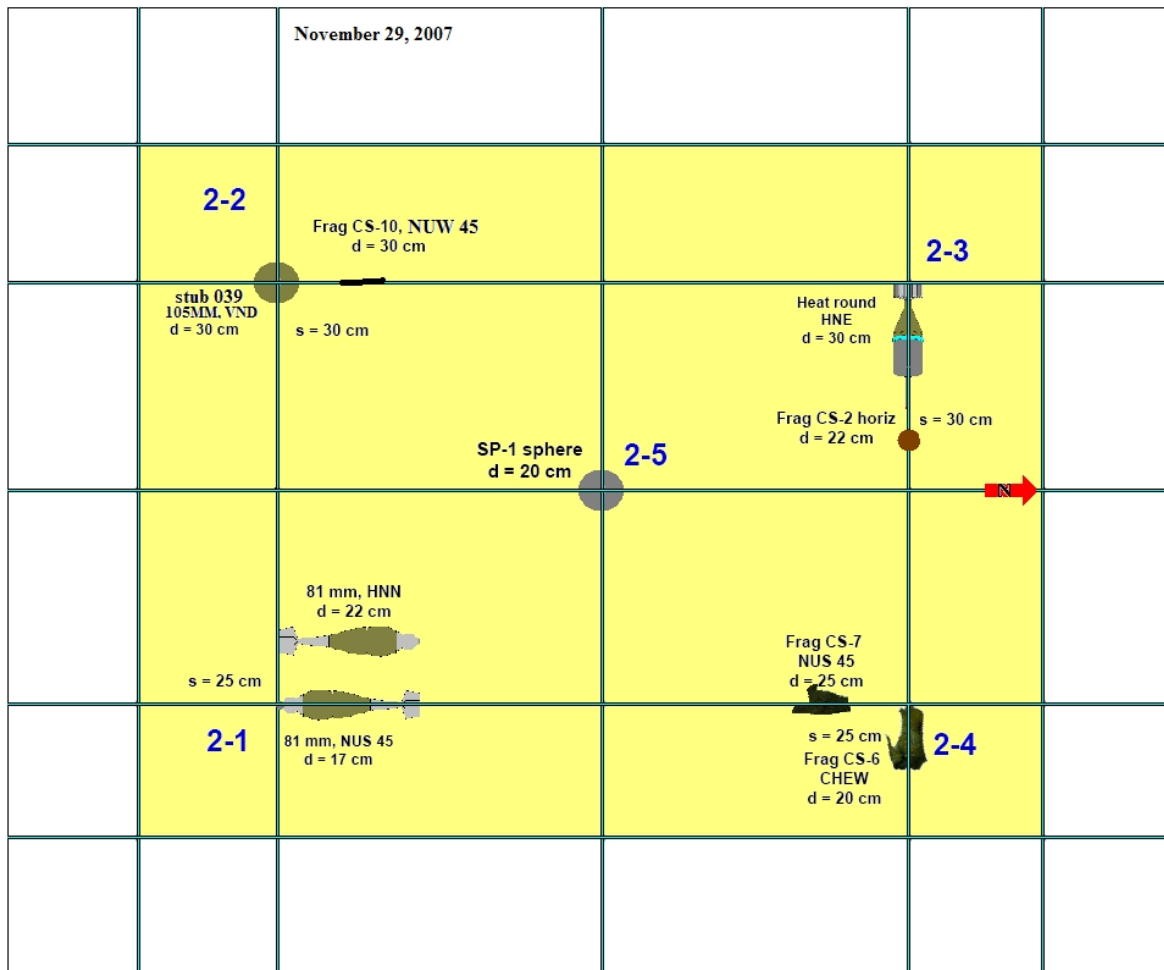


Figure 5.4.1: Contents of test plot #2 blind test suite #2.

5.4 Blind Test Suite #2 – CRREL Test Plots with Beacon Positioning

On October 23, 2008, CRREL personnel acquired data over 15 target clusters in the CRREL test plots. Each target cluster consisted of either one or 2 emplaced targets. The test plot emplacements consisted of 5 target clusters in 3 separate 20'x20'x8' concrete plots. The items in each cluster are shown in Figs. 5.4.1–5.4.3. In these figures, a red box around an alternate target indicates a target that used to be in that position, but was thereafter replaced with the target listed. Target designations such as LG-22 and so forth are CRREL designations and refer to different pieces of scrap with specifications available upon request. Test plot #1 was not used for this suite of tests.

The GEM-3⁺ including the functioning beacon positioning system was used to acquire data over all 15 target clusters. Appendix C.3 describe the data processing of this data while in Sec. 5.4.a, the results of a multi-object NSMS inversion [98, 99, 134] is presented. References to “lithos” and data paths in general are CRREL/Dartmouth specific. All relevant files are available upon request.

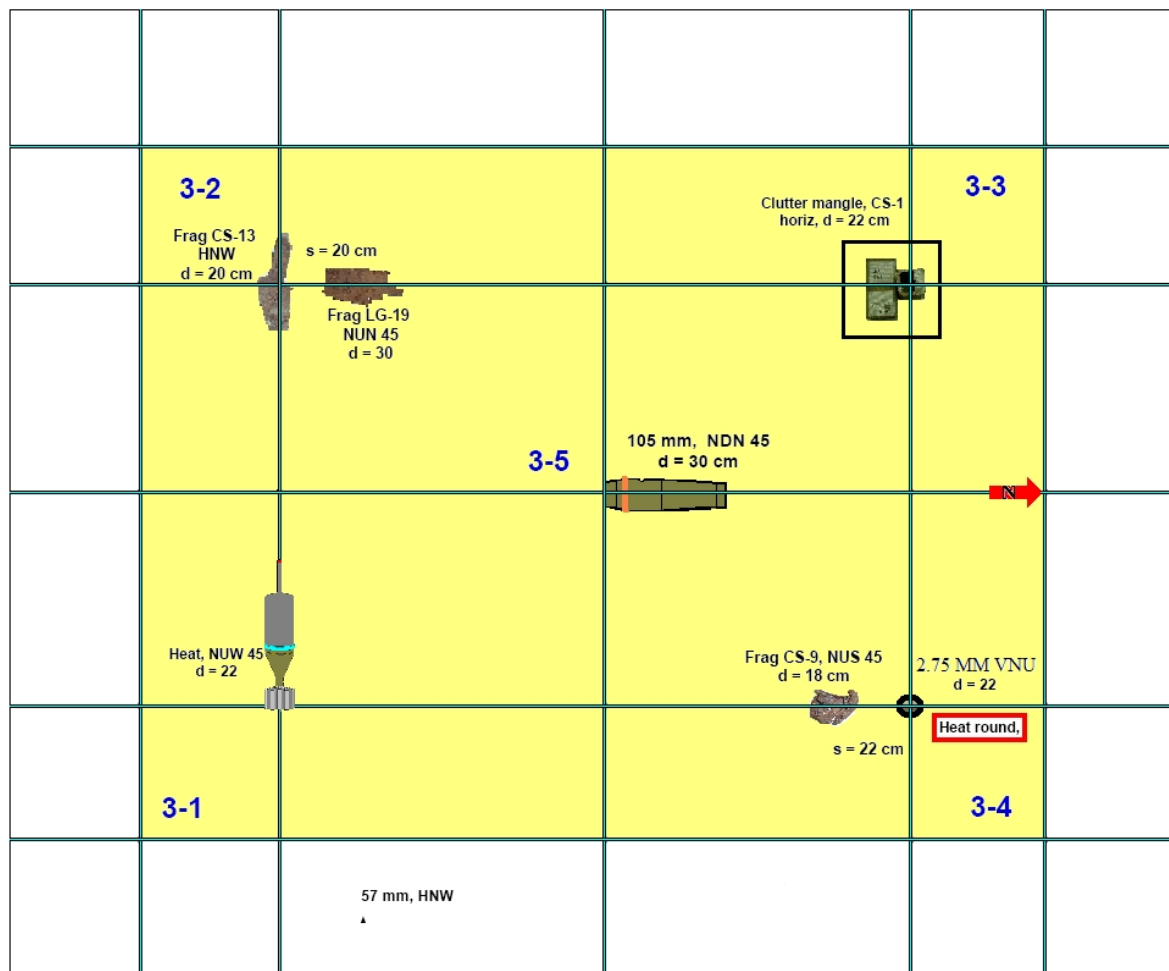


Figure 5.4.2: Contents of test plot #3 blind test suite #2.

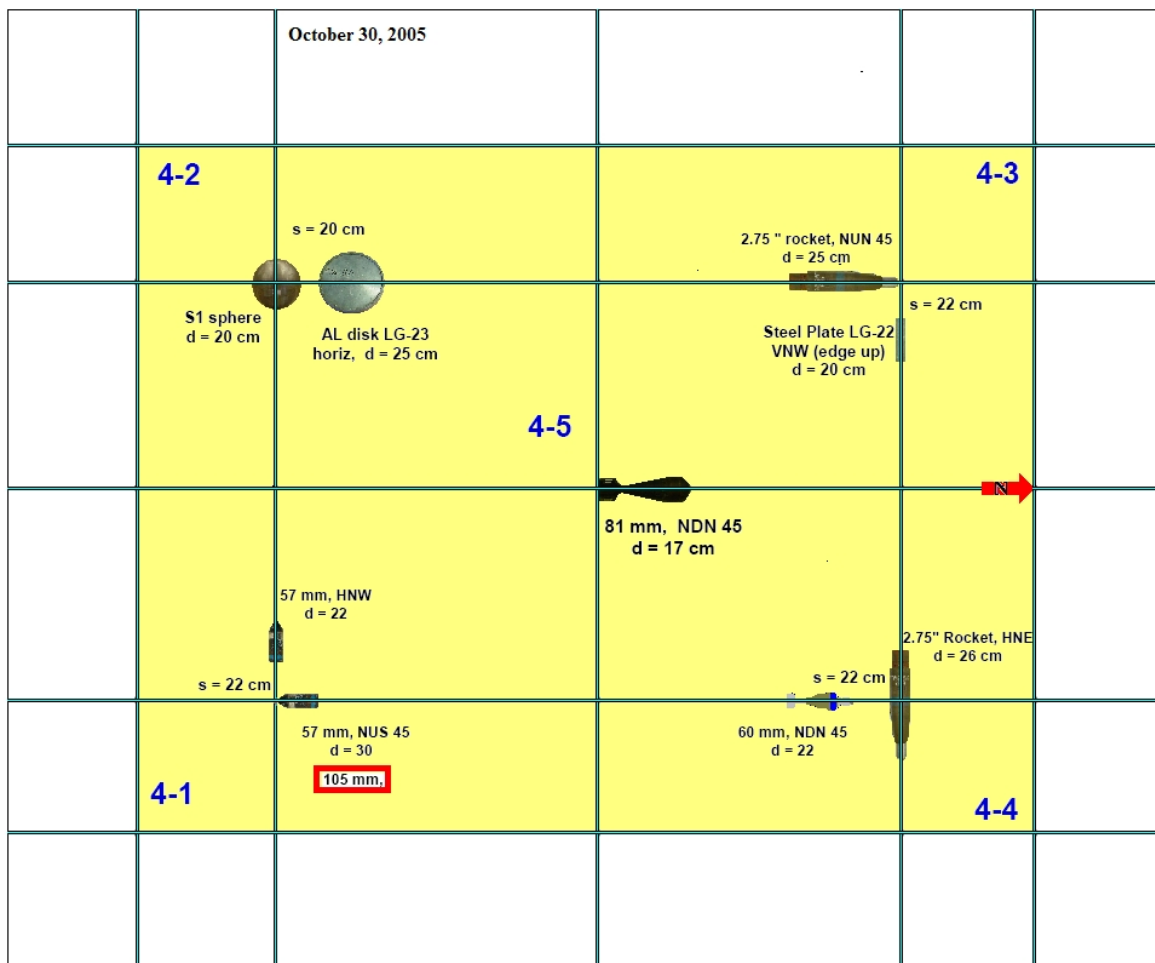










Figure 5.4.3: Contents of test plot #4 blind test suite #2.











5.4.a Blind Test Suite #2 Results

The results for the multiobject NSMS inversion are presented on the next two pages.

The inverted results for this multi-object NSMS method are mixed but encouraging. The iterative multi-object approach here is a slow, somewhat “brute force”ish method. Also remember that this data has background subtraction issues as outlined in the last sections. Even with these difficulties, the technique here was able to correctly identify individual UXO in about half of the cases presented (the green highlighted boxes). For many other cases, the method correctly distinguished between UXO and clutter (yellow boxes), but only rarely produced a full misclassification (red boxes).

GEM 3D plus processing results for multi objects :

Blind test #	Object #1 / correct object #1	Object #2 / correct object #2
1 : Tp2-1	 81 mm	 2.75 inch / 81mm
2 Tp2-2	 105 mm	Empty hall Frag CS-10
3 Tp2-3	 105 mmHR	Clutter Frag CS-2
4 Tp2-4	 Scrap H-83 / Frag CS-6	Clutter Frag CS-7
5. Tp3-1	 381 / 105mm HEAT	 60mm / empty
6 Tp3-2	Clutter Frag CS-13	 Scrape H-259 / Frag LG-19 Or a clutter

7 Tp3-3	 Sibert Scrap H-83 / Clutter mangle CS-1	
8 Tp3-4	A clutter / 2.75" rocket	A Clutter
9 Tp3-5	Signals are too weak to get meaningful information 	
10 Tp4-1	 57 mm	 Blu- 26 / 57 mm
11 Tp4-2	 105 mm / S1 sphere	 81 mm / Aluminum disk LG-23
12 Tp4-3	 105 HR / 2.75" rocket	 57 mm / Steel plate LG-22
13 Tp4-4	 381 / 2.75" rocket	 BDU-26 / 60mm

6 Conclusions and Implications

SERDP project MM-1537 entitled “Handheld Frequency Domain Vector EMI Sensing for UXO Discrimination” is complete. The SERDP project MM1537 has resulted in a unique frequency domain instrument that adds transverse receivers to the standard GEM-3 platform while also incorporating several advances in hardware and software. The most notable other hardware advance aside from the transverse receiver coils (the 3 \mathcal{D} part of GEM-3 \mathcal{D}^+), a positioning system based on the primary field of the instrument itself has been designed and installed which yields subcentimeter accuracy out about 2.5 meters from the beam containing two triaxial receivers.

Alongside the hardware advances made during this project, the accompanying software and models are also of note. The normalized surface magnetic charge (NSMS) model was advanced and adapted for the GEM-3 \mathcal{D}^+ . As well the Standardized Excitations Approach (SEA) was similarly adapted and applied to $\mathcal{J}_{\text{gemd}}$ data. These physics based rigorous models boast arbitrary fidelity and can take into account any primary field and predict the response from any physical target. A method to extract an absolute scale which translates GEM-3 \mathcal{D}^+ ppm into physical quantities (Amps/meter) was also derived and published.

The GEM-3 \mathcal{D}^+ is now a fully functioning EMI instrument capable of vector sensing of magnetic anomalies while being well located within a limited range. The transverse receivers add critical data diversity and information to rigorous models and help in inversion routines. For precise, queued interrogation of anomalies, the GEM-3 \mathcal{D}^+ provides diverse, accurate, frequency domain data of the secondary EMI field suitable for inversion and discrimination with high fidelity, rigorous models.

A Appendices – Supporting Data

B List of Scientific/Technical Publications

Publications produced in whole or part with funds from this project during FY06 are [5, 98, 105, 110, 111, 121, 126, 134–139].

C Other Supporting Materials

C.1 Data Acquisition Sequence from the GEM-3 \mathcal{D}^+

Running Gem-3D with GPS unit.



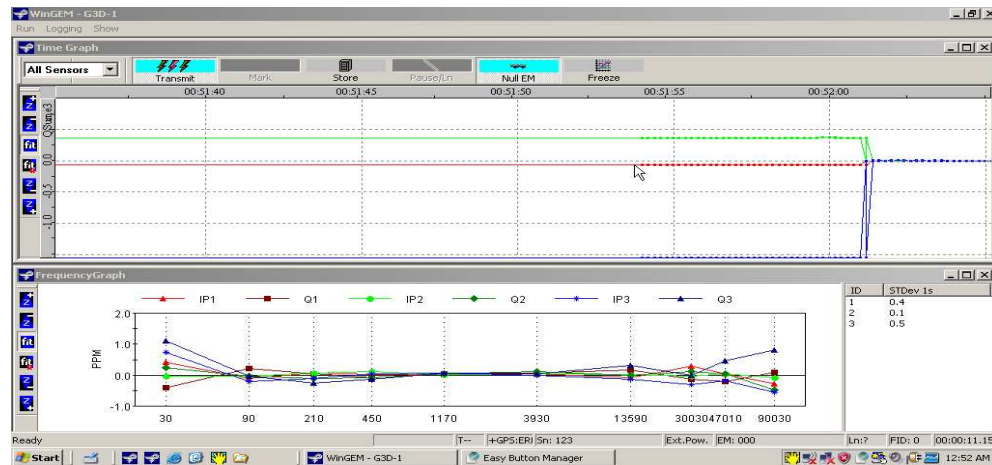
You must follow these instruction to the letter or you will not have good data.

Turn on:

- 1.) **Gem-3D** – Battery or Power Supply – 11.6 volts DC
- 2.) **GPS** – Battery or Power Supply – 12 volts DC
- 3.) **Computer**
- 4.) Start: **WinGem v4**



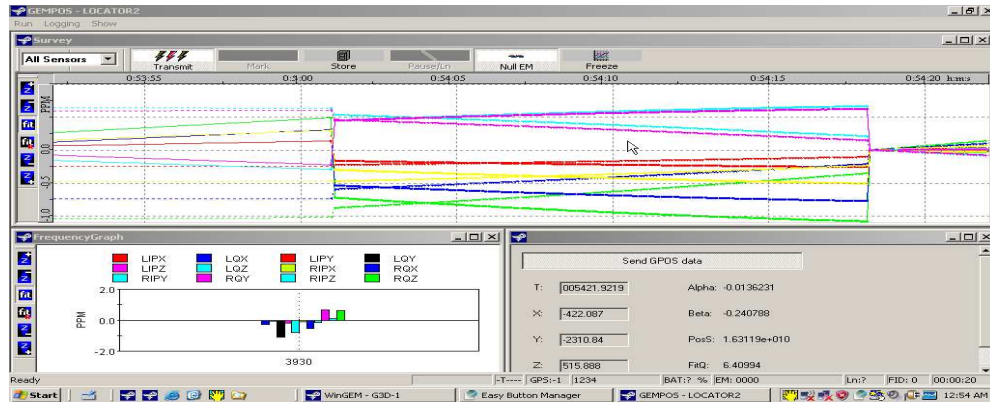
Press the **Transmit** button – Then the **Null Em** Button – zero it.



- 5.) Start: **GEMPOS**



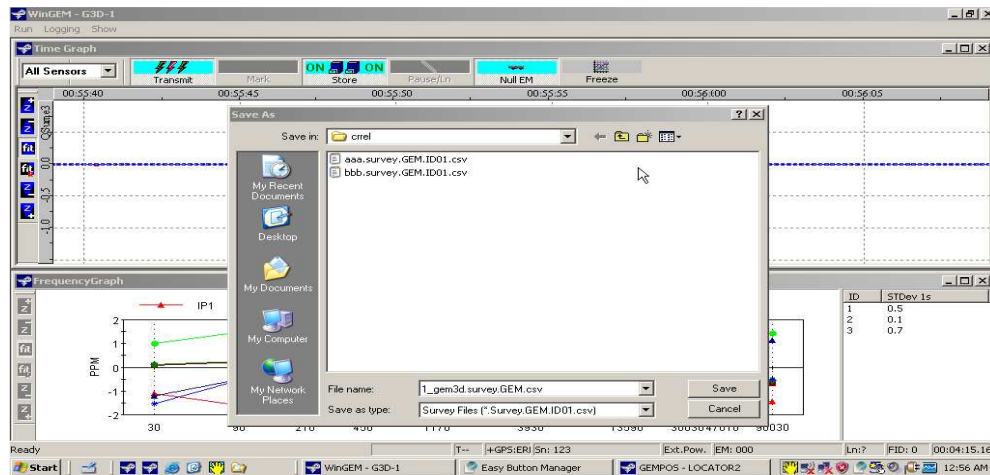
- 6.) Press the **Transmit** button – Then the **Null Em** Button – zero it.



- 7.) Then minimize reduce screen by hitting the minus sign.
Do not shut off, to silence beeping.



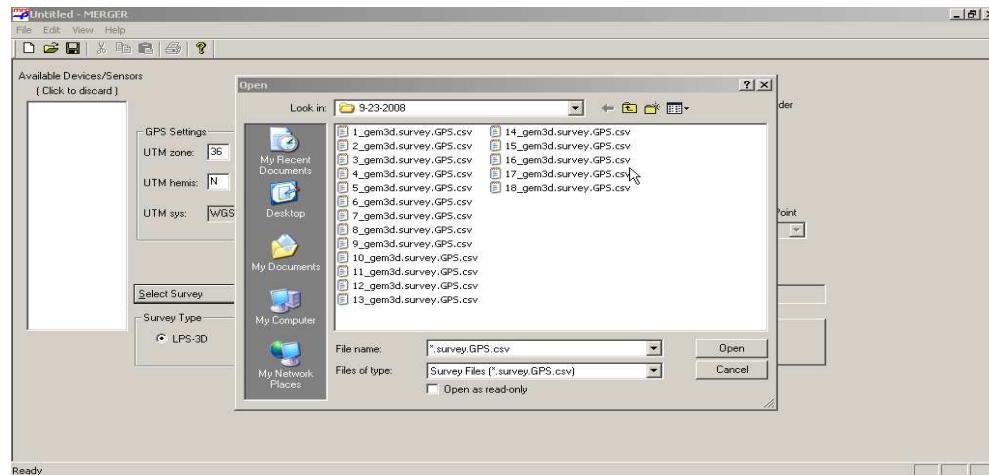
- 8.) Go back to **WinGem** - you are ready to test - Press the **Store** Button
You can use automatic file names or create your own.



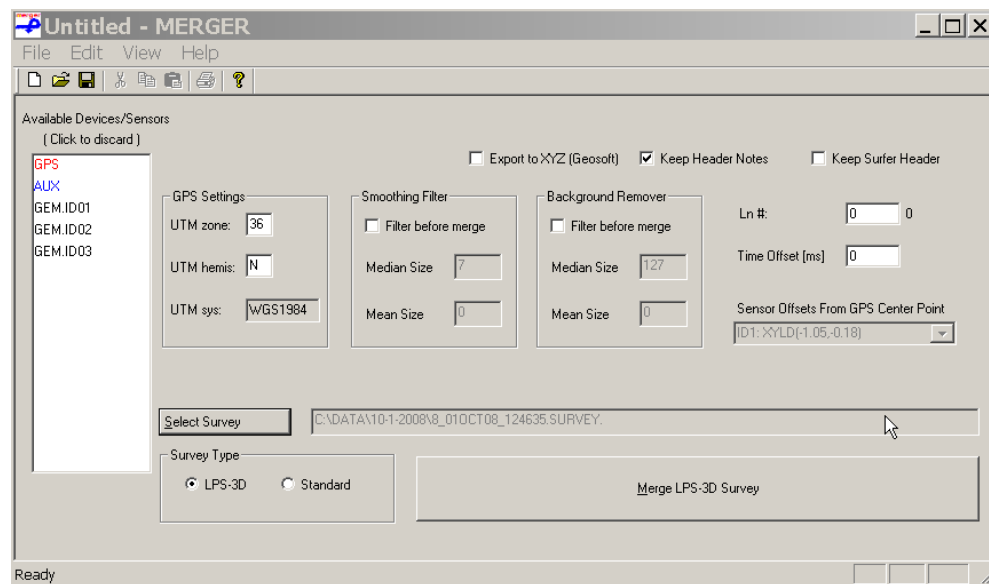
- 9.) Press **Store** again when test is finished.
- 10.) Then minimize screen by hitting the **minus sign**.
Do not shut off.
- 11.) You must run Merge after each test or data will be lost.
- 12.) Start: Merge



13.) Press **Select Survey** – find the test that you have just finished and open it



14.) Then press **Merge LPS-3d Survey** button. When **Merge** is finished it will close automatically.



15.) Check data with  and  **Microsoft Office Excell**

16.) data should look like this.

Microsoft Excel																
File Edit View Insert Format Tools Data Window Help																
Type a question for help																
100%																
Dgem AutoShapes																
A1 System=LocalPos																
GEM3D_SURVEY.GEM_ID01.ALL.csv																
1	System=LocalPos															
2	45	Total Samples In File														
3	Info Date	2008	Time	21	DataLabel: ID01											
4	Note1															
5	Note2															
6	X	Y	Z	ALPHA	BETA	Q	LPSTim	LPSmsO	PowerLnI1_30Hz	Q1_30Hz	I1_90Hz	Q1_90Hz	I1_210Hz	Q1_210Hz	I1_450Hz	
7	-0.156	-1.17	-0.222	-0.01	-0.03	8	29.59	77399787	1.32E+09	3.90E+02	#####	3.90E+02	#####	3.88E+02	#####	3.86E+02
8	-0.156	-1.17	-0.222	-0.01	-0.03	8	30.00	77399987	1.31E+09	3.89E+02	#####	3.90E+02	#####	3.88E+02	#####	3.86E+02
9	-0.157	-1.171	-0.222	-0.01	-0.03	8	30.00	77400187	1.3E+09	3.90E+02	#####	3.90E+02	#####	3.88E+02	#####	3.86E+02
10	-0.156	-1.17	-0.222	-0.01	-0.03	8	30.00	77400387	1.18E+09	3.89E+02	#####	3.90E+02	#####	3.90E+02	#####	3.86E+02
11	-0.156	-1.17	-0.222	-0.01	-0.03	8	30.00	77400587	1.3E+09	3.89E+02	#####	3.90E+02	#####	3.88E+02	#####	3.86E+02
12	-0.156	-1.17	-0.222	-0.01	-0.03	8	30.00	77400787	1.3E+09	3.89E+02	#####	3.90E+02	#####	3.88E+02	#####	3.86E+02
13	-0.156	-1.17	-0.222	-0.01	-0.03	8	30.01	77400987	1.27E+09	3.89E+02	#####	3.90E+02	#####	3.88E+02	#####	3.86E+02
14	-0.156	-1.17	-0.222	-0.01	-0.03	8	30.01	77401187	1.25E+09	3.91E+02	#####	3.90E+02	#####	3.88E+02	#####	3.86E+02
15	-0.156	-1.17	-0.222	-0.01	-0.03	8	30.01	77401387	1.29E+09	3.89E+02	#####	3.90E+02	#####	3.88E+02	#####	3.86E+02

Not this.

Microsoft Excel

File Edit View Insert Format Tools Data Window Help

Type a question for help

Draw AutoShapes

A1 .System=LocalPos

1_GEM3D_SURVEY_GEM.ID01.ALL.csv

	A	B	C	D	E	F	G	H	I	J	K	L	M	N	O	P
1	.System=LocalPos															
2	45	Total Samples In File														
3	Info Date:	2008	Time: 19	DataLabel: ID01												
4	Note1:															
5	Note2:															
6	X	Y	Z	ALPHA	BETA	Q	LPSTim	LPSmsO	PowerLnI1_30Hz	Q1_30Hz	I1_90Hz	Q1_90Hz	I1_210Hz	Q1_210Hz	I1_450Hz	
7	*	*	*	*	*	*	*	*	2.38E+09	3.90E+02	#####	3.90E+02	#####	3.89E+02	#####	3.87E+02
8	*	*	*	*	*	*	*	*	2.38E+09	3.89E+02	#####	3.90E+02	#####	3.89E+02	#####	3.87E+02
9	*	*	*	*	*	*	*	*	2.35E+09	3.91E+02	#####	3.90E+02	#####	3.89E+02	#####	3.87E+02
10	*	*	*	*	*	*	*	*	2.36E+09	3.89E+02	#####	3.90E+02	#####	3.89E+02	#####	3.87E+02
11	*	*	*	*	*	*	*	*	2.34E+09	3.90E+02	#####	3.90E+02	#####	3.89E+02	#####	3.87E+02
12	*	*	*	*	*	*	*	*	2.36E+09	3.90E+02	#####	3.90E+02	#####	3.89E+02	#####	3.87E+02
13	*	*	*	*	*	*	*	*	2.38E+09	3.89E+02	#####	3.90E+02	#####	3.89E+02	#####	3.87E+02
14	*	*	*	*	*	*	*	*	2.38E+09	3.90E+02	#####	3.90E+02	#####	3.89E+02	#####	3.87E+02
15	*	*	*	*	*	*	*	*	2.35E+09	3.90E+02	#####	3.90E+02	#####	3.89E+02	#####	3.87E+02
16	*	*	*	*	*	*	*	*	2.34E+09	3.90E+02	#####	3.90E+02	#####	3.89E+02	#####	3.87E+02
17	*	*	*	*	*	*	*	*	2.37E+09	3.90E+02	#####	3.90E+02	#####	3.89E+02	#####	3.87E+02
18	*	*	*	*	*	*	*	*	2.37E+09	3.90E+02	#####	3.90E+02	#####	3.89E+02	#####	3.87E+02

17.) You are ready to start your next test.

C.2 Beacon Positioning System Construction Details



Progress Report

on

Handheld Frequency-Domain Vector EMI Sensor for UXO Discrimination

Contract Number: W913E5-06-C-0011

April 2007

from

Geophex, Ltd.

605 Mercury Street

Raleigh, NC 27603

1. Progress Summary

This report covers our progress on the Beacon navigator. CRREL issued a contract modification early 2007 so that this task is completed in FY07. As of this reporting, we have completed the physical construction of the coils and housing. Early this month, we started electronic wiring and assembly.

2. Navigator Geometry and Construction

The *Beacon Navigator* is to be used for accurately locating the GEM-3D active EMI sensor Geophex built for CRREL. Figure 1 shows how it works: the GEM transmitter acts as an active beacon that can be located by a pair of receiving coils in the vicinity, each of which consists of three orthogonal coils. This method accurately produces the sensor's position, as well as the sensor's orientation as defined by two tilt angles. Tests have shown that the method produces accuracy of better than a centimeter when the receiving coils are at a range of several meters.

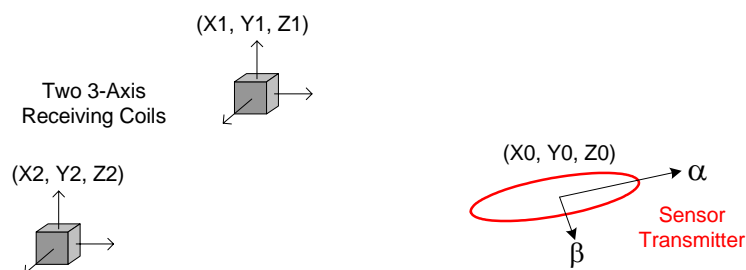


Figure 1. A pair of 3D coils measure the magnetic field generated by the EMI sensor. The six coil outputs are sufficient to determine both the sensor location and tilt angles.

We built in 2006 a prototype *Beacon Navigator* housed in a 10cm x 10cm x 1.5m PVC tube that contains a 3D coil at each end. The output of the prototype navigator is routed by hardware (~10m long) to the GEM-3 sensor. The *Navigator* computes the sensor location using the voltage output from the coils and sends the results to the GEM-3 that merges the location data with the sensor data. Under this CRREL project, we will refine the existing navigator by improving and simplifying its performance, and producing an advanced navigator. We will then

integrate the Navigator with the GEM-3D, using the Bluetooth wireless communication so that it will be completely detached from the sensor operator.

Calibration: Since the relative geometry of the two 3D navigator coils is fixed, only a few ground-truth points are sufficient for a full calibration. One-time calibration is sufficient for its lifetime usage.

3. Progress Status

3.1 Navigator Sensing Coils

Table 1 shows the preconstruction design figures of the three nested coils. The z-axis coil (the middle of the nest), for instance, has a mean winding cross-section of 6.8 cm x 6.8 cm and has 2,000 turns of #34-gauge wire. The turns for other nested coils are adjusted to have a similar area-turns product to equalize their voltage outputs. Table 1 also shows predicted inductance (in Henry) and resistance (in ohm) for each coil.

As designed				
Rx - Z	Middle Section			
2000 turns	0.873 AWG#34	9.25	area x turn (m*m)	
0.068 a (m)	0.334 inductance (H)	64	x-sec (mm**2)	
0.068 b (m)	474.9 resistance (ohm)	0.703	time constant (msec)	
Rx - X	Outermost			
1784 turns	0.873 AWG#34	9.25	area x turn (m*m)	
0.072 a (m)	0.290 inductance (H)	57.088	x-sec (mm**2)	
0.072 b (m)	448.5 resistance (ohm)	0.647	time constant (msec)	
Rx - Y	Innermost			
2260 turns	0.873 AWG#34	9.26	area x turn (m*m)	
0.064 a (m)	0.387 inductance (H)	0.766	time constant (msec)	
0.064 b (m)	505.1 resistance (ohm)			

Table 1. Design figures of the three nested coils

Figure 2 shows actual coils constructed based on the design figures. Each of the two sensing coils is wound on a light-density, 3-inch plastic cube that contains a pair of recessed grooves for coil on each axis. The coils are to be mounted at the ends of a 3" x 3" x 5 ft square PVC tube, as shown in Figure 3.

Table 2 shows the measured inductance, resistance, and resonance frequency of actual coils that were built based on the design figures. The predicted and actual are close within manufacturing accuracy.

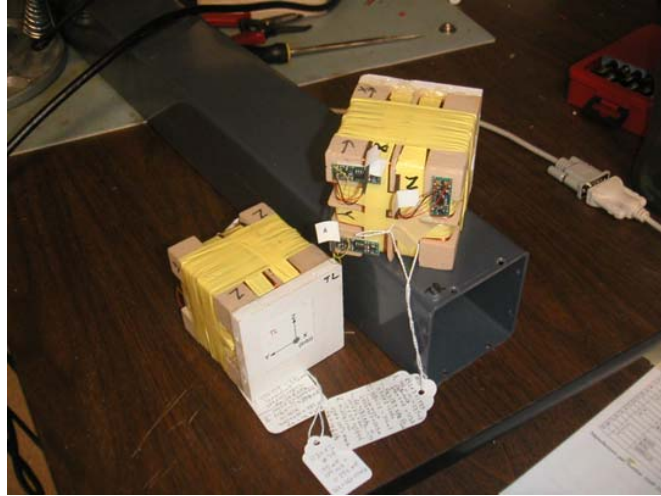


Figure 2. Two 3-D nested sensing coils with preamps attached



Figure 3. Square PVC tube housing

Actual						
Coil 1			Coil 2			Rx-Z
half	half	total	half	half	total	
0.116	0.117	0.323	0.117	0.117	0.334	ind (H)
240	241	481	235	235	470	res (Ohm)
		14.7			14.6	res freq (kHz)
						Rx-X
0.102	0.101	0.288	0.101	0.101	0.287	ind (H)
230	229	460	226	226	452	res (Ohm)
		16.3			15.7	res freq (kHz)
						Rx-Y
137	137	0.393	0.138	0.138	0.394	ind (H)
263	263	537	253	253	507	res (Ohm)
		13.8			13.1	res freq (kHz)

Table 2. Measured inductance, resistance, and resonance frequency of the actual coils

3.2 Sensing Electronics

The final electronic design for the navigator is still in progress. Two primary design issues are:

- Wireless communication with the GEM-3D and
- Automatic gain control scheme for each preamp to prevent input saturation when the GEM-3 is close to the navigator.

The second issue is a newly-discovered: when the GEM-3D is at less than, say, 1 m from the navigator, the front-end voltage becomes high to saturate the preamp. We are currently working on an automatic gain-control scheme to deal with this issue.

Figure 4 shows the main DSP section that will process the 6-channel time-series data.



Figure 4. DSP electronics for the navigator

4. Plan for the Next Reporting Period

We will continue the electronic assembly of the navigator. We expect to fire it up within the next month and to begin the test and calibration phase.

5. Estimated Percentage of Contract Completion for Year 2 Task: 40%

C.3 GEM-3 \mathcal{D}^+ Data Processing - Static and Dynamic

C.3.a Introduction

This short document explains the internal structure of the program for data read-in and analysis of GEM-3 \mathcal{D}^+ files.

Two cases are considered:

1. The “Beacon sliding on a grid” data taken in the lab by Ben Barrowes on 10/7/08. This set is stored on lithos in directory

DATA/gem3dplus/3D_10-7-2008_Ben/

and is henceforth called Ben.

2. The “Beacon free form” data taken over the test plots by Kevin O’Neill on 10/23/08. This set is stored in

DATA/GEM-3D+_OCT-23-08_TESTPLOTS_EXPORT/

and is called Kevin from now on.

From now on when I refer to a “file” I really mean a collection of three `.csv` files: `ID01`, `ID02`, and `ID03`, corresponding to the GEM-3 \mathcal{D}^+ ’s three receivers.

C.3.b Reading the data

1. All filenames start with an identifying number. The ranges (of usable files) are [21 : 49] (29 files) for Ben and [1,3,4,8,9,12 : 18,21,22] (14 files) for Kevin. The variable `Ncase` ranges from 1 to 29 (14).
2. Some files have a strange feature: `ID01` has one more line than either `ID02` or `ID03`. This happens both in Ben’s and in Kevin’s data.

Kevin’s writeup mentions a “slight timing asynchronization” in the data he studied (`(2-1)`, or `3_*` in our present notation), which happens to be one of those cases. He suggests two solutions: interpolating or just ignoring the small differences.

I have taken the second route and simply deleted the first row when the set is problematic. At some point I tried interpolating (since each datafile includes the time at which each point was measured) but did not see much of a difference. I can redo this if necessary.

3. The previous version of the data-reading procedure made some use of UNIX system calls to determine the filenames and read in the values. I fixed that feature, which made it both system-dependent and slow, and replaced it with Matlab-only functions.

As it stands, the procedure can read `.csv`-like files that need not be all numeric. The only ad hocs here respond to Kevin’s having deleted most of the headers and the “LPSTime” column that presumably was preventing him from using `csvread`.

4. All three files corresponding to a given “file” are read at once and stored in a 3D array.

- Each receiver provides its own position/tilt information. I have kept this as both a 2D matrix (e.g., X_{pos} , with leading capital, is $N_{pt} \times 3$, where N_{pt} is the number of measurements) and as an averaged array (x_{pos} , all lowercase).

We do note that question arises as to the accuracy of the measurement locations given by the beacon system. A look at X_{pos} and the other two such variables reveals two columns that are identical and distinct from the third. The differences are most notable for the x -coordinate, where they reach 3 cm and are not random but periodic and roughly $\pi/2$ out of phase with the actual x -values. (See Fig. C.3.2 for a plot.)

- We also delete rogue points in which the location information was patently wrong, for example featuring large discontinuities. In Ben's case, it is straightforward to find those points, because they had a yaw angle of exactly zero. In Kevin's case we had to find them by hand.

C.3.c Background subtraction

C.3.c.(1) Initial approach We start by noting that we neglected the angular information in the background subtraction. In all cases some effort was put into holding the sensor as level and well-aligned with the beacon coordinate system as possible.

Ben took a whole background file, $N_{case} = 2$, which makes the subtraction straightforward: just read in that file, average over all points, and subtract the average from each data file. We do not have to be too observant of the height in this case, as there is no soil.

Kevin's files are a little different, since he takes the background values from the data themselves. (Also, his "calibration" file is over a shotput.) In his words,

The program next asks you to enter some data point number around which it will average (± 2 points) to obtain a background to subtract from all data treated subsequently. It's often hard to come up with a good choice, which has implications for deeper processing. Here we're just doing some exploratory visualization so it's not so important.

Now, however, is the time to perform the "deeper processing" he mentions. We cannot use Ben's background file, since that does not include soil response.

On the other hand, Kevin chooses his background point thus:

In any case, in the favorable case shown here, point #25 occurs after the surveying has gotten under way and is around the beginning of the first sweep; and there isn't much going on in either of the two response measures. Thus we enter this and the program averages over points 23–27, plotting the resulting background profile so you can see if anything wacky is going on, i.e. more strange than usual.

This gives rise to two related possibilities for finding the background:

- Decide upon a fixed number of background points, sort the measurements in decreasing order of distance from the center, and use the (averaged) furthest measurements as background.
- Carry out a multi-file survey and use the very furthest measurements as background, after averaging them.

Now, how do we determine an "optimal" number of background points that will not skew the measurements? We must look at the way the (frequency by frequency) average for the furthest

points change as we increase or decrease **Nbk**; also, we want to see how it compares to the field values themselves.

It turns out the background values so chosen exceed the combined background + UXO measurements in a few cases, and moreover the response is not flat. This may well be due to the height dependence of the soil response, which is nominally h^{-3} . On the other hand, the response of a dipole is approximately d^{-6} , which lends confidence to our taking the points presumably furthest from the target.

The user can control (dictate) **Nbk**, the number of points to take as background. The program finds a “center” point defined by $\vec{r}_c = x_c\hat{x} + y_c\hat{y} + z_0\hat{z}$, where x_c and y_c are the averages of x and y and z_0 is the lowest possible value of z , centers the positions there, and measures the radial distance from that origin to every measurement point. It then counts the **Nbk** points furthest from the origin, averages their field values, and uses this as a background. The function takes **Nbk** = 20 as default, though that value can be changed.

C.3.c.(2) Two-height approach The method described above has some flaws. First, it mashes together “background” data corresponding to different heights, which can bias the results. Also, the distance from the “center,” which we estimate as the average of the x - and y -locations, may not—and in multi-object cases will not—coincide with the center of anything, and thus it may turn out that the background points are in fact right on top of a target.

We then had to find a background-subtraction technique that would try to overcome these problems. In the end we implemented an ad hoc two-height approach.

Kevin’s measurements consist of two zigzags, one close to the ground making five passes over the measurement area and the other retracing the original in the opposite direction and some 10 cm above. The measurements were taken by hand, so the separations between the two zigzags are not necessarily clear-cut, and in some cases there are “higher” points that are actually closer to the ground than some in the “lower” zigzag. In our procedure, however, we assume two distinct, consecutive heights.

We start by finding by hand a single point, halfway in the transition region between the two zigzags, and divide each data set into the “before” and “after” intervals. We then find a five-consecutive-point interval for each of the zigzags that represents the best compromise between the following desirable (and often conflicting) features:

1. The interval is far from the center of the measurement trajectory.
2. The points lie at roughly the same height, one representative of the corresponding zigzag
3. The five points lie along a fairly smooth path so the mean of the field values is a reasonable average.
4. The resulting fields will have these characteristics:
 - The z -field should be positive in as many points as possible.
 - The x - and y -fields should have roughly as many positive values as negative, and the zero crossings should be roughly at the center of each sweep.

We concentrated on the quadrature parts of the fields, since they are presumably less affected by ground effects and did not have the large anomalous dc shift that the inphase parts had. Moreover, the quadrature response is positive at all frequencies, so any negative amplitudes will be due to geometry.

5. The above rules should hold in as large a range of frequencies as possible.

It is this method that we used in the end to prepare the data for further processing.

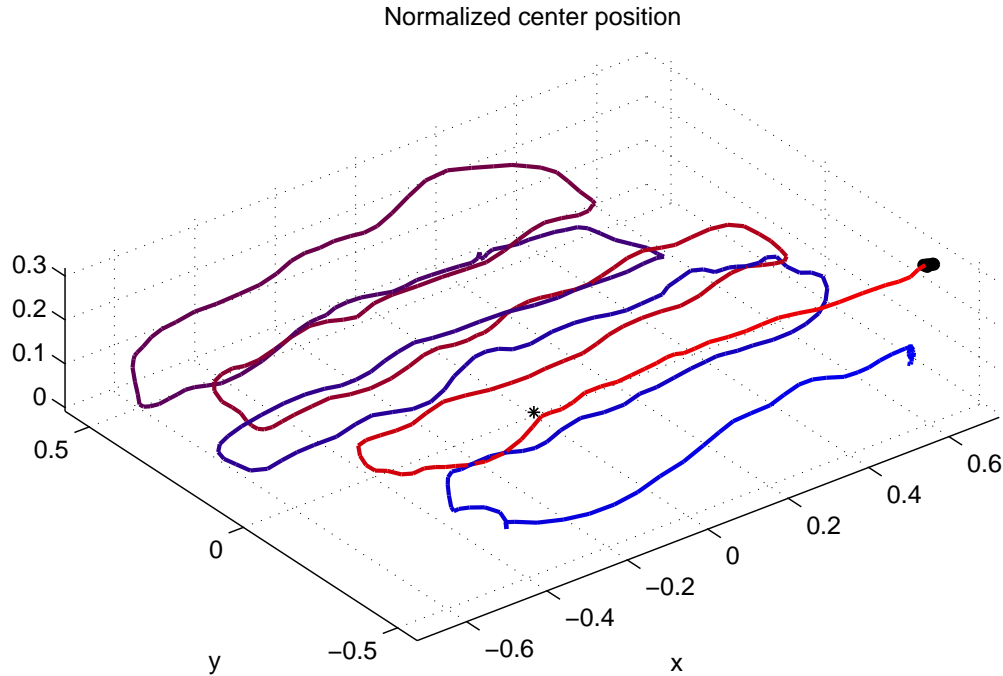


Figure C.3.1: Sensor position in the example data run. The convention in this and the following figures is: the sensor “warms up” as it takes data: *i.e.*, the trajectory is initially blue and transitions into red during the run. The background points are black dots.

C.3.d An example of the first approach

As an example we include our analysis of Kevin’s file $N_{\text{case}} = 2$, corresponding to location 2-1.

For this example we use the first approach to background subtraction. We choose $N_{\text{bk}} = 10$ in this case; the points happen to lie at the very end of the data run, and appear as black dots on Fig. C.3.1. The black star in that plot is the center from which the background points are most distant.

Figures C.3.3 and C.3.4 respectively show the inphase and quadrature parts of the background-subtracted secondary field at $f = 450$ Hz. On the left-hand-side panel we have the raw values. The dashed lines represent the background value, computed by averaging the field values component by component at the N_{bk} points, which appear in the figure as dots. On the right-hand-side panels we have the values obtained after subtracting the background.

The quadrature parts are further depicted as “profiles” on Fig. C.3.5.

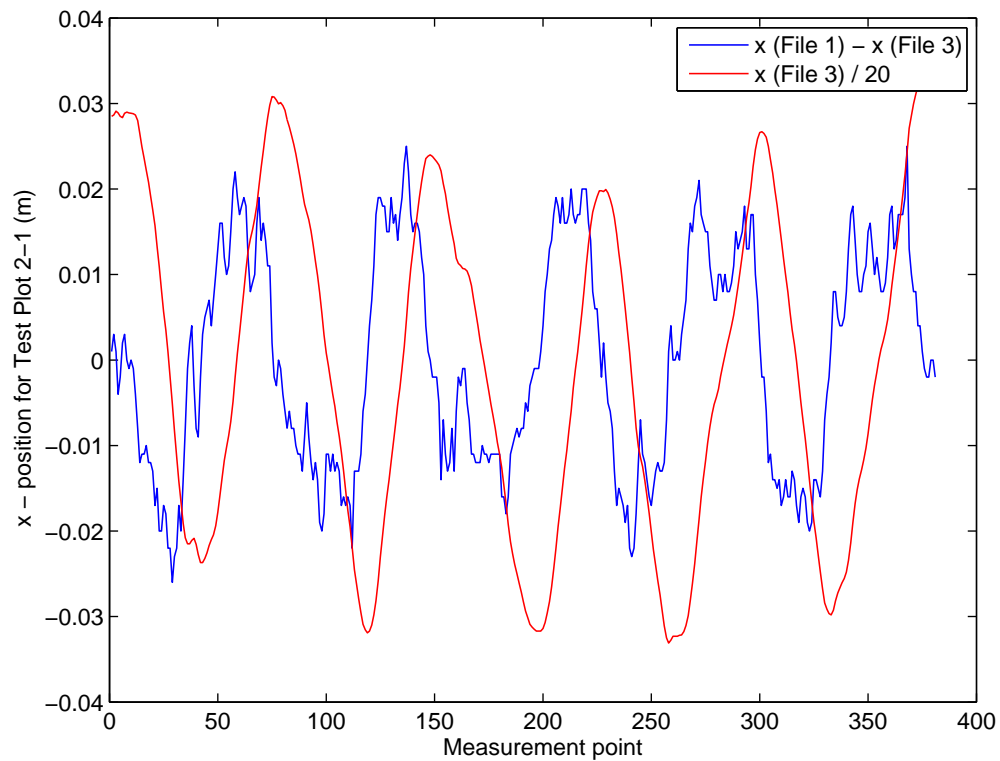
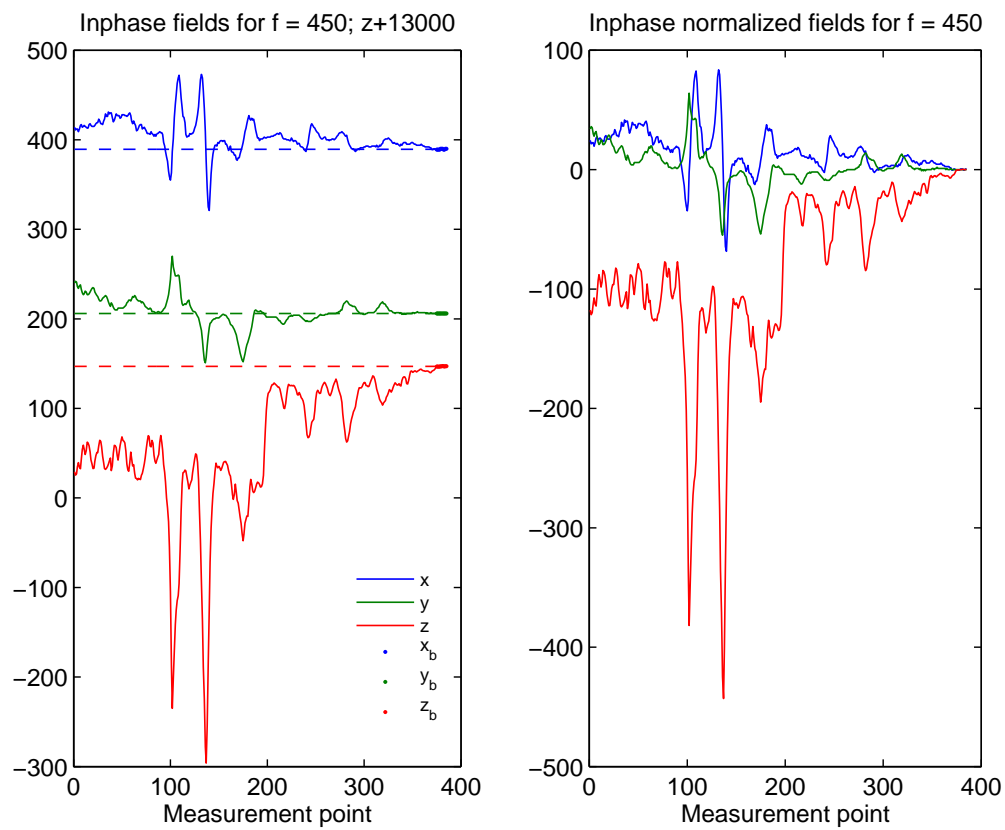
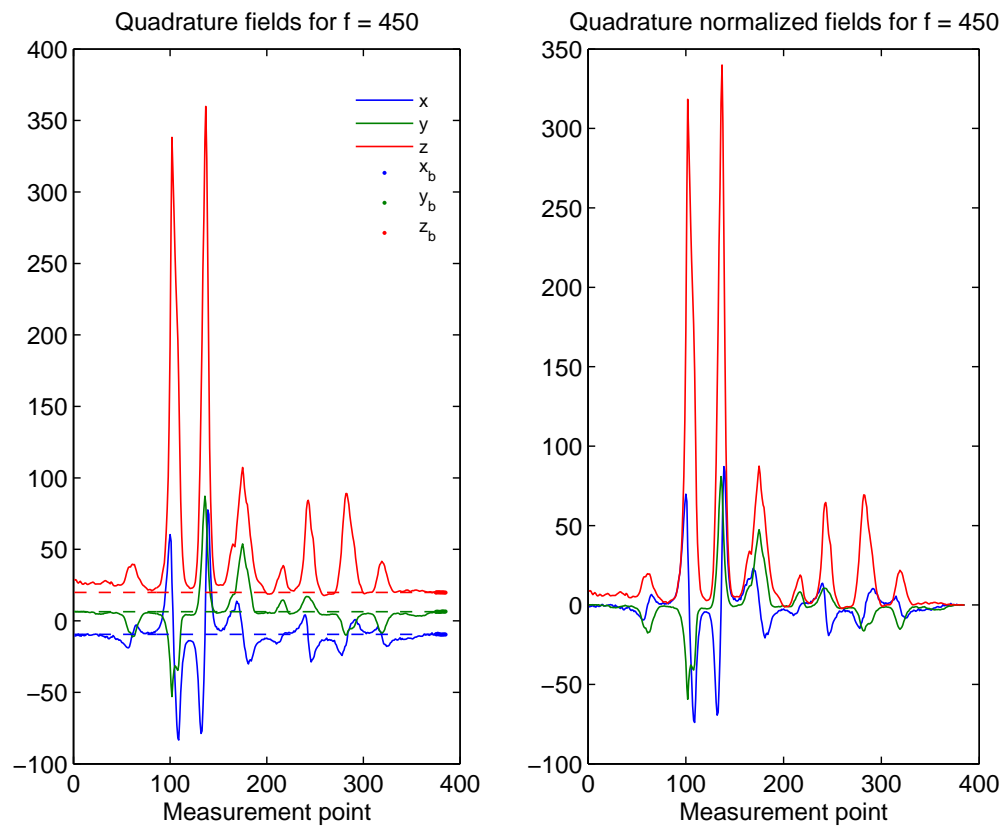
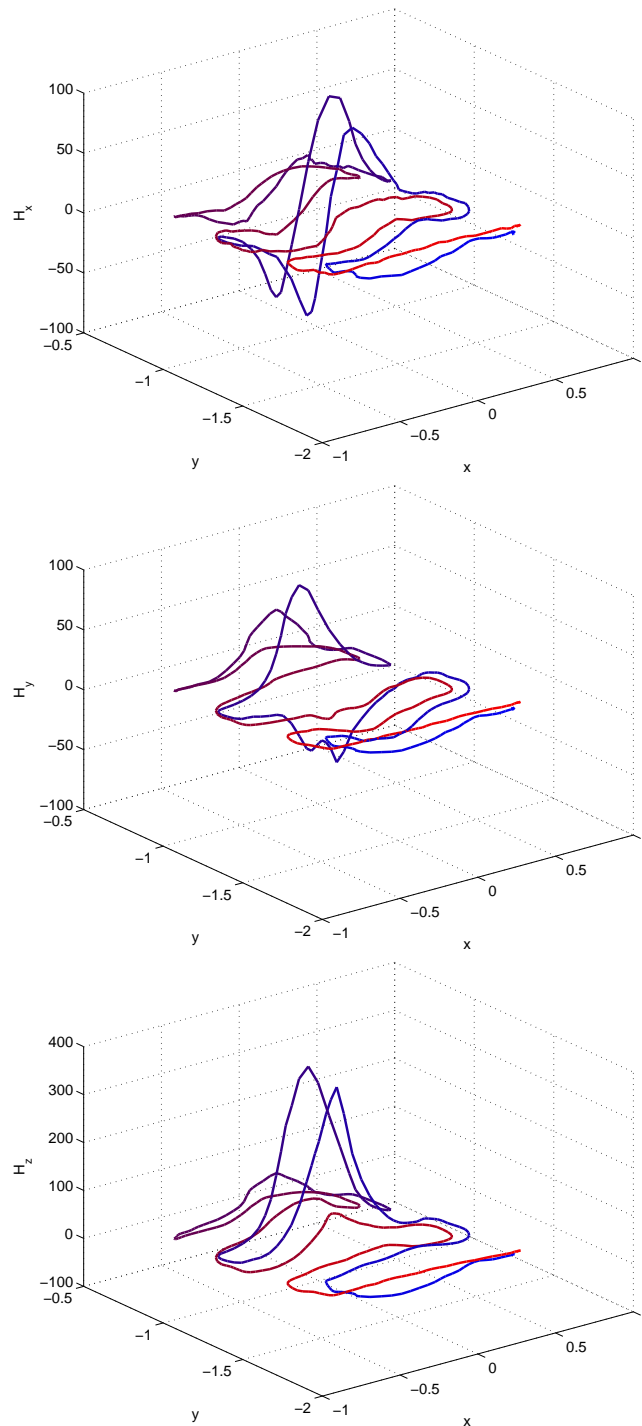


Figure C.3.2: Discrepancy in the x position between the first and third data files of a set.

Figure C.3.3: Background-subtracted field at $f = 450$ Hz, inphase part

Figure C.3.4: Background-subtracted field at $f = 450$ Hz, quadrature part

Figure C.3.5: Background-subtracted 3D fields at $f = 450$ Hz.

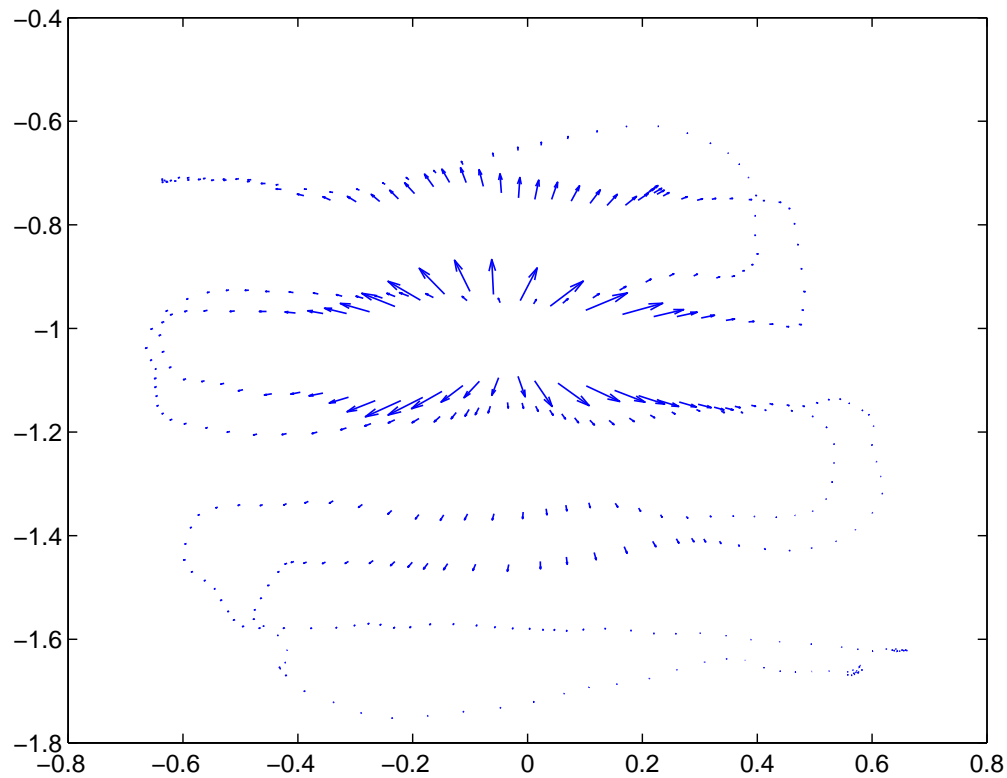


Figure C.3.6: Quiver plot showing the projection on the x - y plane of the quadrature part of the secondary field at $f = 450$ Hz. Joining the tails of the arrows can give a approximate estimate of the locations of the targets.

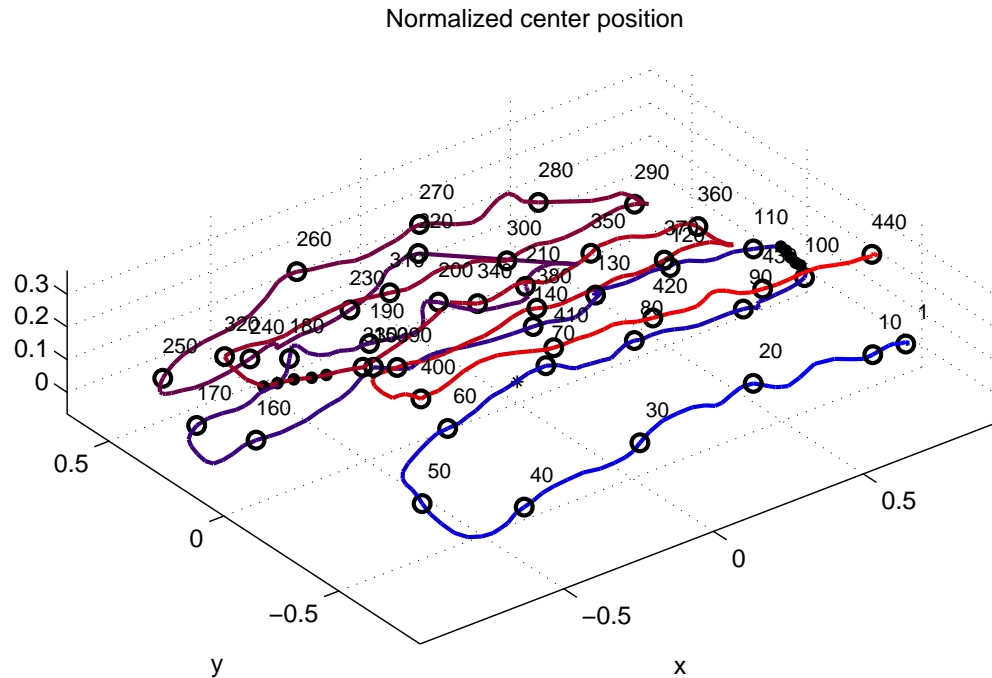


Figure C.3.7: Sensor position in the second example data run.

C.3.e Example of the second approach

To illustrate the second, final background-subtraction method we take another example, location 2-4.

Figure C.3.7 again plots the locations, with labels and hollow markers identifying every 10th point. The background points can be seen as solid black dots, to the left and right of the figure.

Figures C.3.8 and C.3.9 respectively show the inphase and quadrature parts of the background-subtracted secondary field at 3930 Hz. The description is as before: the left-hand-side panel shows raw values, the dashed lines represent the (two-level) background level, the dots depict the points used to find the background. On the right-hand-side panels we have “normalized” fields.

The field profiles of Fig. C.3.10 look two-peaked, and the impression that this plot may have two objects is strengthened by looking at the quiver plot in Fig. C.3.11.

References

- [1] I. J. Won, D. A. Keiswetter, and D. R. Hansen. GEM-3: A monostatic broadband electromagnetic induction sensor. *J. Environ. Eng. Geophys.*, 2:53–64, 1999. [viii](#), [93](#), [94](#), [97](#)
- [2] Benjamin E. Barrowes, Kevin O’Neill, Tomasz M. Grzegorzczak, Xudong Chen, and Jin A. Kong. Broadband analytical magnetoquasistatic electromagnetic induction solution for a conducting and permeable spheroid. *IEEE Trans. on Geoscience and Remote Sensing*, 42(11):2479–2489, November 2004. [viii](#), [92](#), [96](#), [98](#), [101](#)
- [3] Fridon Shubitidze, Kevin O’Neill, Irma Shamatava, Keli Sun, and Keith D. Paulsen. Fast and accurate calculation of physically complete EMI response by a heterogeneous metallic object. *IEEE Trans. on Geoscience and Remote Sensing*, 43(8):1736–1750, August 2005. [viii](#), [97](#), [100](#)
- [4] I. J. Won, D. A. Keiswetter, D. Hansen, E. Novikova, and T. M. Hall. Gem-3: a monostatic broadband electromagnetic induction sensor. *Jour. Envir. Eng. Geophysics*, 2(1):53–64, 1997. [4](#), [67](#)

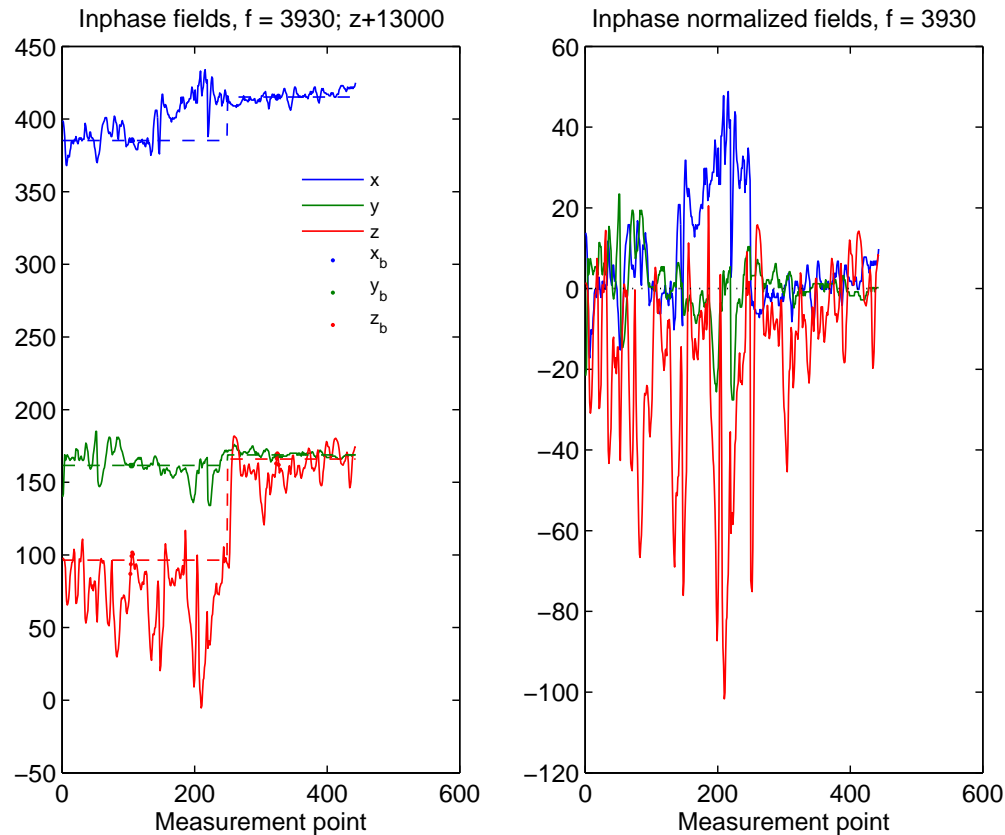


Figure C.3.8: Background-subtracted field at $f = 3930$ Hz, inphase part.

- [5] Tomasz M. Grzegorzczak, Beijia Zhang, Jin Au Kong, Benjamin E. Barrowes, and Kevin O'Neill. Electromagnetic induction from highly permeable and conductive ellipsoids under arbitrary excitation - application to the detection of unexploded ordnances. *IEEE Trans. on Geoscience and Remote Sensing*, 46(4):1164–1176, April 2008. [33](#), [127](#)
- [6] Yogadhis Das, John E. McFee, Jack Toews, and Gregory C. Stuart. Analysis of an electromagnetic induction detector for real-time location of buried objects. *IEEE Trans. Geosci. Remote Sens.*, 28:278–288, May 1990. [33](#)
- [7] Lawrence Carin, Haitao Yu, Yacine Dalichaouch, Alexander R. Perry, Peter V. Czipott, and Carl E. Baum. On the wideband EMI response of a rotationally symmetric permeable and conducting target. *IEEE Trans. Geosci. Remote Sens.*, 39:1206–1213, June 2001. [33](#), [38](#)
- [8] Thomas H. Bell, Bruce J. Barrow, and Jonathan T. Miller. Subsurface discrimination using electromagnetic induction sensors. *IEEE Trans. Geosci. Remote Sens.*, 39:1286–1293, June 2001. [33](#), [38](#)
- [9] Leonard R. Pasion and Douglas W. Oldenburg. A discrimination algorithm for UXO using time domain electromagnetics. *J. Environ. Eng. Geophys.*, 6:91–102, 2001. [33](#), [38](#)
- [10] Yan Zhang, Leslie Collins, Haitao Yu, Carl E. Baum, and Lawrence Carin. Sensing of unexploded ordnance with magnetometer and induction data: Theory and signal processing. *IEEE Trans. Geosci. Remote Sensing*, 41:1005–1015, May 2003. [33](#)
- [11] Keli Sun, Kevin O'Neill, Fridon Shubitidze, Irma Shamatava, and Keith Paulsen. Fast data-derived fundamental spheroidal excitation models with application to UXO discrimination. *IEEE Trans. Geosci. Remote Sens.*, 43:2573–2583, Nov. 2005. [34](#), [39](#), [40](#), [41](#)

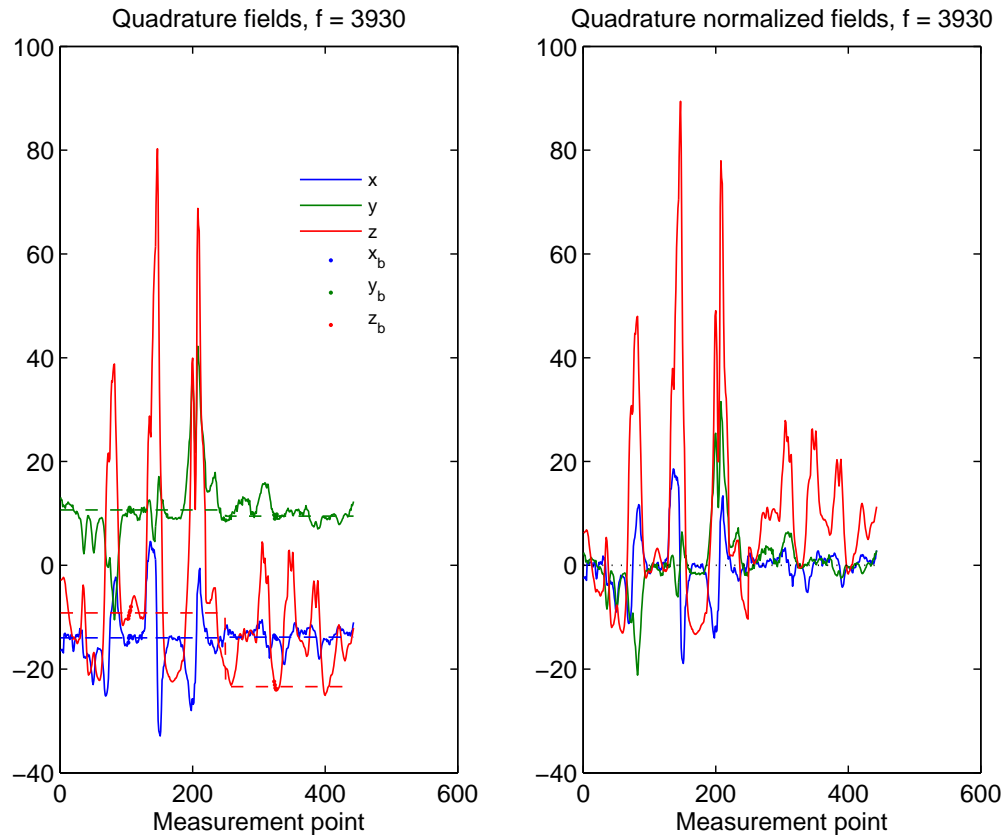
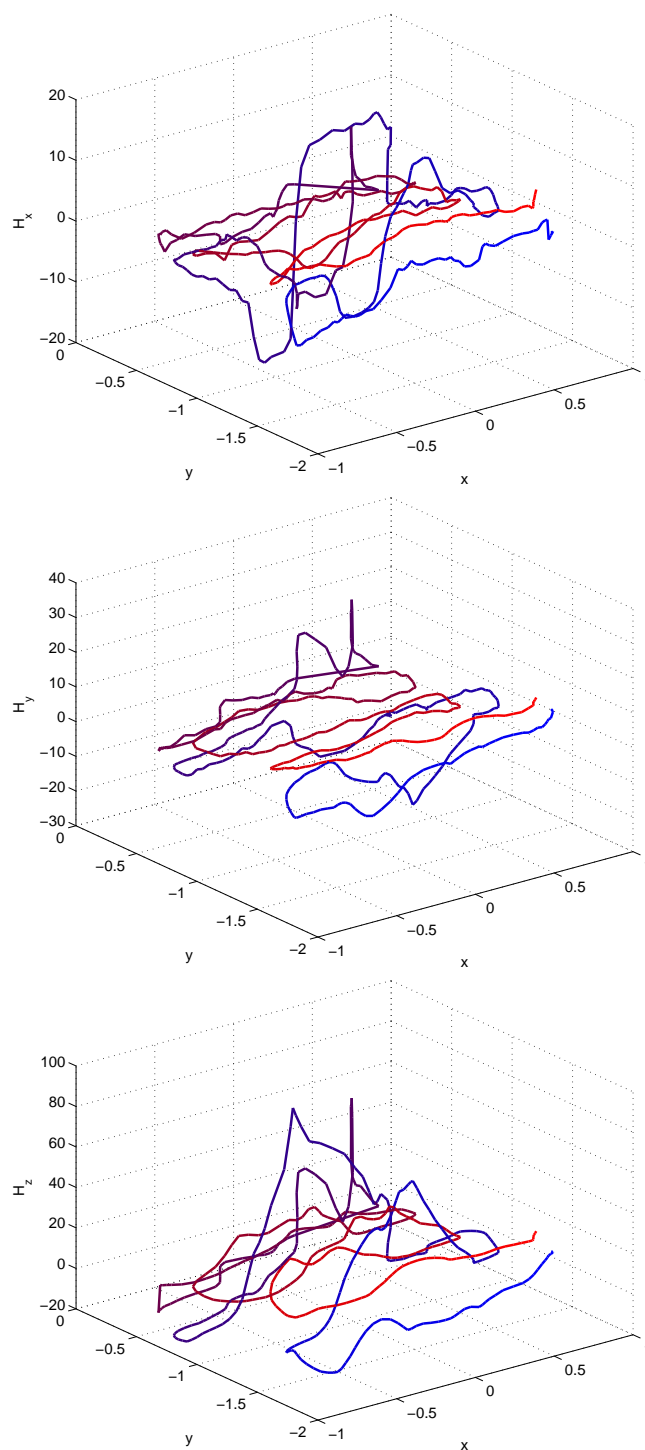


Figure C.3.9: Background-subtracted field at $f = 3930$ Hz, quadrature part.

- [12] Keli Sun, Kevin O'Neill, Benjamin Barrowes, Irma Shamatava, Juan Pablo Fernández, Fridon Shubitidze, and Keith Paulsen. Data-derived SEA for time domain EMI sensing of UXO. In Progress in Electromagnetics Research Symposium (PIERS) Proceedings, page 330, Beijing, Mar. 2007. [34](#)
- [13] Juan Pablo Fernández, Benjamin Barrowes, Kevin O'Neill, Irma Shamatava, Fridon Shubitidze, and Keli Sun. A data-derived time-domain SEA for UXO identification using the MPV sensor. In Russell S. Harmon, J. Thomas Broach, and John H. Holloway, Jr., editors, Detection and Sensing of Mines, Explosive Objects, and Obscured Targets XIII, volume 6953 of Proceedings of SPIE, pages 6953–1H, Bellingham, WA, Mar. 2008. [34](#), [40](#)
- [14] Fridon Shubitidze, Benjamin Barrowes, Irma Shamatava, Juan Pablo Fernández, and Kevin O'Neill. Data-derived generalized SEA applied to MPV TD data. In Applied Computational Electromagnetics Symposium (ACES), Niagara Falls, ON, Mar.–Apr. 2008. [34](#), [39](#)
- [15] Irma Shamatava, Fridon Shubitidze, Benjamin Barrowes, Eugene Demidenko, Juan Pablo Fernández, and Kevin O'Neill. The generalized SEA and a statistical signal processing approach applied to UXO discrimination. In Russell S. Harmon, J. Thomas Broach, and John H. Holloway, Jr., editors, Detection and Sensing of Mines, Explosive Objects, and Obscured Targets XIII, volume 6953 of Proceedings of SPIE, page 695353, Bellingham, WA, Mar. 2008. [34](#), [39](#)
- [16] I. J. Won, Dean A. Keiswetter, David R. Hanson, Elena Novikova, and Thomas M. Hall. Gem-3: A monostatic broadband electromagnetic induction sensor. J. Environ. Eng. Geophys., 2:53–64, Mar. 1997. [34](#)
- [17] I. J. Won, Dean A. Keiswetter, and Thomas H. Bell. Electromagnetic induction spectroscopy for clearing landmines. IEEE Trans. Geosci. Remote Sensing, 39:703–709, Apr. 2001. [34](#)
- [18] Benjamin E. Barrowes, Kevin O'Neill, et al. Handheld frequency domain vector EMI sensing for UXO discrimination. SERDP MM1537-FY06 Annual Report. Hanover, NH: U. S. Army Corps of Engineers, ERDC-CRREL, Dec. 2006. [34](#)

Figure C.3.10: Background-subtracted 3D fields at $f = 3930$ Hz.

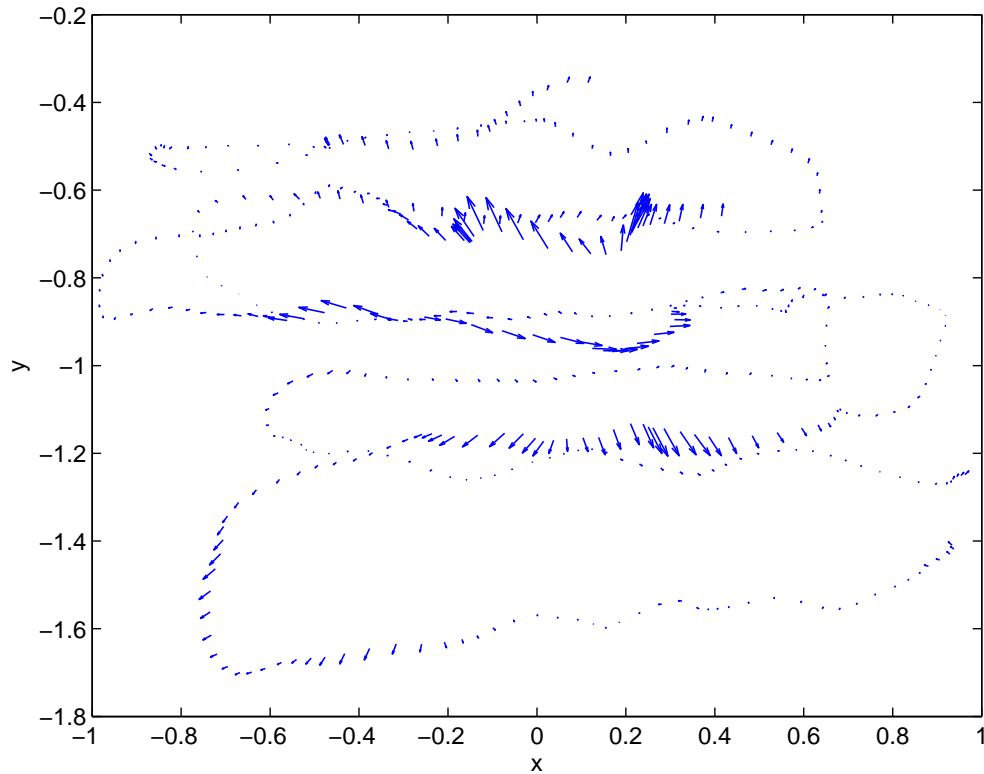


Figure C.3.11: Quiver plot showing the magnitudes of the x - and y -components of the quadrature part of the secondary field at $f = 3930$ Hz. Joining the tails of the arrows can give an approximate estimate of the locations of the targets.

- [19] William R. Smythe. Static and Dynamic Electricity. McGraw-Hill, New York, 3rd edition, 1968. [35](#), [70](#)
- [20] Julius Adams Stratton. Electromagnetic Theory. McGraw-Hill, New York, 1941. [35](#)
- [21] Derek F. Lawden. Elliptic Functions and Applications. Springer, New York, 1989. [35](#)
- [22] Digital compass users guide, OS1x00 & OS3x00. Fall River, MA: OceanServer Technology, Inc., 2007. [37](#)
- [23] Jean-Luc Boiffier. The Dynamics of Flight: The Equations. Wiley, Chichester, UK, 1998. [37](#)
- [24] Richard C. Aster, Brian Borchers, and Clifford H. Thurber. Parameter Estimation and Inverse Problems. Elsevier, Burlington, MA, 2005. [37](#), [41](#)
- [25] Itzhack Y. Bar-Itzhack and Kenneth A. Fegley. Orthogonalization techniques of a direction cosine matrix. IEEE Trans. Aerosp. Electron. Syst., AES-5:798–804, Sep. 1969. [37](#)
- [26] Norbert Geng, Carl E. Baum, and Lawrence Carin. On the low-frequency natural response of conducting and permeable targets. IEEE Trans. Geosci. Remote Sens., 37:347–359, Jan. 1999. [38](#)
- [27] Keli Sun, Kevin O’Neill, Benjamin Barrowes, Juan Pablo Fernández, Fridon Shubitidze, Irma Shamatava, and Keith Paulsen. Dumbbell dipole model and its application in UXO discrimination. In J. Thomas Broach, Russell S. Harmon, and John H. Holloway, Jr., editors, Detection and Remediation Technologies for Mines and Minelike Targets XI, volume 6217 of Proceedings of SPIE, page 621706, Bellingham, WA, Apr. 2006. [38](#)
- [28] Philip M. Morse and Herman Feshbach. Methods of Theoretical Physics. McGraw-Hill, New York, 1953. [39](#)
- [29] George Arfken. Mathematical Methods for Physicists. Academic Press, San Diego, 3rd edition, 1985. [40](#)

- [30] Lloyd Nicholas Trefethen. Numerical Methods in Matlab. SIAM, Philadelphia, 2000. 40
- [31] Per Christian Hansen. Rank-Deficient and Discrete Ill-Posed Problems: Numerical Aspects of Linear Inversion. SIAM, Philadelphia, 1998. 41
- [32] James R. Wait. A conducting sphere in a time varying magnetic field. Geophysics, 16:666–672, 1951. 41
- [33] J. E. Simms R. L. Van Dam and J. M. H. Hendrickx. Classification of magnetic susceptibility anomalies and their relevance to UXO detection. FastTIMES, 10(2):48–51, 2005. 45, 74, 87
- [34] Remke L. Van Dam, Jan M.H. Hendrickx, Bruce Harrison, Brian Borchers, David I. Norman, Samuel Ndur, Chris Jasper, Patrick Niemeyer, Robert Nartey, David Vega, Lucas Calvo, and Janet E. Simms. Spatial variability of magnetic soil properties. volume 5415, pages 665 – 675, Orlando, FL, United states, 2004. URL <http://dx.doi.org/10.1117/12.540693>. 45, 74, 87
- [35] R. J. Larson J. E. Simms and E. W. Smith. Uxo standardized test sites: Ypg soils description, 2003. URL <http://aec.army.mil/usaec/technology/uxo03c02.html>. 45, 74, 87
- [36] Benjamin Barrowes and Kevin O’Neill. Electromagnetic induction soil response and the gem-3d+. white paper, CRREL, April 2007. 50
- [37] J. R. Wait. A conducting sphere in a time varying magnetic field. Geophysics, 16:666–672, 1951. 52
- [38] J. R. Wait and K. P. Spies. Quasi-static transient response of a conducting and permeable sphere. Geophysics, 34:789–792, Oct. 1969. 52, 69
- [39] Nicolas Lhomme, Leonard R. Pasion, Stephen D. Billings, and Douglas W. Oldenburg. Inversion of frequency domain data collected in a magnetic setting for the detection of uxo. volume 6953, pages The International Society for Optical Engineering (SPIE) –, Orlando, FL, United states, 2008. URL <http://dx.doi.org/10.1117/12.780153>. 54
- [40] Leonard R. Pasion, Douglas W. Oldenburgs, Stephen D. Billings, and David Sinex. Soil compensation techniques for the detection of buried metallic objects using electromagnetic sensors. volume 6553, pages SPIE –, Orlando, FL, United states, 2007. URL <http://dx.doi.org/10.1117/12.728483>. 54
- [41] Kevin A. Kingdon, Leonard R. Pasion, and Douglas W. Oldenburg. Investigating the effects of soils with complex magnetic susceptibility on emi measurements using numerical modelling of maxwell’s equations. volume 7303, pages The International Society for Optical Engineering (SPIE) –, Orlando, FL, United states, 2009. URL <http://dx.doi.org/10.1117/12.818662>. 54
- [42] Y. Li and L.R. Pasion. Evaluating the effects of magnetic susceptibility in UXO discrimination problems. Poster Presented at Partners in Environmental Technology Technical Symposium and Workshop, Washington, DC, Dec. . sponsored by SERDP and ESTCP. 55, 78
- [43] L. Pasion, S. Walker, D. Oldenburg, S. Billings, and J. Foley. Evaluating the effectiveness of varying transmitter waveforms for UXO detection in magnetic soil environments. Symposium on the Application of Geophysics to Engineering and Environmental Problems, Atlanta, Georgia, April 3–7, 2005 . 55, 78
- [44] S. Walker, L. Pasion, S. Billings, Y. Li, J. Foley, and D. Oldenburg. Examples of the effect of magnetic soil environments on time domain electromagnetic data. Symposium on the Application of Geophysics to Engineering and Environmental Problems, April 3-7, 2005. 55, 56, 78
- [45] S. Billings, L. Pasion, D. Oldenburg, and J. Foley. The influence of magnetic viscosity on electromagnetic sensors. Proceedings of EUDEM-SCOT2, International Conference on Requirements and Technologies for the Detection, Removal and Neutralization of Landmines and UXO, 2003. 55, 66, 78, 83
- [46] Irma Shamatava, K. O’Neill, Fridon Shubitidze, Keli Sun, and Keith D. Paulsen. Treatment of a permeable non-conducting medium with the EMI-BOR program. Proceedings of SPIE - The International Society for Optical Engineering, 5794(PART I):287 – 295, 2005. ISSN 0277-786X. 55, 78
- [47] Fridon Shubitidze, Kevin O’Neill, Irma Shamatava, Keli Sun, and Keith Paulsen. Analyzing multi-axis data versus scalar data for UXO discrimination. Proceedings of SPIE - The International Society for Optical Engineering, 5794(PART I):336 – 345, 2005. ISSN 0277-786X. 55, 78

- [48] K. Sun, K. O'Neill, F. Shubitidze, I. Shamatava, and K.D. Paulsen. Discrimination of UXO buried under magnetic soil. Proceedings of SPIE - The International Society for Optical Engineering, 5794(PART I):308 – 319, 2005. ISSN 0277-786X. [55](#), [66](#), [78](#)
- [49] A preliminary investigation of the effects of soil electromagnetic properties on metal detectors. [55](#), [83](#)
- [50] K. O'Neill, F. Shubitidze, K. Sun, I. Shamatava, and K.D. Paulsen. EMI obscuration of buried UXO by geophysical magnetic permeability, anthropogenic clutter, and by magnitude disparities. Proceedings of the SPIE - The International Society for Optical Engineering, 5811(1):91 – 103, 2005. ISSN 0277-786X. [55](#), [66](#), [78](#)
- [51] G. Ware. Geonics em63 multichannel em data processing algorithms for target location and ordnance discrimination. Technical report, Environmental Security Technology Certification Program, UX-0035, 2003. [55](#), [78](#)
- [52] F. Shubitidze, K. O'Neill, S.A. Haider, Keli Sun, and K.D. Paulsen. Application of the method of auxiliary sources to the wide-band electromagnetic induction problem. IEEE Transactions on Geoscience and Remote Sensing, 40(4):928 – 42, 2002/04/. ISSN 0196-2892. [56](#)
- [53] I. Shamatava, F. Shubitidze, K. O'Neill, K. Sun, and K.D. Paulsen. An efficient, user-friendly program for computing electromagnetic induction (EMI) responses from heterogeneous objects subject to state-of-the-art sensors. Proceedings of the UXO/Countermining Forum, 2004. [56](#)
- [54] F. Shubitidze, K. O'Neill, K. Sun, I. Shamatava, and K.D. Paulsen. A hybrid full mas and combined mas/tsa algorithm for electromagnetic induction sensing. Applied Computational Electromagnetics Society Journal, 19(1 B):112 – 126, 2004. ISSN 1054-4887. [56](#)
- [55] Fridon Shubitidze, Kevin O'Neill, Irma Shamatava, Keli Sun, and Keith D. Paulsen. Fast and accurate calculation of physically complete EMI response by a heterogeneous metallic object. IEEE Transactions on Geoscience and Remote Sensing, 43(8):1736 – 1750, 2005. ISSN 0196-2892. [56](#), [78](#), [79](#), [80](#), [81](#), [82](#)
- [56] Beijia Zhang, Kevin O'Neill, and Jin Au Kong. Absolute calibration of EMI measurements and application to soil magnetic susceptibility inference. Journal of Environmental and Engineering Geophysics, 13(3):222 – 235, 2008. ISSN 10831363. [59](#)
- [57] L. Tsang, J. A. Kong, and K. H. Ding. Scattering of Electromagnetic Waves: Theories and Applications. Wiley-Interscience, 2000. [61](#)
- [58] F. Shubitidze, K. O'Neill, I. Shamatava, K. Sun, and K.D. Paulsen. Analyzing the effects of conductive and permeable soil on the EMI response for UXO discrimination. Mathematical Methods in Electromagnetic Theory, MMET, Conference Proceedings, pages 455 – 457, 2004. [66](#)
- [59] Fridon Shubitidze, Kevin O'Neill, Irma Shamatava, Keli Sun, and Keith Paulsen. Analysis of geological soil effects on EMI responses relevant to UXO discrimination. Proceedings of SPIE - The International Society for Optical Engineering, 5794 (PART I):296 – 307, 2005. ISSN 0277-786X. [66](#)
- [60] D.C. Fraser. Magnetite mapping with a multicoil airborne electromagnetic system. Geophysics, 46(11):1579 – 1593, 1981. ISSN 00168033. [66](#)
- [61] Zhiyi Zhang and D.W. Oldenburg. Recovering magnetic susceptibility from electromagnetic data over a one-dimensional earth. Geophysical Journal International, 130(2):422 – 434, 1997. ISSN 0956540X. [66](#)
- [62] Zhiyi Zhang and Douglas W. Oldenburg. Simultaneous reconstruction of 1-d susceptibility and conductivity from electromagnetic data. Geophysics, 64(1):33 – 47, 1999. ISSN 00168033. [66](#)
- [63] Les P. Beard and Jonathan E. Nyquist. Simultaneous inversion of airborne electromagnetic data for resistivity and magnetic permeability. Geophysics, 63(5):1556 – 1564, 1998. ISSN 00168033. [66](#)
- [64] Haoping Huang and I. J. Won. Characterization of UXO-like targets using broadband electromagnetic induction sensors. IEEE Trans. on Geosci. Remote Sens., 41(3):652–663, March 2003. [66](#), [67](#)
- [65] Haoping Huang and Douglas C. Fraser. Airborne resistivity and susceptibility mapping in magnetically polarizable areas. Geophysics, 65(2):502 – 511, 2000. ISSN 00168033. [66](#)

- [66] Beijia Zhang, Kevin O'Neill, Tomasz M. Grzegorzczuk, and Jin Au Kong. Use of EMI response coefficients from spheroidal excitation and scattering modes to classify objects via SVM. volume 6217, page 621708. SPIE, 2006. URL <http://link.aip.org/link/?PSI/6217/621708/1>. 67
- [67] Xudong Chen. Inverse Problems in Electromagnetics. PhD thesis, Massachusetts Institute of Technology, June 2005. 67
- [68] Ping Gao, L. Collins, P.M. Garber, N. Geng, and L. Carin. Classification of landmine-like metal targets using wideband electromagnetic induction. IEEE Trans. Geosci. Remote Sens. (USA), 38(3):1352 – 61, 2000/05/. ISSN 0196-2892. 67, 78, 88
- [69] S. J. Norton and I. J. Won. Identification of buried unexploded ordnance from broadband electromagnetic induction data. IEEE Trans. on Geoscience and Remote Sensing, 39(10):2253–61, Oct. 2001. 67
- [70] J. P. Fernández, B. Barrowes, K. O'Neill, Irma Shamatava, F. Shubitidze, and Keli Sun. A data-derived time-domain SEA for UXO identification using the MPV sensor. SPIE, 2008. 67
- [71] B. E. Barrowes. Electromagnetic Scattering and Induction Models for Spheroidal Geometries. PhD thesis, Massachusetts Institute of Technology, January 2004. 69
- [72] C. O. Ao. Electromagnetic Wave Scattering by Discrete Random Media with Remote Sensing Applications. PhD thesis, Massachusetts Institute of Technology, May 2001. 69
- [73] Henning Braunsch. Methods in Wave Propagation and Scattering. PhD thesis, Massachusetts Institute of Technology, February 2001. 69
- [74] J. van Bladel. Electromagnetic Fields. Hemisphere Pub. Corp., 1985. 70, 97
- [75] Robert A. Schill Jr. General relation for the vector magnetic field of a circular current loop: A closer look. IEEE Transactions on Magnetics, 39(2):961–967, March 2003. 70, 97
- [76] D. E. Ferguson. Fibonacci searching. Communications of the ACM, 3(12):648, 1960. 71
- [77] Keli Sun, K. O'Neill, F. Shubitidze, S.A. Haider, and K.D. Paulsen. Simulation of electromagnetic induction scattering from targets with negligible to moderate penetration by primary fields. IEEE Transactions on Geoscience and Remote Sensing, 40(4):910 – 27, 2002/04/. ISSN 0196-2892. 71
- [78] J. Wait. Electromagnetic Wave Theory. Harper and Row, New York, 1985. 74
- [79] D.M. Cargile, H. H. Bennett, R. A. Goodson, T. A. DeMoss, , and E. R. Cespedes. Advanced UXO detection/discrimination technology demonstration, kahoolawe, hawaii. Technical report, U.S. Army Engineer Research and Development Center. Department of Defense, 2004. Technical Report UX-0035, Environmental Security Technology Certification Program. 78
- [80] L. R. Pasion, S. D. Billings, and D. Oldenburg. Evaluating the effects of magnetic susceptibility. UXO Discrimination Problems SAGEEP Conference, Feb 10-14 2002. 78
- [81] Remke L. Van Dam, J. Bruce J. Harrison, Jan M.H. Hendrickx, Brian Borchers, Ryan E. North, Janet E. Simms, Chris Jasper, Christopher W. Smith, and Yaoguo Li. Variability of magnetic soil properties in hawaii. Proceedings of SPIE - The International Society for Optical Engineering, 5794(PART I):157 – 164, 2005. ISSN 0277-786X. 78
- [82] L. Carin, H. Yu, Y. Dalichaouch, A.R. Perry, P.V. Czipott, and C.E. Baum. On the wideband EMI response of a rotationally symmetric permeable and conducting target. IEEE Transactions on Geoscience and Remote Sensing, 39(6):1206 – 1213, 2001. ISSN 0196-2892. 78, 88
- [83] J.T. Miller, T.H. Bell, J. Soukup, and D. Keiswetter. Simple phenomenological models for wideband frequency-domain electromagnetic induction. IEEE Transactions on Geoscience and Remote Sensing, 39(6):1294 – 1298, 2001. ISSN 0196-2892. 78, 88
- [84] Yan Zhang, L. Collins, Haitao Yu, C.E. Baum, and L. Carin. Sensing of unexploded ordnance with magnetometer and induction data: theory and signal processing. IEEE Transactions on Geoscience and Remote Sensing, 41(5):1005 – 15, 2003/05/. ISSN 0196-2892. 78, 88
- [85] Discrimination and classification of buried unexploded ordnance using magnetometry. 78, 88

- [86] N. Geng, C.E. Baum, and L. Carin. On the low-frequency natural response of conducting and permeable targets. IEEE Trans. Geosci. Remote Sens. (USA), 37(1):347 – 59, 1999/01/. ISSN 0196-2892. 78, 88
- [87] L. R. Pasion and D. W. Oldenburg. A discrimination algorithm for UXO using time domain electromagnetics. J. Engg & Envir. Geophys., Vol. 20:pp91–102, 2001. 78, 88
- [88] Keli Sun, Kevin O'Neill, Fridon Shubitidze, Irma Shamatava, and Keith D. Paulsen. Fast data-derived fundamental spheroidal excitation models with application to UXO discrimination. IEEE Transactions on Geoscience and Remote Sensing, 43(11):2573 – 2582, 2005. ISSN 0196-2892. 78, 79, 80, 88
- [89] T.H. Bell, B.J. Barrow, and J.T. Miller. Subsurface discrimination using electromagnetic induction sensors. IEEE Transactions on Geoscience and Remote Sensing, 39(6):1286 – 93, 2001/06/. ISSN 0196-2892. 78
- [90] F. Shubitidze, K. O'Neill, I. Shamatava, K. Sun, and K.D. Paulsen. Analysis of EMI scattering to support UXO discrimination: Heterogeneous and multi objects. Proceedings of SPIE - The International Society for Optical Engineering, 5089(2): 928 – 939, 2003. ISSN 0277-786X. 78, 79, 80, 81, 82
- [91] Serdp: Statement of need, 2006. URL <http://www.serdp.org/>. 78
- [92] M.G. Andreassen. Scattering from bodies of revolution. IEEE Transactions on Antennas and Propagation, AP-13(2):303 – 310, 1965. URL <http://dx.doi.org/10.1109/TAP.1965.1138406>. 79, 85
- [93] Walter L. Anderson. Fast hankel transforms using related and lagged convolutions. ACM Transactions on Mathematical Software, 8(4):344 – 368, 1982. ISSN 0098-3500. 79, 85
- [94] Gregory A. Newman, Gerald W. Hohmann, and Walter L. Anderson. Transient electromagnetic response of a three-dimensional body in a layered earth. Geophysics, 51(8):1608 – 1627, 1986. ISSN 0016-8033. 79
- [95] I. J. Won, D. A. Keiswetter, and T. H. Bell. Electromagnetic induction spectroscopy for clearing landmines. IEEE Trans. on Geoscience and Remote Sensing, 39(4):703–709, April 2001. 84, 88
- [96] J.D. McNeill and M. Bosnar. Application of time domain electromagnetic techniques to UXO detection. 1996. 84, 88
- [97] F. Shubitidze, K. O'Neill, B.E. Barrowes, I. Shamatava, J.P. Fernandez, K. Sun, and K.D. Paulsen. Application of the normalized surface magnetic charge model to UXO discrimination in cases with overlapping signals. Journal of Applied Geophysics, 61(3-4):292 – 303, 2007. ISSN 0926-9851. 88
- [98] F. Shubitidze, B. Barrowes, J. P. Fernández, Irma Shamatava, and K. O'Neill. NSMC for UXO discrimination in cases with overlapping signatures. SPIE, 2007. 88, 120, 127
- [99] F. Shubitidze, B. Barrowes, and K. O'Neill. Normalized surface magnetic charge for UXO discrimination: multiple objects. SERDP Partners Symposium, November 2006. Poster. 88, 120
- [100] F. Shubitidze, B. Barrowes, J. P. Fernández, and K. O'Neill. Combined NSMC and Pseudo-Spectral Finite-Difference Method for Inverting a Buried Object Location. Symposium on the Application of Geophysics to Engineering and Environmental Problems, 2007 . 88, 89
- [101] T.H. Bell, B.J. Barrow, and J.T. Miller. Subsurface discrimination using electromagnetic induction sensors. IEEE Trans. on Geoscience and Remote Sensing, 39(6):1286 – 1293, June 2001. 88
- [102] Leonard R. Pasion, Stephen D. Billings, Douglas W. Oldenburg, and Sean E. Walker. Application of a library based method to time domain electromagnetic data for the identification of unexploded ordnance. J. Appl. Geophys., 61:279–291, Mar. 2007. 88
- [103] K. Sun, K. O'Neill, C.-C. Chen, H. S. Youn, F. Shubitidze, I. Shamatava, , and K.D. Paulsen. Highly contaminated UXO sites: combination of GPR and EMI for discrimination of clustered scatterers. SAGEEP, 2005. 88
- [104] F. Shubitidze, B. Barrowes, I. Shamatava, J. P. Fernández, and K. O'Neill. Data derived generalized SEA applied to MPV TD data. ACES conference, March 30 - April 4, 2008. 88
- [105] Irma Shamatava, F. Shubitidze, Eugene Demidenko, B. Barrowes, J. P. Fernández, and K. O'Neill. The Generalized SEA and a statistical signal processing approach applied to UXO discrimination. SPIE, 2008. 88, 127

- [106] F. Shubitidze, B. E. Barrowes, K. O'Neill, I. Shamatava, J. P. Fernández, K. Sun, and K.D. Paulsen. The generalized SEA to UXO discrimination in geophysical environments producing EMI response. Proceedings of the SPIE - The International Society for Optical Engineering, 2006. 88
- [107] Fridon Shubitidze, Juan Pablo Fernández, Benjamin E. Barrowes, Irma Shamatava, and Kevin O'Neill. Normalized Surface Magnetic Source model applied to Camp Sibert data. In Applied Computational Electromagnetics Symposium (ACES), Monterey, CA, Mar. 2009. 89
- [108] Fridon Shubitidze, David Karkashadze, Benjamin E. Barrowes, and Kevin O'Neill. A new physics based approach for estimating a buried object's location, orientation and magnetic polarization from EMI data. Journal of Environmental and Engineering Geophysics (JEEG), accepted for publication. 89
- [109] F. Shubitidze, B. Barrowes, I. Shamatava, J. P. Fernández, and K. O'Neill. Combining NSMC and High Quality MPV-TD Data for UXO Discrimination. Proc. IEEE Int. Geosci. Remote Sensing Symp. (IGARSS), 2008. 89
- [110] F. Shubitidze, D. Karkashadze, B. Barrowes, and K. O'Neill. An analytical expression for estimating a buried object's location, orientation and magnetic polarization to support UXO discrimination. XIIth International Seminar/Workshop on Direct and Inverse Problems of Electromagnetic and Acoustic Wave Theory (DIPED), 2007. 89, 127
- [111] Xudong Chen, Kevin O'Neill, Tomasz M. Grzegorzczuk, and Jin Au Kong. Spheroidal mode approach for the characterization of metallic objects using electromagnetic induction. IEEE Trans. on Geoscience and Remote Sensing, 45(3):697–706, March 2007. 92, 127
- [112] H. Braunisch, C. O. Ao, K. O'Neill, and J. A. Kong. Magnetoquasistatic response of conducting and permeable spheroid under axial excitation. IEEE Trans. on Geoscience and Remote Sensing, 39(12):2689–2701, December 2001. 92
- [113] C. O. Ao, H. Braunisch, K. O'Neill, and J. A. Kong. Quasi-magnetostatic solution for a conducting and permeable spheroid with arbitrary excitation. IEEE Trans. on Geoscience and Remote Sensing, 40(4):887–897, April 2002. 92, 93, 96
- [114] Leslie Collins, Ping Gao, Deborah Schofield, John P. Moulton, Lawrence C. Makowsky, Denis M. Reidy, and Richard C. Weaver. A statistical approach to landmine detection using broadband electromagnetic induction data. IEEE Trans. on Geosci. Remote Sens., 40(4):950–962, April 2002. 92
- [115] Kevin O'Neill, Keli Sun, Fridon Shubitidze, Irma Shamatava, and Keith D. Paulsen. Accounting for the effects of widespread discrete clutter in subsurface EMI remote sensing of metallic objects. IEEE Trans. on Geosci. Remote Sens., 44(1):32–46, January 2006. 92
- [116] Ashley B. Tarokh and Eric L. Miller. Subsurface sensing under sensor positional uncertainty. IEEE Trans. on Geosci. Remote Sens., 45(3):675–688, March 2007. 92
- [117] Lihan He, Shihao Ji, Waymond R. Scott Jr., and Lawrence Carin. Adaptive multimodality sensing of landmines. IEEE Trans. on Geosci. Remote Sens., 45(6):1756–1774, June 2007. 92
- [118] David Williams, Chunping Wang, Xuejun Liao, and Lawrence Carin. Classification of unexploded ordnance using incomplete multisensor multiresolution data. IEEE Trans. on Geosci. Remote Sens., 45(7):2364–2373, July 2007. 92
- [119] Ping Gao, Leslie Collins, Philip M. Garber, Norbert Geng, and Lawrence Carin. Classification of landmine-like metal targets using wideband electromagnetic induction. IEEE Trans. on Geoscience and Remote Sensing, 38(3):1352–1361, May 2000. 92
- [120] Yan Zhang, Xuejun Liao, and Lawrence Carin. Detection of buried targets via active selection of labeled data: Application to sensing subsurface UXO. IEEE Trans. on Geosci. Remote Sens., 42(11):2535–2543, November 2004. 92
- [121] Beijia Zhang, Kevin O'Neill, Jin Au Kong, and Tomasz M. Grzegorzczuk. Support vector machine and neural network classification of metallic objects using coefficients of the spheroidal mqs response modes. IEEE Trans. on Geoscience and Remote Sensing, 2007. accepted for publication. 92, 127
- [122] Ashley B. Tarokh and Eric L. Miller. Subsurface sensing under sensor positional uncertainty. IEEE Trans. on Geoscience and Remote Sensing, 45(3):675–688, March 2007. 92
- [123] Beijia Zhang, Kevin O'Neill, Tomasz M. Grzegorzczuk, and Jin Au Kong. Use of EMI response coefficients from spheroidal excitation and scattering modes to classify objects via SVM. In Proc. of SPIE, volume 6217, pages 621708(1–11), 2006. 92

- [124] Keli Sun, Kevin O'Neill, Fridon Shubitidze, Irma Shamatava, and Keith D. Paulsen. Theoretical analysis and range of validity of TSA formulation for application to UXO discrimination. IEEE Trans. on Geoscience and Remote Sensing, 42 (9):1871–1881, September 2004. [93](#)
- [125] Irma Shamatava, Kevin O'Neill, Fridon Shubitidze, Keli Sun, and Chi O. Ao. Evaluation of approximate analytical solutions for EMI scattering from finite objects of different shapes and properties. In Proc. IEEE Int. Geosci. Remote Sensing Symp. (IGARSS), pages 1550–1552a, 2002. Toronto, Canada. [93](#), [97](#)
- [126] Tomasz M. Grzegorzczuk, Benjamin E. Barrowes, and Kevin O'Neill. Modeling highly permeable and conductive ellipsoidal clutter for the detection of UXO in the electromagnetic induction regime. Proc. IEEE Int. Geosci. Remote Sensing Symp. (IGARSS), 2008. [93](#), [127](#)
- [127] E. W. Hobson. The theory of spherical and ellipsoidal harmonics. Chelsea publishing company, 1965. [93](#)
- [128] Oliver Dimon Kellogg. Foundations of Potential Theory. Springer-Verlag, 1967. [93](#)
- [129] William D. MacMillan. The theory of the potential. Dover, 1958. [95](#)
- [130] Edmund C. Stoner. The demagnetizing factors for ellipsoids. Philosophical Magazine, 36(263):803–820, December 1945. [96](#)
- [131] J. A. Osborn. Demagnetization factors of the general ellipsoid. Physical Review, 67(11-12):351–357, June 1-15 1945. [96](#)
- [132] Fridon Shubitidze, Kevin O'Neill, Shah A. Haider, Keli Sun, and Keith D. Paulsen. Application of the method of auxiliary sources to the wide-band electromagnetic induction problem. IEEE Trans. on Geosci. Remote Sens., 40(4):928–942, April 2002. [97](#)
- [133] W. R. Smythe. Static and Dynamic Electricity. McGraw-Hill, 3rd edition, 1968. [97](#)
- [134] F. Shubitidze, K. O'Neill, B. Barrowes, J. P. Fernández, I. Shamatava, K. Sun, and K.D. Paulsen. Application of the normalized surface magnetic charge model to UXO discrimination in cases with overlapping signals. J. Appl. Geophys., 61 (3-4):292–303, Mar. 2007. [120](#), [127](#)
- [135] J. P. Fernández, B. Barrowes, K. O'Neill, Irma Shamatava, and F. Shubitidze. A vector handheld frequency-domain sensor for UXO identification. SPIE, 2009. [127](#)
- [136] J. P. Fernández, Keli Sun, B. Barrowes, K. O'Neill, Irma Shamatava, and F. Shubitidze. Inferring the location of buried UXO using a support vector machine. SPIE, 2007. [127](#)
- [137] Irma Shamatava, B. Barrowes, F. Shubitidze, J. P. Fernández, and K. O'Neill. Estimating soil's effective magnetic susceptibility from EMI data. SPIE, 2007. [127](#)
- [138] F. Shubitidze, B. E. Barrowes, K. O'Neill, I. Shamatava, K. Sun, and K.D. Paulsen. Total normalized surface magnetic charge for UXO discrimination. NATO Advanced Study Institute "Imaging for Detection and Identification", 23 July–5 August 2006. Ciocco, Italy. [127](#)
- [139] F. Shubitidze, B. Barrowes, K. O'Neill, and I. Shamatava. Advanced EMI modeling and processing approaches for UXO discrimination. Proceedings of the 11-th International Conference on Mathematical Methods in Electromagnetic Theory, June-26-29, 2006. Kharkiv, Ukraine. [127](#)